Hyperthermal Molecular Beam Dry Etching of III-V Compound Semiconductors

by

Isako Hoshino

B. Sc., Materials Science and Engineering
Massachusetts Institute of Technology (1989)

Submitted to the Department of Materials Science and Engineering
in partial fulfillment of the requirements for the degree of

Doctor of Philosophy

in
Electronic Materials

at the

Massachusetts Institute of Technology

June 1997

© Massachusetts Institute of Technology 1997.
All rights reserved.

Author ______________________________
Department of Materials Science and Engineering
2 May 1997

Certified by ______________________________
Clifton G. Fonstad, Jr.
Professor of Electrical Engineering
Thesis Supervisor

Accepted by ______________________________
Linn W. Hobbs
John F. Elliott Professor of Materials
Chairman, Departmental Committee on Graduate Students

MASSACHUSETTS INSTITUTE
OF TECHNOLOGY

JUN 1 6 1997

Science

Hyperthermal Molecular Beam Dry Etching of III-V Compound Semiconductors

by

Isako Hoshino

Submitted to the Department of Materials Science and Engineering
on 2 May 1997, in partial fulfillment of the
requirements for the degree of
Doctor of Philosophy in Electronic Materials

Abstract

A novel ultra-high vacuum (UHV) compatible dry etch reactor was designed, constructed, and characterized. The etch mechanism is dependent solely on the chemical reactivity of a neutral etchant gas, enhanced by its kinetic energy, and does not utilize any plasma or ion source in obtaining directionality or acceleration. This thesis work is the first reported demonstration of molecular chlorine etch of InP at chlorine pressures of 1×10^{-7} torr with no ion, plasma, photon, or e-beam assistance.

The etchant gas was accelerated to supersonic speeds through the use of free-jet expansion nozzle coupled with a skimmer in differentially pumped vacuum chambers. By varying the nozzle temperature and the concentration of chlorine in a gas matrix, the energy of the incident beam can be varied. The directionality of the molecular beam produced was maintained by using it in an UHV environment with operating background pressures of 1×10^{-7} torr or lower. As the translationally-activated molecules contribute to collision-induced dissociative chemisorption, a chemical reaction can be initiated in an otherwise unreactive material system.

Two quantitative *in–situ* process monitoring methods were also devised for this work: (1) a surface roughness measurement method using reflected 633 nm wavelength He–Ne laser intensity, and (2) a low-temperature calibration of the substrate holder thermocouple through monitoring the vacuum background pressure increase during the initial stages of substrate temperature ramping.

InP and GaAs substrates were etched using a translationally-activated molecular chlorine beam. Both directional and (111) crystallographic preferential etch profiles were observed. The crystallographic preferential etch was the predominant etch profile, while directional etching was achieved when the beam energy was increased. Etch rates ranging from $0.2\,\mu$m/hour to $2.0\,\mu$m/hour were obtained at substrate temperatures ranging from 200°C to 350°C under various beam energy conditions. Some Cl_2–InP etch mechanics are also proposed and discussed in this thesis.

Thesis Supervisor: Clifton G. Fonstad, Jr.
Title: Professor of Electrical Engineering

Acknowledgments

My tenure as a graduate student turned out to become one of the bleakest era of my life. I lost several people whom I cared or loved dearly to the Elysian Fields, and was faced with many devastating disappointments. As a result, I had a very difficult time keeping one foot in front of the other. The light at the end of the tunnel always felt very elusive, and many times, it felt as though I would never find it, let alone get near it. I cannot but wonder if I would have been able to get through it all without the countless supports I received from my family and friends. As I am writing up the last few sentences of my Ph.D. thesis and dancing away towards the exit door (the *front* door, not the emergency exit!), I would like to take this opportunity to acknowledge those who were vital to my success.

My first thanks goes to my thesis advisor, Prof. Clif Fonstad, for his kindness, patience, support, and understanding throughout my graduate career; and also for allowing me the freedom to take control of every aspect of my thesis project. I am certain that the skills I have gained through dealing with many aspects in and out of the labs will be put to great use once I am out in the "real world."

I also would like to thank my thesis committee members, Professors Klavs Jensen, Lionel Kimerling, and Michael Rubner for their time and their patience, and supplying me with the extra encouragements whenever one was needed. Through them, I was able to retain my identity as a Materials Scientist (more of an Engineer, actually) surviving amidst hoards of Electrical Engineers.

My most heart-felt thanks goes to Dr. Leonard Ketelsen, my fellowship mentor, advisor, and friend at AT&T Bell Laboratories, now Lucent Technologies. It was pure chance that we were assigned to work together under the GRPW Fellowship. However, through the years, he has become one of my foremost supporter in my struggles. His unconditional support and understanding in whatever I did or believed, and his firm belief in my potentials and abilities were invaluable. I am at a loss for words to express my thanks to him. Thank you Len, for *everything.*

Thank you Dr. Cathy Lore for helping me pull out of my darkest days. I probably would not have made it through and be here if you were not available to see me that day, right before my frantic flight to Phoenix. Your guidance through my search of self has helped me regain my equilibrium and my life. Thank you!

I am grateful to all my colleagues in the Compound Semiconductor Materials and

Devices Research group, past and present, for making the working environment pleasant. I've been here waaaay too long, and since the list of them has grown considerably, I will not be able to list the names of every single one of them. But to those who did help me, you have my most sincere thanks. Special recognitions go to my officemates Lung-Han Peng and Steve Patterson, who sat through all my "babbling" sessions and tears with sympathetic ears. You two are *the* best. Thank you Prof. Sheila Prasad for all her warm support and advice, and for those constant reminders so that I would not forget to do one of the basic necessities of survival: "Eat, Isako, EAT!" Thank you Raj Aggarwal for 10 years worth of camaraderie, Janet Pan for all those interesting late-night conversations during the endless lab hours, Krishna Shenoy for his smiles and bringing reality back into my head, Joe Ahadian for his unwavering faith in my abilities, and Yakov Royter for "letting me play with his Mac." Thank you Tom Broekaert, Geoff Burns, Woo-Young Choi, Richard "Yosef" Singer, and Jim Vlcek for welcoming me into the group so long ago. I will never forget how all of you gave me the ultimate crash course in learning how to literally disassemble the MBE and put it back together in a different lab in a span of few days on my first day on the job. Perhaps that fearless attitude towards the "mother of all vents" prompted me to singly take on the monster KBE project, which took a Herculean effort and blood sacrifices to get this far... Thank you Henry Choy for your endless enthusiasm and energy which inspired me, and gave me the sorely-needed second breath of life during the last few months of my graduate career. Good luck to Donald Crankshaw whom I'm leaving to fend by himself against the onerous SPARCs, Macs, and Wintels as the new sys. admin., but I firmly believe they are in good, capable, and caring hands. And to the remaining group members, a "good luck" wish to your futures!

My appreciation also extends to Steve Goldstein at Analog Devices for volunteering for the tedious task of proof-reading my thesis, and to Aitor Postigo-Resa for helping me getting started with the laser reflectance roughness measurement idea. Thank you to Angela Odoardi Mickunas for patiently dealing with all those endless piles of purchasing paperwork my project, in conjunction with the ever-so-mucked-up EREQ–SAP, has generated (yes, *seven* requisition books worth of PO's!!!). Smiles and friendly conversation from Charmaine Cudjoe and Olga Arnold were always a pleasure everyday.

I am eternally grateful to Livia Racz, Grace Chen, Matt Machlis, Andrew Tomkins, Sharon Furcone, Jeff LeBlanc, and Andy Karanicolas. Thank you so much for always being there when I needed a friend. I would have gone completely insane from loneliness and general desperation long ago (I'm not saying that I *didn't* go nuts for other reasons) without help from all of you.

My thank you's continue on to my coaches, Mr. Harold "Hatch" Brown of the varsity sailing team, and Mr. Pasquale "Range, Melaragno" Melaragno of the varsity pistol team, both now happily retired, for providing me with the sanctuaries to escape to in time of need, and for all those warm encouragements and advices I received. They have become my second fathers and I will forever cherish all the memories of their gentle

kindness.

(...I sometimes wonder what would have happened if on that fateful Thursday afternoon during the first week of my freshmen year, I didn't blow off the tennis team tryouts and never visited the Sailing Pavilion... For whatever whimsical reason I decided to go "check out the sailing team" that day, I'm really glad that I did, as my life has never been the same since and has given me much joy in the world. But I digress...)

Last but not least, to my oldest MIT friend and sailing buddy for over 11 years, "Mr. Sail-Low" Marc Lie. Thank you for helping and seeing me though all the emotional rollercoasters I experienced all these years, by being the stabilizer I needed to regroup myself and find the strength to face the facts and the future. You're the best partner one can ever hope for, and I am ever so grateful that you are also my friend. If you ever need a "half-pint" crew, you know where to find me.

All have left MIT long ago, but I couldn't have made it through all these difficult and depressing years without all the care, kindness and support from all of them. Thank you everybody, again!

I have learned the true values of friendship in the past few years, but more strongly, the value of a close-knit family. Mom, Boone, Denise, Gene and Kenton... We were separated by at least 3000 miles (more like 8000 miles), but the thought of a growing family has been the greatest highlights of my life during the past few years. I love you all dearly, and I hope you are proud of me as much as I am of you. Thank you so much for your support and love. To not-so-little Bleach, I send a big furry hug for brightening up my day-to-day life.

And to Dad... It's probably not quite the "doctor" you had in mind, but finally I am "Dr. Hoshino"! I really wished you could have been here to witness my accomplishments. I love you and miss you very much, and always will.

Some interesting statistics for the record — during my graduate career:

- number of nuts and bolts used to construct the KBE system: approximately 1200
- total known purchase amount made (sans shipping, over-head, etc.) for the construction of the KBE system: $ 247,085.20
- total stipend, tuition, and health insurance cost spent (yes, graduate students *are* expensive...): $ 324,890
- ...of which covered by fellowship granted from AT&T GRPW: $ 265,108
- raw flight miles traveled on United Airlines between November 1992 and March 1993: 76,186 miles
- total frequent flier mileage earned on United Airlines: 420,546 miles
- total free domestic airplane tickets earned on United Airlines: 28 roundtrips

Dedication

To the one who dedicated his life work in hopes of saving the lives of others—

Takao Hoshino, M. D., D. M. Sc.

Professor of Neurosurgery
Brain Tumor Research Center
University of California, San Francisco

February 18, 1937 – January 28, 1993

Table of Contents

Table of Contents . . . 11
List of Figures . . . 15
List of Tables . . . 21

1 Introduction **23**
1.1 Motivation . . . 23
1.2 Available Etch Methods . . . 24
1.3 Thesis Project . . . 26
1.4 Thesis Organization . . . 27

2 Background **29**
2.1 Supersonic Nozzles . . . 29
2.2 Free Jet Expansion and Freezing . . . 33
2.3 Seeding . . . 36
2.4 Skimmer . . . 37
2.5 Maintaining the Molecular Flow Regime . . . 40

3 Kinetic Beam Etch System Design **43**
3.1 Introduction . . . 43
3.2 Ultra-High Vacuum Requirements . . . 45
3.2.1 Differentially Pumped UHV Chambers . . . 46
3.2.2 Pumps . . . 47
3.2.3 System Bake-out . . . 49
3.3 The Source Chamber . . . 50
3.3.1 Design Parameters . . . 50
3.3.2 Skimmer . . . 50
3.3.3 Nozzle Stage . . . 53
3.4 Source Flange . . . 54

3.5 The Main Chamber . . . 54
3.5.1 Substrate Manipulator . . . 56
3.5.2 Laser Reflectivity Measurement . . . 57
3.5.3 Residual Gas Analyzer . . . 57
3.6 The Transfer Tube . . . 58
3.6.1 Sample Loading Port . . . 60
3.7 The Process Control System . . . 60
3.7.1 The Nozzle . . . 60
3.7.2 Nozzle Heater . . . 63
3.7.3 Gas Controllers . . . 64

4 KBE System Operation **67**
4.1 Substrate Preparation . . . 67
4.1.1 Substrate Patterning . . . 67
4.1.2 Substrate Mounting . . . 68
4.2 Etchant Preparation . . . 69
4.2.1 Nozzle . . . 69
4.2.2 Gas Preparation . . . 70
4.3 *In-Situ* Measurement Procedures . . . 71
4.3.1 Pressure Measurements . . . 71
4.3.2 Laser Reflectivity Measurements . . . 73
4.3.2.1 Surface Roughness Measurements . . . 73
4.3.2.2 Oxide Desorption Temperature Determination . . . 76
4.3.2.3 Laser Reflectivity Measurement Plot Characteristics . . . 77
4.4 The Etch Run . . . 84
4.5 Vacuum Chamber Maintenance . . . 87

5 Experimental Results **89**
5.1 Methane–Hydrogen System . . . 89
5.2 Chlorine–Hydrogen System . . . 91
5.3 Data Analysis for InP System . . . 91
5.3.1 Etch Mechanics of InP and Molecular Chlorine . . . 91
5.3.2 Desorbed Gas Species . . . 93
5.3.3 Effect of Substrate Heating . . . 94
5.3.3.1 Etch Morphology . . . 94
5.3.3.2 Etch Rate . . . 102

5.3.4 Etch Profile 104
5.3.5 Effect of Gas Flow Rate 107
5.3.6 Effect of Changes in the Beam Energy 109
5.3.7 Summary of InP–Chlorine Etch 112
5.4 Data Analysis for GaAs System 115
5.4.1 Desorbed Gas Species 115
5.4.2 Etch Profile 116
5.4.3 Etch Rate 116

6 Conclusion **121**
6.1 Summary 121
6.2 Recommendations for Improvement 121
6.3 Future Applications 124
6.4 Impact of the Project 125
6.5 Concluding Thoughts 126

A Design Schematics **127**
A.1 Source Flange 127
A.2 Main Chamber 132
A.3 Source Chamber 142
A.4 Transfer Tube 152
A.5 Nozzle 160
A.6 Miscellaneous Schematics 167

B Vendor Source List **173**
B.1 General Vacuum Parts 173
B.1.1 Pumps 173
B.1.2 Vacuum Pressure Gauges 174
B.1.3 Gatevalves 174
B.2 Electrical Systems 174
B.2.1 Flow Controller Switching System 174
B.2.2 Gatevalve Switch Box 175
B.2.3 Instrument Rack 175
B.3 Vacuum Chambers 175
B.3.1 General Construction Contractors 175

B.3.2 Main Chamber 176
B.3.3 Source Chamber 176
B.3.4 Transfer Tube 176
B.4 Nozzle 177
B.4.1 Nozzle Support Structures 177
B.4.2 Nozzle Heater Materials 177
B.5 Gas Manifold 178
B.5.1 Gas Controller Instrumentation 178
B.5.2 Gas Panel 178
B.5.3 Miscellaneous Gas Piping 179

References 180
Biographical Note 187

List of Figures

1-1 Different Etch Profiles 24

2-1 Doser nozzle design 30
2-2 Effusive source nozzle with a collimator and two-stage differential pumping. 31
2-3 Supersonic nozzle design. This diagram shows the nozzle setup utilizing the three-stage differential pumping setup. 32
2-4 Typical supersonic expansion profile with flow lines and shock fronts. x_m is the distance between the Mach disk and the nozzle. 34
2-5 Illustration of skimmer interference phenomena at different gas densities 38

3-1 The Kinetic Beam Etching system. The highest point of the system is approximately 6.5 feet. 44
3-2 Photo of the source chamber supported on a movable stage. Under close inspection, the nozzle can be seen through the 6 inch viewport. 51
3-3 Photo of skimmer mounted on its holder and six inch double-sided Conflat^{TM} flange. The skimmer is held in place by a retainer ring on the back side of the holder. 52
3-4 Nozzle stage with nozzle installed. 53
3-5 The main chamber. The chamber is wrapped in aluminum foil for better thermal distribution during frequent baking necessary to maintain UHV background pressures. 55
3-6 Transfer tube seen from the back of the KBE system. 59
3-7 The load lock seen from the inside. The sample holder and a moly block is seen attached to the transfer rod. The rods on the bottom of the transfer tube will be used to adjust the height of the substrate carrier tracks once it is installed. The big hole on the bottom of the cylinder leads to the ion pump. 61

3-8 The nozzle. The length from the tip of the nozzle to the base of the vacuum side of the 2.75 inch OD flange is approximately 19 inches. . . . 62

3-9 The finished nozzle heater on a 1/4 inch OD tubing, placed next to a penny. This heater was pulled out of the nozzle assembly after being used at 850°C for over 40 hours after the nozzle failed due to orifice clogging. Other than some carbon scorch marks, no degradation was observed mechanically or electrically. 65

3-10 Picture of the gas panel assembly consisting of four mass flow controllers. 66

4-1 A small InP sample mounted on a molybdenum sample holder block using indium paste. 69

4-2 A typical plot recorded during the substrate temperature ramp to 280°C at 15°C/min. The vertical axis is the pressure or the light intensity and the horizontal axis is time. In this plot, the indium melting burst pressure temperature is 144°C. 72

4-3 Plot showing the correlation of R_q values between roughness measured by atomic force microscope and laser reflectivity measurement. 76

4-4 Laser reflectance intensity measurement of thermally desorbed oxide on GaAs substrate. A slight change in intensity decrease rate can be observed approximately one minute after the intensity decrease starts. . . 78

4-5 Laser reflectance intensity measurement of thermally desorbed oxide on InP substrate. A slight change in intensity decrease rate, similar to the one observed for GaAs substrates can also be observed approximately one minute after the intensity decrease starts. 79

4-6 The pressure and laser reflectivity plot of an InP substrate etched with chlorine. This is an example where the increase in roughness stops for a duration. 81

4-7 The pressure and laser reflectivity plot of an InP substrate etched with chlorine. This is an example where the roughness of the surface actually improves within the first few minutes into the etch run, before eventually decreasing gradually with time. 82

4-8 Pressure and laser reflectivity plot showing the surface smoothing effect prompted by the chlorine. 83

4-9 Sample Etch Log. 85

5-1 Polymer beads forming on the surface of the InP substrate seen under optical microscope. The diagonal line-like pattern is from the original oxide mask. 400X 90

5-2 Schematic diagram of the definitions of various etch features referred to in this thesis. 95

5-3 SEM micrographs showing "trench" and "river" etch morphology. The etch rate in the canals are enhanced in comparison to the rest of the etched surface. 96

5-4 Photo showing the trenches forming alongside the etch masks near the upper limit of the low temperature etch regime. The distance between the dark grey masks is approximately 30 μm. 1800X, 1 kev 97

5-5 InP etched at 351°C. A filmy residue can be observed to uniformly cover the entire surface area where it was exposed to chlorine. The width of the river in the foreground is approximately 7 μm. 1700X, 1 kev 98

5-6 A schematic diagram of the contamination path of aluminum into the main chamber. Skimmed chlorine beam reacts with the aluminum skimmer holder and creates $AlCl_x$, and joins the background. However, due to the incoming, under-expanded, high-intensity chlorine beam, $AlCl_x$ is incorporated into the expanding jet stream as explained in Section 2.4. Then it travels into the main chamber along with the chlorine, eventually depositing on the substrate surface. 99

5-7 InP substrate etched at 275°C. Although the plateau surface is rough, no river or trench formation is observed. 4500X, 1 kev 101

5-8 Plot of etch rate vs. substrate temperature at different beam energies. Overall, as the substrate temperature increases. Slope a is In–Cl reaction rate or $InCl_x$ desorption rate limited, slope b is Cl_2 dissociation rate limited, and slope c is Cl_2 dissociation rate limited with aluminum compound deposition hindering the process. 103

5-9 InP substrate exhibiting crystallographically preferential etch profile. Figure 5-9(a) is commonly observed on facets cleaved along the $(1\bar{1}0)$ plane, where Figure 5-9(b) is seen on facets cleaved along the (110) plane. . . . 105

5-10 InP showing the interaction between the two crystallographic preferential etch profiles at intersection between the (110) and ($1\bar{1}0$) planes. Due to the formation of a "lip" near the mask junction, the mesa along the ($1\bar{1}0$) plane exhibits a thicker mesa top. The width of the base of the mesa near the bottom of the photo is approximately 5.5 μm. 4000X, 1 kev 106
5-11 InP substrate exhibiting a directional etch. It exhibits the combined characteristics of the trench etch and the faster plateau etch of the mid-temperature regime. The mesa is approximately 4 μm high. 11,000X, 1 kev 107
5-12 SEM micrographs of narrow channel etch exhibiting high anisotropy. . . 108
5-13 The schematic diagram showing the mechanism attributed in creating the directional etch. Unreacted chlorine which landed on the etch mask becomes thermally excited thus begins to diffuse along the mask surface. It eventually finds its way to the mask edge, and subsequently continues on to travel along the exposed substrate surface. Higher concentration of chlorine around the vicinity of the sidewall enhances the etch rate around the etch mask. 110
5-14 The etch results obtained were tabulated with respect to substrate temperature and chlorine beam energy. As optimum etch profile was being investigated, most of the experiments were conducted at the substrate temperature around 275°C where no river or trench morphology is present. This summary plot indicates a trend of directional etch obtained at higher beam energy. The morphology dependence caused by aluminum contamination was ignored for the purpose of determining which substrate temperature and beam energy will create a certain morphology in this diagram. 113
5-15 SEM micrographs of GaAs substrate etched under chlorine exhibiting crystallographic preferential etch. 117
5-16 Picture of GaAs substrate with aluminum deposit layer. A slightly enhanced etch rate is observed under the peeling layers, causing a shallow river morphology. 118

A-1 Source Flange: Front View 128
A-2 Source Flange: Cross Section A–A' 129
A-3 Source Flange: Cross Section B–B' 130

A-4 Source Flange: Cross Section C–C' 131
A-5 Main (Etch) Chamber Front View 133
A-6 Main (Etch) Chamber Rear View 134
A-7 Main (Etch) Chamber Side View 135
A-8 Main (Etch) Chamber Vertical Cross Section 136
A-9 Main (Etch) Chamber Cross Section A–A' 137
A-10 Main (Etch) Chamber Cross Section B–B' 138
A-11 Main (Etch) Chamber Cross Section C–C' 139
A-12 Main (Etch) Chamber Cross Section D–D' 140
A-13 Main (Etch) Chamber Support Stage 141
A-14 Source Chamber Side View 143
A-15 Source Chamber Top View 144
A-16 Source Chamber Cross Section A–A' 145
A-17 Source Chamber Cross Section B–B' 146
A-18 Source Chamber Support Collar 147
A-19 Source Chamber Support Collar Cross Section A–A' 148
A-20 Source Chamber Support Collar Cross Section B–B' 149
A-21 Source Chamber Movable Stage Top View 150
A-22 Source Chamber Movable Stage Side Views 151
A-23 Transfer Tube Chamber-side Side View 153
A-24 Transfer Tube Transfer Rod-Side Side View 154
A-25 Transfer Tube Cross Section A–A' 155
A-26 Transfer Tube Cross Section B–B' 156
A-27 Regulated bellows flange to connect the transfer rod 157
A-28 Modified 8 Inch Conflat Blank Flange: used as the temporary load lock door 158
A-29 Transfer Tube Stage 159
A-30 Nozzle Assembly 161
A-31 Nozzle Tip 162
A-32 Nozzle Support Tubing 163
A-33 Nozzle Inner Tubing 164
A-34 Nozzle Mounting Flange 165
A-35 Nozzle Centering Ring 166
A-36 Skimmer Holder Flange 168
A-37 Skimmer Holder 169

A-38 Cryo Protection Screen 170
A-39 Mass Flow Controller Panel 171

List of Tables

4.1 Comparison of roughness measurements made by laser reflectivity measurement and atomic force microscope. 75

5.1 List of relevant materials involved in the InP etch and their chemical properties. 94

5.2 List of relevant materials involved in the GaAs etch and their chemical properties 116

Chapter 1

Introduction

1.1 Motivation

The ability to clean and etch the surface of a semiconductor wafer has always been of interest to semiconductor processing and fabrication researchers. Through etching, either for patterning mesas or for general surface cleansing, many devices are defined and fabricated. Therefore, understanding the nature and the effect of the etchants and the etching methods to the delicate features of semiconductor surfaces becomes one of the most critical parameters in increasing or decreasing the yield of the devices made. As the etching step is one of the most important steps during device processing, in general, etching techniques having the most controllable etch rates, etch profiles, material selectivities, and are least damaging to the surfaces are constantly sought after.

In addition, the ability to pattern a structure and etch *in-situ* between heterostructure growth is also of great interest. If one can clean, grow heterostructures, pattern, etch, and proceed with regrowth without breaking vacuum, the potential advancement for device processing technology is great. Aligned with this goal, currently much effort is made in maskless pattern etch methods, such as focused ion-beam etch [1][2][3][4] or photoetching [5]. In order for these methods to be successful, it is essential to find an etching technique compatible with heterostructure growth methods. For high-pressure growths such as metal organic chemical vapor epitaxy (MOCVD), dry etch methods that use relatively high pressures are compatible. However, growth methods which use an ultra-high vacuum system, such as molecular beam epitaxy (MBE), will require etch methods which can also take place in an ultra-high vacuum environment.

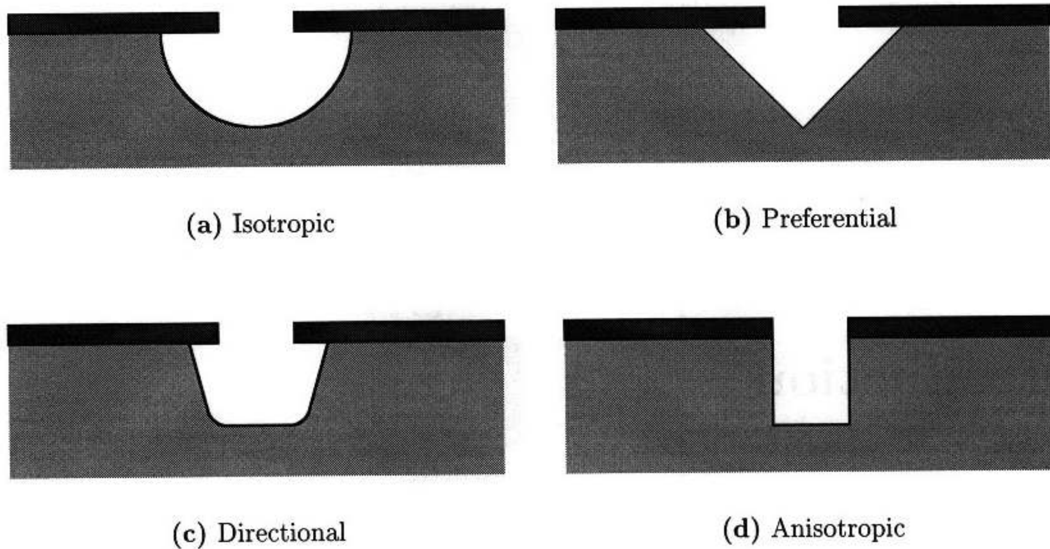

(a) Isotropic (b) Preferential

(c) Directional (d) Anisotropic

Figure 1-1: Different Etch Profiles

1.2 Available Etch Methods

The oldest and most widely used etching method is chemical wet etching. Wet etching involves using reactive chemicals in an aqueous solution consisting of such chemicals as hydrochloric acid (HCl), nitric acid (HNO_3), hydrogen peroxide (H_2O_2), sulfuric acid (H_2SO_4), etc. The etch is accomplished by immersing the substrate into the etching solution. This method is known for its simplicity, material selectivity, producing little or no damage to the etched surface, and relatively fast etching rates. The etch rate itself is, in general, difficult to control, and it is difficult to obtain a consistent etch depth without the use of a pre-designed etch-stop layer. The etch rate itself is also very difficult to control. Another disadvantage is that due to the inherent aqueous nature of wet etches, it is difficult to maintain clean etching conditions. The biggest drawback is that wet etching can only produce either an isotropic etch as illustrated in (Figure 1-1(a)), or preferential etch along the crystallographic planes (Figure 1-1(b)). This character makes it difficult to produce an etch pattern that is faithful to the patterning mask, and also can not produce a very high depth-to-width etching aspect ratio as illustrated in Figures 1-1(a) and 1-1(d). Therefore, this type of etch is not suitable to pattern VLSI (very large-scale integrated circuit) devices.

Consequently, more sophisticated techniques have been developed using dry etching processes, involving plasma fields, ion beams, electron beam bombardment or the com-

bination of the aforementioned methods. Some examples of such systems are reactive ion etching (RIE), reactive ion beam etching (RIBE), high-density plasma etching, ion bombardment assisted etching (IBAE, also known as CAIBE–chemically assisted ion beam etching) and ion milling etching (sputtering). Unlike wet etch, most of the above techniques occur under a controlled low to high vacuum environment; therefore, it is possible to maintain a high degree of cleanliness. In addition, by changing its process parameters, the above techniques can achieve very anisotropic etch profiles (Figure 1-1(d)), as well as isotropic etch profiles. Some impressive demonstrations regarding its precise control over the etch profiles have been seen [6][7].

However, these techniques involve high energy ions or plasmas that can heavily damage the surface of the single-crystal substrate. Damage is caused by contamination of surface through physical sputtering [8][9], radiation damage, ion charge transfer, dielectric capacitor effect [10], or the combination thereof. Dielectric capacitor effect[1] is known as one of the most problematic damages inherent in any etch systems using electrical biasing and charged particles. Any damage sustained by the substrate or its epitaxial layers during such process inhibits subsequent single crystalline epitaxial overgrowth, and is detrimental to device performance, unless some additional crystalline reconstruction is done prior to the next processing step. It is possible to diffuse out some of the crystal defects by means of rapid thermal annealing (RTA). However, for dielectric layer damage, there are no remedies after it is destroyed. For these reasons, currently, low-energy ion-assisted dry etch systems and neutral molecular etch techniques are being investigated in earnest [11] [12].

To this date, there have been many studies regarding low-damage etching methods for silicon-based semiconductor device processing. In contrast to the mature silicon fabrication technology, technology for compound semiconductor device processing is still in its infancy. Like silicon, compound semiconductors are also being processed using plasma and ion etching methods. However, due to its multiple-element nature, a compound semiconductor is more susceptible to damage than its silicon counterparts. Also, it is known that while silicon anneals very easily after processing, ridding compound semiconductors of defects is more difficult. In compound semiconductors, instead of the defects diffusing out towards the surface, the damaged region has a tendency to

[1]Dielectric capacitor effect occurs when thin dielectrics are present near the surface of the substrate to be etched. The charged particles accumulate on either side of the dielectric material, and upon shut down of the reactor, charge discharge occurs, destroying thin dielectric layers, which destroys devices using thin oxides for operation, such as field-effect transistors.

getter impurities and defects and give rise to preferential segregation [13]. Any cluster of defects can severely lower the electron mobility of the material, and also create carrier recombination traps, resulting in dark-line defects (DLD) and other optical defects. For compound semiconductors used in optoelectronic devices, defects such as DLD can severely affect their light-emitting or photodetecting properties.

1.3 Thesis Project

The importance of developing a useful low energy, dry etch especially for compound semiconductors is clear. Therefore, through this thesis project, an attempt to create an ultra-high vacuum compatible dry etch reactor for compound semiconductors was made.

The purpose of this thesis project was to build and characterize a dry-etch reactor system which: (1) can etch semiconductors with a directional etch profile, (2) is ultra-high vacuum compatible, and (3) can etch with little or no crystalline damage. The system was targeted to be used for group III–V compound semiconductors, although enough versatility was designed into the system with ability to be used for other material systems, and allow further expansion of capabilities in the future.

To avoid any radiation or sputtering damage, no ionic source is used. Instead, this etching system uses neutral gas molecules, and the etch mechanism relies purely on the chemical reaction between the substrate surface and the etchant molecule. To overcome the reaction threshold energy barrier between the substrate and the etchant, the molecule is accelerated by means of supersonic expansion, and uses its kinetic energy as the reaction activation energy source. Using the supersonic, or free-jet expansion nozzle, it is also possible to accelerate the molecule beyond its thermal limit using the process called "seeding". Thus, it is possible to obtain enough kinetic energy to overcome the activation energy of the etch reaction, but without excess energy to damage the crystal structure. Also, the ultra-high vacuum environment allows the etchant gas stream to maintain a molecular beam profile, which in turn will allow a line-of-sight etch, and consequently a directional (Figure 1-1(c)) or perhaps an anisotropic etch. In essence, it was designed to be somewhat of a hybrid wet-dry etch reactor (react like a wet etch, but with the characteristic of dry etch).

1.4 Thesis Organization

This thesis is organized in the following manner. First, some technical background relevant to the reactor design will be discussed. Then the actual design of the kinetic beam etching (KBE) reactor will be presented, followed by the characterization of the reactor. Some basic models of the possible kinetics involved in the etching process will also be discussed. The thesis will conclude with some future recommendations on its use and enhancements.

When a particular etch profile is mentioned in this thesis, to avoid confusion and to differentiate between "anisotropic" and "directional" etch profiles, the term "anisotropic" is only used when there is virtually no undercut of the mask (Figure 1-1(d)). The term "directional" is used to describe any non-isotropic etch profile with the depth-to-undercut aspect ratio of greater than three-to-one (Figure 1-1(c)).

Chapter 2

Background

2.1 Supersonic Nozzles

Much rare gas dynamics research has been centered around creating a jet source which can produce high-intensity, high-velocity molecular beams. Especially for surface chemists, the ability to obtain such a molecular beam is highly desirable when investigating a surface–gas reaction. There are two main conventional nozzle designs. One conventional nozzle design, shown in Figure 2-1, is what is referred to as a "doser" style nozzle which consists of a pipe with a length much longer than the tube opening diameter, injecting the gas into the vacuum chamber. The doser style nozzle relies purely on the flux rate of the gas being pumped into the vacuum chamber. Due to its high flux nature, it is not very well suited for obtaining a high-intensity beam in an ultra-high vacuum environment.

The other conventional nozzle design, shown in Figure 2-2, consists of a gas reservoir with an opening, and the beam intensity relies solely on the effusion rate of the gas through the orifice. This nozzle design is frequently referred to as an "effusive source," "Knudsen source," or "oven source" nozzle. Its flux distribution follows the cosine law; therefore, collimation is required to produce a well defined beam.

Using the effusive source design, it is possible to obtain a molecular beam with the average translational energy of about $2\,k_BT$ [14][15], where k_B is the Boltzmann constant and T is the nozzle stagnation temperature. Until 1950, the maximum attainable intensity of the jet was limited by a "cloud" formation, a large scattering center, at the effusion orifice, thereby diminishing the intensity of the beam at the beam source. At the time, the only method of minimizing the cloud formation was to keep the Knudsen

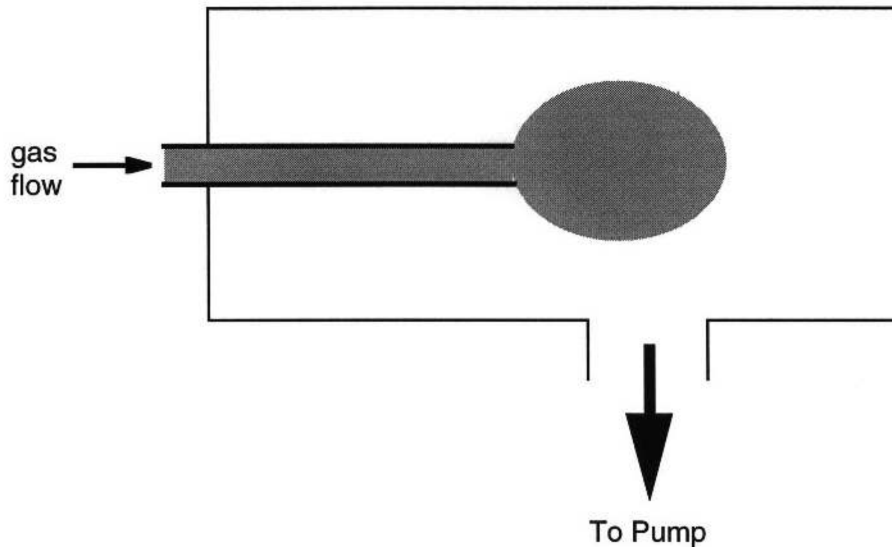

Figure 2-1: Doser nozzle design

number[1], K_n, of the gas at the orifice less than one to provide continuum flow[2] at the source.

Typically the flux, F, of such an effusive source at temperature T_0 can be expressed as:

$$F = \frac{1}{4} n_s \left(\frac{8 k_B T_0}{\pi m} \right)^{\frac{1}{2}}, \tag{2.1}$$

where n_s is the molecular number density, and m is the molecular weight of the gas.

In 1951, Kantrowitz and Grey introduced a novel nozzle design theory [16] which was implemented first by Kistiakowsky and Slichter [17]. They theorized and demonstrated that a high-intensity molecular beam can be created from a beam extracted from an under-expanded supersonic continuum jet expansion from a high-pressure gas reservoir into a low-pressure ambient background through a small orifice [18] (Figure 2-3). This novel design essentially eliminated the cloud formation, which was the limiting factor in producing a high-intensity beam in effusive sources, thus allowing production of highly

[1] Knudsen number (K_n) is a dimensionless number used in fluid dynamics and is defined as the ratio of mean free path in the nozzle stagnation chamber to the nozzle exit diameter. It loosely measures the amount of interaction between free molecules in a confined area.

[2] Continuum flow is defined as any fluid entity exhibiting all the macroscopic thermodynamic and transport properties. Typically this means that $K_n \ll 1$.

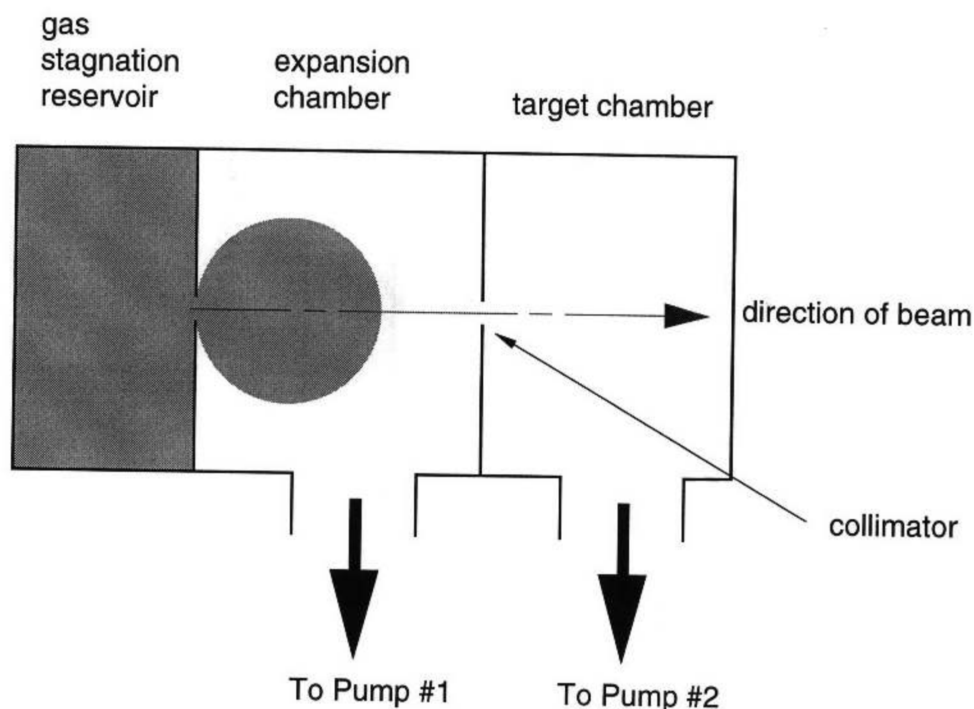

Figure 2-2: Effusive source nozzle with a collimator and two-stage differential pumping.

directional, high-intensity molecular beams.

This supersonic nozzle phenomenon can by described as follows. When a gas undergoes free expansion into a vacuum chamber, more of the gas moves along the centerline axis of the nozzle opening, instead of following the spherical expansion of an effusive source. This directionality results in an increase of the average intensity of the gas flow direction along the centerline axis by several orders of magnitude relative to that of an effusive source [19]. Furthermore, by placing a skimmer, which resembles a hollow truncated cone, along the centerline of the expansion, extraction of a highly directional beam is possible. As the gases encounter the skimmer, only the molecules traveling along the centerline axis proceed downstream, and all others are deflected away. At this point, the continuum flow of the gas turns molecular due to a sudden drop in the molecular collision rate downstream of the skimmer orifice.

The key property of such an expansion nozzle is that the molecular thermal energies can be readily converted into one primary translational degree of freedom [20], thus accelerating the molecules to supersonic velocities downstream of the skimmer. Since most of the internal thermal energy is directly converted into kinetic energy, the molecules

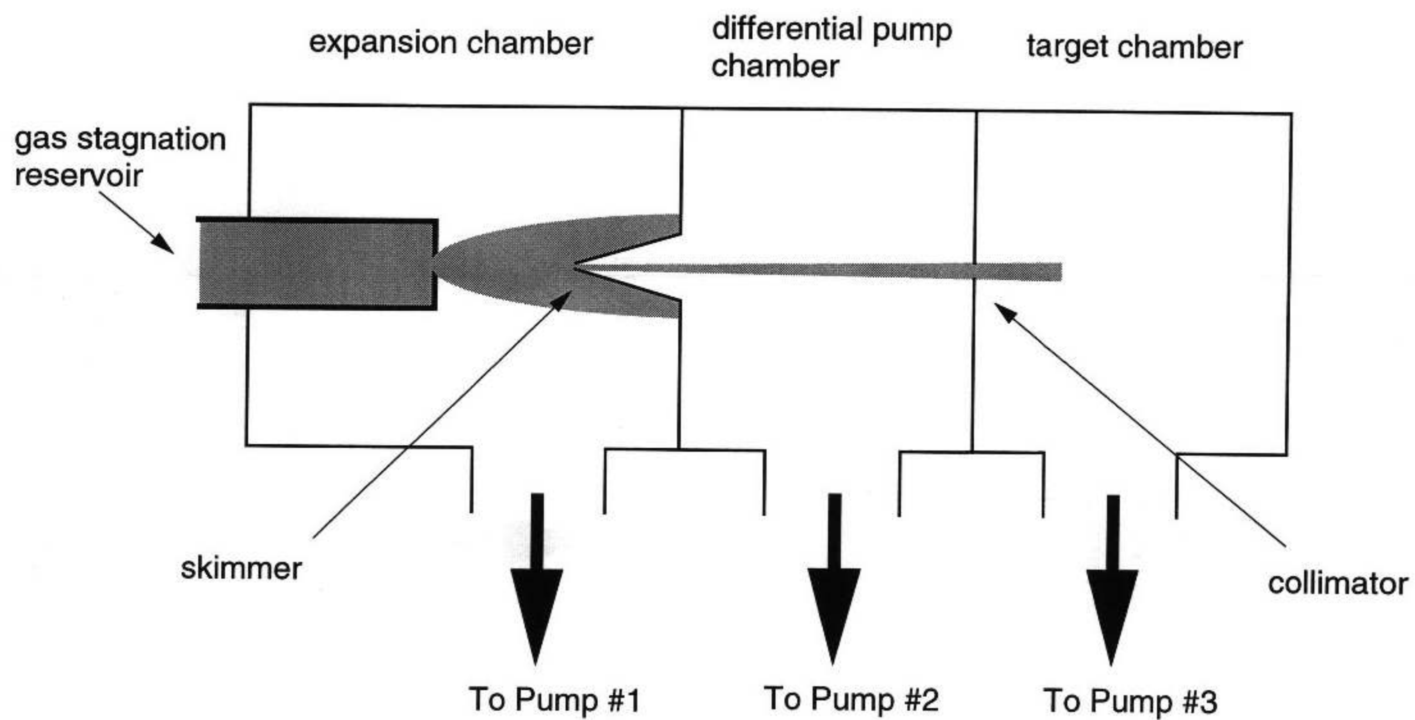

Figure 2-3: Supersonic nozzle design. This diagram shows the nozzle setup utilizing the three-stage differential pumping setup.

emerging from the nozzle are in rotationally and vibrationally "cold" states [21]. This phenomenon is known as "freezing." As the nozzle stagnation pressure is increased, the nozzle yields translationally faster and internally colder molecules with higher intensity and narrower velocity distributions [22]. As an added bonus, such supersonically expanded molecules are able to attain higher mean kinetic energy, $\frac{5}{2} k_B T$, than those produced by the effusive source [23].

2.2 Free Jet Expansion and Freezing

The typical expansion profile of supersonic jet is shown in Figure 2-4, and the flux attainable by the supersonic nozzle can be expressed as:

$$F_0 = 0.146 C A_n P_0 \left(\frac{m}{T_0}\right)^{\frac{1}{2}}, \tag{2.2}$$

$$C = \gamma^{\frac{1}{2}} \left\{ \left[\frac{2}{(\gamma+1)}\right]^{\frac{(\gamma+1)}{(\gamma-1)}} \right\}^{\frac{1}{2}}, \tag{2.3}$$

where γ is the ratio of the constant pressure to constant volume specific heats of the gas, A_n is the area of the nozzle orifice in cm^2, P_0 is the nozzle stagnation pressure (pressure inside the nozzle) in torr, m is the mass of the gas in g/mole, and T_0 is the initial gas temperature in Kelvins.

In addition to Equation 2.2, the flux and velocity distributions of nozzle sources are often expressed in terms of Mach number, M, which is the ratio of the flow velocity to the velocity of sound for the gas at temperature T with the nozzle reservoir temperature T_0:

$$M = \frac{v}{a} , \tag{2.4}$$

$$v = \sqrt{\frac{2k_B}{W}\left(\frac{\gamma}{\gamma-1}\right)(T_0 - T)} , \tag{2.5}$$

$$a = \sqrt{\frac{\gamma k_B T}{W}} , \tag{2.6}$$

$$W = \sum_{i=1}^{n} x_i m_i , \tag{2.7}$$

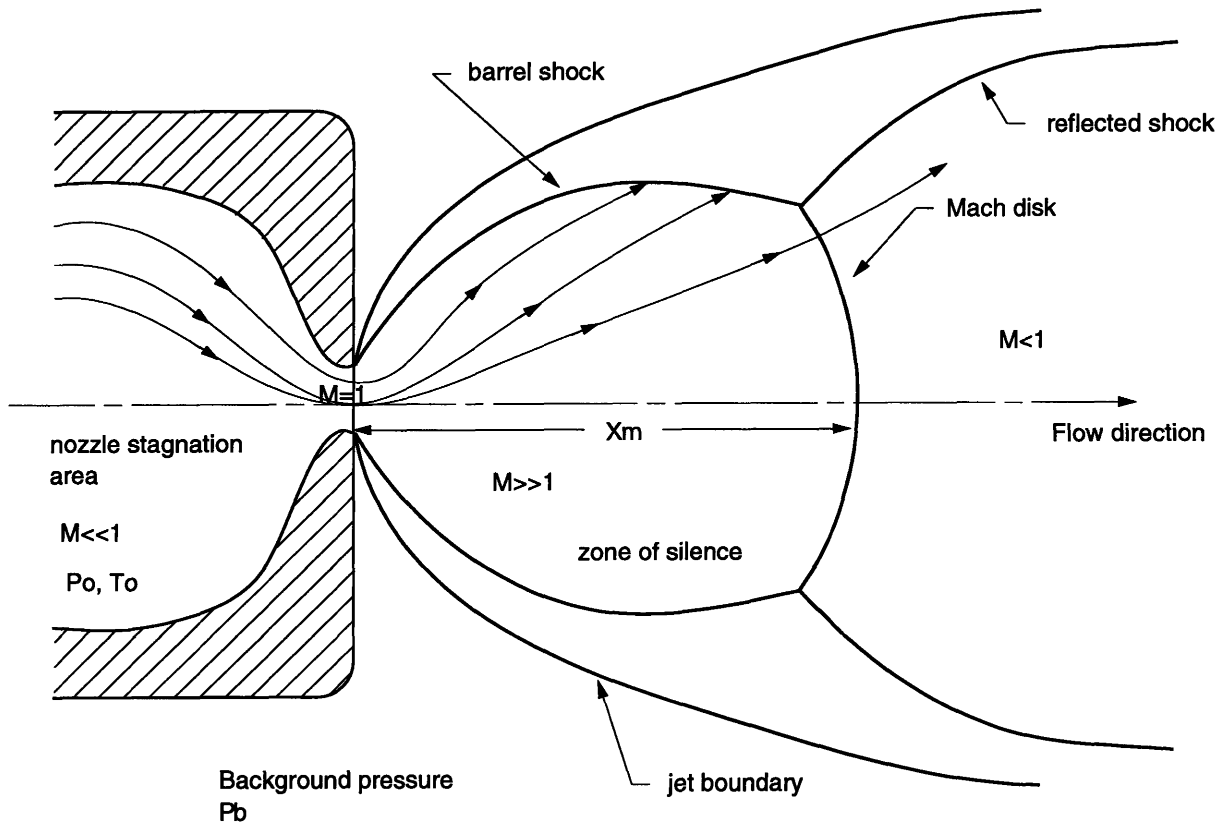

Figure 2-4: Typical supersonic expansion profile with flow lines and shock fronts. x_m is the distance between the Mach disk and the nozzle.

where v is the maximum attainable velocity of the gas when cooling from temperature T_0 to T, x_i and m_i are the mole fraction and molecular weight of the gas species present, respectively, and W is the average molecular weight of the gas mixture.

Mach numbers are usually associated with the velocity of sound. However, in rare gas dynamics, the Mach number is usually viewed more as the dimensionless number which characterizes the efficiency of the conversion of the thermal energy to translational energy of the expanding jet. Thus, for a project such as this, it is desirable to obtain as high a Mach number as possible, as this implies high kinetic energy.

If $T \ll T_0$, which is the likely case in free jet expansions as T usually approaches few Kelvins, the maximum, or "terminal" velocity, v_{max}, attainable by the molecule is:

$$v_{max} = \sqrt{\frac{2k_B}{W}\left(\frac{\gamma}{\gamma-1}\right)T_0} \ . \tag{2.8}$$

As with v_{max}, the Mach number also approaches its terminal value, M_T as $T \to 0\,K$ which is represented as:

$$M_T \cong 1.17\left(\frac{d}{\lambda_0}\right)^{\frac{(\gamma-1)}{\gamma}} , \tag{2.9}$$

where d is the orifice diameter of the nozzle and λ_0 is the mean free path[3] of the molecules in the stagnation region. Using M_T, the final beam temperature T can be defined as:

$$T = T_0\left[\frac{1+(\gamma-1){M_T}^2}{2}\right]^{-1} . \tag{2.12}$$

[3]The mean free path λ_0 of a gas is defined as the mean distance traveled by molecules between collisions. The mean free path of an ideal gas is given by

$$\lambda_0 = 1.26\,\nu\,(k_B T)^{\frac{1}{2}}, \tag{2.10}$$

$$\nu = \frac{\mu}{\rho} \ , \tag{2.11}$$

where ν is the kinematic viscosity, k_B is the Boltzmann constant, T is the temperature, μ is the fluid viscosity in kg/(m·sec), and ρ is the fluid density [24].

The flow velocity, v, defined in Equation 2.5 can also be expressed in terms of M_T as:

$$v = v_{max} M_T \left\{ {M_T}^2 + \left[\frac{2}{(\gamma - 1)} \right] \right\}^{-\frac{1}{2}} . \tag{2.13}$$

2.3 Seeding

Using the supersonic nozzle design has further advantages over conventional effusive source designs. It exhibits a unique property when a heavier molecule is mixed with a lighter molecule. As shown in Equations 2.14 and 2.15, at a given thermal energy, the lighter molecule can reach a higher terminal velocity than the heavier molecule can upon expansion.

$$E_{KE} = \frac{1}{2} m v^2 \tag{2.14}$$

$$= \frac{5}{2} k_B T \ . \tag{2.15}$$

By changing the average molecular weight of the gas by means of introducing a small concentration of heavier gas molecule into a matrix of lighter molecules, it is possible to vary the average kinetic energy after expansion. This phenomena is known as "seeding" and is caused by the collision of the faster, lighter molecules with the heavier molecules, and the transfer of some of their kinetic energy to the heavier molecules, resulting in the heavier molecules attaining a higher velocity. By strategically mixing gases with different molecular weights, it is possible to increase the kinetic energy (E_{KE}) of the heavier molecule beyond what it would have otherwise achieved under thermal equilibrium conditions. Therefore, this condition is also known as "hyperthermal expansion." When a gas mixture with molecular weight of m_1 and m_2 is allowed to expand supersonically, the average kinetic energy of the molecule of interest can be expressed as:

$$E_{KE} = \frac{5}{2} k_B T \frac{m}{W} \ , \tag{2.16}$$

where m is the molecular weight of the species of interest.

For example, a pure chlorine gas at room-temperature in a supersonic nozzle has

an average energy of about 0.75 kcal/mole [4]. If the nozzle temperature is increased to 150°C, the average kinetic energy increases to about 2 kcal/mole. Likewise, pure methane (CH_4) gas at 700°C has an energy of about 4.5 kcal/mole. If a gas mixture of 10% methane and 90% hydrogen gas is used at 700°C, the kinetic energy of the methane increases to 11 kcal/mole, and if the concentration of methane is further reduced to 1%, the kinetic energy of the methane can reach about 34 kcal/mole.

By carefully controlling the seeding and freezing phenomenon, it is possible to vary and control the incident energy of the molecules, which is one of the very important controllable parameters to have in a dry etch reactor.

2.4 Skimmer

As explained in Section 2.1 the skimmer takes a vital role in the supersonic nozzle setup. In this project, in addition to eliminating the "cloud" formation, it also acts as the collimator and the only physical barrier between the differentially pumped chambers.

In general, skimmers are shaped like a cone with a truncated tip. The dimensions and the angles of the structure are optimized so that while it minimizes the shock structures[5] that form at the entrance when exposed to supersonically expanding jet, it maximizes the conductance of the molecules through the skimmer going into the downstream chamber. The edges of the skimmer entrance must be razor-sharp to minimize scattering effects. Although the skimmer is primarily placed to reduce scattering downstream, if not properly positioned or designed it can become a major scattering center itself, significantly decreasing the flux and intensity as illustrated in Figure 2-5. Much research has been done on the actual interaction of the skimmer with an expanding gas source [25] [19]. However, a detailed discussion of the topic is beyond the scope of this thesis. Therefore, only a simple, physical explanation of the skimmer scattering phenomena will be presented here.

[4]The following unit conversions hold:

$$
\begin{aligned}
1\, kcal/mole &= 4.19 \times 10^{3}\ joules/mole \\
&= 2.61 \times 10^{21}\ eV/mole \\
&= 4.3 \times 10^{-2}\ eV/particle.
\end{aligned}
$$

[5]Shock structures, or shock waves provide a mechanism to change the direction of a supersonic flow and reduce the supersonic flow to subsonic values if the change in direction is not sufficient to meet a boundary condition.

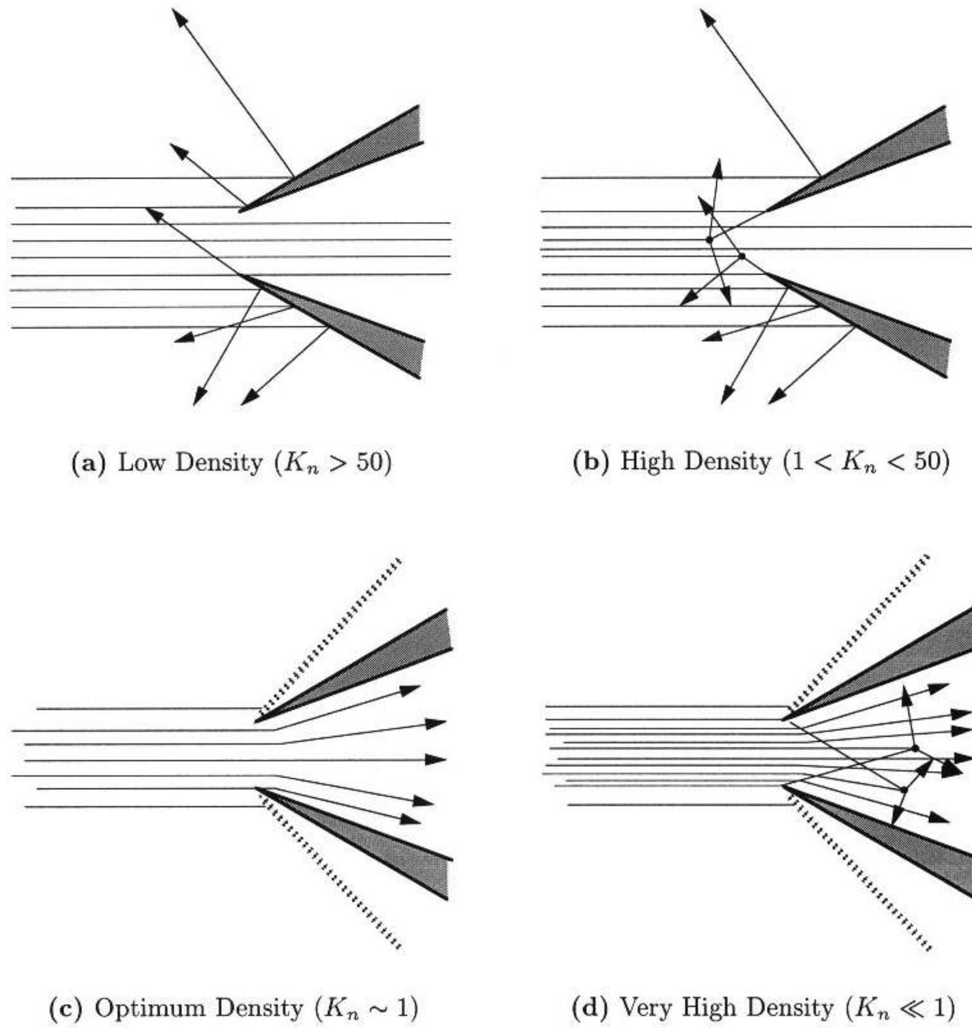

(a) Low Density ($K_n > 50$)

(b) High Density ($1 < K_n < 50$)

(c) Optimum Density ($K_n \sim 1$)

(d) Very High Density ($K_n \ll 1$)

Figure 2-5: Illustration of skimmer interference phenomena at different gas densities

By varying the placement of the skimmer entrance within the "zone of silence" (see Figure 2-4), it is possible to change the molecular density at which the skimmer encounters (closer to the nozzle orifice, the higher the gas density). And depending on the gas density encountered, very different behavior of the skimmer-molecule interaction can be observed. For very low jet densities ($K_n > 50$), the flow is nearly free molecular, and the molecules pass through the skimmer opening without encountering many reflected ones. The reflected molecules join the background and contribute to the increase of the background pressure. However, since their density is low enough, effects from such reflected molecules are negligible (Figure 2-5(a)). As the density of the flow increases ($1 < K_n < 50$), the number of reflected molecules increases, in turn interfering with the incoming molecules (Figure 2-5(b)). As the jet intensity further increases ($K_n < 1$), the flux of the incoming molecules becomes high enough to drive the reflected molecules downstream. At this point, an oblique shockwave is created along the external walls of the skimmer (Figure 2-5(c)). If the incident intensity is further increased ($K_n \ll 1$), the molecules downstream of the skimmer become subject to scattering (Figure 2-5(d)), thus decreasing the overall intensity. There are more complex and rigorous approaches to this problem [26]. However, from these simple explanations, the importance of the proper skimmer positioning with respect to the nozzle is apparent.

In determining the correct skimmer location with respect to the nozzle, the opening of the skimmer must be located within the "zone of silence" (see Figure 2-4) where the gas is expanding isentropically[6]. The boundary of the "zone of silence" is determined by the barrel shock and the Mach disk shock boundaries. Empirically [27], it was confirmed that the Mach disk distance, x_m, from the nozzle along the centerline of the flow was related to the ratio of the stagnant nozzle pressure to the background pressure, regardless of different γ values. Mach disk location can be determined using Equation 2.17,

$$x_m = 0.67 \left(\frac{P_o}{P_b}\right)^{\frac{1}{2}} d \ , \tag{2.17}$$

where d is the nozzle orifice diameter.

Using Equation 2.17 for this project, the optimum skimmer–nozzle distance was calculated [18] as somewhere between 1 and 2 cm, depending on the type of gas and stagnant nozzle pressure used.

[6]Isentropic flow is a frictionless adiabatic flow. A system is said to be "adiabatic" if the total heat Q of the system is constant (*i.e.* $\delta Q \equiv 0$).

2.5 Maintaining the Molecular Flow Regime

Once a gas is introduced into a vacuum, its ability to maintain the molecular beam profile is purely dependent on the amount of scattering it encounters. If there are not enough free molecules in the vacuum chamber, so that molecules change direction only when they hit the chamber walls and not through collisions with other free molecules, it can be said that there is a free molecular flow, or it is in a molecular beam regime. This regime is technically defined as when the mean free path of the molecule is larger than the characteristic dimensions of the vacuum chamber. The merits of having large mean free path values are discussed in Section 3.2.

In order to ensure maintenance of the molecular beam regime, the background pressure of the chamber needs to be at least two to three orders of magnitude lower than the beam intensity. As the gas load is extremely high for any single pump to maintain the required vacuum levels, the use of a differential pumping system setup is frequently used in supersonic nozzle-based vacuum chamber designs [15]. A differentially pumped system is a vacuum system which is divided in to a series of separately pumped chambers connected only through narrow orifices through which the beam passes (See Figure 2-3). By spreading the gas load in stages, it is possible to maintain the required vacuum levels at the experimental chambers without the use of an extremely high pumping rate.

In determining the required pump rates, it is necessary to know what the gas load of the vacuum chambers will be. The flow rate F_0 in g/sec of a supersonic nozzle can be determined using Equations 2.2 and 2.3. The typical number for the total flux from a supersonic nozzle with an orifice of about 50 μm diameter is about 1×10^{19} particles/sec. In the expansion, or source chamber, since the distance the molecule needs to travel before exiting into the next differential pumping chamber is on the order of 1–2 cm, keeping the background pressure at 1×10^{-4} torr is usually sufficient.

The pumping speed, S_{pump}, needed to maintain a certain background pressure, P_b, can be expressed as:

$$S_{pump} = \frac{flux}{P_b} \quad . \tag{2.18}$$

For the expansion chamber, where the majority of the injected gases are present,

$$\begin{aligned} flux_{source} &= F_0 \\ &\cong 1 \times 10^{19}\, particles/sec \\ &\cong 3.09 \times 10^{-1}\, torr \cdot l/sec. \end{aligned} \tag{2.19}$$

For the main chamber, the reactor was designed so that a beam spot size approximately 2 cm in diameter will reach the target by passing through a skimmer with a 1 mm diameter opening. Assuming that the angular distribution of the gas coming out of the nozzle is spherically symmetric, the intensity, I, of the beam in units of particles/area^2·sec at a distance, x, from the nozzle can be represented as [28]:

$$I = \frac{F_0}{2\pi x} \; . \tag{2.20}$$

As the distance between the nozzle and the target in this project reactor is approximately 27 cm + x_d, where x_d is the distance between the nozzle and the skimmer, the maximum beam intensity in the main vacuum chamber is approximately 2.18×10^{15} particles/cm^2·sec. With a cross sectional spot size diameter d_{target} downstream in the main chamber, $flux_{main}$ can be calculated as:

$$\begin{aligned} flux_{main} &= \text{intensity} \times \text{area} \\ &= I \cdot \pi \left(\frac{d_{target}}{2}\right)^2 \\ &\cong 7 \times 10^{15}\, particles/sec \\ &\cong 2.16 \times 10^{-4}\, torr \cdot l/sec. \end{aligned} \tag{2.21}$$

To keep this beam in molecular flow, the P_b of the main chamber must maintain vacuum levels of at least 1×10^{-7} torr. Using Equation 2.18, in order to keep the background pressure of 1×10^{-4} torr or lower in the source and 1×10^{-7} torr or lower in the main chamber, minimum pumping speeds of approximately 3100 l/sec and 2200 l/sec, respectively, are necessary. However, since the pump rate would increase with the square of the nozzle exit diameter, for nozzle hole diameters of 60 μm and 75 μm (the dimensions used in this project) the actual required pumping speeds would be much higher.

Following the above discussions, the quantitative merit of using the differential pumping method can now be presented. It was calculated that only two pumps on

the order of 3500 l/sec are sufficient to maintain the molecular beam profile in the differentially pumped system. However, if the differential pumping system is not utilized, the pump rate required to maintain the molecular beam profile would be on the order of 3×10^6 l/sec. From these comparisons, the advantage of its use is clear.

Chapter 3

Kinetic Beam Etch System Design

3.1 Introduction

The Kinetic Beam Etch (KBE) system shown in Figure 3-1 was designed and constructed as the first step towards the construction of a cluster tool which is to include the existing Riber 2300 solid-source molecular beam epitaxy (MBE) system. The ultimate goal of this cluster tool is to be able to grow, pattern, etch, and regrow III–V compound semiconductor heterostructures without breaking vacuum, and exposing the substrate to atmosphere.

As a part of a cluster tool, one of the foremost design considerations was size and means of connecting the KBE system to the existing equipment. This prerequisite meant that the height at which the substrate travels between the chambers was predefined. Although this requirement seemed to be trivial, it proved to be a severe limitation in design flexibility as will be discussed in Section 3.2.2. During the design phase of this project, care was given so that the KBE system will have maximum flexibility in adapting to future alterations or additions of capabilities.

The following sections will describe the highlights of KBE system design restrictions and considerations explored during the design and construction phase of this project. All schematics mentioned in this section and other relevant design schematics can be found in Appendix A, and all parts, equipment and their vendors used for this system are listed in Appendix B.

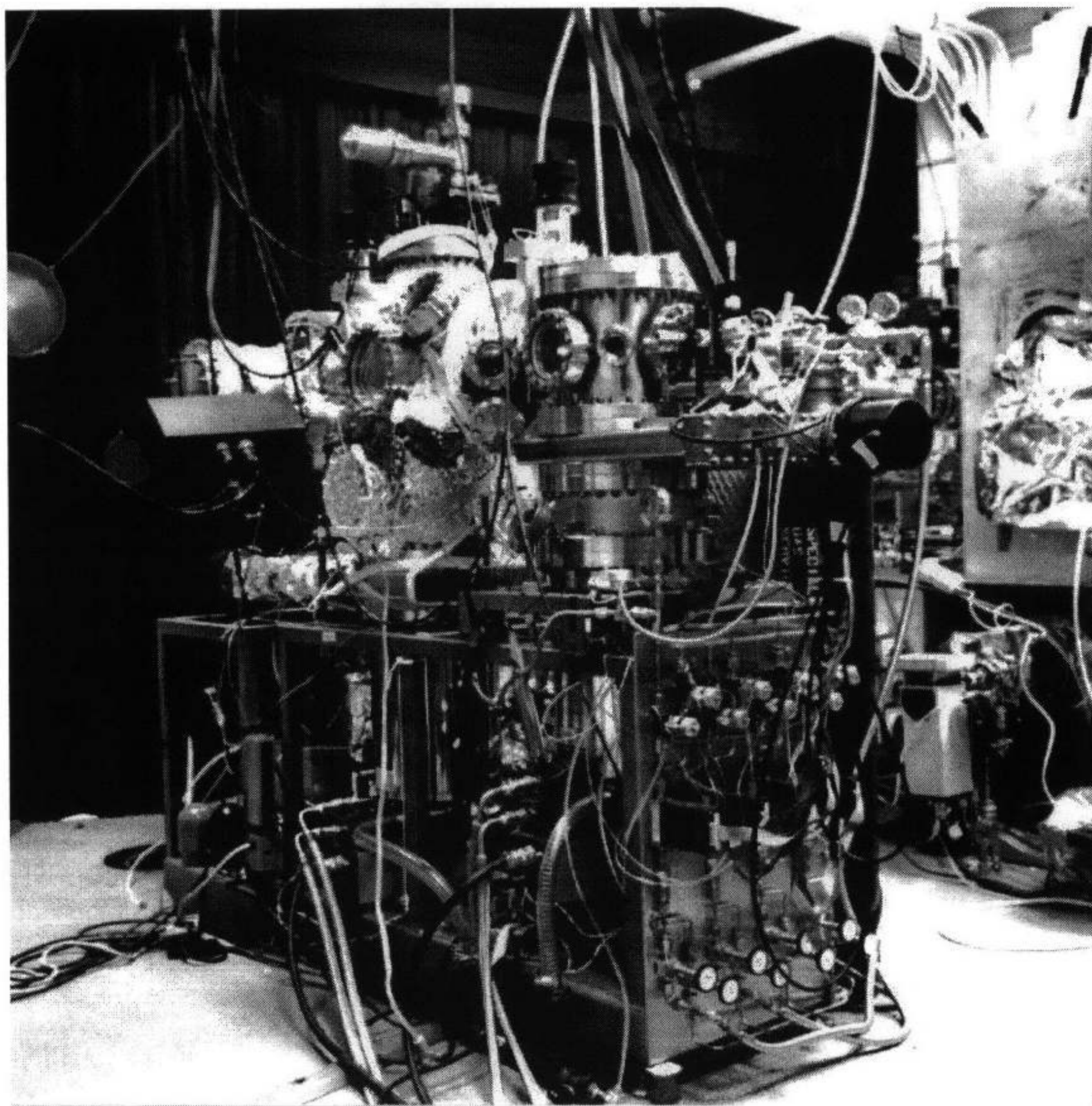

Figure 3-1: The Kinetic Beam Etching system. The highest point of the system is approximately 6.5 feet.

3.2 Ultra-High Vacuum Requirements

One of the greatest attractions in using ultra-high vacuum (UHV)[1] system is cleanliness. With idle background pressure of 1×10^{-8} torr or lower, the amount of gaseous contaminant is very small. At standard room temperature, there are approximately 2.5×10^{19} molecules present in one cubic centimeter of air at 1 atm, or 760 torr. At 1 torr, there are approximately 3.3×10^{16} molecules/cm^3. At UHV conditions which typically are at 1×10^{-8} torr or lower pressures, the approximate gaseous particle count drops to about 3×10^{7} molecules/cm^3 or lower.

In addition to cleanliness, the greatest advantage of using UHV chambers is the ability to maintain a very long particle mean free path because of low molecular density. Once a molecule is moving in one direction, it does not change its course until it encounters another molecule. In a vacuum, since the background particle counts are so low, the only collision a molecule will encounter is with the chamber walls. This condition allows the possibility of creating and maintaining molecular beams or a highly directional gas injection profile, which is important if obtaining a line-of-sight etch is desirable. Under standard room temperature and pressure (1 atm or 760 torr and 300 K), the average mean free path of air is approximately 0.63 μm [29], which means that the average molecule will travel 0.63 μm before it encounters another molecule and scatters. If a vacuum chamber is designed so that the characteristic chamber dimension is less than the mean free path, one can assume that any gas particle injected into the chamber will maintain its velocity until it hits the chamber wall, or any other matter placed in its path, such as the target substrate. Inside a UHV vessel, where typical background pressure is 1×10^{-8} torr or lower, the average mean-free-path becomes approximately 63 meters. From this calculation, a vacuum chamber with its characteristic dimension less than 63 meters would easily maintain a molecular beam profile within it.

There are several standard design considerations for a system to be UHV compatible. In order to achieve UHV conditions, all vacuum-exposed surfaces must be bakable to a minimum of 200°C. Also, it is most desirable to use materials with low outgassing properties. Most vacuum systems are constructed with electropolished 304 stainless steel for these reasons. Chambers made of polished aluminum also are available. Aluminum

[1]Vacuum level is roughly differentiated into three regimes: low vacuum, high vacuum and ultra-high vacuum. Low vacuum usually means vacuum of 1×10^{-3} torr or lower (lower vacuum = higher pressures), high vacuum is usually in 1×10^{-7} torr or lower. Ultra-high vacuum usually denotes vacuum systems with a pressure of 1×10^{-8} torr or lower pressures. Incidentally, interstellar space is thought to have a vacuum level of 1×10^{-13} torr.

and aluminum alloy chambers, which are lighter, easier to machine, and have high heat conductivity (easy to heat uniformly and bake for outgassing), are very attractive materials to use for UHV vessels. Also, because the interior of the aluminum alloy chamber can be made chemically inert by its oxide layer, it is especially suited for corrosive gas use. However, they are costly to manufacture, and as their compatibility with stainless steel systems, which most pumps and other UHV equipments are made of, are only sporadically researched [30], 304 stainless steel is currently the most widely used construction material.

In order to measure the vacuum level, a UHV nude ionization gauge was installed on each KBE vacuum chamber as a standard equipment. The ionization gauge, or "ion" gauge is controlled by an ion gauge controller (Granville–Phillips[2] Series 350 Ion Gauge Controller) capable of measuring the pressure ranges of 1×10^{-3} to 1×10^{-13} torr.

Most UHV chambers are connected through a flange port, usually equipped with a knife edge. Ports are sealed using a metal gasket, popularly made with pure copper, or silver-coated copper. By the compression of the soft metal between the knife edges of the flanges, a leak-proof vacuum seal is made.

3.2.1 Differentially Pumped UHV Chambers

The most efficient method to obtain an effective free-jet expansion and to maintain a molecular beam profile beyond the skimmer is to use a differentially pumped chamber setup. By isolating the gas expansion section from the rest of the chambers, and by having a dedicated vacuum pump for the gas expansion section, it becomes considerably easier to maintain the low background pressure required to keep the molecular beam profile using moderate pumping speeds. This efficient pumping method leads to a differentially pumped system design, with multiple chambers, each with its own pumping system to help maintain the desired vacuum level (Figure 2-3). Also by introducing a collimator between the chambers, it is possible to create a beam with a narrower velocity distribution. However, in this project, such severe selectivity was not necessary; therefore, only two stages of differentially pumped chambers were used. The underlying theory of this setup is discussed in Section 2.5.

[2]Granville–Phillips Company 800 Turnpike Street, Suite 300, North Andover MA 01815. tel: (508) 688-8262

3.2.2 Pumps

Usually, when dealing with a gas-injected UHV system, it is most sensible to select a vacuum pump with high gas throughput. Turbomolecular pumps and diffusion pumps are popular classes of vacuum pumps with very high throughputs. However, standard turbomolecular pumps require some type of bearing lubrication to accommodate their high-speed rotating vanes, and diffusion pumps use hydrocarbon or synthetic oil to pump the gas molecules. Any hydrocarbons back-streamed into the UHV system greatly reduce its cleanliness. Most of the time, this problem is resolved by placing a hydrocarbon trap at the inlet port of the pumps. Such traps are usually made of cryogenic grids or collars, which help prevent the hydrocarbon from backing into the vacuum chamber through entrapment. However, having such traps greatly reduces pumping speeds, as they lower the conductance at the pump inlet.

Diffusion pumps are virtually maintenance free, and are capable of very high pumping speeds. Also, they have the best pump-speed-to-price ratio. However, because of the heavy use of oil, they are not very well suited for UHV use, and if they are used, heavy precautions against hydrocarbon back-streaming are necessary. Also, they are physically large, and require a lot of space, especially for pumping at high speeds. Since they rely on gravitational force as a vital part of their pumping mechanism, diffusion pumps can only be connected to a vacuum chamber in an upright orientation.

Turbomolecular pumps are usually compact, and with the use of magnetic levitation bearings instead of lubricating oils, they are extremely effective in pumping in UHV conditions without the fear of hydrocarbon contamination. However, this is also the most expensive type of pump available. Also, reliable pumps with very high pumping speeds in excess of 3000 l/sec, necessary for high gas flux systems, are hard to find. In addition to high cost, turbomolecular pumps are well known for catastrophic failure modes. Especially at high pumping speeds, they need to be frequently monitored and maintained to prevent any such costly and hazardous accidents.

Two other pumps frequently used in UHV systems are ion pumps and cryogenic pumps. Both pumps are well known for their clean operation, since they do not use any lubricants for operation, and have no moving parts in contact with the vacuum. The greatest disadvantage of these pumps is their low throughput.

Ion pumps operate by ionically charging molecules and reactively implanting them into its sidewalls and elements by accelerating the ions through a strong magnetic field. As mentioned earlier, ion pumps are not suited well for high-flux applications. If the chamber pressure pumped by an ion pump is too high, the element in the ion pumps

will heat up due to the high ion bombardment flux. Thus in turn reduces its pumping speed and eventually lead to thermal overload and subsequent shutdown. Also, since the gases are embedded in the inner walls (or elements), there is a saturation point where it can no longer effectively pump. The element lifetime limitation can be circumvented by periodically replacing the elements.

Cryogenic pumps operate by maintaining their adsorbing materials at a very low temperature (typically around 65 K for the first-stage, and 10 K for the second-stage condenser array temperatures) and condensing or trapping gases upon them. A cryogenic pump's pumping capacity is limited by the adsorption volume of its condenser array. Although it has a high retention capacity for condensible gases with condensation temperatures 10 K or higher, the total pumping capacity is severely limited for non-condensing gases such as helium or hydrogen. Once the amount of condensed gases reaches its capacity, it must be regenerated[3]. Although cryogenic pumps are one of the most efficient method to pump a UHV system, just like the ion pumps, they are not suitable for high-flux applications.

For the KBE system, as discussed in Section 2.5, it was determined that both the source chamber and the etching chamber needed at least 3500 l/sec pumping speed. For such high pumping speed requirements, the most logical pumps to use were diffusion pumps with cryogenic traps. However, diffusion pumps with the necessary pumping capacity were far too large to use, given the limitation on the chamber heights. Therefore, for the sake of size, turbomolecular pumps became a favored choice. However, turbomolecular pumps with such high pumping capacities were too expensive. Fortunately, thanks to recent advancement in cryogenic pump technology, high-capacity cryogenic pumps with automated regeneration controllers became available. Because of its cleanliness, and relative small size for the pumping speed, CTI[4] On-Board 10 Cryogenic Pumps which offered 5000 to 8000 l/sec pumping speed were chosen for use on both the source (free-jet expansion) chamber and the etching chamber. The problem of throughput was resolved by frequent regeneration of the pumps, which was simplified by the use of their automated regeneration capabilities.

[3]Regeneration of cryogenic pumps requires the warming up of the traps and baffles, purging the condensed gas out of the condensing arrays using dry nitrogen gas, and re-cooling them to operating temperatures. Using the CTI On-Board 10 Cryogenic Pump Controller, for a complete regeneration, normally takes approximately 2.5–3 hours for a cold-to-cold regeneration cycle.

[4]CTI Cryogenics 9 Hampshire Street, Mansfield MA 02148. tel: (508) 337-5000

3.2.3 System Bake-out

Once the vacuum chambers have been checked for leaks using helium gas and a residual gas analyzer, it is necessary to heat the stainless steel surfaces exposed to the vacuum in order to drive off any gaseous species adsorbed or absorbed on it. This is frequently referred to as "baking." To prevent leaks from developing, it is necessary to be able to heat a vacuum chamber a minimum of temperature differentials to avoid thermal stresses, especially at metal-to-metal and metal-to-glass seals. Once it was proven to be leak-proof, the stainless steel chambers of the KBE system were heated by wrapping it with a high-temperature heating strap with a percentage temperature controller (Omega[5] Percentage Temperature Controller, 120 V and 240 V). However, due to the low heat conductance of stainless steels, uniform heating of the chambers was not possible. In order to compensate for the low heat conductances, the entire chamber was first completely and tightly wrapped using heavy-duty aluminum foils. After the aluminum foils were in place, heating straps were coiled around the aluminum foil-covered vacuum chambers. Also to minimize convective and radiative heat loss, the heat-strapped chamber was again encased in aluminum foil. This allowed for a more even distribution of the heat, minimizing thermal stresses.

Once the heating straps were operational, the vacuum chambers were baked at approximately 180°C for two weeks in order to attain the UHV vacuum pressures for the first time. The typical idle background pressure achieved for this system was about 5×10^{-10} torr. Once the UHV pressure was obtained, as long as non-corrosive gases were used, baking was only necessary after the chamber was vented and exposed to atmosphere, and only for a few days. However, when using chlorine gas as the main injected gas species, much chlorine and chlorine compounds were adsorbed onto the exposed interior surfaces of the chamber, acting as a major outgassing source. The mechanism and the actual material of the chlorine compounds were not determined. However, to keep the idle pressure of the chamber to acceptable levels, the chamber needed to be baked for a minimum of 24 hours at 180°C every 8 hours of chlorine use.

[5] Omega Engineering Box 4047, Springdale Station, Stamford CT 06907. tel: (203) 359-1660

3.3 The Source Chamber

The chamber where the free jet expansion occurs is referred as the "source" chamber shown in This section will describe the design parameters considered to construct the source chamber. Section A.3 shows the schematics of the source chamber and Figure 3-2 is a photograph of the chamber.

3.3.1 Design Parameters

The two primary functions of the source chamber were: (1) to allow free-jet expansion, and (2) to act as the first stage differentially pumped chamber. Since this chamber has the highest injected gas load, it was important to maximize the conductance to the cryo pump. Also, as it was not certain if one cryo pumps would have enough pumping speed, a consideration was given to allow additional cryo pump to be connected later if needed. These considerations led to a barrel-like design with two 14 inch OD flanges which would attach directly to the cryo pump(s) (Figures A-14 and A-15). The cryogenic pump was connected to the source chamber through a 13.25 inch OD pneumatically actuated gatevalve. The pneumatic switch of the gatevalve was fed through a relay so that it would be triggered to close in the event of: (1) power failure, (2) failure of the heat exchanger unit used to cool the pump compressors, (3) if the second-stage temperature of the cryo pump cold head array reached above 25 K, and (4) when the regeneration cycle of the cryogenic pump was initiated. All these interlocks prevented the chamber from being accidentally vented due to the unscheduled failure of the cryogenic pump, which would cause it to regurgitate the contents of its condenser array back into the chamber.

3.3.2 Skimmer

The skimmer for the KBE system was purchased commercially from Beam Dynamics[6]. The material of choice for the skimmer was nickel, for its hardness and resistance to corrosion. The height and the base dimensions of the cone were 1 inch each. The entrance opening was 1 mm in diameter. It was mounted on a skimmer holder machined out of aluminum, and held in place by a retainer ring as shown in Figure 3-3. The skimmer holder was placed between the source chamber flange and the gatevalve leading to the main chamber using a double-sided Conflat™ flange. The double-sided flange

[6]Beam Dynamics, Inc. 708 East 56th Street, Minneapolis, MN 55417. tel: (612) 823-8151

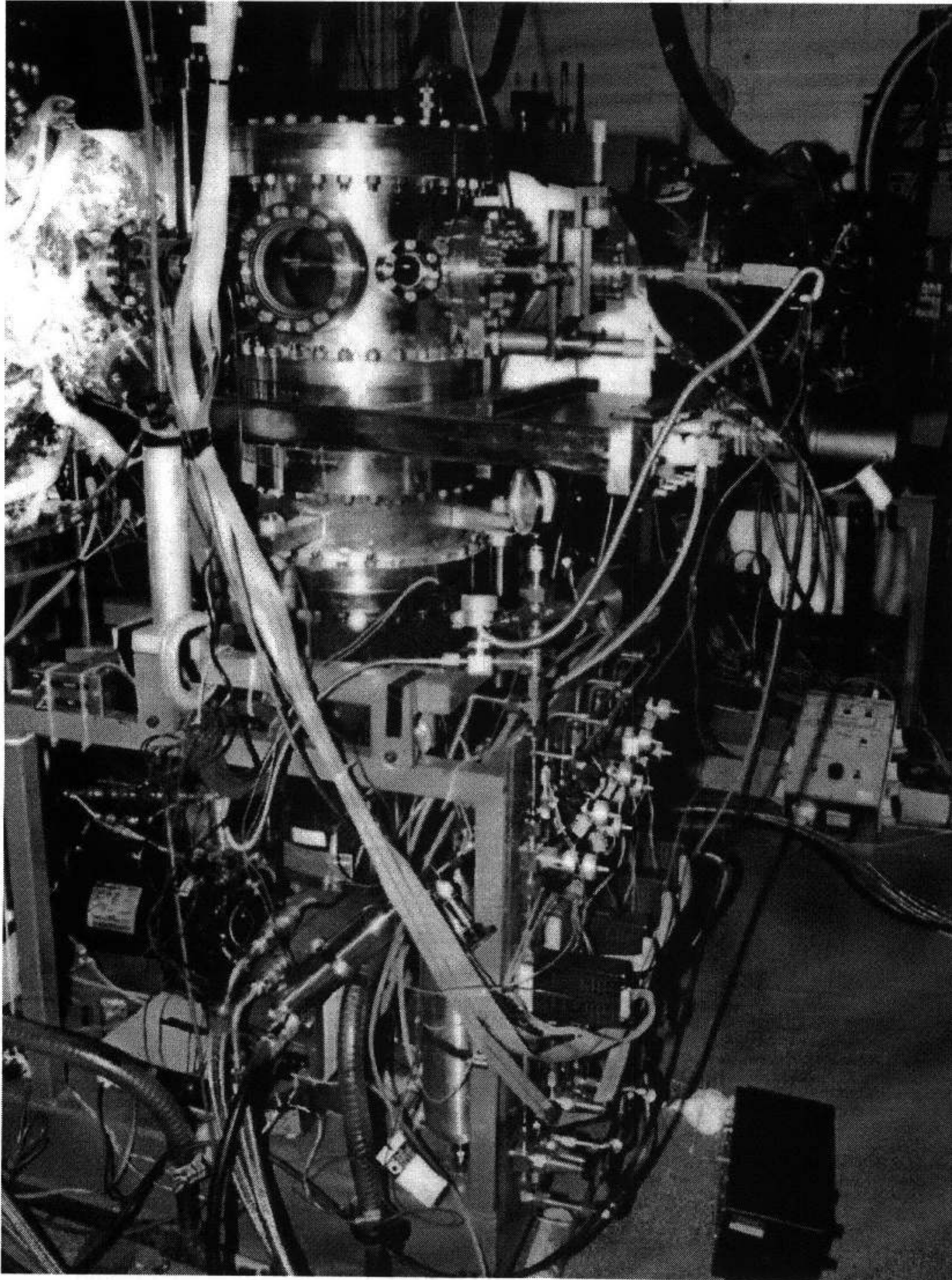

Figure 3-2: Photo of the source chamber supported on a movable stage. Under close inspection, the nozzle can be seen through the 6 inch viewport.

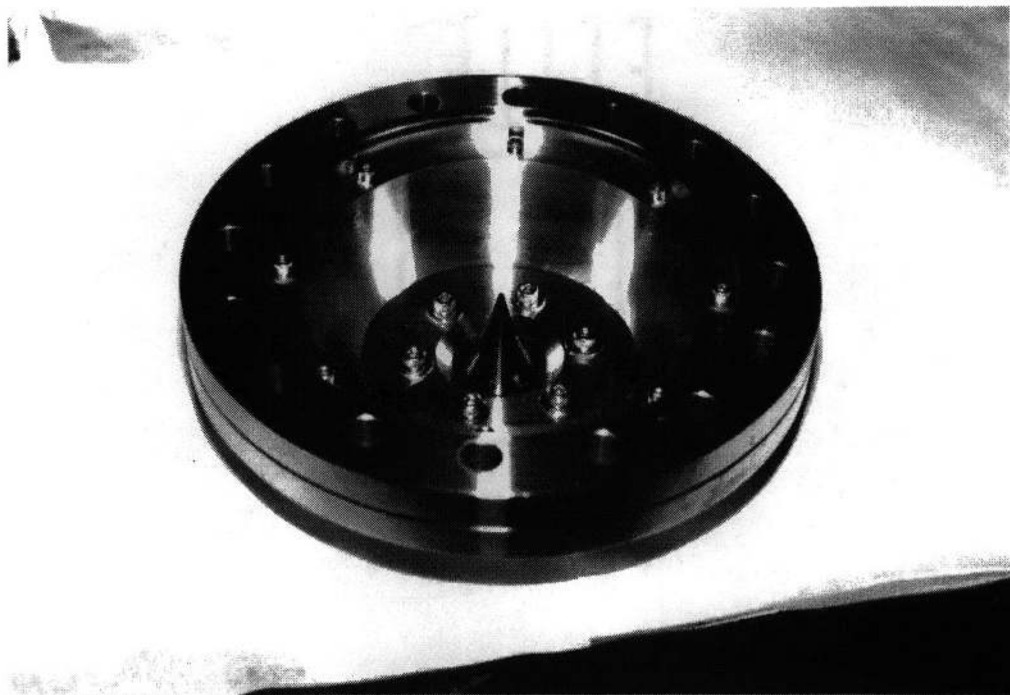

Figure 3-3: Photo of skimmer mounted on its holder and six inch double-sided Conflat^{TM} flange. The skimmer is held in place by a retainer ring on the back side of the holder.

was custom machined so that when the skimmer holder assembly was put in place, the base of the skimmer cone was approximately 1/4 inch from the gatevalve assembly. This distance was calculated to give approximately 1/8 inch clearance between the gatevalve assembly and the retainer ring, which resulted from a desire to minimize the distance between the skimmer and the next differentially pumped chamber so as not to lose too much beam intensity at the target.

Since some degradation of the skimmer after continual use of corrosive gases was expected, the source chamber was placed on a stage with a roller which rested on the top railing of the main chamber stage (Figure A-21). This setup allowed the source chamber to be readily pulled away from the main chamber when the skimmer needed replacement.

3.3.3 Nozzle Stage

A Thermionics[7] model EC–1600 X–Y–Z stage with multiple mini-ports was mounted on the 6 inch flange directly opposite the skimmer. The mounted nozzle stage is shown in Figure 3-4. The optional non-tapped mounting flange was placed on the nozzle stage,

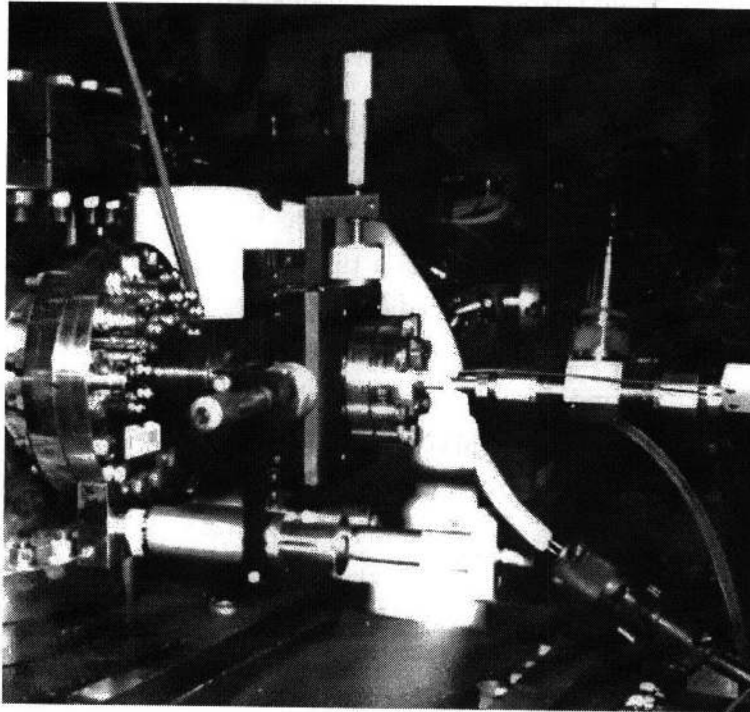

Figure 3-4: Nozzle stage with nozzle installed.

to allow the addition of an angular controller if some angular correction for the nozzle was needed. The nozzle assembly was mounted on the stage with 2 inch movement in the Z–direction and 1 inch in the X–Y plane. With the use of 3/4 inch OD tubing as the nozzle support tube, this allowed approximately 1/8 inch freedom in the X–Y plane. As the nozzle was constructed to very tight tolerances, the 1/8 inch movement was deemed sufficient for most of the alignment purposes. All translational motion of the stage is precision controlled by the use of micrometers.

[7]Thermionics Laboratories, Inc. 22815 Sutro, Hayward CA 94540. tel: (510) 538-3304

3.4 Source Flange

The source flange is a large 14 inch OD flange which connects the source chamber to the main chamber. It consists of one 6 inch OD port in the center of the 14 inch flange. The 6 inch flange is referred to as the "main" etch port. The main etch port is where the supersonic expansion chamber was connected through a gatevalve.

In addition to the main etch port, four additional 4.5 inch OD etch ports were also placed on the source flange. These extra flange ports were designed so that two of the four "secondary" etch ports were looking directly at the substrate when the substrate was facing the main port, and the remaining two facing the substrate when the substrate manipulator was turned 45 degrees off the main etch port. The secondary etch ports were intended to be used as either a secondary gas injection port for a "doser" style nozzle, or perhaps a nozzle equipped with a tungsten filament to "crack" the etchant gases to perform an etch using neutral radical gases.

For this thesis project, two of the four secondary etch ports were fitted with zero-length quartz viewports, and were used as laser interferometry windows.

An extra 4.5 inch OD port was also added which looked directly at the substrate when it was facing the main port. This port was designed to be used for a group–V effusion cell should providing a group–V overpressure became necessary. Fortunately for this project, it was not necessary to use the effusion cell port.

Several mini 1.33 inch OD flange ports were also strategically placed in the event the use of a shutter for the effusion or the etch ports became necessary.

3.5 The Main Chamber

The primary function of the main chamber is to maintain the molecular beam profile after the skimmer, and to provide a means to place the substrate into the beam path. The chamber was designed with the use of a cryogenic pump mentioned in Section 3.2.2. Figure 3-5 shows the main chamber, and the schematic design for this vacuum chamber can be found in Section A.2.

Many expansion ports were added on to the body of the chamber to allow the addition of (1) an Auger spectroscope, (2) reflective high energy electron diffraction equipment, (3) extra ion pumps, and (4) a residual gas analyzer. All viewports were placed to allow shutters to be attached to protect them from being coated by the etch products or from the arsenic effusion cell, if it was used. Provisions were also made to

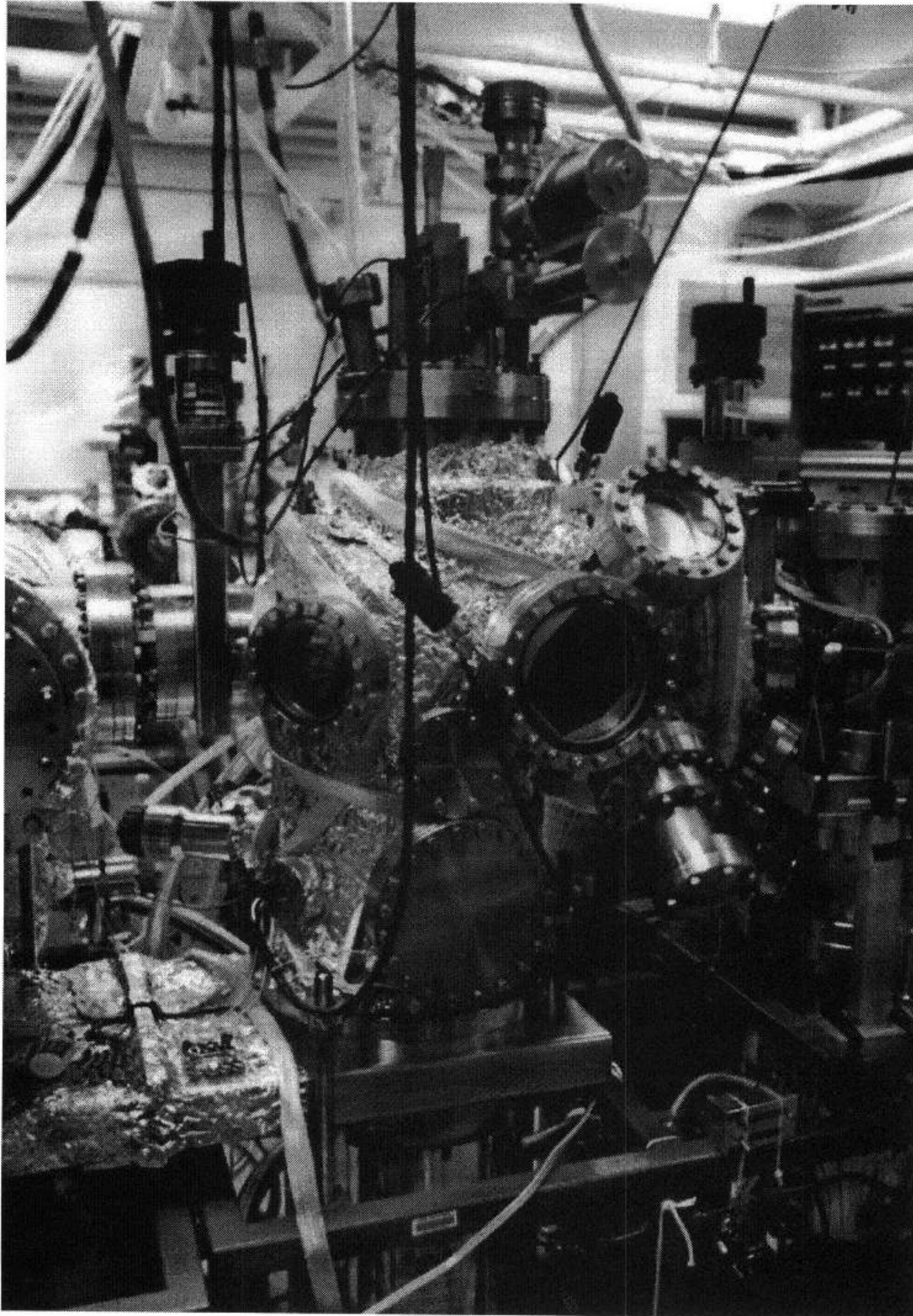

Figure 3-5: The main chamber. The chamber is wrapped in aluminum foil for better thermal distribution during frequent baking necessary to maintain UHV background pressures.

accommodate the use of a cold finger to cool the sample, and various feedthrough ports for the addition of guillotine-like shutters to protect the viewports, or other sensitive equipment.

3.5.1 Substrate Manipulator

A substrate manipulator from a Riber[8] 2300 MBE system was used. It allowed use of a substrate up to 2 inches in diameter. The rotatable sample manipulator arm is mounted on an X–Y–Z translational stage, with approximately 270 degrees of rotational freedom in the horizontal plane, and a rotatable sample holder in the vertical plane. It was also equipped with a substrate heater capable of heating the substrate up to 1400°C and an ion gauge for measuring beam equivalent pressures. The ion gauge on the manipulator is referred to as the "flux" gauge. The flux gauge was used primarily to align the nozzle beam to the skimmer, and also to measure the amount of gas being injected into the main chamber during operation.

The substrate heater temperature was controlled using a Eurotherm[9] controller (Eurotherm 818P4 temperature controller) and a Type C thermocouple. The heater was driven using a Lambda DC variable power supply. Since, without group–V overpressure, the substrate could not be heated beyond 500°C without destroying GaAs and 400°C for InP substrates, a small power supply was sufficient for this work. Typically to sustain a 300°C substrate temperature, 6 volts at 2.5 amperes was needed.

As noted in Section 2.4, the distance between the nozzle and the skimmer was determined to be somewhere between 1–2 cm. In order to have a beam spot size of approximately 2 cm diameter hitting the target substrate, a total distance of about 30 cm from the nozzle and the target was needed. The substrate manipulator port was positioned and the ports on the source flange (Section A.1) were designed to meet this requirement.

In anticipation of accidents involving substrate and substrate holders falling off of the substrate manipulator chucks, a measure to prevent the blocks from falling straight into the cryo pumps were taken. A protection screen (Figure A-38) was designed to act as a barrier between the main chamber and the cryo pump body while the gatevalve between the pump and the chamber is open. It was designed to minimize the reduction of the conductance to the pump, and also so that it can be placed into the chamber

[8] Riber/Instruments SA Group 6 Olsen Avenue, Edison NJ 08820. tel: (908) 494-8660
[9] Eurotherm Corporation 11485 Sunset Hills Road, Reston VA 22090. tel: (703) 437-3184

through an 8 inch OD (6 inch diameter hole) port opening and assembled in place. The screen was machined out of a 1/2 inch aluminum sheet, and a 8 AWG soft stainless steel wire was used to make a net-like grid. The screen was suspended approximately 1 inch above the gatevalve using three aluminum brackets hooked onto the view ports of the main chamber.

3.5.2 Laser Reflectivity Measurement

Although feedthrough ports were available, the KBE system was not equipped with a reflective high-energy electron diffraction system. Therefore, it was important to equip the system with another means to monitor the surface roughness *in–situ* during the etch. For this purpose, a laser reflectivity measurement setup was placed on the main chamber.

A 1.5 mW, 633 nm wavelength helium–neon laser (Uniphase[10] model 1101P Helium-Neon laser with 1201-1 power supply) with approximately 0.63 mm beam spot size was chosen for its stable mode sweep and power output specification. The polarized laser beam was reflected off of the substrate surface and the reflected beam intensity was detected using a silicon detector (Coherent[11] Model 212 Power meter with Photodetector) through a 633 nm (±5 nm FWHM) band-pass filter (Newport[12] model 10LF10-633 filter with LH100 lens holder). The signal was amplified (Omega AmpII) and plotted onto an X–Y chart recorder (Hewlett–Packard model 7046B Chart Recorder). A voltage offset circuit was added to allow monitoring whenever the input signal was too high for the chart recorder to compensate internally. The discussion of data from this reflectivity measurement is presented in detail in Section 4.3.2.

3.5.3 Residual Gas Analyzer

In most ultra-high vacuum systems, it is important to be able to detect the cleanliness of the vacuum. Residual gas analyzers, also frequently referred to as mass spectrometers or quadrupole analyzers, are a very convenient method to obtain such data. By detecting the mass of the free gas in the vacuum, the residual gas analyzer, or RGA, will allow the

[10]Uniphase Corporation 163 Baypointe Parkway, San Jose CA 95134. tel: (408) 434-1800, (800) 644-8674

[11]Coherent Inc., Components Group 2301 Lindbergh, Auburn CA 95602. tel: (916) 888-5107

[12]Newport Corporation 1791 Deere Avenue, Irvine CA 92714. tel: (714) 863-3144, (800) 222-6440

determination of gaseous contaminants inside the chamber. The RGA is also frequently used to perform a leak check by using a gas not highly present in atmosphere, usually helium. The leak is detected by spraying the helium around the flanges where leakage is suspected, and seeing if the RGA detects the mass 4 (helium) within the chamber. Also, a 4-to-1 ratio of nitrogen to oxygen gas registering on the RGA is a fair indication that there is a leak to atmosphere.

An RGA is also used to determine how clean the system is. Immediately after chamber exposure to atmosphere, an RGA unit registers a high concentration of peaks 18, 28 and 32, which are water, nitrogen and oxygen gas, respectively. By monitoring the decrease of these three species, it is possible to determine if all the traces of atmosphere contaminants have been eliminated.

In the KBE system, the RGA has another vital role besides the usual ones of leak detection and cleanliness monitoring. By using the RGA during the etch runs, it is possible to detect what volatile etched species are being created.

The Hiden Analytical Laboratories[13] HAL-II residual gas analyzer with mass detection of 1–300 amu and a partial pressure detection limit of 5×10^{-13} torr was placed on the main chamber. It was initially placed directly above the cryogenic pump port with the intent to analyze any gases which are being pumped away. However, due to the insensitivity of detecting the product species, it was moved towards the front of the main chamber, directly aligned with the substrate holder when it faced the etchant beam. This line-of-sight placement allowed for higher detection probability of minor etched species.

3.6 The Transfer Tube

The main purpose of the transfer tube was act as a shuttle "corridor" for the substrates to travel between the vacuum chamber systems once the cluster tool was completed. A photograph of the transfer tube is shown in Figure 3-6. It is to be fitted with magnetically coupled substrate "carriers" which are designed to handle up to six substrate holder blocks (molybdenum blocks, or moly blocks), and move along a rail running through the tube. The rail was to be aligned to the proper height of the vacuum chambers using linear motion feedthroughs which line the bottom part of the tube which supports the rail.

[13] Hiden Analytical Laboratories 77 Route 202 North, Suite H, Peterborough NH 03458. tel: (603) 924-5008

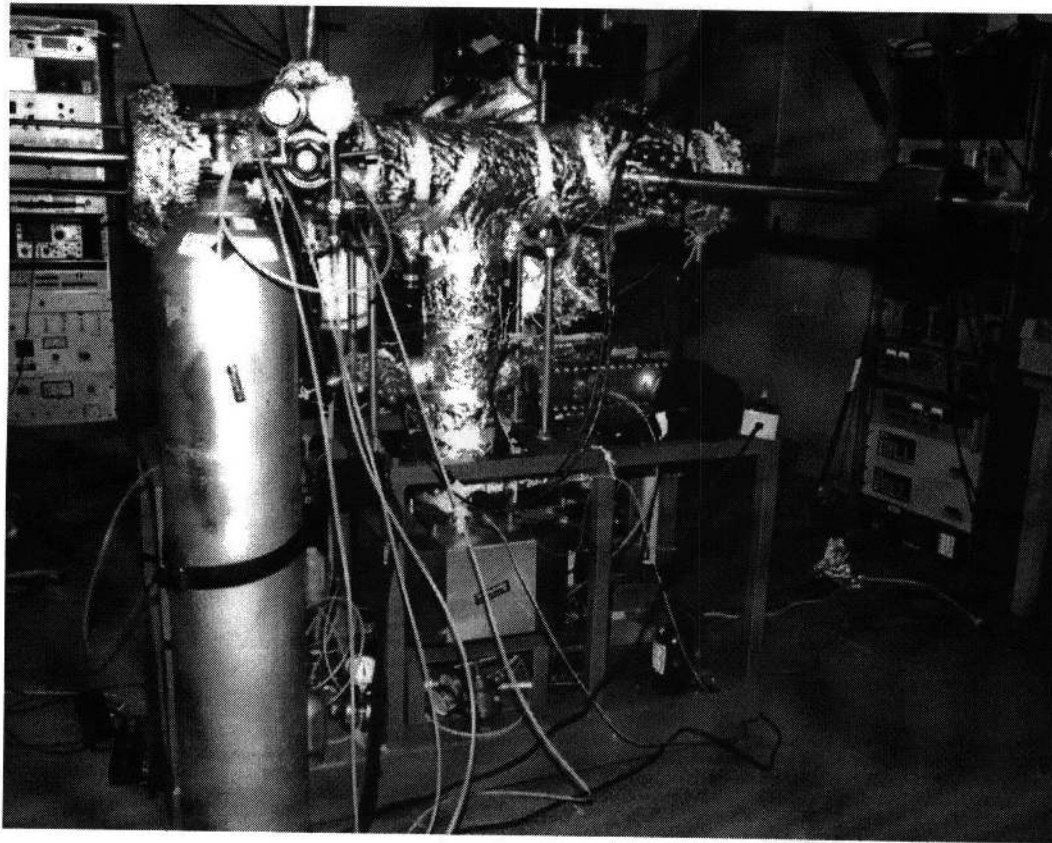

Figure 3-6: Transfer tube seen from the back of the KBE system.

The transfer tube was set on a different stage than the main and source chambers to allow ease in transportation and configuration. It is also sectioned into two, with a 10 inch gatevalve isolating the tubes, so that both the KBE and Riber 2300 solid-source MBE can be vented independently, and can be completely isolated in the event of some catastrophic vacuum failure in one of the systems. For this project, only half of the whole transfer tube system was constructed until the functionality of the KBE was proven and the KBE and the adjoining MBE system were ready to be joined.

Each section of the transfer tube was designed to be pumped using an 8 inch ion pump (Perkin–Elmer[14] 270 l/sec ion pump). Each section also has two 6 inch ports directly facing two 8 inch ports. The 8 inch ports were designed to connect to a neigh-

[14]Perkin–Elmer Physical Electronics Division 6509 Flying Cloud Drive, Eden Prairie MN 53344. tel: (612) 828-6100, (800) 237-3603

boring vacuum chamber through a gatevalve. The 6 inch ports were used to install the linear–rotary translation rods or "transfer rods," which are magnetically coupled linear translation rods of approximately 27 inches in length, with rotary capabilities to allow transferring the substrates between different vacuum chambers. With both sections of the transfer tube, it is possible to connect the MBE, KBE, load lock and a fourth vacuum chamber system together.

3.6.1 Sample Loading Port

Although the transfer tube would eventually be connected to the existing MBE machine, it was designed to be a stand-alone system while the project was being create,. Therefore, for temporary purposes it was necessary to alter one of the ports as a loading port. The interior of the load lock is shown in Figure 3-7. A 10 inch OD to 8 inch OD Conflat™ adaptor flange was placed on a 10 inch port. An 8 inch blank Conflat™ was modified (see Figure A-28) to allow an aluminum bracket with an Viton™ O-ring used on Large-Flange™ to snugly fit while allowing the O-ring to seal against the Conflat™ knife edge. Although it could not seal beyond 5×10^{-9} even after a long bake, this O-ring based flange allowed for quick and repeatable opening and closing of the UHV tube without allowing too many contaminants to enter the main chamber.

To accommodate the frequent vent to atmospheric pressures, the transfer tube was equipped with Convectron™ vacuum gauges made by Granville–Phillips[15] in addition to the standard ion gauge, so that the pressures between atmosphere (760 torr) to 1×10^{-3} torr can be measured.

3.7 The Process Control System

3.7.1 The Nozzle

The key instrument in supersonic expansion is the nozzle. Fundamentally it needs to act as a reservoir for etchant gases, heat tank, and have a small orifice opening into the vacuum chamber. It needs to be UHV leak-free, high-temperature resistant, and mounted on an X–Y–Z stage so that it can be easily aligned with the skimmer. Also, beam stability (vibration insensitivity) and manufacturability are important concerns.

[15]Granville–Phillips Company 800 Turnpike Street, Suite 300, North Andover MA 01815. tel: (508) 688-8262

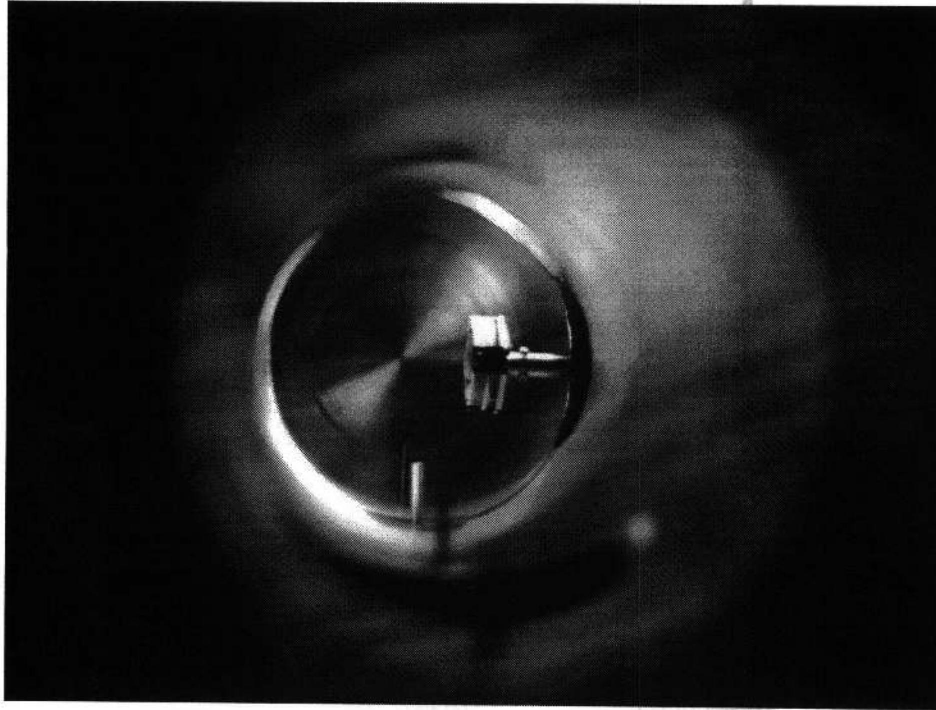

Figure 3-7: The load lock seen from the inside. The sample holder and a moly block is seen attached to the transfer rod. The rods on the bottom of the transfer tube will be used to adjust the height of the substrate carrier tracks once it is installed. The big hole on the bottom of the cylinder leads to the ion pump.

The nozzle assembly was made out of five distinct parts: (1) nozzle tip, (2) support tube, (3) inner gas tube, (4) flange, and (5) nozzle heater. All parts except for the nozzle heater were made of metal. Electropolished, 1/4 inch OD, 0.035 inch wall seamless stainless steel 316L tubing was used as the inner tube, chosen for its resistance to high temperature and commercial availability. The support tube was machined out of 3/4 inch OD, 0.065 inch wall seamless stainless steel 304 tubing. A standard 2.75 inch OD Conflat^{TM} flange was machined to allow socket welding of the 3/4 inch support tube on the vacuum side. Figure 3-8 illustrates the fully assembled nozzle structure.

Initially, the nozzle tip was machined out of 3/4 inch OD nickel 200 rod. Although highly corrosion-resistant, it could not withstand the high nozzle temperatures (in excess of 700°C), and high stagnation pressures caused the nozzle tip to fail through the metal rupture failure mode [31]. In its place, Inconel 600 super alloy was chosen for its

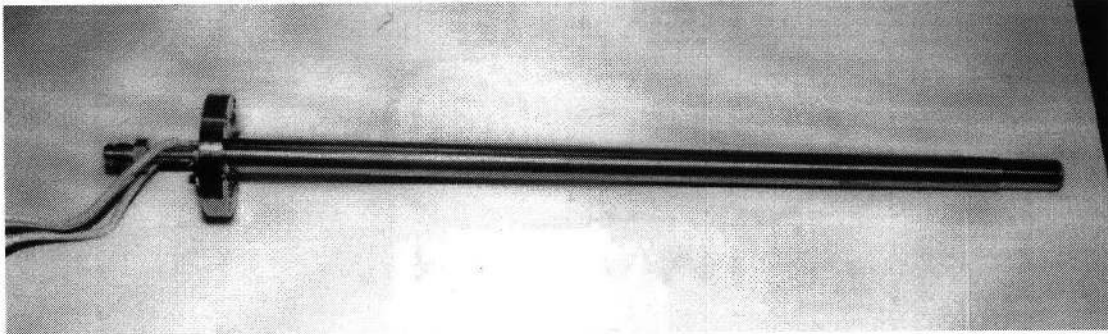

Figure 3-8: The nozzle. The length from the tip of the nozzle to the base of the vacuum side of the 2.75 inch OD flange is approximately 19 inches.

resistance to high-temperature stresses.

The most difficult part of manufacturing the nozzle tip was creating the small diameter hole. There were two drilling methods available for this project. The first method was through electrical discharge machining (EDM). However, since EDM can only work on thin plates (approximately 0.015 inches or less), the tip of the nozzle needed to be countersunk. This countersinking proved to be time consuming and difficult. The second method was laser drilling. For this project, the laser drilling method was chosen. A 65±4 μm diameter hole was laser-drilled into a machined nozzle tip using an excimer laser (Resonetics Micromachining[16]), with a hole taper of about 7%.

All of the metal parts were first welded together in accordance with UHV leak tolerances. Then the nozzle heater (discussed in detail in Section 3.7.2) was slid onto the inner tube. After the heater was in place, a 1/4 inch VCR fitting was butt-welded onto the inlet end of the inner nozzle tube. The VCR fitting leads to series of manual and pneumatically actuated valves (Swagelok Nupro™ [17] BNV-51 packless valves) connected to the gas control and the exhaust system. The weight of the valve dangling at the end of the inner nozzle tube was supported by an aluminum retainer ring secured onto the nozzle flange using several machine screws. A Type K thermocouple probe (Omega 1/16 inch OD thermocouple probe) was inserted between the support tube and the inner tube to measure the approximate nozzle temperature.

[16]Resonetics Micromachining Inc. 4 Bud Way, Building 21, Nashua NH 03063. tel: (603) 886-6772

[17]Cambridge Valve and Fitting 50 Manning Road, Billerica MA 01821. tel: (617) 272-8270

3.7.2 Nozzle Heater

The ability to heat the nozzle is one of the most important aspect of process control of the KBE setup. Since KBE uses the thermal energy of the gas to control the beam incident energy, it was imperative to create a robust, manufacturable nozzle heater.

Due to logistical problems, it was not possible to use simple resistive heating by directly running a current through the nozzle. A seamless, electro-polished 1/4 inch OD 316L stainless steel tubing with 0.035 inch wall thickness was encased inside a seamless 3/4 inch OD 304 stainless steel tubing with 0.065 inch wall thickness, which acted as a support structure for the thinner tubing. Therefore it became a design challenge to create a way to heat the 1/4 inch OD tube with 1/8 inch clearance (see Figure A-30 for the cross section diagram of the nozzle structure).

Since no commercial heaters suitable for this application were available, it was necessary to design a heater to fit inside a 3/4 inch OD tube and around a 1/4 inch OD tube. The necessary requirements were: electrical insulation between the pipes and the heating wires, the ability to heat to high temperatures without disintegrating in air, ability to fit between the tubes, ability to place the heater in position after most of the welding of the nozzle structure was done, and ability to heat the defined region uniformly.

The design difficulty was resolved using Zircar[18] moldable ceramic products and nickel–chromium ribbon wire. Ni–Cr ribbon exhibits great thermal expansion when a current is passed through. Therefore special considerations were needed to secure the wire in place to prevent the wire movement caused by the thermal expansion from creating an electrical short circuit, in addition to previously mentioned requirements.

A 1/32 inch thick 99.9% pure alumina sheet (Zircar DM Refractory Sheet) was first wrapped around a 1/4 inch tube to create an electrically insulating sleeve. A 1/8 inch wide, 0.005 inch thick 80-20 Ni–Cr wire ribbon (National Electrical Wires[19], 80–20 Nickel-Chrome wire ribbon, 0.9 Ω/ft resistance) was wound tightly around the sleeve, leaving approximately 1 mm gap between the coils. When approximately 4 inches of coiled region was obtained, the wires were electrically insulated between the coils and securely locked in place using a 99.9% pure alumina cement (Zircar Alumina Cement). Once enough alumina cement was built up to insure electrical insulation, one of the lead wires was doubled back so that both ends of the ribbon wire exited in the same

[18]Zircar Products Inc. 110 North Main Street, Florida NY 10921. tel: (914) 651-4481
[19]National Electrical Wires 7 Executive Drive, Toms River NJ 08755. tel: (908) 240-5383

direction. Then the heater coil was wrapped again with the alumina sheet to prevent any heat expansion from causing the wires to pop out of place. The Ni–Cr wire ribbon was then butt spliced to a 16-gauge copper wire using a pure aluminum butt splice. Since the amount of heat exposure around the wire splice during a high-temperature use was unknown, aluminum was chosen over the conventional tin as a splicing material. The reasoning behind this choice was that once aluminum oxidizes, it becomes corrosion-resistant, and also has a higher melting temperature than tin. The 16-gauge copper wire was threaded through a 1/8 inch OD single-hole ceramic thermocouple tubing (Omegatite[20] 450 ORX–11618) to aid in electrical insulation. The rigid ceramic tubing (Al_2O_3 based material) also acted as a pushing rod, so that the heater tube could be pushed through the nozzle clearance towards the nozzle tip after the nozzle pieces were welded together.

Once the heater solidified, it was sintered at 600°C, and tested to ramp up to at least 900°C before it was installed in the nozzle. On average, nozzle heaters had 3 ohm resistance, enough to heat a stainless steel pipe to 900°C at 15 volts. These heaters were able to run at 900°C continually in atmosphere without any change in resistivity or degradation in performance or appearance as shown in Figure 3-9. The only failure mode observed during this thesis project was from the electrical short-circuit between the Ni–Cr wire layers (ribbon wires welding together) due to poor initial insulation. This problem was alleviated by being more careful of the insulation layers during manufacturing.

3.7.3 Gas Controllers

As one of the means to control the incident energy of the etchant gas, it is necessary to be able to control the source gas mixtures. Therefore, a gas manifold with the ability to control the gas mixture, maintain a steady pressure and with a proper exhaust system was needed.

For maximum flexibility, four mass flow controllers (MKS Instruments[21], MFC-1461C) and a pressure transducer (MKS Instruments, Baratron™ 127AA) was used. Figure 3-10 shows a photo of the gas panel assembly. The flow controllers were coupled with the pressure transducer into a four-channel flow programmer (MKS Instruments,

[20]Omega Engineering Box 4047, Springdale Station, Stamford CT 06907. tel: (203) 359-1660

[21]MKS Instruments 6 Shattuck Road, Andover MA 01810. tel: (508) 975-2350, (800) 227-8766

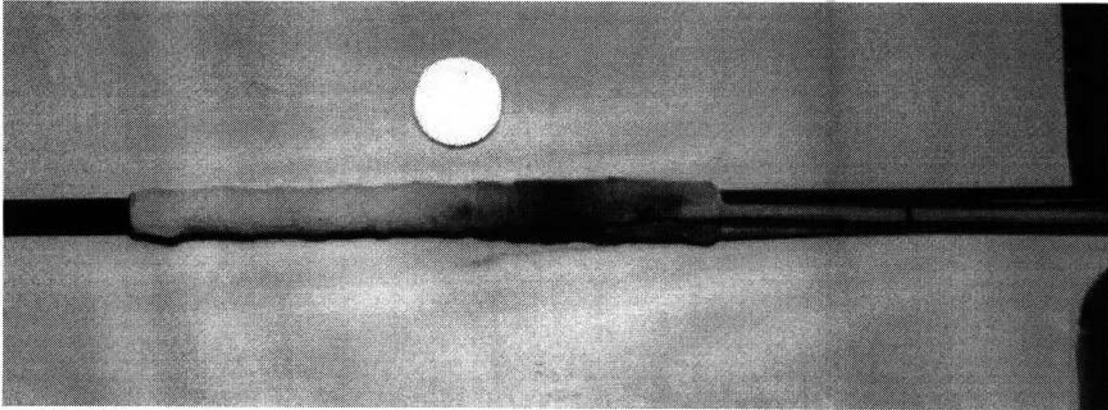

Figure 3-9: The finished nozzle heater on a 1/4 inch OD tubing, placed next to a penny. This heater was pulled out of the nozzle assembly after being used at 850°C for over 40 hours after the nozzle failed due to orifice clogging. Other than some carbon scorch marks, no degradation was observed mechanically or electrically.

147B Multichannel Flow Programmer), so that it had the ability to operate the gas flow in three different modes: (1) mix and flow gases at a fixed flow rate, (2) mix and flow gases at a fixed ratio, and (3) mix and flow gases at a fixed ratio and maintain constant pressure. The four channel controller allowed the three modes of operation to be used simultaneously with any gas combination.

To accommodate the different gases, the four mass flow controllers were plumbed together to allow any combination of the gases to be mixed, and controlled independently. Each flow controller also had a nitrogen purging line, to purge any corrosive chemicals (see Figure A-39). The flow controller panel has two output ports: one for the supersonic nozzle and the other intended for some other secondary nozzle used in the future. The supersonic nozzle output port, the "main" line, was connected to a pressure transducer, a mechanical pressure meter, an active exhaust system, a gas mixing reservoir, and the nozzle itself. The gas reservoir, exhaust, and nozzle were equipped with a packless valve to be operated independently.

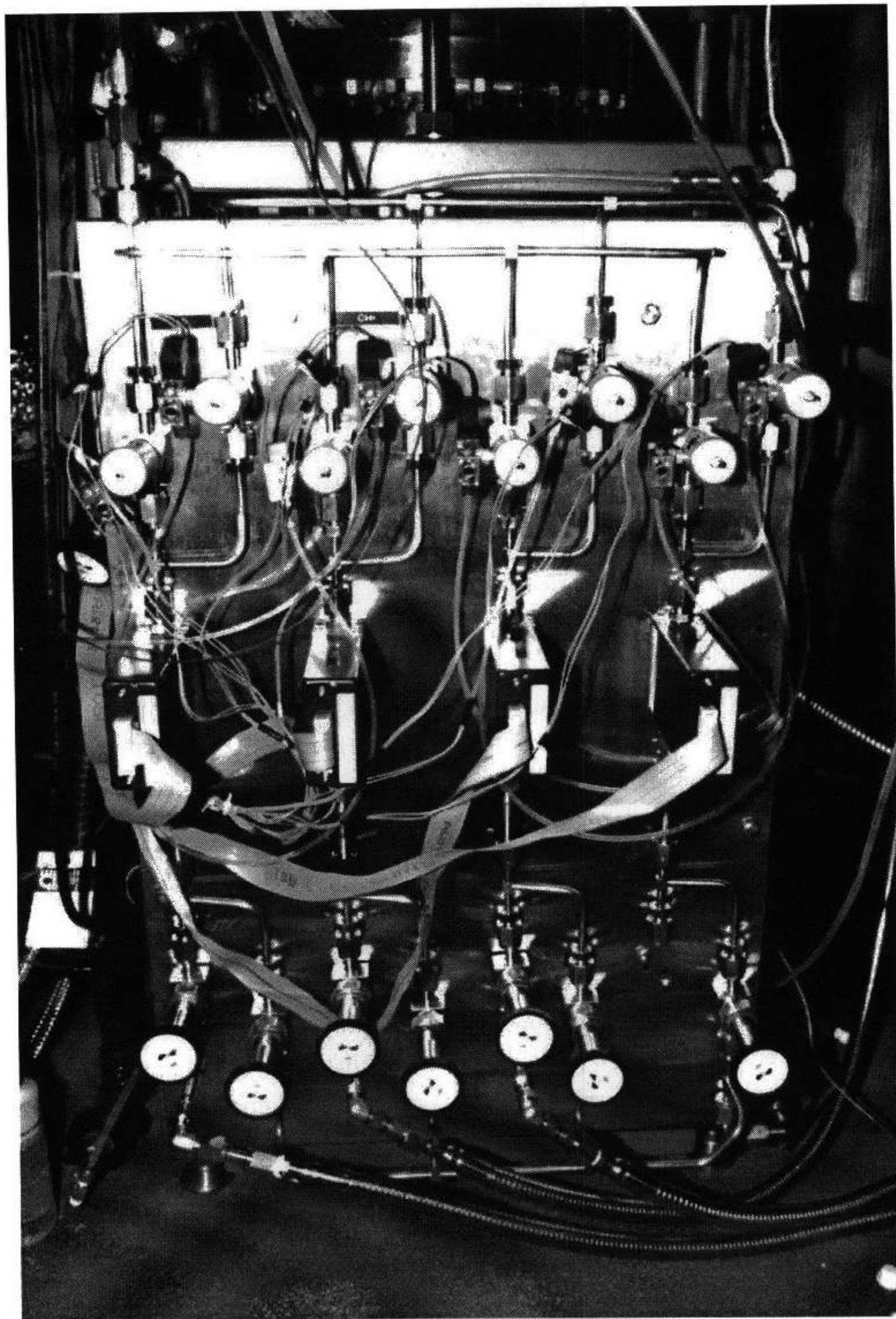

Figure 3-10: Picture of the gas panel assembly consisting of four mass flow controllers.

Chapter 4

KBE System Operation

The details of how the sample substrates were prepared, and the operation and experimental procedures of the Kinetic Beam Etch (KBE) system will be discussed in this chapter.

4.1 Substrate Preparation

4.1.1 Substrate Patterning

There are few methods available to measure the etch rate of a sample. One method is to use the laser interferometry measurement method [32][33][34][35], and measure the etch rate *in–situ.* The other method is to pattern the substrate prior to the experiment so that the etch rate can be measured using a profilometer on the step height made after the mask pattern is removed. The KBE system is designed so that either method can be used. However, in order for laser interferometry to work, it is necessary to use either a substrate with two polished surfaces, or etch an epitaxial layer, as it requires at least two light-reflecting, mirror-like surfaces for effective measurement. Also, if the etched surface becomes too rough, causing too much light scattering at the surface, it would become extremely difficult to use the laser interferometry method. Also, deposits clouding the viewports can alter the laser interferometry results. Therefore, it was decided that the latter (pattern etch) would be used for this project.

Using a patterned substrate as an etch target served two purposes. One, to allow measurement of the etch rate, and two, to allow viewing of the etch profile and determining the amount of mask undercutting. One of the most important criteria for a material to be used as a pattern mask is that the material will not degrade readily in

the etch environment. Another is the stability of the pattern under the etching condition. Use of photoresists is a common mode of etch patterning. However, they are not stable in a heated environment, and due to their organic nature, outgas considerably, rendering them unsuitable for use in an UHV environment. In addition, the photoresist was expected to degrade when exposed to the etchant gas; therefore, it was discounted as a prospective etch mask material. A metal mask, using thermally evaporated aluminum is an alternative to photoresists, and was initially used. However, after few experimental runs, it was found that some reaction occurred at the junction between the III–V compound semiconductor substrate surface and the aluminum mask after heat treatment, making the post-etch mask stripping process difficult and unreliable. The third alternative is to use an inert, silicon dioxide (SiO_2) mask. The ease in placing, patterning, and removing it from the surface of a III–V compound semiconductor, its chemical resistivity to the etchant gas, and its thermally stable nature, made SiO_2 a good choice for the mask pattern material.

All substrates used were epi-ready 2 inch wafers, with a polished (100) surface. For SiO_2 deposition, the substrates were first placed in a sputterer and approximately 3000 Å of SiO_2 was sputtered onto the surface.

The SiO_2-coated substrate was then patterned using either the Microposit S1813[1] positive or NR-8 3000[2] negative photoresists. The exposed SiO_2 was then etched using buffered-oxide etch (BOE)[3]. After the pattern transfer, the photoresists were removed using the standard solvent clean[4].

The patterned substrates were kept in a nitrogen dry box until ready for use.

4.1.2 Substrate Mounting

All substrates were mounted on a substrate mounting block made of molybdenum known as a "moly block", using 99.9999% (6N) pure indium as an adhesive. Figure 4-1 shows the mounted sample. The indium is applied by placing the moly block on a hot plate heated to approximately 165°C, and melting a small amount of indium and spreading it evenly on the surface of the block. The front surface of the moly block, which will be

[1]Shipley Inc., 455 Forest Street, Marlborough MA 01752.

[2]Futurrex Inc., 44–50 Clinton Street, Newton, NJ 07860. tel: (201) 579-1324

[3]Buffered oxide etch, or BOE, is a 7-to-1, ammonium hydroxide-to-hydrogen fluoride solution used to etch oxides.

[4]Standard solvent clean consists of three 5 minute immersions in 1,1,1-trichloroethane, three 5 minute immersions in acetone, and three 5 minute immersions in methanol.

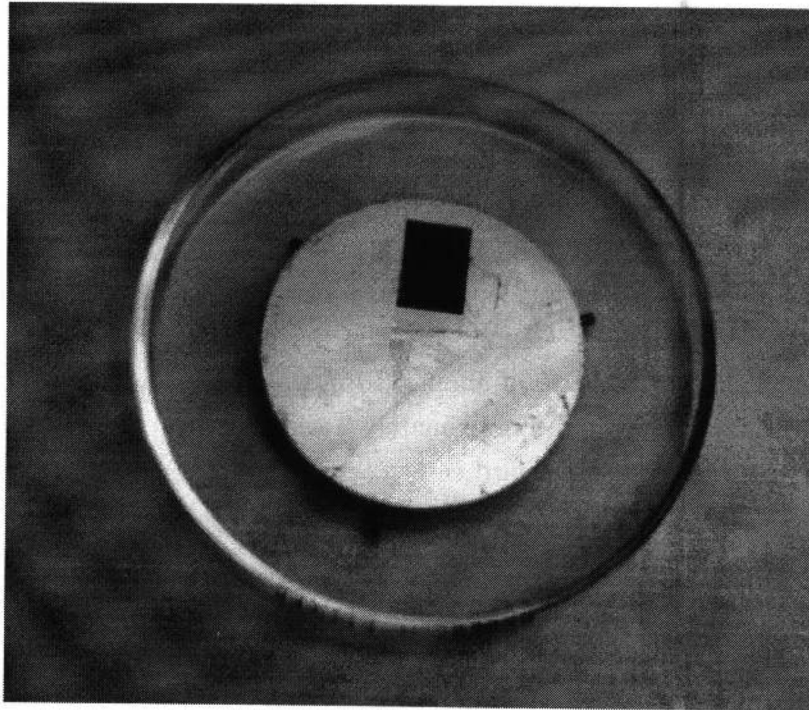

Figure 4-1: A small InP sample mounted on a molybdenum sample holder block using indium paste.

in direct line-of-sight exposure to the etch beam, was completely covered with the thin film of indium. This indium coverage gave three desired results: to protect the moly block from direct exposure to the corrosive etchant gas, to aid in uniformly heating the substrate, and to enable the use of the indium melting point for the purpose of *in–situ* thermocouple calibration (see Section 4.3.1 for details). The substrate sample is then placed on the thin indium film, allowing surface tension to hold the sample in place, even at high temperatures.

4.2 Etchant Preparation

4.2.1 Nozzle

The nozzle was first purged using nitrogen gas, by means of flooding the nozzle with nitrogen and then exhausting the gas using a mechanical roughing pump. Then it was pressurized with nitrogen to approximately 2 atm, and the gatevalve between the source chamber and the main chamber was opened allowing the gas to enter into the etch

chamber. The substrate manipulator was then rotated so that the flux gauge was looking directly into the gas stream. The correct positioning of the flux gauge is determined by watching the ion gauge controller readout of the flux gauge, and maximizing the signal strength.

Using the X–Y–Z nozzle stage, the nozzle was aligned to the skimmer opening by maximizing the flux gauge signal on the substrate manipulator. After recording the maximum pressure signal on the flux ion gauge controller, the nozzle was again evacuated using the mechanical pump.

With a nozzle orifice diameter of about 60 μm, the flux recorded on the mass flow controller to maintain 1500 torr (approximately 2 atm) nozzle stagnation pressure was approximately 50 to 60 sccm (standard cubic centimeter per minute), and nitrogen gas beam-equivalent pressure (BEP) was 1.2×10^{-6} torr. The total flow rate can be adjusted by changing the nozzle stagnation pressure. However, to maintain a suitable free–jet expansion for this system, the stagnation pressure had to be kept above 0.5 atm. Roughly, at a nozzle stagnation pressure of about 3500 torr (approximately 5 atm), the flow rate is approximately 70 sccm, and at 500 torr (approximately 0.7 atm), the flow rate is approximately 13 sccm. The beam flux into the main chamber can be adjusted by changing the distance between the nozzle and the skimmer.

4.2.2 Gas Preparation

There are two methods of injecting gas. One method, and the most frequently used in this project, is to directly pipe the gas into the nozzle from the gas tanks, referred to as the "live" feed method. The other method is to pre-mix the gas and contain it in a gas reservoir and use the etchant gas mixture from the reservoir, referred to as the"reservoir" feed method. The live feed method works well when using a pure etchant gas which requires no mixing, or the flux of the gas is high enough that the flow rate is well above the controllable level of the gas flow controllers. The reservoir feed method works well when the flux is too low to accomplish a sustained, precise flow control, and needs to use a constant gas mixture ratio.

The gas manifold system was made so that either method could be used. The live feed method only requires the use of a flow controller coupled with the pressure transducer which enables the flow controllers to maintain a constant pressure. If the use of a gas mixture is necessary, the flow controller combined with the pressure transducer can maintain a constant pressure and gas mixture ratio. If the flow rate of the nozzle is too low (less than 5 sccm per gas element), it would be necessary to "store" the gas

into a reservoir large enough to maintain a reasonable nozzle pressure throughout each etch run.

4.3 *In–Situ* Measurement Procedures

Two *in–situ* measurement methods were used to aid in calibrating and observing the etch procedures. One is recording of the pressure change throughout the initial phase of the etch experiment, and the other is recording of the laser reflectance measurement. Using the Hewlett–Packard 7046B Chart Recorder, it was possible to plot both simultaneously. This section will cover the procedures and observations made during a typical etch run.

4.3.1 Pressure Measurements

The analog output of the ion gauge controller of the main chamber was plotted using a chart recorder. By charting the change in pressure during initial substrate heating, much information can be obtained.

The pressure recording was commenced when the substrate temperature controller read 50°C. This arbitrary starting temperature was chosen to allow stabilization of the temperature controller and the substrate heater after the initial current spike associated with the triggering of the controller relay, and to facilitate comparison between plots. As the time base of the chart recorder and the temperature ramp rate were kept constant (100 sec/in), in the event of misrecording of the temperature or the pressure, the discrepancy can be easily detected. A typical pressure plot is shown in Figure 4-2.

Typically, the background pressure rises as the substrate temperature is increased at a constant rate, caused by the outgassing of water molecules from the substrate and the substrate holder. At around 120°C, the pressure rate of rise decreases, allowing the pressure to stay constant or slightly decrease. This change in rate is caused by the attrition of the outgassing rate of the H_2O molecules. Usually, at or around 150°C, a spike-line increase of pressure, referred to as the "blip", can be detected. The blip point was later determined as caused by the melting of indium, and the burst of pressure is thought to be caused by the gases trapped within the indium "glue" escaping when the metal melts. By monitoring the temperature at which the blip is recorded, which can occur anywhere between uncalibrated temperature readings of 100°C and 160°C, it is possible to calibrate the thermocouple of the substrate heater *in–situ* , and enable control of the actual etch temperature with precision.

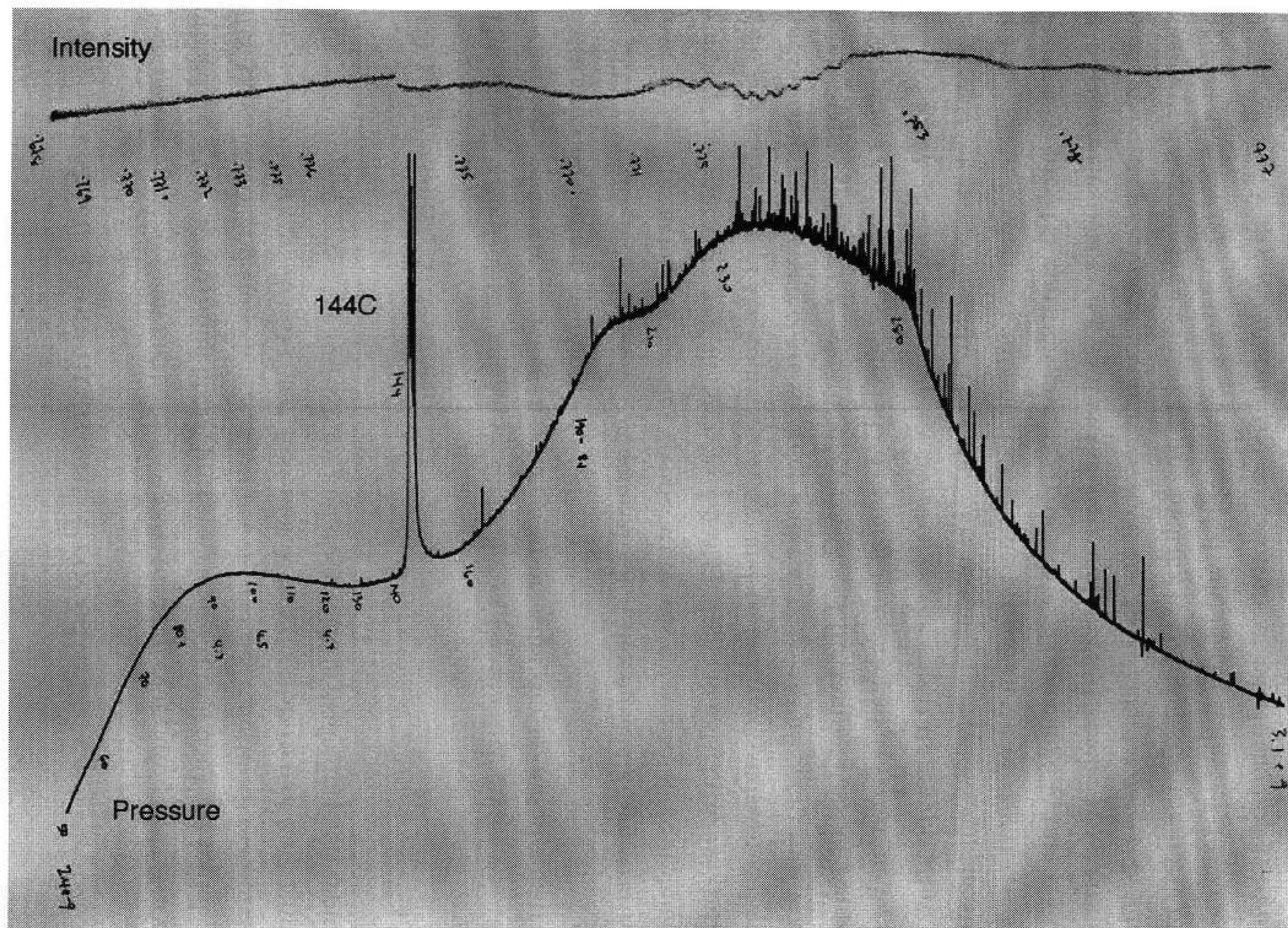

Figure 4-2: A typical plot recorded during the substrate temperature ramp to 280°C at 15°C/min. The vertical axis is the pressure or the light intensity and the horizontal axis is time. In this plot, the indium melting burst pressure temperature is 144°C.

When the temperature reaches around 170°C the pressure again commences a rapid increase. This increase in pressure is assumed to be caused by the combination of vaporization of indium off of the substrate holder and the outgassing of contaminants entrapped during substrate mounting from the melted indium. The pressure increase slows around 210°C, but again resumes its rapid increase. This third increase in pressure rise is attributed to the resident indium chloride compounds adsorbed onto the substrate manipulator being outgassed. Some of the relevant reaction product properties are listed in Table 5.1. At or around 240°C the pressure again starts to level out, and eventually begins to decline.

The assurance of similar degrees of outgassing of the adsorbed species were determined by observing the pressure drop by the time it reached the maximum outgassing temperature (usually uncalibrated 280°C). At the end of the substrate temperature ramp-up cycle, if the pressure does not stop increasing by the time it reaches the outgassing temperature, it was regarded that the outgassing was incomplete and that not all of the volatile species adsorbed onto the substrate holder and the sample were allowed to outgas. In such case, the maximum outgassing temperature was increased steadily until a decrease in outgassing rate was observed to maintain similar substrate cleanliness conditions. However, for most practical purposes, 280°C was sufficient to observe the attrition of the rate of desorption of contaminants.

The pressure plot gave two very important pieces of information: the thermocouple calibration point, and cleanliness of the substrate after outgassing which allowed consistent substrate conditions prior to the experiments. In addition, by combining the laser reflectivity measurement on the same chart, the timed response between the point of etchant gas exposure to the beginning of the roughening can also be observed.

4.3.2 Laser Reflectivity Measurements

4.3.2.1 Surface Roughness Measurements

Polarized He–Ne laser light was reflected off of the substrate surface, and the specular reflected light intensity was recorded. It was found that during the thermal oxide desorption the reflected light intensity decreased in a consistent manner. Lavoie *et al.* [36] explains that such a decrease in intensity is attributable to an increase in the surface roughness of the substrate, contributing to increased scattered light at the surface. It is shown that the reflected laser light is sensitive enough to detect such minute changes in the surface conditions.

Lavoie further explains that the increase in the roughness of the substrate surface is caused by the thermal desorption of the oxide, and the magnitude of the roughness is proportional to the thickness of the initial oxide layer. It was also shown that if approximately 0.5 μm of a buffer layer was allowed to grow on the oxide-desorption-roughened substrate, the reflected intensity returned to the initial value, implying that the any damage obtained during the thermal oxide desorption is a recoverable one. Although Lavoie used diffused reflected light[5] for measurements instead of the directly reflected light like the one installed on the KBE system, the underlying reasoning still stands.

From the explanation that the laser beam intensity fluctuation was being scattered by the roughening of the surface, the correlation between the decrease in the reflected intensity and the actual roughness (R_q, or also commonly addressed as root-mean-square roughness, RMS) measured by atomic force microscope was made. In determining the order of the roughness, a simple light-scattering expression [37][38] for randomly rough surfaces was used:

$$\frac{I_f}{I_i} = exp\left\{-\left(\frac{4\pi d\cos\theta}{\lambda}\right)^2\right\} , \qquad (4.1)$$

where I_f is the reflected final intensity, I_i is the initial reflected intensity, θ is the incident angle of the laser beam off normal incidence, d is the standard deviation of the height of the surface (surface roughness), and the λ is the wavelength of the laser.

Atomic force microscope, or AFM, is a popular tool used to investigate the topology of a sample. It is a high-resolution profilometer which uses the force between the sample surface and a very sharp probe tip mounted on a cantilever [39] to measure the topography. The height measurement is accomplished by detecting the deflection of the cantilever using a laser beam. The typical height resolution is in the few nanometer scale for scans up to 130 μm. However, under smaller scanning range, it is capable of detecting the height at an atomic scale. With the AFM, roughness is calculated through the use of Equation 4.2 [40]:

$$R_q = \left\{\frac{1}{N}\sum_{i=1}^{N}(Z_i - Z_{avg})^2\right\}^{\frac{1}{2}} , \qquad (4.2)$$

[5]Diffused reflectivity measurement is accomplished by detecting the non-specular light scattered from a laser beam incident on the front surface of the sample.

Substrate	Initial R_q	Laser Refl. R_q	AFM R_q
InP 025	0.4 nm	47 nm	30 nm
InP 042	0.4 nm	24 nm	15 nm
InP 043	0.4 nm	11 nm	7 nm
InP 044	0.4 nm	42 nm	27 nm

Table 4.1: Comparison of roughness measurements made by laser reflectivity measurement and atomic force microscope.

where Z is the height of a given point, Z_{avg} is the average of the Z values within the given area, Z_i is the Z value at point i, and N is the number of points within the given area.

In order to make a direct correlation between surface roughening and the roughness measurements taken using the laser reflectivity measurement, a controlled roughening of the substrate was performed. The change in reflectance was recorded, translated into roughness, and the results compared with the roughness measurement taken using AFM.

The surfaces of the InP and GaAs substrates were control-roughened by either exposing to the chlorine beam for a few minutes, or by thermally desorbing oxides, and the change in reflectivity was measured. The roughness of the surface measured by the laser reflectivity measurement method is calculated using Equation 4.3, which is derived from Equation 4.1:

$$d = \left(\frac{\lambda}{4\pi\cos\theta}\right)\sqrt{\ln\frac{I_i}{I_f}}\ . \tag{4.3}$$

For the KBE setup, the wavelength, λ, was 633 nm, and the angle of incidence, θ, was approximately 40 degrees. The correlation of the laser reflectance measurement and the roughness measured using AFM is shown in Figure 4-3. From this plot, it is clear that there is a strong correlation between the signal detected using the laser reflectivity measurement and actual roughness of the surface, and that the use of Equation 4.1 is valid. The result also proves that the comparative roughness can be easily monitored *in–situ* using the laser reflectivity measurement, and roughness value as small as 10 nm can be reasonably detected.

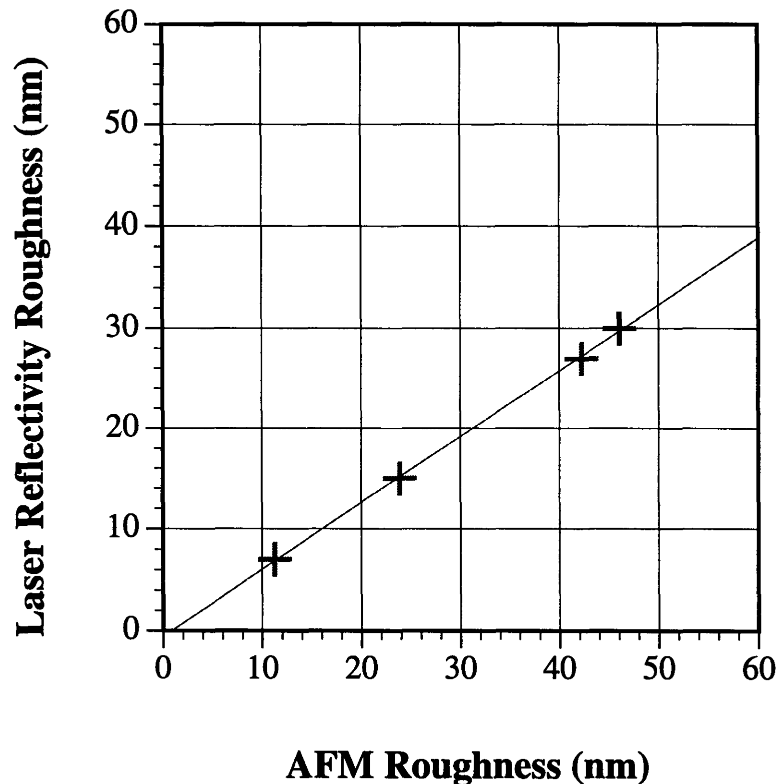

Figure 4-3: Plot showing the correlation of R_q values between roughness measured by atomic force microscope and laser reflectivity measurement.

4.3.2.2 Oxide Desorption Temperature Determination

Usually in a UHV system, reflective high-energy electron diffraction spectroscopy, commonly known as RHEED, is used as a standard method in observing the surface topology and conditions. However, from the fact that roughening of the surface is produced when the oxide begins to desorb from the substrate surface and can be detected using the laser reflectivity measurement, it was possible to determine the exact temperature at which InP and GaAs will start desorbing their native oxides under no group–V over-pressure without the use of RHEED. Also, since a subtle change in the rate of roughening can be recorded when a different surface is exposed, laser reflectivity measurement also became a convenient tool to determine when the substrates commenced decomposing without the group–V over-pressures.

For the thermal oxide desorption control experiment, a substrate without any SiO_2 pattern was mounted on the moly block as all other substrates would be, and heated at

the temperature increase rate of 25°C/min. A typical plot for GaAs oxide desorption attempt is shown in Figure 4-4, and in Figure 4-5 for InP substrates.

During the temperature increase, the reflected laser intensity shows a much different character in contrast to the pressure plot. The intensity usually remains unchanged throughout the increase in temperature until around 400°C except for perhaps a small fluctuation in intensity at or around 140°C, which is determined as the melting temperature of indium (see Figure 4-2). The fluctuation in the intensity is presumed to be caused by the movement of the substrate as the substrate floats on the liquified indium until it stabilizes.

For InP substrates, a sharp decrease in the reflected light intensity is observed around 420°C. The decrease continues as the temperature rises, until the substrate is destroyed due to extreme phosphide desorption. For GaAs, the decrease in intensity commences around 500°C, and then reaches some stable state. This "flatline" did not change even after the substrate was heated to 800°C. For both materials, as the intensity decreases, a small fluctuation is observed approximately one minute after the commencement of the decreasing slope. For both substrates, the fluctuation point is accompanied by a slight change in the background chamber pressure slope. For InP substrates, the small fluctuation usually is observed around 510°C which is considered as the indium oxide desorption temperature. The fluctuation point of GaAs substrate could not be correlated with a particular temperature as at substrate temperatures above 550°C, the power supply reached its maximum output capability, thus affecting the substrate temperature ramp rate. Although unconfirmed, it is assumed that the fluctuation point is caused by the completion of the desorption of the oxide layer for both material systems.

From the above results, it was determined that InP substrates can be safely heated in UHV with no group–V over-pressures up to 375°C and GaAs substrates to 500°C without the fear of degrading the surface of the substrates.

4.3.2.3 Laser Reflectivity Measurement Plot Characteristics

A similarity between recorded laser reflectivity plots was observed between the oxide desorption and chlorine-induced roughness. Both plots show an initially roughly linear increase in roughness. Also, shortly after the drop in intensity commences, it exhibits a change in the slope for a short duration, and then continues to decrease in intensity. The changes observed in the slope are assumed to be correlated with the completion or near-completion of oxide desorption. However, with chlorine-induced roughness in InP substrates, this change in reflectivity is more pronounced. Also, in most cases, the

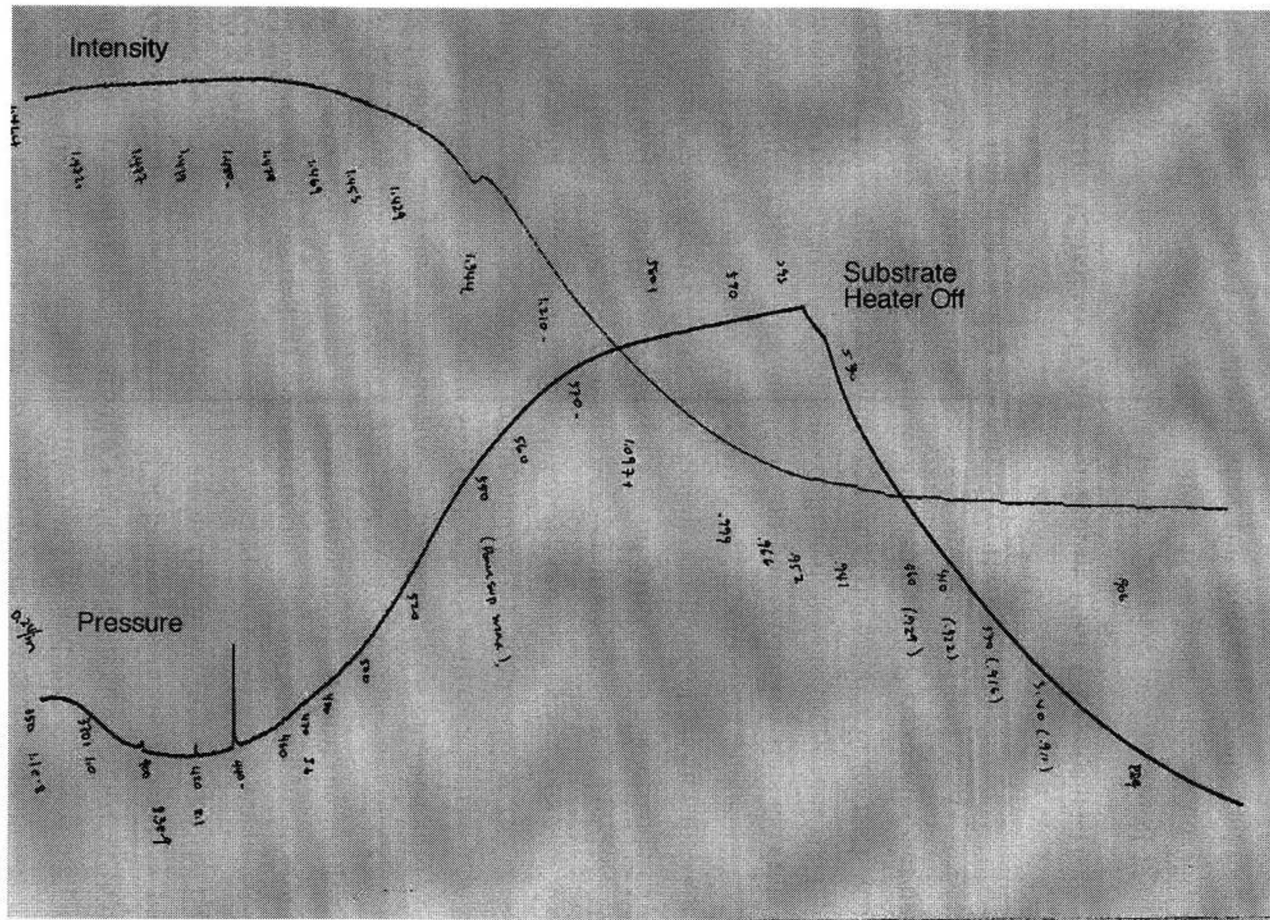

Figure 4-4: Laser reflectance intensity measurement of thermally desorbed oxide on GaAs substrate. A slight change in intensity decrease rate can be observed approximately one minute after the intensity decrease starts.

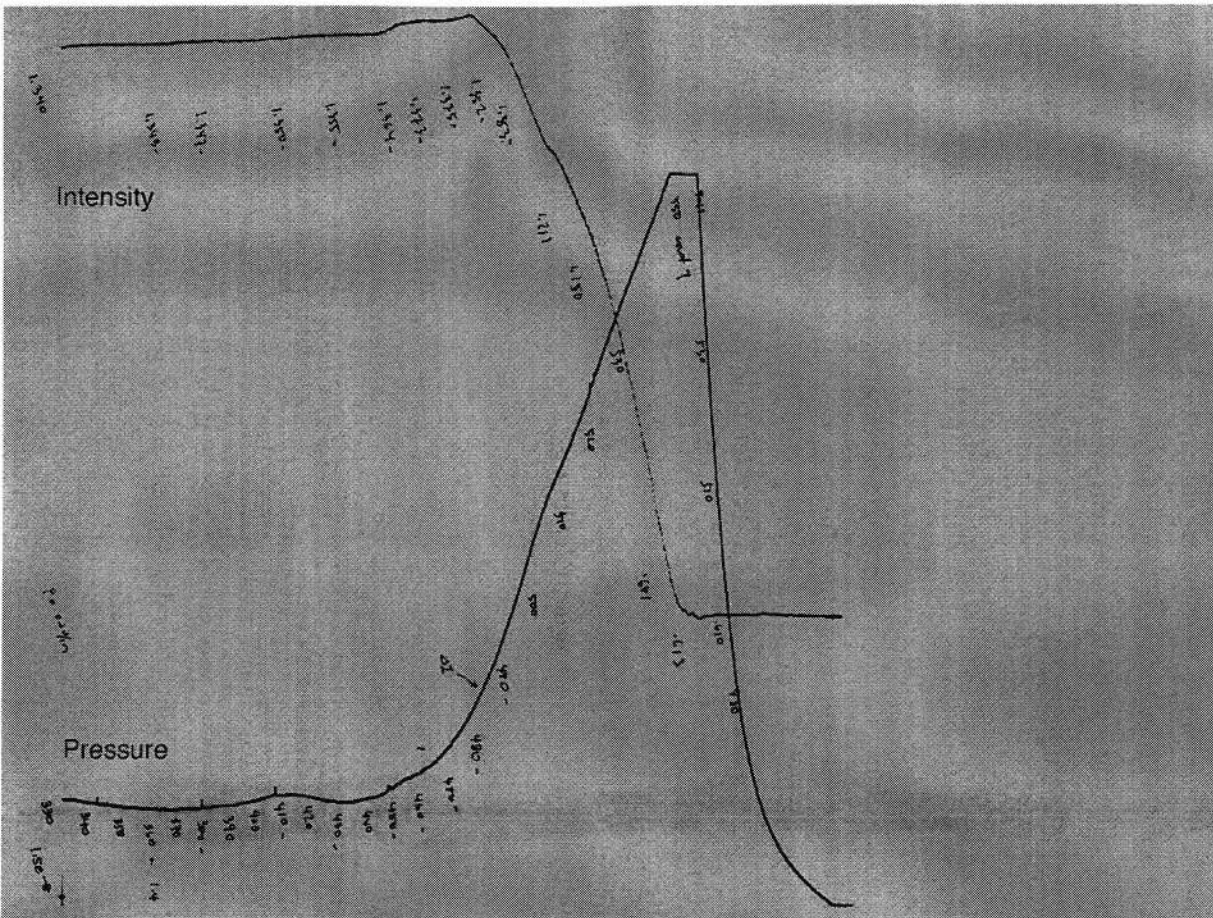

Figure 4-5: Laser reflectance intensity measurement of thermally desorbed oxide on InP substrate. A slight change in intensity decrease rate, similar to the one observed for GaAs substrates can also be observed approximately one minute after the intensity decrease starts.

slope after the fluctuation point is usually less than before the fluctuation. In addition, instead of the momentary "hesitation" of the roughness increase as with the thermal oxide desorption, there are two distinct roughness increase profiles. In one case, it reaches a level-point as shown in Figure 4-6, and then continues to roughen. In another, instead of a "flat", a minima is reached as shown in Figure 4-7, and the intensity increases for a short duration before it continues on with the increase in roughness. These plots signify that during the chlorine etch, after some initial layer is etched away, some sort of surface smoothing occurs.

The reasons of how or why the roughness decreases or stabilizes once the oxide etch is completed could not be proven, since the KBE system was not equipped with a quantitative surface analytical instrument. However, it is hypothesized that perhaps chlorine has a higher etch rate with indium oxide (In_2O_3) in comparison to InP. In addition, it is thought that the oxide etches unevenly perhaps due to uneven chlorine flux distribution. Once some InP surface is exposed, the oxide continues to etch at a faster rate than the InP, thus in effect allowing InP to act like a mild etch-stop layer, aiding in leveling out the surface. This difference in the etch rate in effect improves the surface smoothness. Since InP is also highly reactive with chlorine, once all the oxide is stripped, the etching continues, eventually leading to a rough surface, but at a different roughening rate.

Another curious observation is that some surface smoothing also occurs when the gas flow is temporarily blocked as shown in Figure 4-8. This phenomenon is assumed to be caused by chlorine migration at the surface, aiding in levelling out the rough surface by etching the rough peaks which have higher surface to volume ratios first. Unfortunately, as with the change in the roughness increase rate after the oxide is etched away, given the lack of quantitative surface analytical equipment on the KBE system, the exact mechanics of this change in light reflectivity could not be proven.

However, this increase in laser reflectance signal when the chlorine beam was interrupted and then resumed signifies that there is a different surface available between the InP substrate which was introduced to chlorine for the first time after exposure to air, and after it has been exposed for a while. This phenomenon also highly suggests that the initial sharp decrease in the laser reflectance signal with a different slope as after the "fluctuation" is indeed due to the oxide layer.

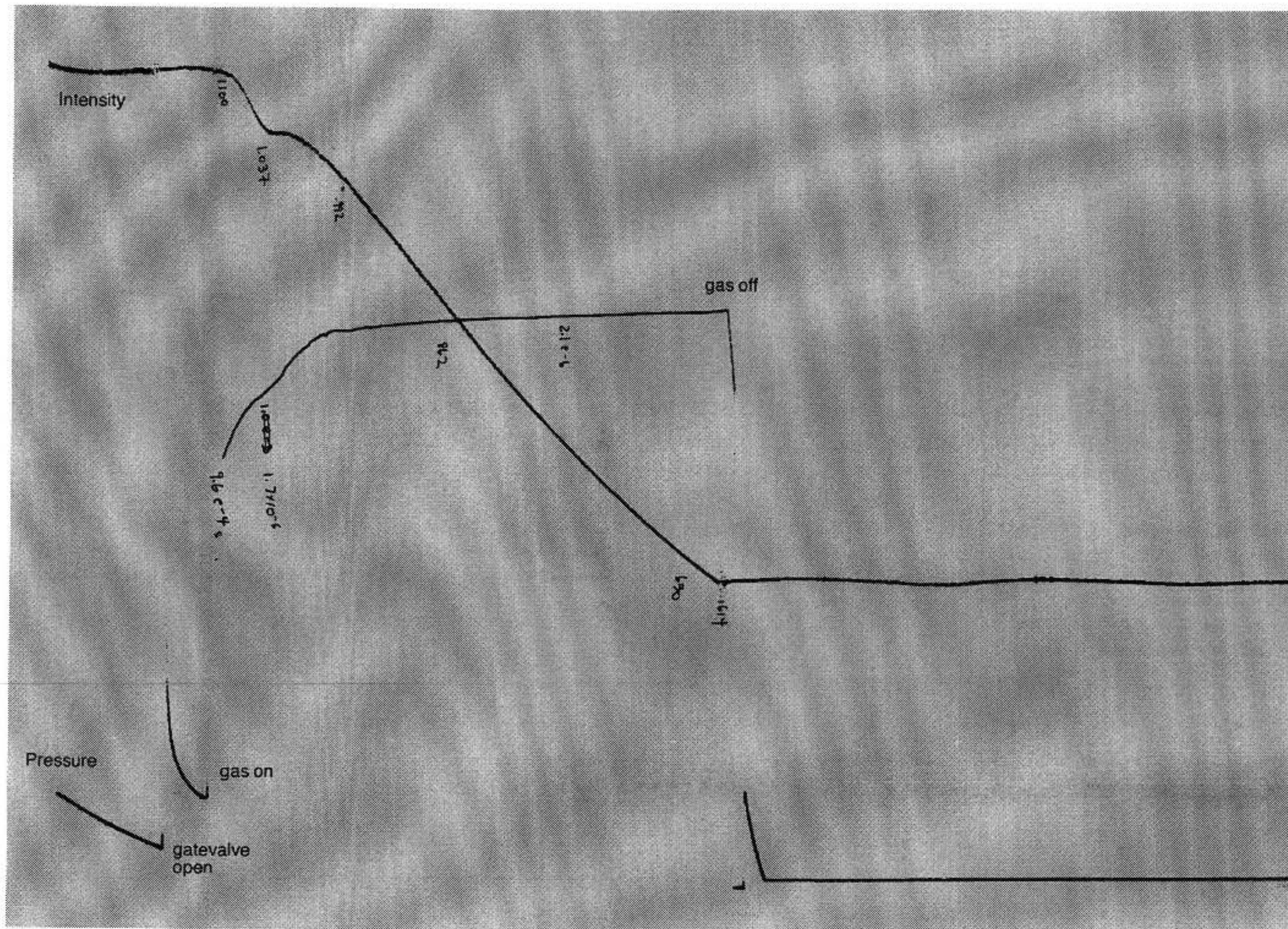

Figure 4-6: The pressure and laser reflectivity plot of an InP substrate etched with chlorine. This is an example where the increase in roughness stops for a duration.

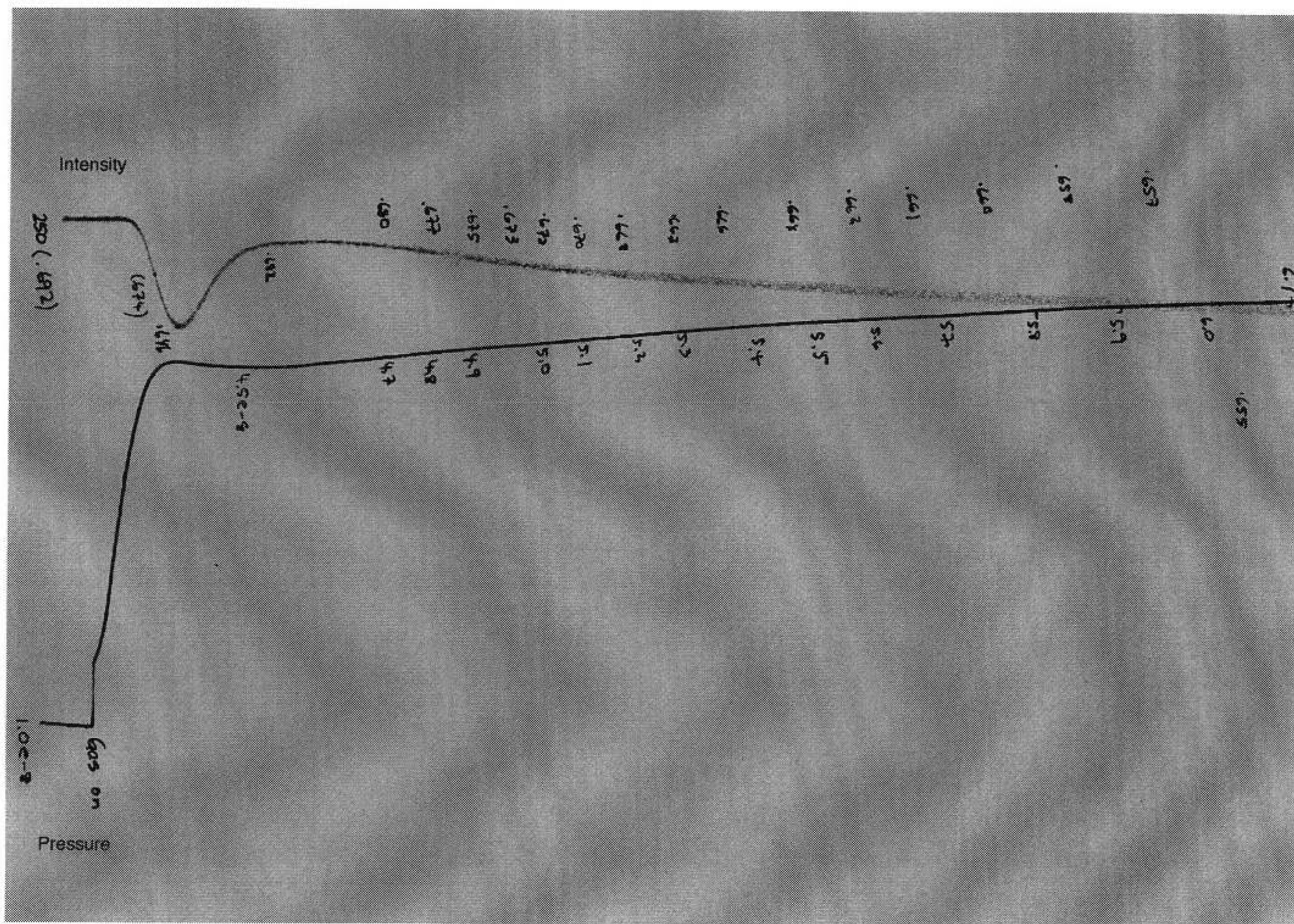

Figure 4-7: The pressure and laser reflectivity plot of an InP substrate etched with chlorine. This is an example where the roughness of the surface actually improves within the first few minutes into the etch run, before eventually decreasing gradually with time.

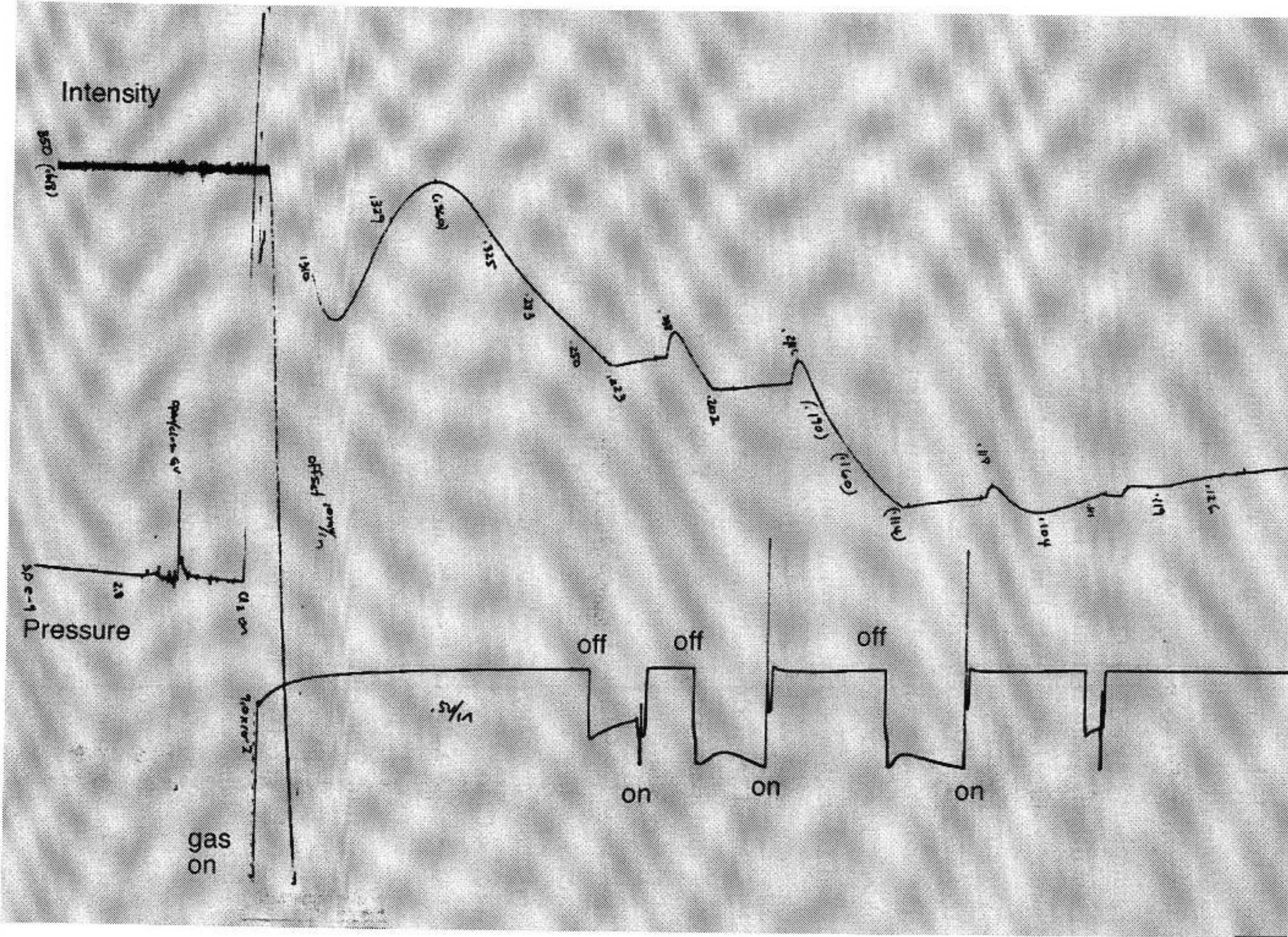

Figure 4-8: Pressure and laser reflectivity plot showing the surface smoothing effect prompted by the chlorine.

4.4 The Etch Run

A prepared sample on the moly block is first placed into the transfer tube, which acts as a temporary load lock, and the chamber is pumped down first using a mechanical pump, and subsequently by an ion pump. Once the pressure of the transfer tube reaches approximately 5×10^{-7} torr or lower, the sample can be loaded into the main chamber.

Once the sample is in the main chamber, the nozzle is aligned with the skimmer (see Section 4.2.1 for details), and the nitrogen beam equivalent pressure is noted for future reference. Then the substrate is placed in the beam path, using the reflected laser beam as a guide[6]. Once the sample is secured and locked in place, the substrate is rotated so that the He–Ne laser beam is reflected off the substrate surface and so that the sample is placed in the molecular beam path, as the beam is not centered with respect to the substrate holder. The photodetector signal is maximized using an X–Y–Z stage, and the signal is fed through a signal amplifier and a volt meter. The signal is then sent through a voltage offset and then recorded using the X–Y chart recorder.

The analog output from the main chamber ion gauge controller is also fed through a voltage offset and recorded on the same X–Y chart recorder to plot the reflected intensity and the pressure change simultaneously (See Figures 4-6, 4-7, and 4-8 for sample recorded etch run outputs).

On the Etch Log (see Figure 4-9 for a sample of the Etch Log), the pressures for the source and main chambers are recorded as the "idle pressure" before any heater elements are turned on.

The stability of the reflected laser beam intensity is observed first, and once it is satisfactory, the substrate heater is activated to ramp up the substrate temperature at a rate of 15°C/min. The chart recorder is started when the substrate temperature controller reads 50°C. The rise and fall of the pressure is recorded during any ramp up or ramp down of the substrate heater, and during the initial phase of the etch. The temperature of the "blip" indium burst pressure is noted on the Etch Log to be used to calibrate the actual substrate temperature later, or to adjust the temperature controller programming to reach a certain target temperature. While the substrate temperature is increasing, the nozzle heater is turned on, ramped up at 60°C/min, and allowed to stabilize.

[6] By making the reflected beam hit the same spot on the detector viewport, it is possible to maintain similar orientation of the (100) surface of the substrate with respect to the beam between the different etch runs.

Substrate #: ____________________ Date: ____________________

Wafer Manufacturer: ____________________ Wafer Lot#: ____________________

Mask Material: ____________________ RGA Diskette #: ____________________

Mask Pattern: ____________________

Substrate

Outgas: ramp to____________ °C hold ________min @____________ °C/min ramp rate

$T_{m,In}$ = ______________°C – 156°C = ΔT = _________°C

Target T_{sub} = ___________°C + ΔT = _______°C

$T_{sub@etch}$: ____________________ °C for ___________ min Heater: _______ volts _______ amps

Nozzle

T_{nozzle} : ______________ °C P_{SET}: ____________________ volts

$P_{reservoire,start}$: ____________________ $x10^3$ torr $P_{reservoire,end}$: ______________ $x10^3$ torr

Etch

gas type: ______________________ ratio: ______________ etch rate: ____________Å/min

IG	idle state (torr)	background (torr)	start (torr)	time = (torr)	end (torr)
P_M					
P_F					
P_S					
P_{nozzle}					

comments:

Figure 4-9: Sample Etch Log.

Once the substrate is sufficiently outgassed and reaches the etch temperature, the gatevalve between the main and the source chamber is opened, usually causing a temporary sharp increase in pressure in the main chamber. Once the pressure in the main chamber restabilizes, the pressures of the source chamber and the main chamber are again recorded as the "background pressure" on the Etch Log. Then the valve on the nozzle that leads to the gas source is opened, allowing the gas to flood the nozzle. The sample is now exposed to the supersonic beam, and any observations made are recorded on the Etch Log.

At the conclusion of the etch run, the gas in the nozzle cavity is first evacuated using a roughing pump, and then the gatevalve between the source and the main chambers is closed. Then the substrate heater is shut off to allow the substrate to cool. After the nozzle reservoir is vacated, it is purged using nitrogen gas, repeating the process a few times to clear any residual corrosive gas out of the nozzle. Once the nozzle is finally evacuated, the valve to the nozzle is closed, and the nozzle heater is also turned off. Both heater power supplies are kept off while in the idling state, to prevent any high currents from being injected into the heater systems.

The substrate is allowed to cool to at least 100°C before it is transferred back into the transfer tube/load lock. Then the transfer tube is vented to slightly above 1 atm using nitrogen gas, and the sample is removed. Usually the next sample is loaded onto the substrate holder at the same time to cut down on pump-down time, as the system is currently designed to have only one sample in the vacuum at a time. The transfer tube is then allowed to pump down using the mechanical pump, until the vacuum level becomes low enough for the ion pump be used. Doing this procedure immediately after the etch run serves two purposes. One is to allow maximum substrate throughput. Second, by allowing the pump to pump a large volume of nitrogen gas, it will flush the roughing pump of any residual corrosive gases remaining after the nozzle has been evacuated.

The transfer tube is pumped down to 1×10^{-3} torr using the mechanical pump. Then the mechanical pump is valved off, and the ion pump is used to pump the chamber down to UHV levels. The gatevalve used to isolate the ion pump is used to throttle the gas intake into the ion pump, until the chamber pressure reaches below 5×10^{-5} torr to prevent thermal overload of the ion pump.

Now, the system is reset for future use.

4.5 Vacuum Chamber Maintenance

While the KBE system was based on the methane–hydrogen gas mix, the main and the source chambers were able to maintain the UHV background pressure during the idle states between the etch runs. However, once a chlorine system was used, etch by-product residues were adsorbed onto the inner vacuum walls, becoming a significant outgassing source. A spectrum taken by the residual gas analyzer (RGA) showed significant amount of mass 150 and 185, suggesting InCl and $InCl_2$. Also, due to the chlorine compounds and evaporating indium glue, the viewports used for the laser reflectivity measurements became coated with milky ivory colored film. In order to remove the coat on the viewports, the main chamber had to be baked out very frequently, with a care to heat the viewport itself. After minimum of 24 hours of baking at 180°C, most of the milky film on the view port glass can be removed.

As for the yellowish-white residue on the interior of the main chamber, the baking temperature achievable under 24-hour slow ramp up rate (to avoid thermal shock to the viewports) was not high enough to remove them. However, periodically baking the main chamber while clarifying the viewports aided in keeping the vacuum level to a workable background pressure. The flux and the main ion gauges also accumulated residues which reduced their sensitivity. The sensitivities were restored by degassing the ion gauge grids by running high current through them.

On average, the etch chamber needed to be heated and outgassed after three, four-hour pure chlorine experimental runs at high background pressures (5×10^{-7} torr or higher).

The source chamber was less severely affected than the main chamber; however, the same yellowish-white milky residue accumulated on approximately the first 8 inches of the nozzle support shaft, around the skimmer holder, and heavily accumulated on the ion gauge. Like the ion gauges in the etch chamber, the ion gauge lost its sensitivity due to the residue accumulation; however, it was cleaned by degassing the ion gauge grid by running high current through them at the end of each etch run. Occasionally the contamination on the ion gauge grid was so severe, it was possible to see a plasma glow of the outgassing material as the grid was being degassed. The residue on the nozzle was removed by heating the nozzle up to 600°C briefly, while running nitrogen gas through it to prevent the orifice from clogging, and to allow any materials outgassed by the high temperatures in the inner nozzle to be to be flushed out.

When the KBE system used a high flux of hydrogen (40 sccm or higher), cryogenic

pumps became nearly saturated after one or two three-hour etch runs. The source chamber cryogenic pump, which was responsible for pumping the majority of the free–expanded gas, needed to be regenerated almost after every three hours of high-flux hydrogen use. The main chamber cryogenic pump was able to sustain stable vacuum level for about two, three-hour hydrogen etch runs, however after that it required a thorough regeneration. The stability of the vacuum can be detected with very unstable ion gauge readings, and a very slow UHV pressure recovery after the gas was turned off.

During the high-flux chlorine runs, cryogenic pumps fared well in maintaining UHV. However, extra long nitrogen purge cycles were required during the pump regeneration to sufficiently outgas the cold head arrays. This phenomenon is attributed to the high outgassing nature of the etched species and reluctance of the chlorine to desorb from the arrays, which also plagued the interior of the vacuum chambers. The necessity of such long purge cycles extended the normal cold-to-cold regeneration time from two hours to up to eight hours, depending on the level of cryo charcoal array contamination.

Chapter 5

Experimental Results

Two different gas systems were used to investigate the effect of hyperthermal etching of indium phosphide and gallium arsenide. The first system was a methane (CH_4)–hydrogen (H_2) system, and the second was a chlorine (Cl_2)–hydrogen system.

5.1 Methane–Hydrogen System

Methane was selected as a potentially ideal etchant gas because the reaction products with the III-V compound semiconductors are very volatile, which is a prerequisite for dry etching to occur. If the product species were not volatile, material would accumulate as the etchant reacts with the target and passivate the substrate surface, resulting in a deposition instead of an etch. The following equations are some of the reactions expected if methane reacts with the III-V substrate.

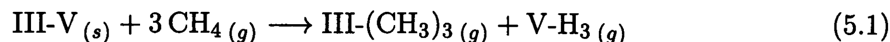

$$\text{III-V}_{(s)} + 3\,\text{CH}_{4\,(g)} \longrightarrow \text{III-(CH}_3)_{3\,(g)} + \text{V-H}_{3\,(g)} \tag{5.1}$$

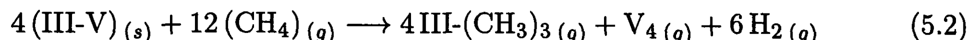

$$4\,(\text{III-V})_{(s)} + 12\,(\text{CH}_4)_{(g)} \longrightarrow 4\,\text{III-(CH}_3)_{3\,(g)} + \text{V}_{4\,(g)} + 6\,\text{H}_{2\,(g)} \tag{5.2}$$

Initially, 10-to-1 and 100-to-1 H_2-to-CH_4 ratio gas mixtures were used to try to etch GaAs and InP substrates. Each mixture was used with the substrate temperatures varying from 150°C to 500°C for GaAs and 150°C to 350°C and InP substrates. The highest nozzle temperature was 900°C. With a 10:1 mixture, a 900°C nozzle tempera-

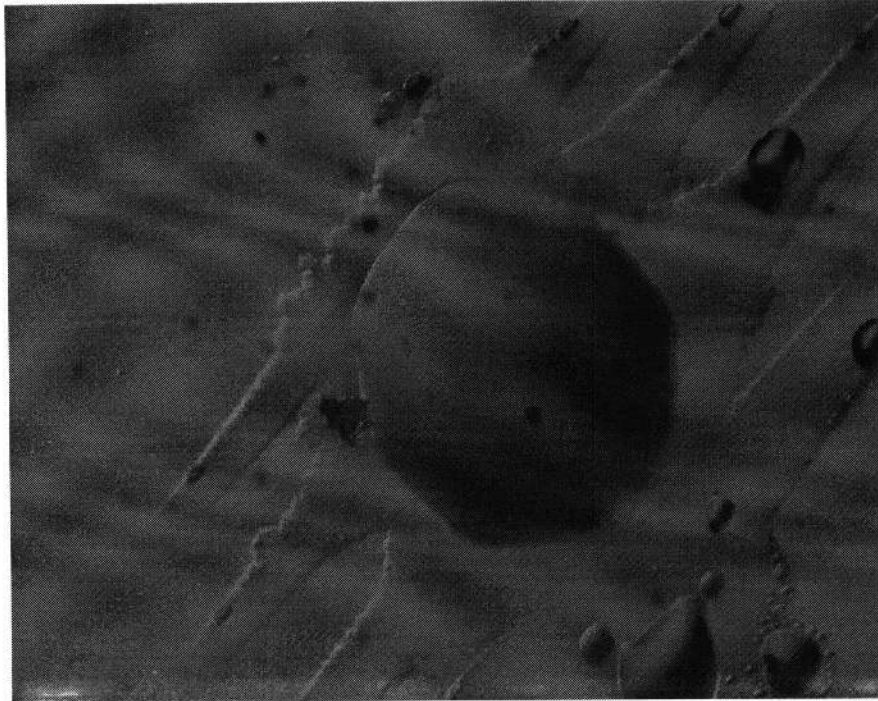

Figure 5-1: Polymer beads forming on the surface of the InP substrate seen under optical microscope. The diagonal line-like pattern is from the original oxide mask. 400X

ture correlates to beam energy of 13 kcal/mole[1] and at 100:1 mixture, 41 kcal/mole. At a nozzle temperature above 750°C, many polymer beads were deposited on the surface of the substrates as seen in Figure 5-1. However, no chemical etch reaction between the substrate and the etchant was observed. This result implied that at maximum incident energy of 41 kcal/mole, CH_4 was below the methane–gallium or methane–indium reaction activation energy with the substrate temperature at 350°C.

After more experimentation, the CH_4–H_2 etchant system was abandoned as the desired etch was not obtained even at the system's maximum beam energy output. It

[1]The following unit conversions hold:

$$\begin{aligned} 1\, kcal/mole &= 4.19 \times 10^{3}\ joules/mole \\ &= 2.61 \times 10^{21}\ eV/mole \\ &= 4.3 \times 10^{-2}\ eV/particle. \end{aligned}$$

is hypothesized that the methane radicals created either through bombardment of the translationally-activated methane or through thermal cracking in the high-temperature nozzle reservoir are not reacting with the substrate surface, and instead, reacting among themselves and depositing as a polymer on the substrate surface. The existence of native oxide is thought to be one of the reasons why the reaction between the substrate and the methyl radicals is not favored. However, the search for finding out how to limit the polymer formation was deemed beyond the scope of this thesis project, and therefore this subject was not pursued.

5.2 Chlorine–Hydrogen System

When the methane system did not work, the etchant was substituted with chlorine (Cl_2). As much research has been performed on the reaction between GaAs and molecular and atomic chlorine gases [41][42][43][44][45], although the basic etch characteristics of the GaAs etch were observed, the reaction between InP and chlorine was primarily investigated in this thesis research.

5.3 Data Analysis for InP System

This section will discuss the observations made on the reaction between hyperthermal chlorine and InP substrates. The InP substrates were etched at substrate temperatures between 196°C and 351°C. Under various experimental conditions, etch rates between $0.2\,\mu$m/hour to in excess of $2.0\,\mu$m/hour were obtained.

5.3.1 Etch Mechanics of InP and Molecular Chlorine

In all literatures reporting InP etch using molecular, non-ion, and non-plasma assisted chlorine etch (using non-supersonic nozzle gas administration method) is reported only for chlorine background pressures of 1×10^{-4} torr or higher [46][47][42]. For substrate temperatures under 300°C, the etch rate is reported as highly dependent on the background chlorine pressure. Reported etch rates for InP substrates around 275°C at chlorine pressures of 1×10^{-4} torr is approximately $6\,\mu$m/hour. However, this etch rate is determined to decline exponentially as the background chlorine pressure is reduced until eventually no etch is observed. From such reports, it is assumed that InP etch

rate of neutral chlorine gas is dependent on the rate of dissociative chemisorption of chlorine onto the InP surface, and that the rate of dissociative chemisorption is dependent on the amount of incident energy of the molecules. The dissociative chemisorption phenomenon can only readily be observed above the pressures of 1×10^{-4} torr, as the pressure of the gas is lowered, the absolute number of the dissociative chemisorption decreases until no discernible reaction can be observed. This pressure-dependency is referred to as the "pressure gap in the reactivity in heterogeneous catalysis" by surface scientists [48]. There are two methods available in order to overcome the energy barrier for the dissociative chemisorption to occur. First is to heat the chlorine gas to a sufficient temperature to increase the vibrational energy of the molecule, thus increasing the probability of dissociative chemisorption. The other is to translationally activate the molecules so that the molecule will dissociate upon impact, which the Kinetic Beam Etch system utilizes as the source of activation of etch reaction.

From the extrapolation of data from the chlorine background pressure vs. etch rate plots seen in the literature, the etch rate of InP using chlorine under chlorine beam-equivalent flux of 1×10^{-7} torr, which is a typical chlorine pressure used in the KBE system, is on the order of $1\times10^{-5}\,\mu$m/hour. Such low etch rate value is considered as non-etching. In the KBE system, typical etch rate obtained using supersonic chlorine molecule is approximately $1.3\,\mu$m/hour. From such results, it is obvious that translationally excited chlorine molecules indeed exhibit higher reactivity than chlorine which is only thermally activated, which is consistent with the assumption that part of the etch mechanics of chlorine etch of InP is limited by the dissociative chemisorption of the chlorine molecules. Similar behavior of enhanced reactivity of translationally-activated molecules while no observance of reactivity with thermally-activated molecules are also reported between molecular fluorine and silicon [49].

The preceding data and literature reports implies that this thesis project is the first reported demonstration of chlorine etch of InP under chlorine pressures below 1×10^{-5} torr without any external energy source such as ion, plasma, or electron beam. Unlike other reports claiming UHV neutral chlorine gas etch, where the operating chamber pressure during the etch process is at 1×10^{-4} torr or higher, KBE is truly the "UHV neutral chlorine etch" as the background pressure maintained during the etch process was usually kept below 1×10^{-7} torr.

5.3.2 Desorbed Gas Species

For the chloride system etching InP substrates, some combination of the following reactions were expected to take place:

$$InP_{(s)} + Cl_{2\,(g)} \longrightarrow In_{(s)} + PCl_{2\,(g)} \tag{5.3}$$

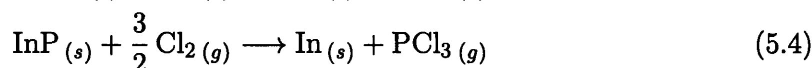

$$InP_{(s)} + \frac{3}{2} Cl_{2\,(g)} \longrightarrow In_{(s)} + PCl_{3\,(g)} \tag{5.4}$$

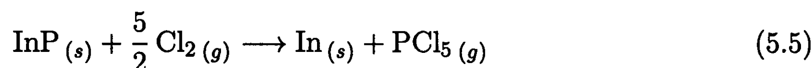

$$InP_{(s)} + \frac{5}{2} Cl_{2\,(g)} \longrightarrow In_{(s)} + PCl_{5\,(g)} \tag{5.5}$$

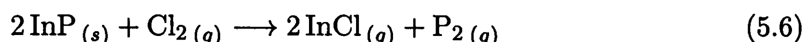

$$2\,InP_{(s)} + Cl_{2\,(g)} \longrightarrow 2\,InCl_{(g)} + P_{2\,(g)} \tag{5.6}$$

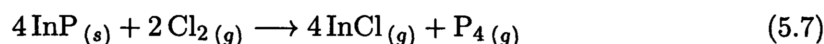

$$4\,InP_{(s)} + 2\,Cl_{2\,(g)} \longrightarrow 4\,InCl_{(g)} + P_{4\,(g)} \tag{5.7}$$

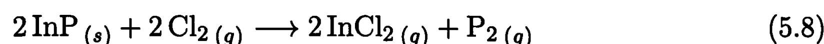

$$2\,InP_{(s)} + 2\,Cl_{2\,(g)} \longrightarrow 2\,InCl_{2\,(g)} + P_{2\,(g)} \tag{5.8}$$

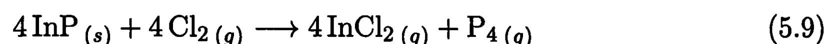

$$4\,InP_{(s)} + 4\,Cl_{2\,(g)} \longrightarrow 4\,InCl_{2\,(g)} + P_{4\,(g)} \tag{5.9}$$

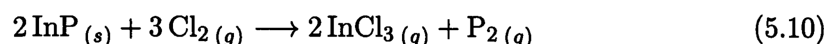

$$2\,InP_{(s)} + 3\,Cl_{2\,(g)} \longrightarrow 2\,InCl_{3\,(g)} + P_{2\,(g)} \tag{5.10}$$

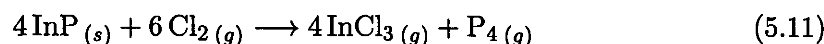

$$4\,InP_{(s)} + 6\,Cl_{2\,(g)} \longrightarrow 4\,InCl_{3\,(g)} + P_{4\,(g)} \tag{5.11}$$

From the residual gas analyzer (RGA) spectrum taken during the etch, only the following species were detected: In (mass 115), InCl (mass 150), $InCl_2$ (mass 185), P2 (mass 62), and P_4 (mass 124). A table of relevant species and their molecular weights are listed in Table 5.1 [50][51][52]. Although $InCl_3$ (mass 221) was not detected using the RGA, the presence of both $InCl_2$ and InCl, which is part of the cracking pattern of $InCl_3$, highly suggests that $InCl_3$ is indeed present. This assumption is drawn from the fact that the $InCl_3$ is rarely detectable using RGA as chlorine is easily dissociated from $InCl_3$ under ionizing conditions [53] and only detected as $InCl_2$ or InCl. Also, as the formation of $InCl_2$ under this type of reaction is highly improbable due to $InCl_2$'s highly unstable molecular structure, it is assumed that the presence of $InCl_2$ is detected only as a part of the cracking pattern of $InCl_3$, and not actually present.

From the above observations, it is implied that only the reactions shown in Equations 5.6, 5.7, 5.10, and 5.11 or their combinations take place during the etch, and none of the phosphorus reacts with the chlorine. As no phosphorus–chlorine compounds were detected, it appears that the phosphorus prefers to desorb (decompose) from the surface as soon as it is exposed at the surface level. This result is consistent with the fact that group–V elements have the tendency to dimerize at the surface, allowing the P_2 and P_4 to form and desorb easily, especially at higher substrate etch temperatures. Although

Species	Mol. Wt. [50]	Melt. T [50]	Boiling T [50]	P_{vap} [51][52]
In	114.82 g	156.6°C	2080°C	
InP	145.79 g	1070°C		
InCl	150.27 g	225°C	608°C	1.2 mm (300°C)
$InCl_2$	185.73 g	235°C	550°C	18 mm (250°C), 1.63 mm (340°C)
$InCl_3$	221.18 g	586°C, subl. 300°C	volat. 600°C	7 mm (390°C)
P_2	61.9 g			
P_4	123.89 g	590°C	200°C	
PCl_2	101.88 g	-28°C	180°C	
PCl_3	137.33 g	-112°C	75.5°C	1 mm (-52°C)
PCl_5	208.24 g	166.8°C	subl. 162°C	1 mm (56°C)
Al	26.9 g	660.4°C	2467°C	
AlCl	62.43 g			
$AlCl_3$ (Al_2Cl_6)	133.34 g (266.68 g)	190°C	decomp. 262°C, 182.7°C, subl. 177.8°C	1 mm (100°C)

Table 5.1: List of relevant materials involved in the InP etch and their chemical properties.

not verified as the etch rate was much slower at lower substrate temperatures and inspection of slower etch rate was not of interest to the project, it is hypothesized that if the etch took place at a suitably lower substrate temperatures, the PCl_x species will begin to form and desorb as the reaction products. When an x-ray elemental analysis and Auger electron spectroscopy were performed on the as-etched surface of the sample, no traces of chlorine was detected.

5.3.3 Effect of Substrate Heating

5.3.3.1 Etch Morphology

In general, the etch rate between substrates etched at temperatures below 260°C exhibited lower etch rate than substrates etched at higher temperatures. As the substrate temperature dependency of dissociative chemisorption probability is usually not observed [48], this difference in etch rate is attributed to the desorption rate of the etch

product, $InCl_x$ compounds. The $InCl_3$ desorption is thought to occur at approximately 250°C or slightly lower. As the increase in etch rate was observed at much higher temperatures than the reported $InCl_3$ desorption temperatures, perhaps some other indium-chlorine compound, such as InCl is thought to be involved in etching InP.

The most curious effect of etching at different substrate temperatures was the development of canal- or channel-like grooves, which are usually much deeper than the mesa etch. There were two distinct types of canals observed: (1) a "trench", which usually exhibits smooth vertical or near-vertical sidewalls as shown in Figure 5-3(a), and (2) a "river", in which the cross sectional view of the canal resembles a parabola, like shown in Figure 5-3(b). The primary etched surface is referred as the "plateau" (see Figure 5-2 for a schematic representation of the etch features).

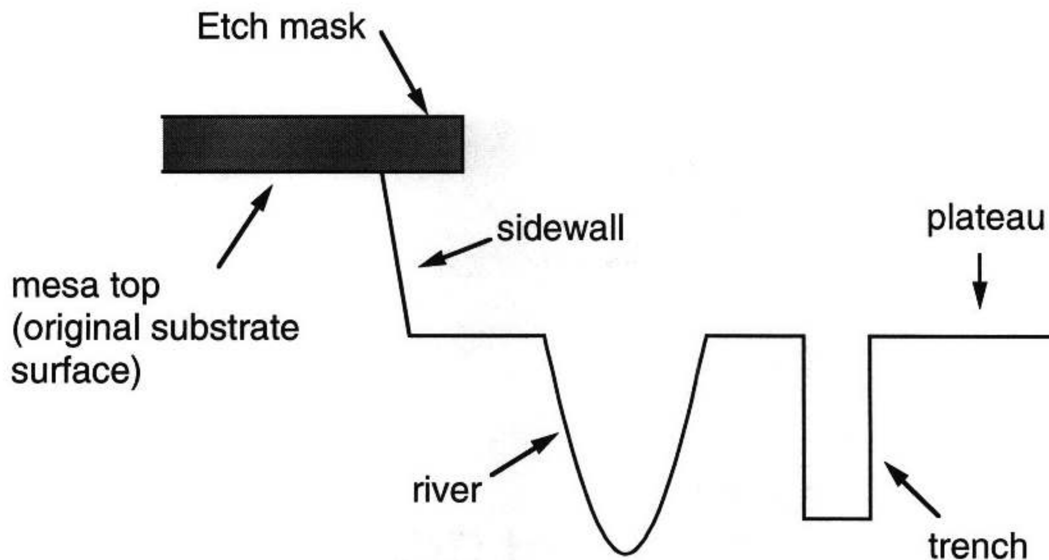

Figure 5-2: Schematic diagram of the definitions of various etch features referred to in this thesis.

The three regimes of "trench" etch, no-canal etch and "river" etch were clearly defined by the substrate temperature during the etch.

The trench etch develops at a substrate temperature lower than 270°C, and the trenches seem to follow the general [110] direction, but not consistently. A high degree of anisotropy is seen within the trench, and as with the rivers, the etch rate within the

(a) Example of "trench" morphology. Width of the trench is approximately 1.4 μm. 6500X, 1 keV

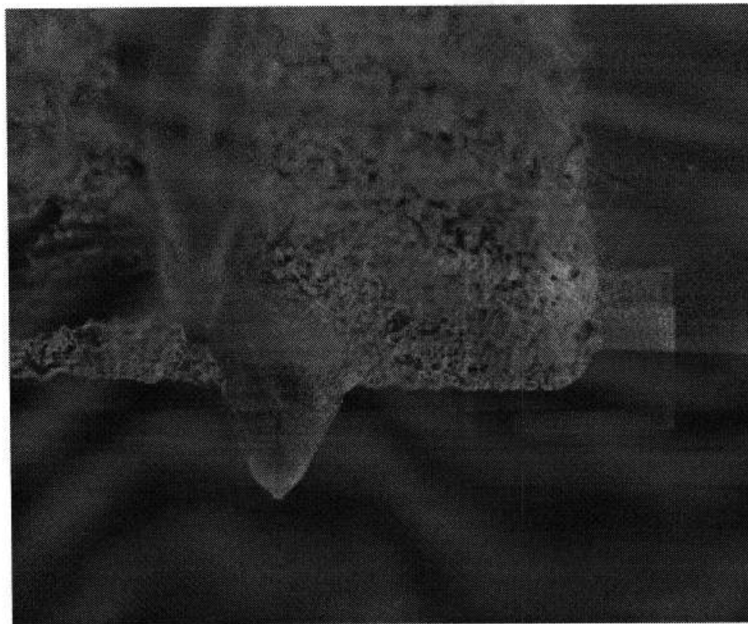

(b) Example of "river" morphology. The widest part of the river is approximately 7.5 μm wide. 2700X, 1 kev

Figure 5-3: SEM micrographs showing "trench" and "river" etch morphology. The etch rate in the canals are enhanced in comparison to the rest of the etched surface.

trench is significantly enhanced. The temperature regime where the trench develops is referred to as the "low temperature" etch regime. The exact mechanics of the trench formation, and the vertical wall formation are not understood.

As the substrate temperature nears the upper limit of the low temperature regime, the majority of the trenches are formed right along side the mask pattern as shown in Figure 5-4. The exact mechanics for this phenomenon are not well understood, but it

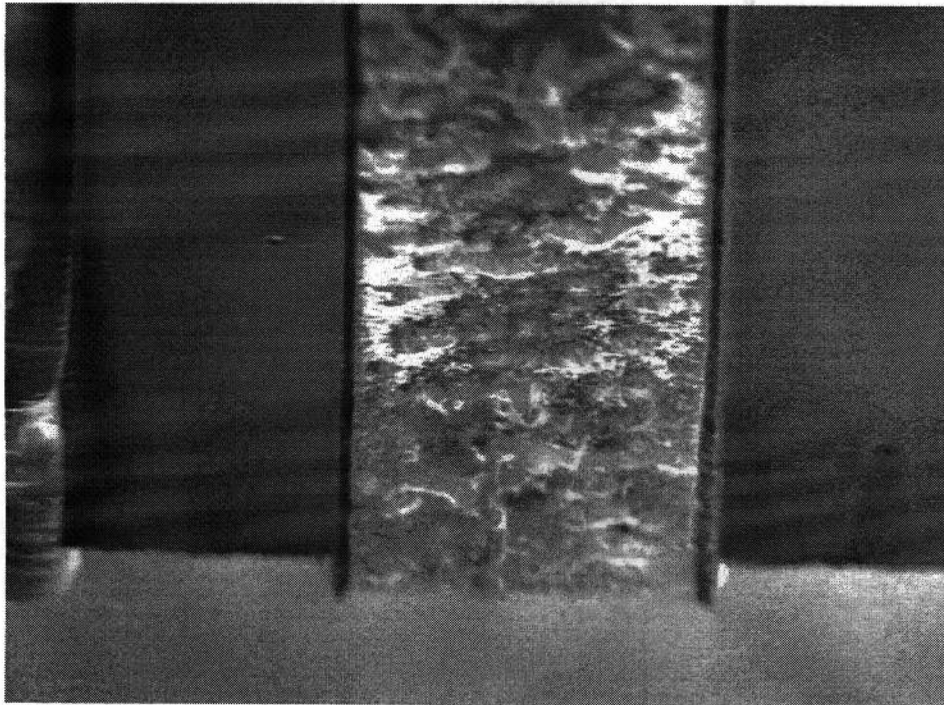

Figure 5-4: Photo showing the trenches forming alongside the etch masks near the upper limit of the low temperature etch regime. The distance between the dark grey masks is approximately 30 μm. 1800X, 1 kev

is assumed to be caused by an enhanced chlorine surface mobility on the SiO_2 surface resulting from an increased substrate temperature. The suspected etch mechanism is illustrated in Figure 5-13, and is explained more in detail in Section 5.3.6.

With the samples etched in the low temperature regime, no contaminants were detected on the surface of the substrate when scanned using x-ray elemental analysis and

Auger electron spectroscopy (AES). This result implies that all chlorine and chlorine compounds are completely desorbed during the etch run as explained earlier. The substrates exhibited etch rates of approximately $0.3\,\mu$m/hour at the primary plateau, and $1.3\,\mu$m/hour at the trenches.

The river etch morphology developed at substrate temperatures higher than 280°C. This temperature regime is referred to as the "high temperature" regime. Typically, the high temperature etch rate is approximately $0.6\,\mu$m/hour. Usually with higher substrate temperatures, a white film-like deposit accumulates at the surface level. Such artifacts and enhanced etch rate within the river seemed to have been caused by the new material formed at the surface at high substrate temperatures, acting like a catalyst, or inhibiting the etch rate of most of the surface except for select areas where the river is formed.

In order to determine the composition of the filmy substance, a sample etched in the high temperature regime was cleaved and placed in the SEM as-is after the etch. Figure 5-5 shows a thin film covering the etched surface. Using the x-ray elemental

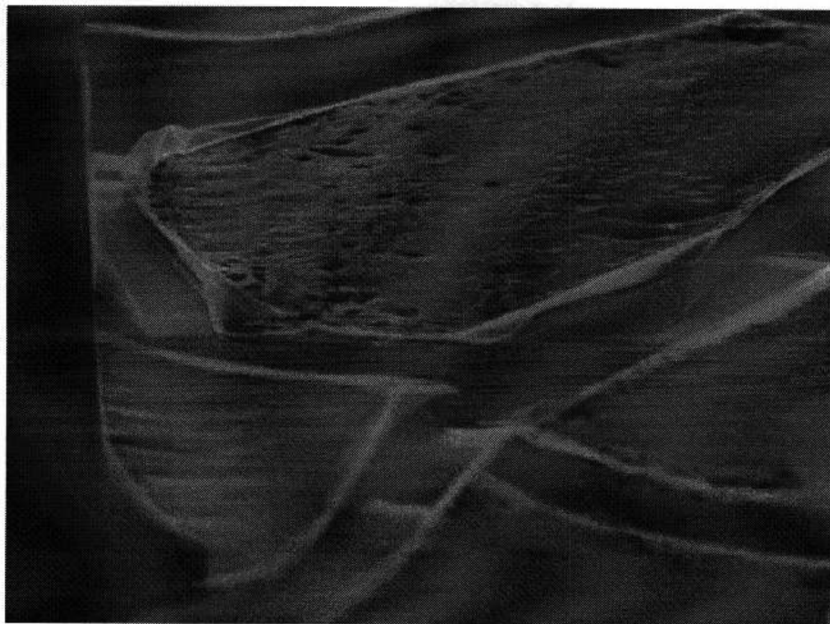

Figure 5-5: InP etched at 351°C. A filmy residue can be observed to uniformly cover the entire surface area where it was exposed to chlorine. The width of the river in the foreground is approximately $7\,\mu$m. 1700X, 1 kev

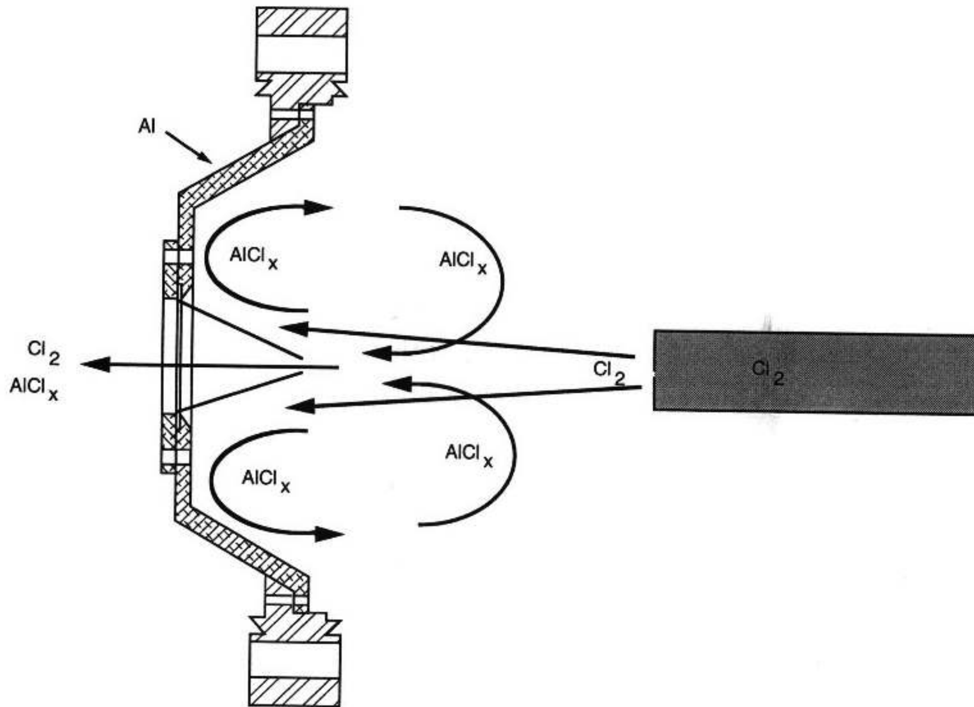

Figure 5-6: A schematic diagram of the contamination path of aluminum into the main chamber. Skimmed chlorine beam reacts with the aluminum skimmer holder and creates $AlCl_x$, and joins the background. However, due to the incoming, under-expanded, high-intensity chlorine beam, $AlCl_x$ is incorporated into the expanding jet stream as explained in Section 2.4. Then it travels into the main chamber along with the chlorine, eventually depositing on the substrate surface.

analysis capability on the SEM, the films were determined as aluminum or aluminum-related compound. The source of the aluminum contamination was traced back to the source chamber.

It was determined that the aluminum was introduced into the etch chamber from the source chamber through the following mechanism. The schematic of the contamination path is illustrated in Figure 5-6. Free-jet expanded chlorine gas in the source chamber is skimmed. As the skimmed chlorine advances and hits the skimmer holder, made of aluminum, they react and become a gaseous aluminum chloride, $AlCl_x$ as in Equation 5.12.

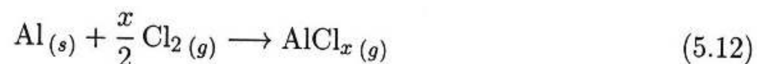

$$Al_{(s)} + \frac{x}{2} Cl_{2\,(g)} \longrightarrow AlCl_{x\,(g)} \tag{5.12}$$

where x is an integer of 1 or 3.

Once reacted, the $AlCl_x$ joins the background molecules in the source chamber. However, instead of being pumped away from the jet stream, the $AlCl_x$ molecules are trapped within the on-coming, under-expanded, high-intensity expanding jet as explained in detail in Section 2.4, and is incorporated within it. The newly incorporated $AlCl_x$ is then funneled through the skimmer into the main chamber along with chlorine molecules. Once in the main chamber, $AlCl_x$ also hits the substrate along with the Cl_2. At substrate temperatures below 280°C, $AlCl_x$ is thought to harmlessly bounce off the substrate surface due to the low sticking coefficient, or that the on-coming Cl_2-induced $AlCl_x$ desorption is greater than the deposition rate. At substrate temperatures above 280°C, it is deposited onto the surface forming a layer of aluminum-based compound, or that the steady-state begins to heavily favor $AlCl_x$ deposition. When the deposition occurs, $AlCl_3$ is thought to decompose to AlCl as shown in Equation 5.13.

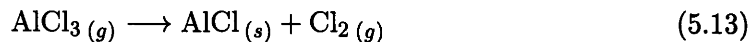

$$AlCl_{3\,(g)} \longrightarrow AlCl_{\,(s)} + Cl_{2\,(g)} \tag{5.13}$$

It is suspected that chlorine is present in the deposited aluminum compound as dissociation of AlCl requires much higher energy than what is obtained in supersonic expansion; however, such evidence was not detected using x-ray elemental analysis method or AES. This observation is attributed to the detection limit of the analytical tools used, and possible oxidation or hydrolysis of the aluminum chloride compound once exposed to atmosphere rendering the results inconclusive.

The introduction of aluminum creates an upper-limit to the substrate temperature useful for etching. To eliminate such aluminum contamination, it is suggested to passivate the aluminum holder exposed to the chlorine beam in the future. Anodizing the holder, or replacing the holder with a material impervious to chlorine is recommended. When the substrate was searched for nickel, chromium, iron, and other metallic materials the chlorine beam is exposed to, none was found on the surface of the substrate at low or high temperatures, which implies all such materials do not contaminate the etchant gas beam. Thus, stainless steel and other nickel and chromium based super alloys would be suitable candidate materials immune to the effects of chlorine, which is harmful to this etch system.

Between the low and high temperature regime is a very small "mid-temperature" regime which spans between 270°C and 280°C. Within the mid-temperature regime, neither the trench nor river formation is observed as shown in Figure 5-7, and only the

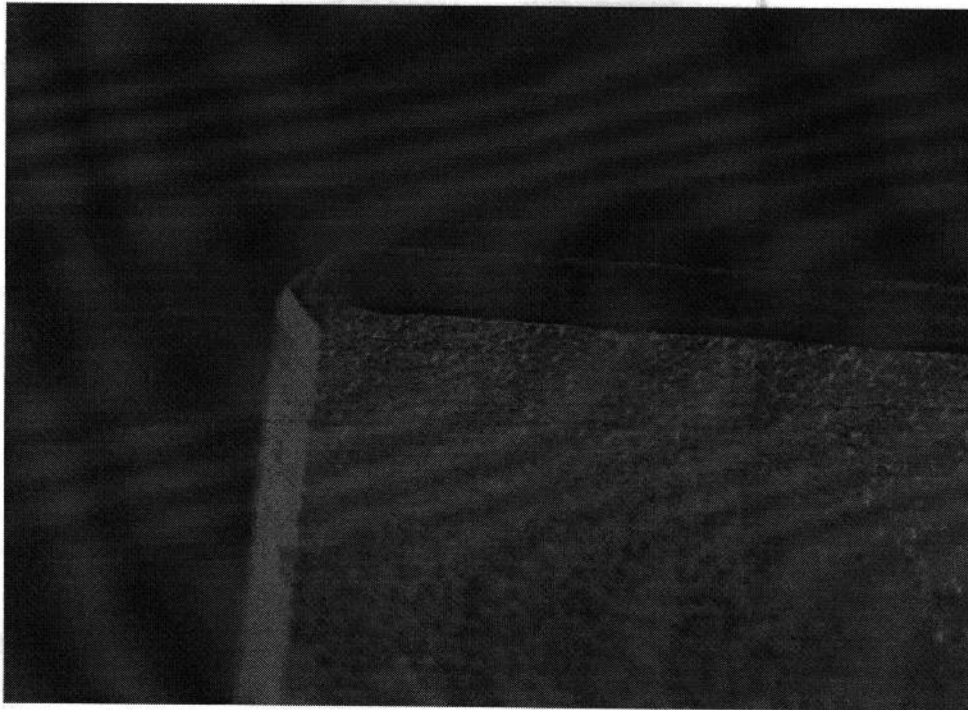

Figure 5-7: InP substrate etched at 275°C. Although the plateau surface is rough, no river or trench formation is observed. 4500X, 1 kev

plateau exists. The substrates etched at the mid-temperature range had etch rates of approximately 1.3 μm/hour.

Through comparison of the etch rates, it is surmised that the trenches created at low temperature etch lead to the plateau-only etch of the mid-temperature range, but this speculation is not confirmed. The difference in the etch rates in the formation of the plateau between the lower and the mid-range temperature regime is speculated to be caused by the difference in the desorption rate of the $InCl_x$ species. Similar increases in the etch rate as the substrate temperature increases are also observed in many plasma- and ion-assisted chlorine etches [46], and the etch rate increase is attributed to the increase in the desorption of the $InCl_x$ species.

The slower etch rate of the plateau etched under high temperature regime is attributed to the aluminum layer deposited on the surface hindering the chlorine from reaching the substrate surface. It is expected that the etch rate will increase and be greater than the mid-temperature range etch rate once the aluminum contamination source is eliminated.

Common to all three substrate etch temperature regimes was the surface morphology of the plateau region. The plateau region exhibited a very rough surface, resembling many pyramid-like artifacts. There are two possible explanations regarding the formation of the rough surface. First explanation concerns the use of the supersonically expanded gas. Under supersonic chlorine etch of single-crystalline silicon, origin of artifacts are attributed to the pit formation at the initial stage of etching [54]. As InP(100) surface exhibited higher reactivity to molecular chlorine than other planes, which is discussed more in detail in Section 5.3.4, the pyramid-like structures are thought to be caused by miniature crystallographic preferential etch mechanism. Therefore, as with Cl_2–silicon system, the initial pit formation contributes to micro-preferential etch profile to occur, resulting in the rough surface. The second explanation is based on the assumption that that there is a low-level contamination at the surface, such as iron, chromium or nickel, which are components of inconel and stainless steels, the major construction materials of the nozzle. It is thought that such contaminants act as a micro-mask and create the roughness. Neither claim was substantiated in the KBE system. However, under auger elemental mapping with a surface detection limit of 0.5 atomic%, no contaminants were found at the surface level; therefore, the contamination theory is considered the less likely of the cause.

5.3.3.2 Etch Rate

The etch rate dependency with respect to the substrate temperature was plotted as shown in Figure 5-8. In general, as the substrate temperature increases, the etch rate increases. At the lower substrate temperatures, the increase in the incident beam energy did not seem to affect the etch rate, suggesting that the etch mechanics is not dependent on the rate of dissociative chemisorption of chlorine, but limited by the desorption of the reacted species, or the actual reaction rate of indium to chlorine. At higher temperatures the etch rate increases dramatically as the beam energy increases. This trend denotes that at substrate temperatures above 260°C, the etch mechanism is no longer limited by the indium chlorine desorption, but to the dissociative chemisorption of chlorine. The etch rate plot is consistent with etch reaction dependent on more than two different mechanisms until around substrate temperature of around 280°C where the aluminum contamination disrupts the "normal" etch mechanism.

At the lower temperature where the etch rate appears to be $InCl_x$ desorption-limited, the activation energy was determined as around 4.3 kcal/mole. The activation energy at the higher temperatures was 39.8 kcal/mole. The activation energy value at lower

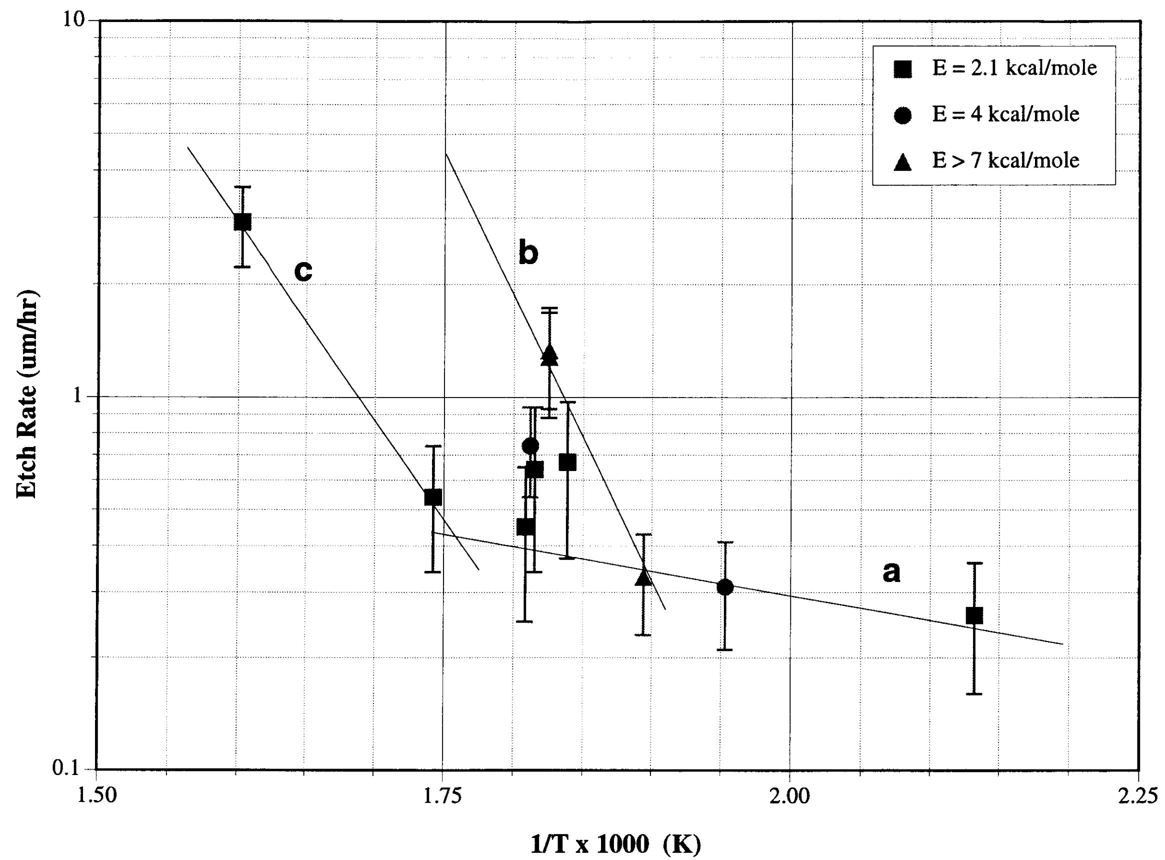

Figure 5-8: Plot of etch rate vs. substrate temperature at different beam energies. Overall, as the substrate temperature increases. Slope *a* is In–Cl reaction rate or $InCl_x$ desorption rate limited, slope *b* is Cl_2 dissociation rate limited, and slope *c* is Cl_2 dissociation rate limited with aluminum compound deposition hindering the process.

temperature was lower than reported value of 7.7 kcal/mole by Furuhata *et al.* [42].

5.3.4 Etch Profile

Using the chlorine-hydrogen etch system, two distinctly different etch profiles were observed: (1) directional etch, and (2) crystallographically preferential etch. Figures 5-9(a) and 5-9(b) shows a typical crystallographically preferential etch profile obtained on InP substrates.

The crystallographic preferential etch is accomplished using a low-energy chlorine beam, usually a 100% chlorine beam. Although the plateau surface was rough, the sidewalls of all crystallographic etch profile showed a very smooth surface. The sidewall profiles made by the supersonic chlorine highly resembles other preferential etches created by wet etch based on sulfuric, phosphoric acids and hydrogen peroxide [55]. As with the wet (111) preferential etch, two different etch profiles were observed when cleaved along the (110) and $(1\bar{1}0)$ planes. The transition of the two etch profiles between the (110) and $(1\bar{1}0)$ planes can be seen in Figure 5-10. Such a characteristic is typical of the preferential etch observed in wet etches of zinc blende-based compound semiconductors [55][56][57], and is attributed to the different surface stability and reactivity of group–III or group–V rich surfaces.

A typical directional etch profile is shown in Figure 5-11. The directional etch profile seems to be achieved when chlorine is seeded within a hydrogen matrix, and the overall beam energy is increased. It is assumed that the trenches develop along the pattern mask is caused by the presence of higher concentration of reactive chlorine in that area in conjunction to the on-coming bombardment of translationally-activated molecules.

The increased chlorine concentration around the mask edge is created when the unreacted, cold chlorine molecules which land on the SiO_2 mask becomes thermally activated through contact with the hot substrate and increases in its surface mobility. The molecule then moves along the mask surface. If such chlorine does not desorb off the mask surface, it eventually find its way to the substrate surface, continuing to travel until it either desorbs off the surface or further reacts with the substrate and desorb as $InCl_x$. The increase in the chlorine concentration at the mask edge, along with bombardment of the directional beam, aids in maintaining the anisotropic aspect of the etch. This mechanism is illustrated in Figure 5-13, and is explained more in detail in Section 5.3.6.

One benefit of this mask edge enhanced etch is that a relatively narrow channel can be etched with high directionality. If the width of the channel is less than twice

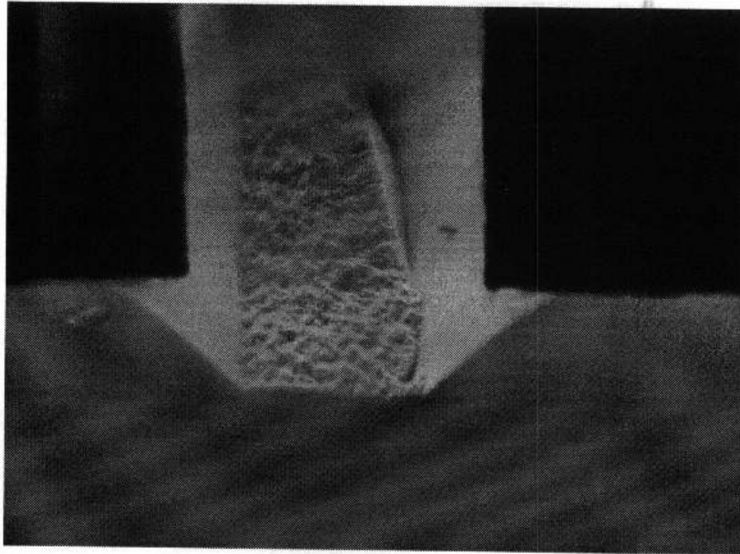

(a) InP substrate cleaved along the $(1\bar{1}0)$ plane. The mesa is approximately 2 μm high. 6000X 1 keV

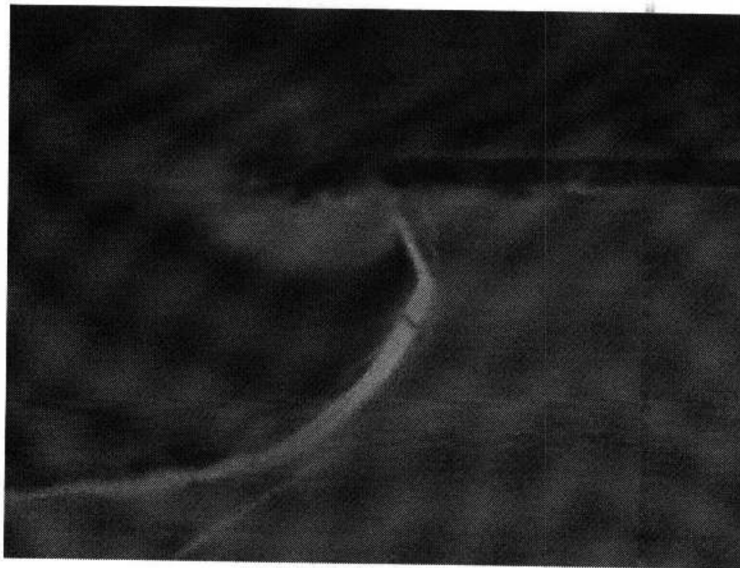

(b) InP substrate cleaved along the (110) plane. The mesa is approximately 2.5 μm high. 17,000X 1 keV

Figure 5-9: InP substrate exhibiting crystallographically preferential etch profile. Figure 5-9(a) is commonly observed on facets cleaved along the $(1\bar{1}0)$ plane, where Figure 5-9(b) is seen on facets cleaved along the (110) plane.

Figure 5-10: InP showing the interaction between the two crystallographic preferential etch profiles at intersection between the (110) and $(1\bar{1}0)$ planes. Due to the formation of a "lip" near the mask junction, the mesa along the $(1\bar{1}0)$ plane exhibits a thicker mesa top. The width of the base of the mesa near the bottom of the photo is approximately $5.5\,\mu$m. 4000X, 1 kev

the width of the boundary layer created by the cascading chlorine molecules, only the trench develops without the plateau (see Figure 5-12(a)). As the channel width widens, the plateau emerges while the the enhanced etch rate adjacent to the mask edge (see Figure 5-12(b)) is retained. This unexpected phenomenon allows for channels $2\,\mu$m wide be etched at an anisotropy of over 4-to-1 height to undercut ratio.

The sidewalls of the directional etch profile showed vertical striations, but smooth surfaces otherwise. These striations are attributed to mask edge imperfections which the features were enhanced and the pattern transferred onto the surface. Although directional, the etch profiles still shows significant lateral etch near the mask–substrate interface. The enhanced lateral etch mechanism is also discussed in Section 5.3.6.

Figure 5-11: InP substrate exhibiting a directional etch. It exhibits the combined characteristics of the trench etch and the faster plateau etch of the mid-temperature regime. The mesa is approximately 4 μm high. 11,000X, 1 kev

5.3.5 Effect of Gas Flow Rate

The InP substrates were etched under varying concentration of chlorine within hydrogen matrix, and different flow rate into the main chamber.

As long as the source was considered operating in the supersonic expansion regime, any significant or conclusive evidence of correlations between the flux of chlorine, background main chamber pressure, and the etch rate were not observed. This phenomenon implies that the etch rate is not dependent on the flux rate of the etchant gas, but is dependent on the actual reaction rate of the reacting species at the surface.

When the beam is not expanded supersonically, the etch rate of InP was reduced dramatically in comparison to etch by supersonic beam. On a substrate etched under non-supersonically expanded stream at a chlorine flux of 13 sccm, simulating a Knudsen source, the mesas under the etch masks were barely defined as the etch rate was extremely slow, and the surface of the plateau region looked very rugged. With the

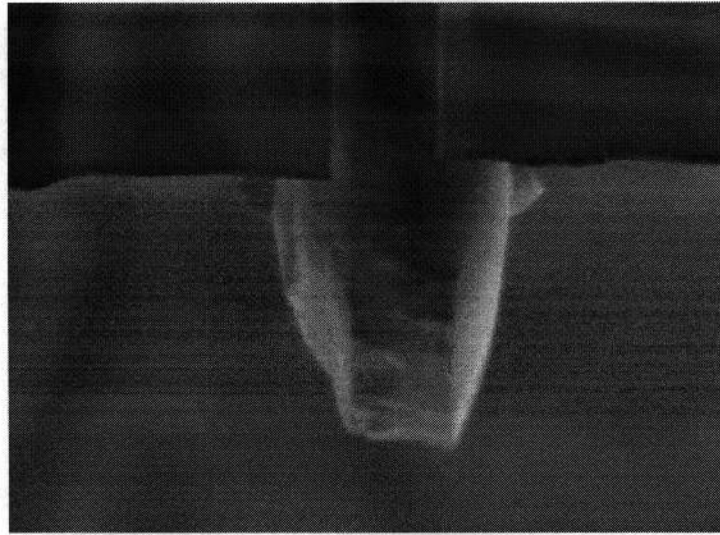

(a) Etch profile of a channel created by a 2 μm wide mask opening. The depth of the etch is approximately 6 μm. 8000X, 1 kev

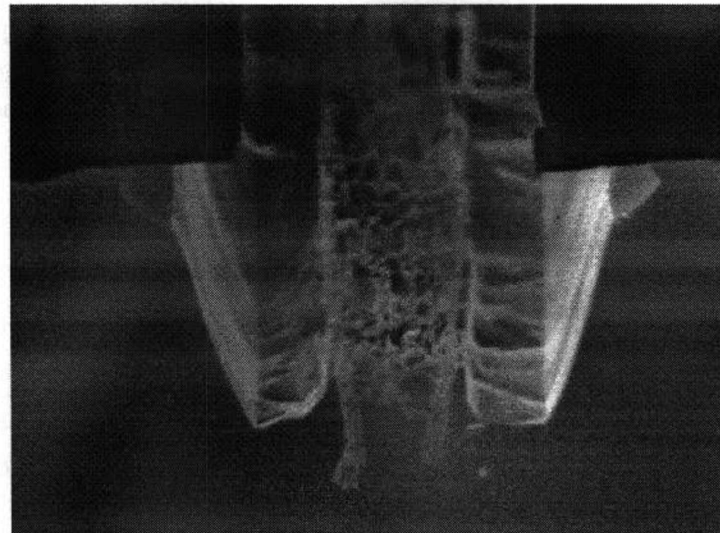

(b) Etch profile of a channel created by a 7 μm wide mask opening. The depth of the area adjacent to the mask is approximately 5.5 μm and the plateau is approximately 4 μm deep from the mesa top. 6500X, 1 kev

Figure 5-12: SEM micrographs of narrow channel etch exhibiting high anisotropy.

substrate etched at the a chlorine flux rate of 6 sccm, but is a supersonic beam, the familiar defined mesas and rough plateau surfaces were observed. From these results, it is clearly evident that it is not the flux of the chlorine at the surface, but the directionality and the translational energy of the beam that enables the InP etch.

All of the preceding observations are consistent with the assumption made in Section 5.3.1, that the etch mechanics involved in the chlorine-InP interaction depends on the dissociative chemisorption of chlorine molecules at the surface, and that at chlorine pressure of 1×10^{-7} torr, the dissociation is induced by the translationally activated molecules.

5.3.6 Effect of Changes in the Beam Energy

The chlorine energy within the molecular beam was varied between 1.5 kcal/mole [2] to 17 kcal/mole, calculated using Equation 2.16. The energy was changed by altering the gas reservoir temperature and by seeding the chlorine gas within a hydrogen gas matrix.

InP substrates etched with chlorine energy above 4 kcal/mole exhibited directional etch profiles as shown in Figure 5-11. The directional etch exhibited a near-vertical etch with enhanced lateral etch near the mask–substrate interface. It is hypothesized that the enhanced lateral etch near the surface is created when the adsorbed chlorine on the mask surface becomes thermally activated and diffuse along the surface of the mask, eventually finding its way to the substrate–mask interface. Once it reaches the substrate, if the chlorine does not desorb it is assumed to react with the substrate, creating the lateral etch profile.

In all incidences of directional etch profile obtained, the etch rate is enhanced along the mask edge, at the base of the sidewall. This phenomenon is attributed to increase in adsorbed chlorine concentration near the mask edge. The schematics for the proposed etch mechanics is illustrated in Figure 5-13. When a rotationally cold chlorine molecule impacts on the SiO_2 surface, it is thought to adsorb dissociatively or physically onto the surface with a limited lifetime. While the Cl_2 is physisorbed on the surface, the

[2] The following unit conversions hold:

$$\begin{aligned} 1\, kcal/mole &= 4.19 \times 10^3\ joules/mole \\ &= 2.61 \times 10^{21}\ eV/mole \\ &= 4.3 \times 10^{-2}\ eV/particle. \end{aligned}$$

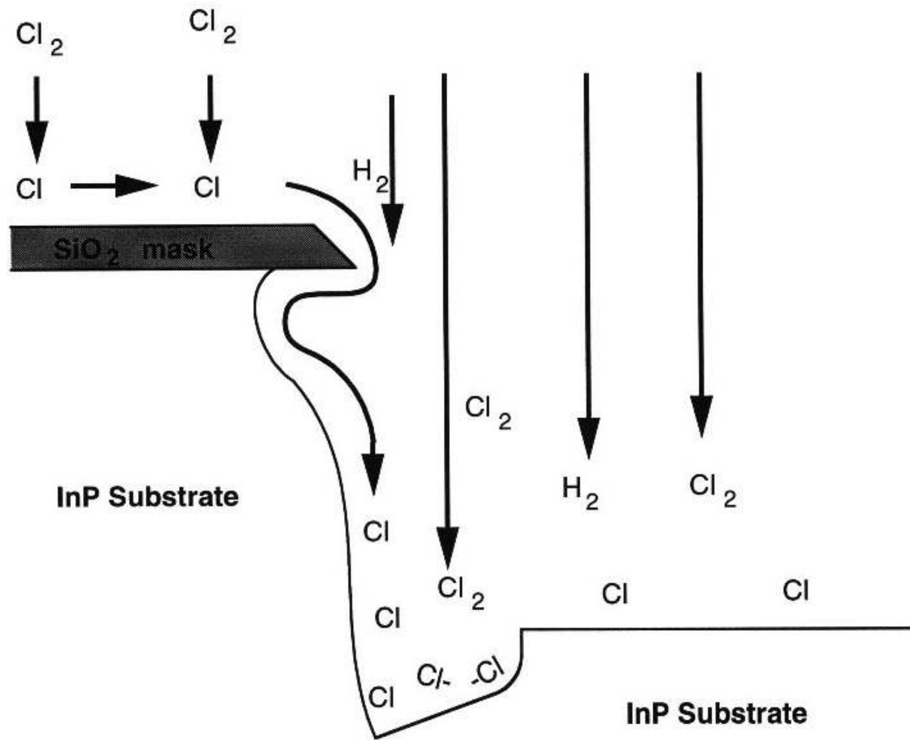

Figure 5-13: The schematic diagram showing the mechanism attributed in creating the directional etch. Unreacted chlorine which landed on the etch mask becomes thermally excited thus begins to diffuse along the mask surface. It eventually finds its way to the mask edge, and subsequently continues on to travel along the exposed substrate surface. Higher concentration of chlorine around the vicinity of the sidewall enhances the etch rate around the etch mask.

heat energy is transferred from the heated substrate to the chlorine, and eventually is vibrationally excited enough to desorb off the surface. However, as the chlorine becomes more thermally activated, the surface mobility of the chemisorbed and physisorbed chlorine also increases, allowing it to move along the surface of the silica mask. Eventually chlorine traveling along the inert SiO_2 finds its way to the edge of the mask and to the exposed InP surface. This phenomenon allows unreacted chlorine to be present around the mask–substrate interface. The enhanced etch rate alongside the mask–substrate interface is thought to be caused by the combination of increase in the unreacted chlorine density in the immediate vicinity of the reacting surface and some SiO_2–InP interface stresses.

The enhanced etch rate along the base of the sidewall is thought to be caused by the increased chlorine concentration also. The increase in chlorine concentration, dissociated or in its diatomic molecular form, along the bottom of the sidewall introduces a possibility of secondary supersonic bombardment phenomenon. It is reported in the literatures as collision-induced dissociative chemisorption [49]. In short, if a layer of physisorbed molecule is bombarded with translationally-activated molecule, it is possible to deform the adsorbed molecule and induce dissociation, thus allowing the chemical to further react with the surface. The increase in the chlorine concentration along the base of the sidewall increases the probability of such collision-induced reaction in comparison to the plateau region, and therefore increase in the etch rate. This phenomenon explains the enhanced etch rate along the bottom of the sidewalls.

The explanation for this phenomenon is supported by the fact that most trench-like enhanced etch rate is not observed around masked area which covers very little surface area, while it is pronounced near the SiO_2 mask that covers a wide surface area. In the preceding explanation, mask surface area which gives enough chlorine molecules to thermally activate and collect, is necessary for this phenomenon to take place. Larger the mask area, more chlorine molecules are temporary trapped on the surface. And more available chlorine on the surface of the SiO_2 mask denotes there will be more chlorine having the opportunity to make its way to the substrate surface leading to enhanced etch rate along the mask edge. It is expected that this mask surface area dependency is highly pronounced when the characteristic width of the mask is on the order of the diffusion length or less. Once the dimensions involved exceeds such length, the dependency between the mask surface area size and the enhanced reaction rate of the substrate in the vicinity of the mask is expected to reach a constant.

From the explanation that the enhanced etch rate around the mask edge is due to

the diffusion of the chlorine molecules from the mask, the order-of-magnitude surface diffusion coefficient D_s, of chlorine on InP substrate can be calculated using a simple diffusion equation based on a random-walk type diffusion mechanism in two-dimensional surfaces:

$$R_n = \sqrt{4\,D_s\,t}\ , \tag{5.14}$$

where R_n is the root-mean-square distance traveled by the molecule during the length of time t. At a substrate temperature of 275°C, D_s was determined as approximately $1\times10^{-16}\,\mathrm{m^2/sec}$. The value seems rather small for surface diffusion, even for a surface temperature of 275°C which is considered low under diffusion condition. However, the slower apparent diffusivity is attributed to the fact that the random-walk mechanism in two dimensions does not account for the reaction and the subsequent desorption of the reaction products. Therefore, in this particular case, surface diffusion constant D_s should be more appropriately referred to as effective diffusion constant, $D_{s,eff}$, to signify that the number is representative of the combination of at least two different mechanisms involved.

When the InP samples are etched using a seeded chlorine beam at low substrate temperatures, the groove formation along the mask edge also is present, but significantly deeper than the grooves formed at higher temperatures. Also, the grooves near the mask edge is not always consistently present. This observation suggests that at lower substrate temperatures, some other kinetics is involved in creating the directional etch. In addition to such grooves, trenches are also prevalent in other exposed surfaces. Although the trenches created near the mask edge can be explained by the above assumptions, it is not well understood how the trenches in the area between the masked areas are created. Unfortunately, this phenomenon could not be adequately addressed during this thesis research.

5.3.7 Summary of InP–Chlorine Etch

The behaviors observed between InP and translationally activated chlorine were summarized in Figure 5-14 and as follows:

- Dissociative chemisorption is thought to occur when chlorine gas encounters InP surface, and such mechanism is vital for the etch reaction.

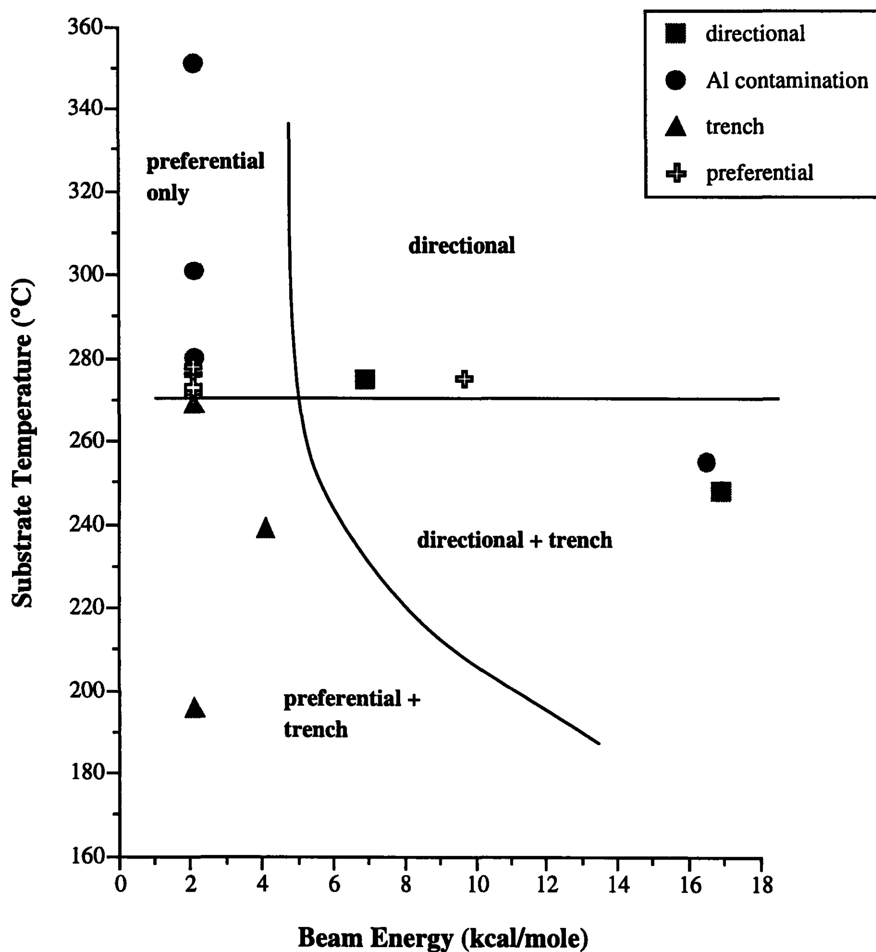

Figure 5-14: The etch results obtained were tabulated with respect to substrate temperature and chlorine beam energy. As optimum etch profile was being investigated, most of the experiments were conducted at the substrate temperature around 275°C where no river or trench morphology is present. This summary plot indicates a trend of directional etch obtained at higher beam energy. The morphology dependence caused by aluminum contamination was ignored for the purpose of determining which substrate temperature and beam energy will create a certain morphology in this diagram.

- Under translationally activated chlorine bombardment, higher incidences of dissociative chemisorption takes place, increasing the InP etch rate.

- Chlorine etches InP preferentially along a crystallographic plane.

- Undercut of the mask is observed, due to the diffusion of the chemisorbed chlorine along the surface, and due to unreacted chlorine molecules scattering off the substrate surface and impinging on the sidewalls.

- Etch rate increases as substrate temperature is raised. This trend is thought to be caused by the increase in the desorption rate of the etch product, $InCl_x$ compounds.

- As the beam energy is increased, the rate of collision-induced dissociative chemisorption becomes much higher where the substrate is exposed to, thus increase in the line-of-sight etch rate. The increase in chemisorbed chlorine in turn creates a directional etch profile.

- However, even if the beam energy is increased, the etch rate at lower substrate temperature does not change very much. This result suggests that at lower temperatures, the etch rate is not dependent on the rate of chemisorbed chlorine generation on the surface. The limiting step is thought to be the desorption rate of $InCl_x$ species.

- At substrate temperatures below 270°C, a "trench" channel morphology is observed. The mechanism for its formation is not understood.

- As the substrate temperature increases to above 280°C, aluminum deposition contamination is observed, along with the emergence of "river" morphology. This phenomenon is thought to be readily eliminated by changing the skimmer holder material, where the contamination originates.

- At substrate temperatures between 270°C and 280°C etch morphology is uniformly rough; however no river or trench formation is observed. The roughness is proposed to have been caused by the initial etch pit formation at the initial stages of the etch.

5.4 Data Analysis for GaAs System

A cursory study was made on chlorine etch of GaAs substrates. The GaAs substrates were etched between 364°C and 374°C. There are few reasons for the choice of this maximum operating temperature on the current KBE setup. Of all the reasons, including the effect of aluminum contamination at higher substrate temperatures, the deciding factor was the enhanced chlorine reactivity with the indium above 300°C, which is used as a substrate adhesive onto the molybdenum substrate holder.

As the substrate etch temperature was increased above 300°C, the reaction rate between the chlorine and the indium film used to hold the substrate in place significantly increased. At a substrate temperature of 300°C, chlorine was able to etch all the indium off the substrate holder within 3 hours, resulting in a loss of the sample (sample falling off the substrate holder), as all of the indium behind the substrate was also etched away. As the etch rate of GaAs was much slower than those of InP, in order to observe any significant etch profiles on GaAs samples, it was necessary to expose them to the chlorine beam for at least 2 hours. During the experiments, the tendency that higher substrate temperature would contribute to faster etch rates was observed. However, due to the indium glue degradation, the highest substrate temperature which can withstand chlorine exposure for the required amount of time was determined to be around 365°C.

Some plans to alter the substrate holding method, using some mechanical means to supplement the indium paste, was proposed but was never implemented. For this thesis project, the demonstration of the ability to etch GaAs, and its basic etch characteristics were shown; however, the optimization of the GaAs etch process was deemed beyond the scope of this project.

5.4.1 Desorbed Gas Species

According to Hou *et al.* [44], one or more of the following reactions are expected to take place in GaAs etched by chlorine:

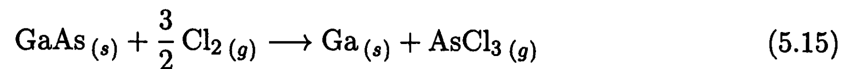

$$\mathrm{GaAs}_{(s)} + \frac{3}{2}\mathrm{Cl_2}_{(g)} \longrightarrow \mathrm{Ga}_{(s)} + \mathrm{AsCl_3}_{(g)} \tag{5.15}$$

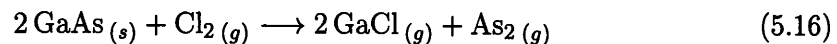

$$2\,\mathrm{GaAs}_{(s)} + \mathrm{Cl_2}_{(g)} \longrightarrow 2\,\mathrm{GaCl}_{(g)} + \mathrm{As_2}_{(g)} \tag{5.16}$$

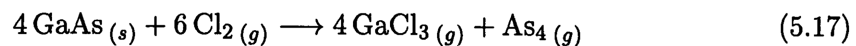

$$4\,\mathrm{GaAs}_{(s)} + 6\,\mathrm{Cl_2}_{(g)} \longrightarrow 4\,\mathrm{GaCl_3}_{(g)} + \mathrm{As_4}_{(g)} \tag{5.17}$$

It is reported that $AsCl_3$ and $GaCl_3$ are predominant species produced with substrate temperature below 200°C. Above substrate temperature of 400°C, more GaCl, As_2, and

Species	Mol. Wt. [50]	Melt. T [50]	Boiling T [50]	P_{vap} [52][58]
Ga	69.72 g	29.8°C	2403°C	
GaCl	105.18 g			
$GaCl_2$	140.63 g	164°C	535°C	~80 mm (367°C)
$GaCl_3$	176.08 g	77.9°C	201°C	80 mm (25°C)
$AsCl_3$	181.28 g	-8.5°C	130.2°C	1 mm (100°C)
Al	26.9 g	660.4°C	2467°C	
AlCl	62.43 g			
$AlCl_3$ (Al_2Cl_6)	133.34 g (266.68 g)	190°C	decomp. 262°C, 182.7°C, subl. 177.8°C	1 mm (100°C)

Table 5.2: List of relevant materials involved in the GaAs etch and their chemical properties

As_4 is produced.

Table 5.2 [50][52][58] shows the list of chemical properties of the reaction species.

5.4.2 Etch Profile

In general, GaAs substrates etched by chlorine exhibited cleaner and smoother plateau surfaces than those of InP substrates (see Section 5.3 for details on InP etch). The etch exhibited a crystallographic preferential etch along the (111) surface as seen in Figure 5-15.

Unlike the InP samples, no trench profile was observed with GaAs substrates. Some shallow river formations were observed. However, as shown in Figure 5-16, the river formations in GaAs substrates are attributed to partial peeling of the aluminum layer, which is also seen on InP samples etched at higher temperatures.

5.4.3 Etch Rate

The etch rate of GaAs was much slower than that of InP etched under similar conditions, but at a lower substrate temperature. This trend is consistent with the etching rates reported by Furuhata *et al.* [42], although the etch rates reported are for much higher chlorine pressures. However, the vapor pressure of $GaCl_x$ is much higher than those of $InCl_x$, it is expected that the etch rate of GaAs using chlorine would be higher at

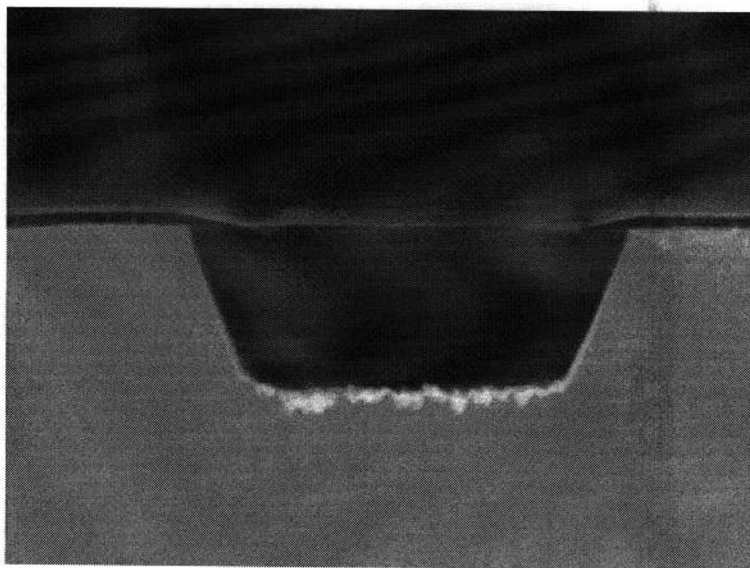

(a) GaAs substrate is cleaved along the $(1\bar{1}0)$ plane. The mesa is approximately 2.5 μm high. 10,000X 1 kev

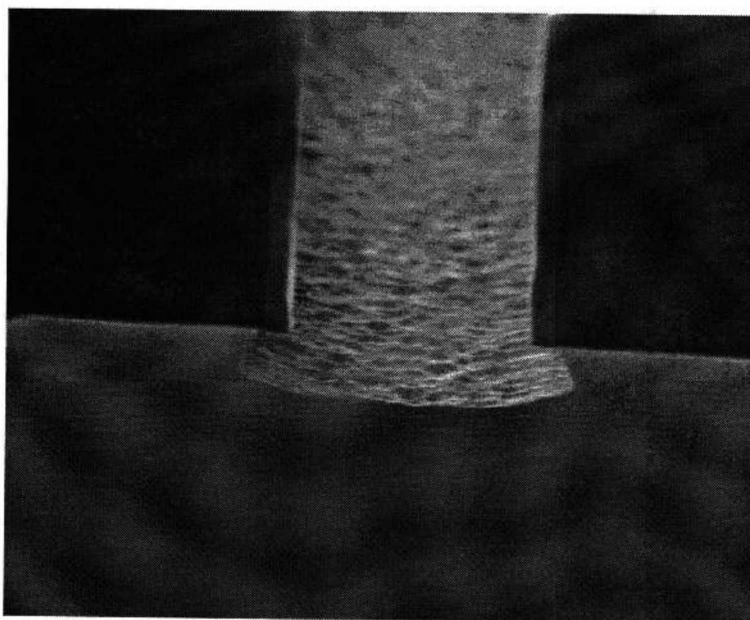

(b) GaAs cleaved along the (110) plane. The mesa is approximately 2.5 μm high. 3500X, 1 kev

Figure 5-15: SEM micrographs of GaAs substrate etched under chlorine exhibiting crystallographic preferential etch.

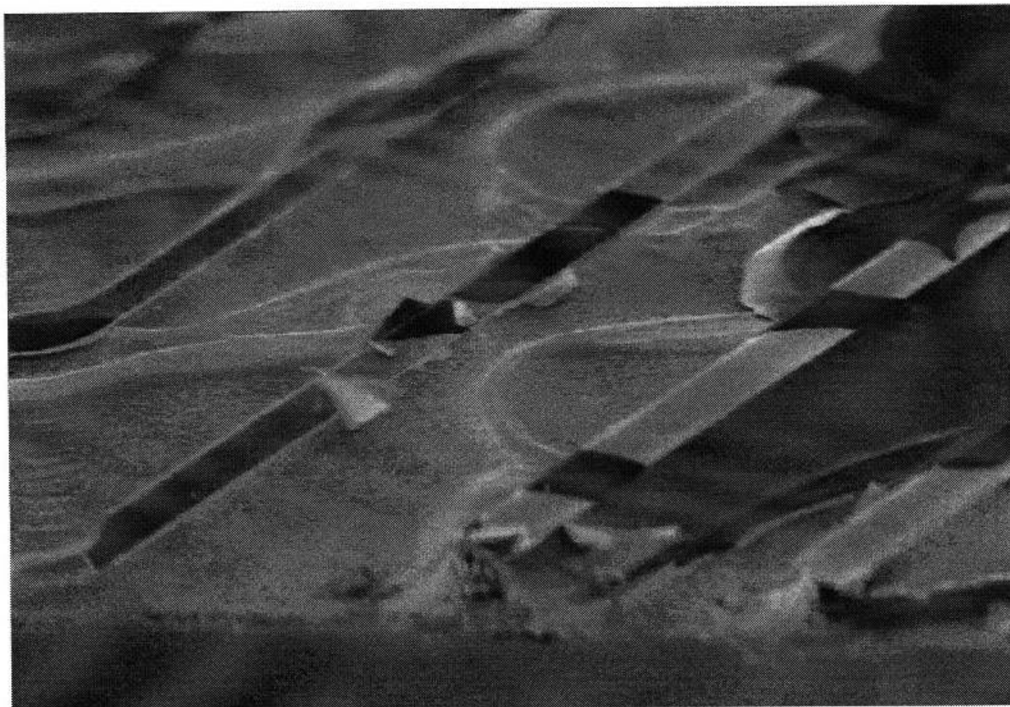

Figure 5-16: Picture of GaAs substrate with aluminum deposit layer. A slightly enhanced etch rate is observed under the peeling layers, causing a shallow river morphology.

lower temperatures where the etch rate was assumed to be $InCl_x$-desorption limited. Although consistent with Furuhata *et al.*, the difference in etch rates between InP and GaAs was much larger than those reported. The best GaAs etch rate achieved using KBE system was approximately 0.8 μm/hour with the substrate temperature of 364°C, whereas the etch rate of InP was approximately 60% faster. One reason for the greater difference between the etch rate of GaAs and InP is attributed to possible chlorine reaction resistance of the native gallium oxide present at the surface of the substrate. Two indications that gallium oxide is much resistant to chlorine etch in comparison to GaAs are as follows: (1) no change in the laser reflectivity roughness is detected at the beginning of the etch as seen with InP samples, and (2) etch rate determined after one hour of chlorine exposure was approximately 0.2 μm/hour whereas the etch rate measured during the last 2 hours of exposure was 1.1 μm/hour. These results suggest that the etch rate radically increases after some initial slow-etch phase.

If the gallium oxide is in fact responsible for slow initial etch rates, the possibility of UHV *in–situ* patterning, etching, mask removal, and subsequent regrowth using

KBE system is very good. It has been demonstrated that it is possible to pattern and selectively remove the gallium oxide using electron beam pattern generator [59][60][61]. It is also known that gallium oxide can be easily removed post-etching, through thermal oxide desorption, or briefly exposing the oxide layer to atomic hydrogen [62][63][64] or gaseous hydrochloric acid [65]. Therefore, if this e-beam patterning is combined with the selectivity hinted between GaAs and gallium oxide surfaces using supersonic chlorine etch method, the realization of *in–situ* patterning is very real, and this avenue of research is worth further exploration.

Another reason for the difference in etch rate between InP and GaAs is thought to be caused by the fact that the optimum substrate etch temperature could not be determined due to the aluminum deposition at temperatures above 290°C, which is thought to aid in inhibiting the chlorine etch mechanism. Therefore, the etch rate is expected to improve significantly when the aluminum contamination is suppressed in the KBE system and the substrate temperature raised to the maximum limit.

Chapter 6

Conclusion

6.1 Summary

In this thesis, a novel ultra-high vacuum compatible, ion- and plasma-source-free dry etch reactor was successfully designed and constructed. It was demonstrated that this Kinetic Beam Etch system is capable of obtaining directional and crystallographically preferential etch profiles on InP and GaAs substrates, with an etch rate ranging from $0.3\,\mu$m to $2\,\mu$m/hour. Since the energies involved in etching the substrate is much lower than the energy needed to introduce crystal defects, although the aspect was not rigorously studied during this project, this technique is thought to be virtually damageless. This project is also the first reported InP etch using neutral molecular chlorine at pressures lower than 1×10^{-4} torr.

The performance of the Kinetic Beam Etch system was characterized using atomic force microscope, scanning electron microscope, and x-ray elemental analysis. An innovative method to calibrate the substrate heater thermocouple *in–situ*, and a novel method to measure the roughness of the substrate surface *in–situ* was developed using the laser reflectance measurement.

The KBE system was characterized so that the parameters governing the different etch profiles and surface morphology were determined, and so that a particular morphology can be reasonably predicted given a set of etch environment.

6.2 Recommendations for Improvement

The following are some suggested items to be considered to improve the current Kinetic Beam Etch system setup in the future.

First, the aluminum skimmer holder must be replaced with a material resistant to supersonically expanding chlorine molecules. Another option is to passivate its current aluminum holder either by coating it with an inert material, or anodizing the aluminum to cover all exposed surface areas with corrosion-resistant aluminum oxide.

Secondly, once the aluminum contamination source is eliminated, some mechanical method to hold the substrate on the molybdenum substrate holder, in addition to the use of indium, should be implemented. During the etch runs, it was clear that the indium glue was being etched away by the chlorine beam and when a sample was being etched for over 3.5 hours at 280°C, or 2 hours above 350°C, the substrate held onto the holder only by indium frequently fell off as all the indium was etched off the block and behind the sample. The use of indium in the KBE is proven to be an invaluable calibration tool. Therefore, instead of just replacing the current substrate mounting method, a mechanical holding method should be implemented as a supplement.

The directionality of the etch profile was proven to be heavily dependent on the reactivity of the etchant gas and the momentum of the impinging molecules. By changing the source etch gas, or its mixture, it is expected that many different types of etch profiles can be obtained. Hydrochloric acid, methyl-bromine, and methyl-iodine are some of the potentially useful etchant chemicals recommended for future investigation.

In addition to trying out new chemicals, optimization of the current chlorine etch is also strongly advised to attempt minimizing the lateral undercuts and enhanced etch rate at the base of the sidewall. As the lateral undercuts were suspected to be caused by the surface diffusion of unreacted chlorine from the SiO_2 mask and scattering of Cl_2 off the no-masked regions here are ideas for such optimization runs:

(1) Lower the substrate temperature

Lowering the substrate temperature will reduce the surface mobility of the etchant once it adsorbs onto the substrate surface, thus confining its effect. This alteration may not eliminate the lateral undercutting of the substrate at the mask–substrate junction, however, it should reduce the width of the enhanced etch rate around the base of the sidewall. Also, as the substrate temperature is lowered, the sticking coefficient of the chlorine will increase. Thus, it should lower the chlorine scattering onto the sidewalls, aiding in the lateral etch rate. For InP samples, the lower substrate temperature may pose a problem due to the evolution of trench morphology. However, for GaAs, it is expected that the trench morphology will not develop at lower substrate temperatures. This speculation is based on the assumption that the trench morphology is somehow related to the desorption rate of

the etch product. As $GaCl_x$ has a higher vapor pressure than $InCl_x$, it is thought that even at lower substrate temperatures, trench will not form on GaAs surfaces.

(2) Lower the translational chlorine beam energy

By lowering the translational activation of the chlorine beam, it is thought that it would reduce the collision-induced desorption of the adsorbed chlorine. Less chlorine scattering will lead to lowering the chlorine scattering onto the sidewalls. As the dissociative chemisorption of chlorine is imperative to etch, the reduction in the total beam energy should be accomplished by keeping the nozzle heater temperature high (promote dissociation), but seeding it in a heavier gas matrix (slow down the molecule).

(3) Seed the chlorine in a non-reactive gas matrix

Collision-induced dissociation was found to have a significant role in chlorine etch. However, by increasing the chlorine energy, the scattering of chlorine from the surface is increased, and is thought to heavily contribute to the lateral etch. Therefore, by seeding chlorine in a heavier, non-reactive gas such as argon or xenon, it is thought that such lateral scattering can be minimized. If chlorine adsorbs onto the substrate surface, if it is collided with a heavier molecule, the collision-induced reaction will still take place (this phenomenon is referred to as "hammer-action induced reaction" [48]). However, even if a non-reacting gas scatters off the substrate, it will not contribute to additional etching, as opposed as if the on-coming chemical was another reactive gas. This, in turn, is speculated in the reduction of overall lateral etch rate.

All of the above mentioned method is easily accomplished in the current KBE setup. However, the use of noble gases may constitute a problem, as cryogenic pumps are notorious for its inability to effectively pump them.

The substrates etched for this thesis project suffered a non-uniform etch, as they were etched while the sample sat stationary in the etch beam path. This problem could be alleviated by allowing the continuous rotation of the sample while it is exposed to the etchant gas. Although the KBE's substrate manipulator has the capability of motorized substrate rotation. However, the mechanism was malfunctioning due to degraded bearings, and therefore the samples could not be rotated during this thesis project.

As shown in Figure 4-8, periodically blocking the chlorine flow onto the InP produced a smoothing effect of the surface shortly after the chlorine flow was resumed. From this observation, the use of a slow chopper or a motorized shutter system is suggested to block

the chlorine flow periodically, taking advantage of this smoothing effect. By optimizing the gas-on, gas-off cycle, it is expected that some improvements in the roughness of the etched horizontal "plateau" surface could be achieved.

Although this etch technique is assumed that it will not introduce any damage to the crystalline structure at the surface, a rigorous surface damage assessment needs to be performed. Much studies are needed, perhaps using electron mobility and photoluminescence techniques, to assess such damages. Studies involving the etch characteristics of heterostructure epitaxial layers also need to be performed to allow such investigation, as well.

6.3 Future Applications

Inevitably, once a system is proven to work, the question of upscaling the system to accommodate larger wafer sizes and possible batch-processing comes up.

KBE system exhibits a promising future in UHV-compatible etching technology, within the cross sectional area of approximately 2 cm in diameter. Unfortunately, its scaling capability is severely limited. The main problem is the pumping speed. In order to increase the area covered by the molecular beam, the skimmer diameter must be enlarged. However, when fewer gas molecules are skimmed off at the source chamber, more gas enters the main chamber, thus increasing its working background pressure. In order to maintain a molecular beam profile, the background pressure must be at least three orders of magnitude lower than that of the beam. This can only be accomplished through higher vacuum pumping speed.

It is also possible to create a larger beam cross-section by increasing the distance between the skimmer and the target substrate. However, by doing so, the intensity of the beam will decrease geometrically. To compensate for the decreased intensity, the nozzle orifice can be enlarged, or the nozzle reservoir pressure increased. This results in higher flow rate, and thus higher background pressure. Then we are back to square one: higher pumping speed.

No matter what one does, with a single nozzle beam source, it is impossible to increase the working surface area beyond few centimeters diameter at best. In order to be able to use KBE system for batch processing, one must consider a different nozzle arrangement. One additional suggestion for upscaling the system is to use an array of nozzles instead of single nozzle–skimmer setup. However, as more gas is injected, more pumping speed is necessary, and we are back to the same problem of attaining a higher

pumping speed.

One of the possibilities of the use of KBE is in applications to Epitaxy-on-Electronics (EoE) processing [66][67]. EoE is an effort to grow GaAs-based light-emitting (LED) and laser diodes upon an already-existing GaAs integrated circuits, thus creating a true integrated optoelectronic chips. When processing any photonic devices once grown on an IC, the use of plasma- or ion-assisted etch can pose severe problems, mainly since the circuits cannot survive a typical post-processing anneal temperatures. With the use of KBE, the possibility of etching smooth sidewalls and mesas without the worry of exposing the IC to high temperatures or to damaging plasma and ions can be extremely useful. Therefore, it is extremely important to map the KBE system regarding its heterostructure etch characteristics, as all photonic devices are based on heterostructure epitaxy technology.

As stated in Section 5.4.3, however, the KBE system does present a unique possibility of realizing the ultimate goal of *in–situ* pattern, etch, etch removal and regrowth, especially in the GaAs system. If this aspect of the system is further explored, the potential may perhaps outweigh some of the difficulties encountered in up-scaling the system for larger wafer sizes.

6.4 Impact of the Project

The largest impact of this thesis project is the fact that group III–V compound semiconductors can truly be etched under UHV conditions using chlorine, without the use of damaging ion or plasma. Although the KBE system is not optimized, and its hidden potential yet explored, it has opened up a new door to the true UHV-compatible, damageless etching. Also due to its versatile design, the etch can be made using any commonly used semiconductor substrates by selecting the appropriate etchant gas. Although in the research laboratory which this equipment resides primarily will be using this technology for III–V compound semiconductor substrate etches, it can be readily adopted to be used for silicon and other substrates by altering the etchant. As the etch chamber is separate from the epitaxial growth chamber, the worry of cross-contamination through etching between different substrate material is negligible, thus making this etch system versatile.

Until now, neutral molecular chlorine, which is a commonly used etchant gas for both GaAs and InP, was not used frequently in conjunction with UHV environment from the fear of chamber degradation due to the use of corrosive gases, and also since

no etch reaction was observed with chlorine pressures lower than 1×10^{-4} torr. However, with the use of translationally activated chlorine, it is shown that chlorine can indeed be used in a true UHV environment for etching purposes. Benefit of using chlorine under such low pressure is paramount. Other than the pressure and cleanliness considerations, the amount of degradation of stainless steel, the typical construction material for UHV vessels, will experience is much reduced. Traditionally, chlorine and other corrosive gas use was not popular because of such issues. Now, research can progress with less concern with maintenance of the vessel, and concentrate on the actual use of the tool.

The introduction of precise substrate temperature calibration and the laser reflectance surface monitoring also opens many opportunities for macroscopic surface reconstruction studies. Traditionally, the use of RHEED was considered sufficient in learning about the condition of the surface. However, through the use of laser reflectance, it is shown that even if the RHEED pattern shows a pristine, single-crystalline surface, when viewed over a large area, the surface is in fact becoming rough. By combining the use of RHEED and laser reflectance surface monitoring, many possibilities of studying surface reconstruction is opened. To study and correlate the RHEED pattern, epitaxy, and the overall smoothness of the epitaxial growth or etch would be a very interesting project to pursue.

6.5 Concluding Thoughts

The Kinetic Beam Etching system setup is ideal for dealing with relatively small scale production, such as for use in research, or for use with a fragment of a substrate wafer. It will adequately serve its purpose for laboratory research, and much of its potential remains to be exploited. However, unless some revolutionary breakthrough takes place in the vacuum pump technology, it is this author's opinion that the supersonic nozzle-based etch reactor is probably not well-suited for use in mass-production purposes for the cost involved in preparing such a system may outweigh the benefits.

Appendix A

Design Schematics

This section contains the design schematics of the Kinetic Beam Etch system. All drawings are drawn to scale unless otherwise noted.

A.1 Source Flange

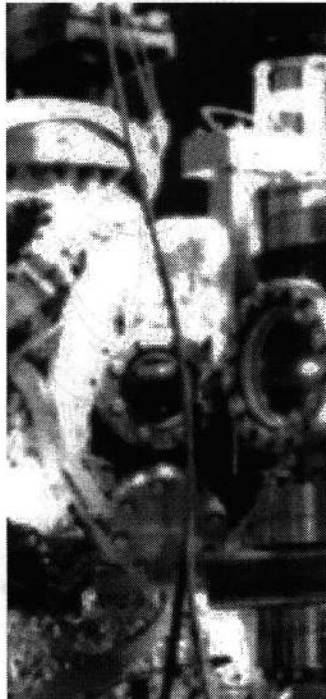

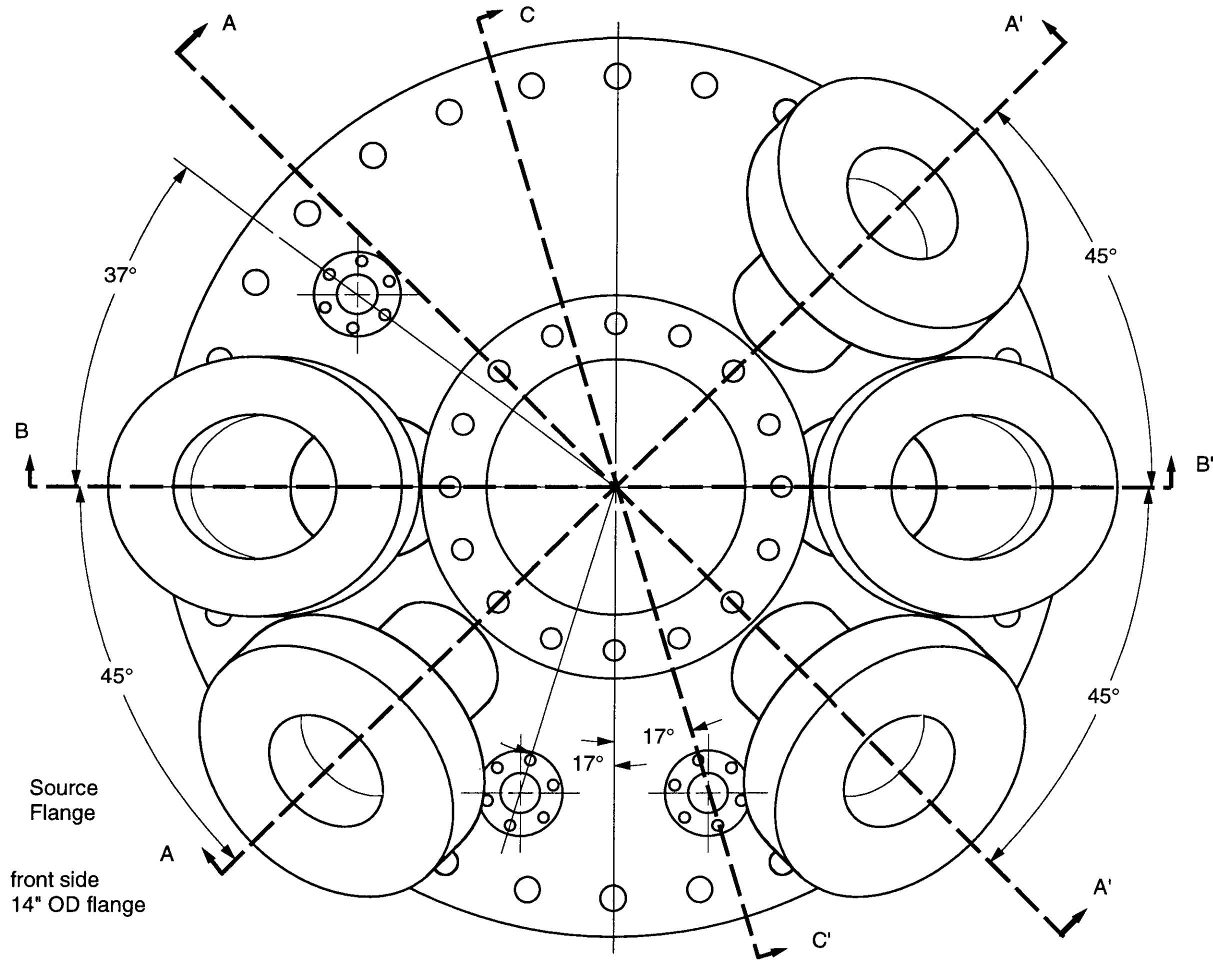

Figure A-1: Source Flange: Front View

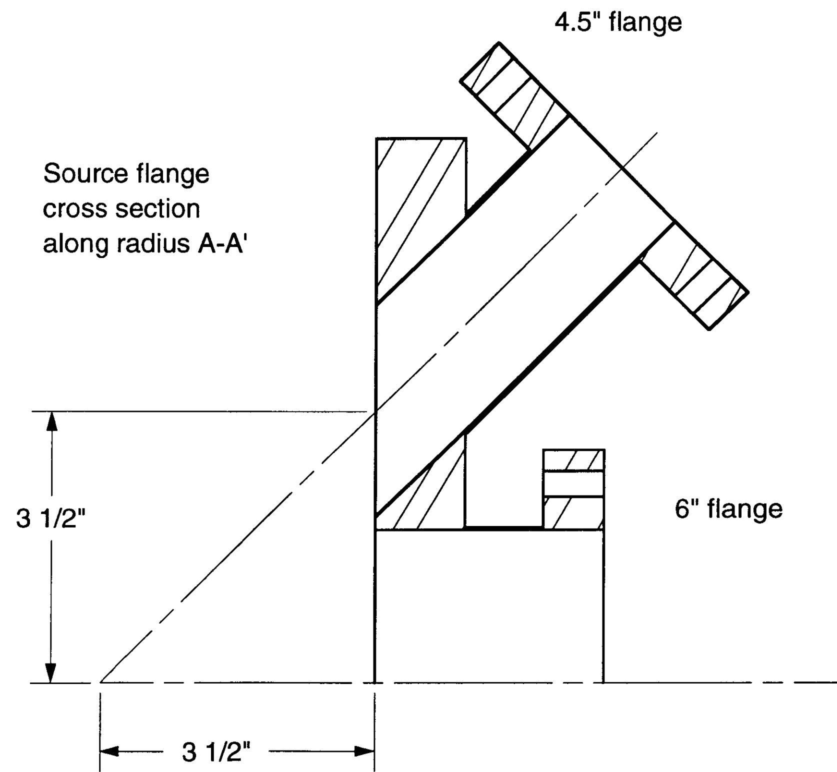

Figure A-2: Source Flange: Cross Section A–A'

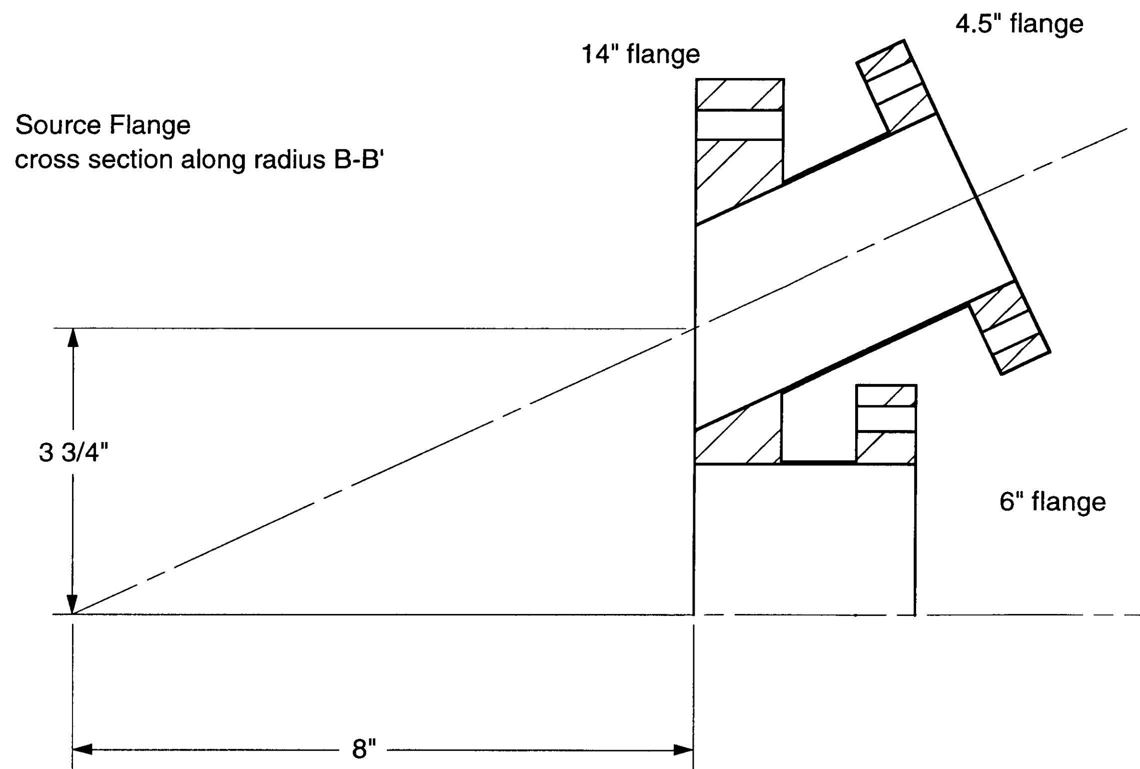

Figure A-3: Source Flange: Cross Section B–B’

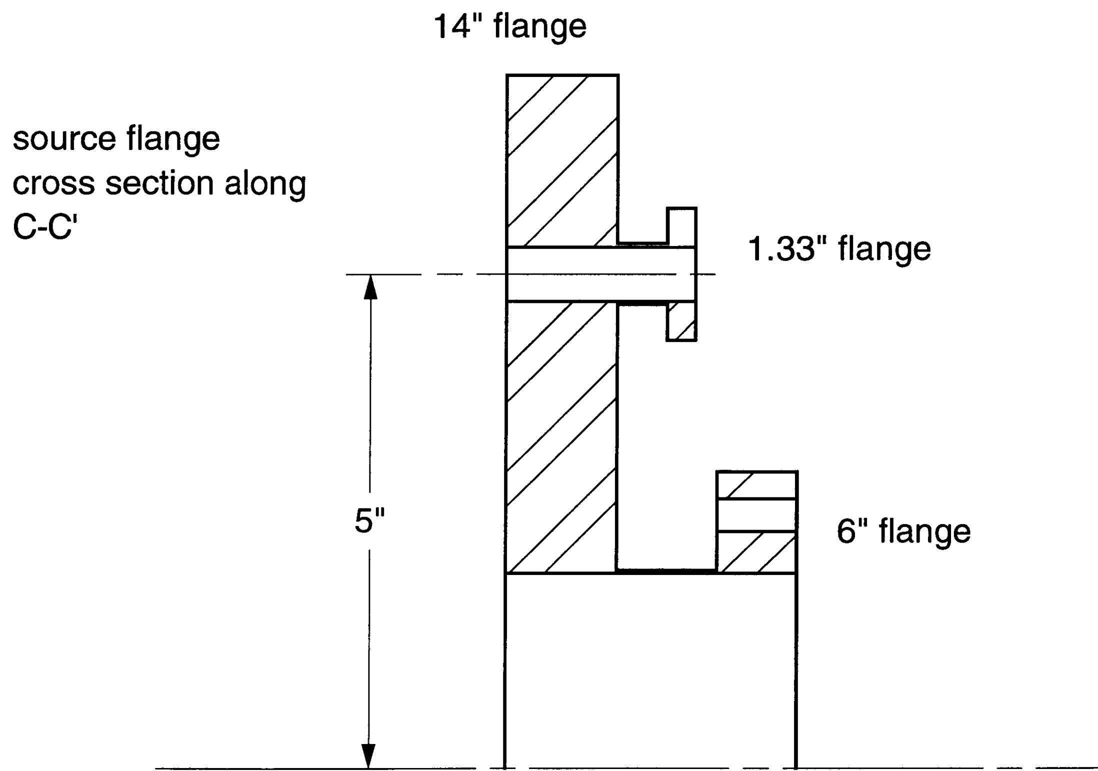

Figure A-4: Source Flange: Cross Section C–C’

A.2 Main Chamber

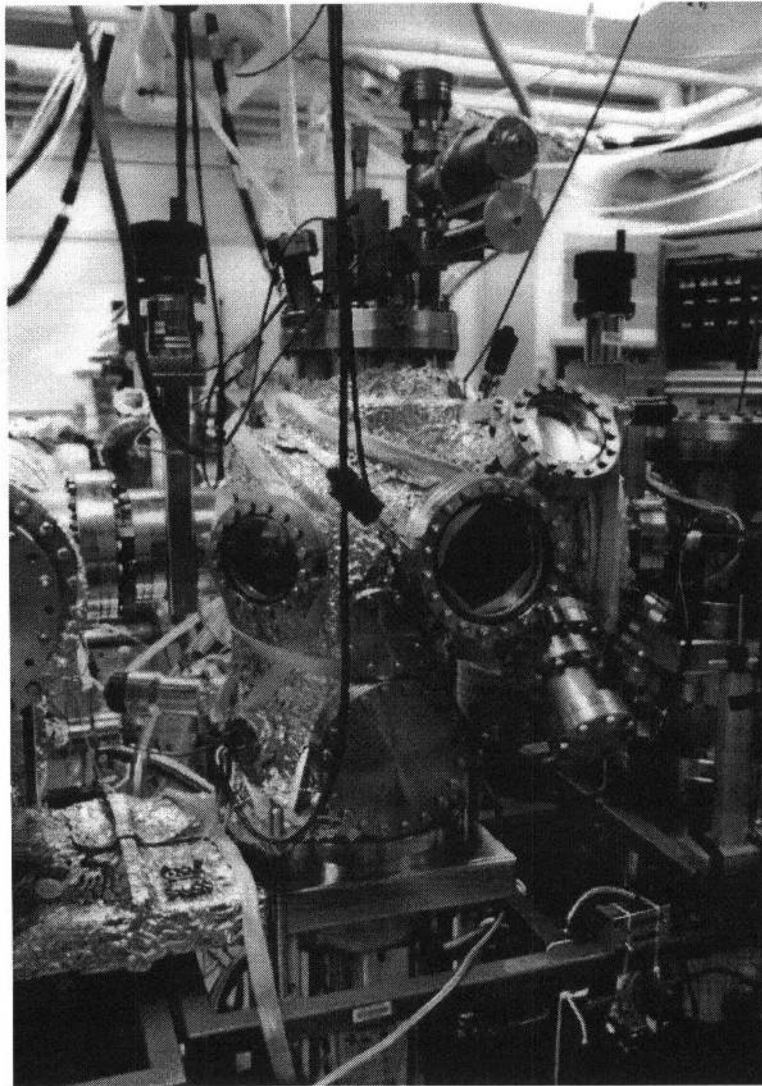

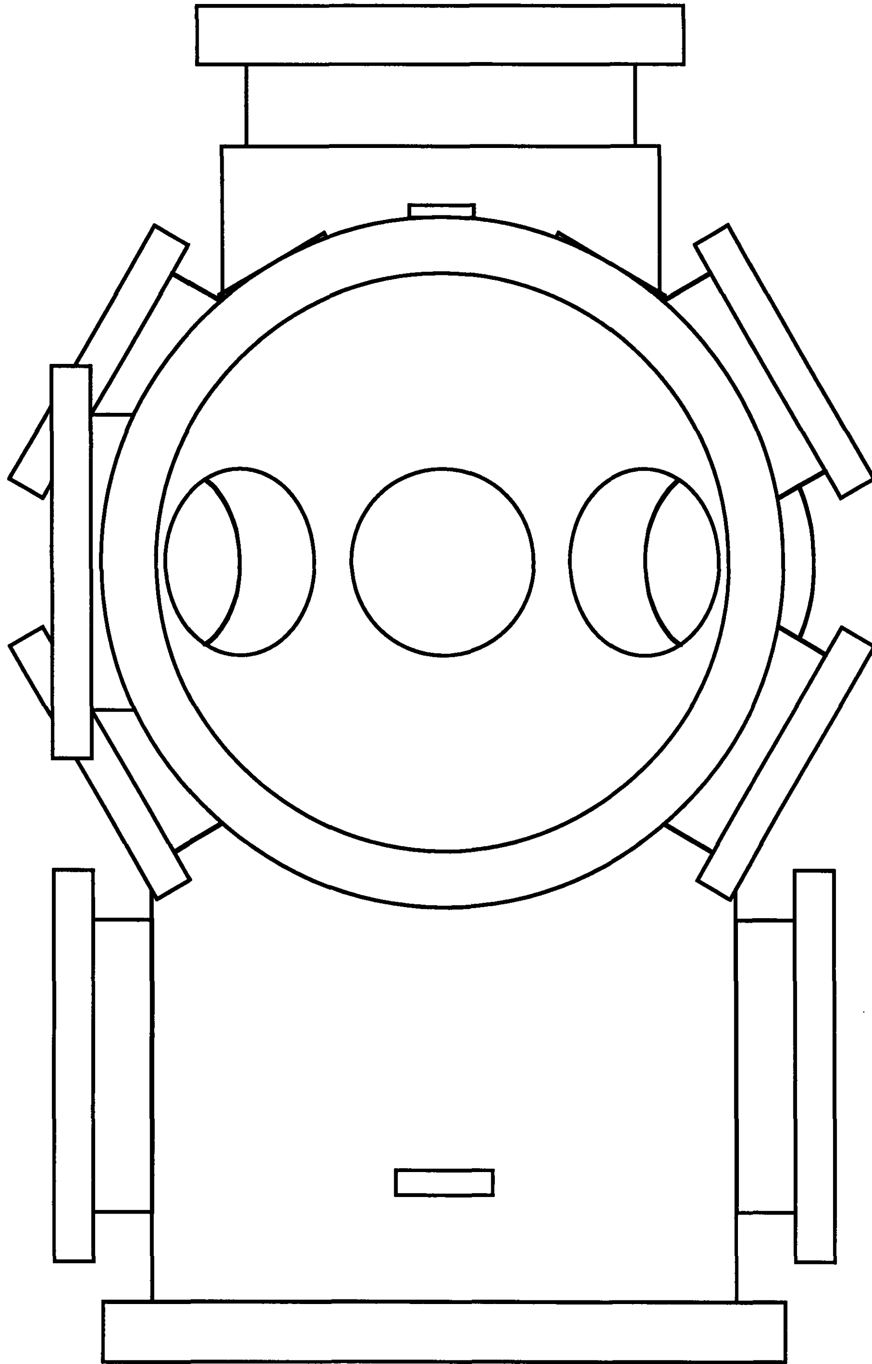

Figure A-5: Main (Etch) Chamber Front View

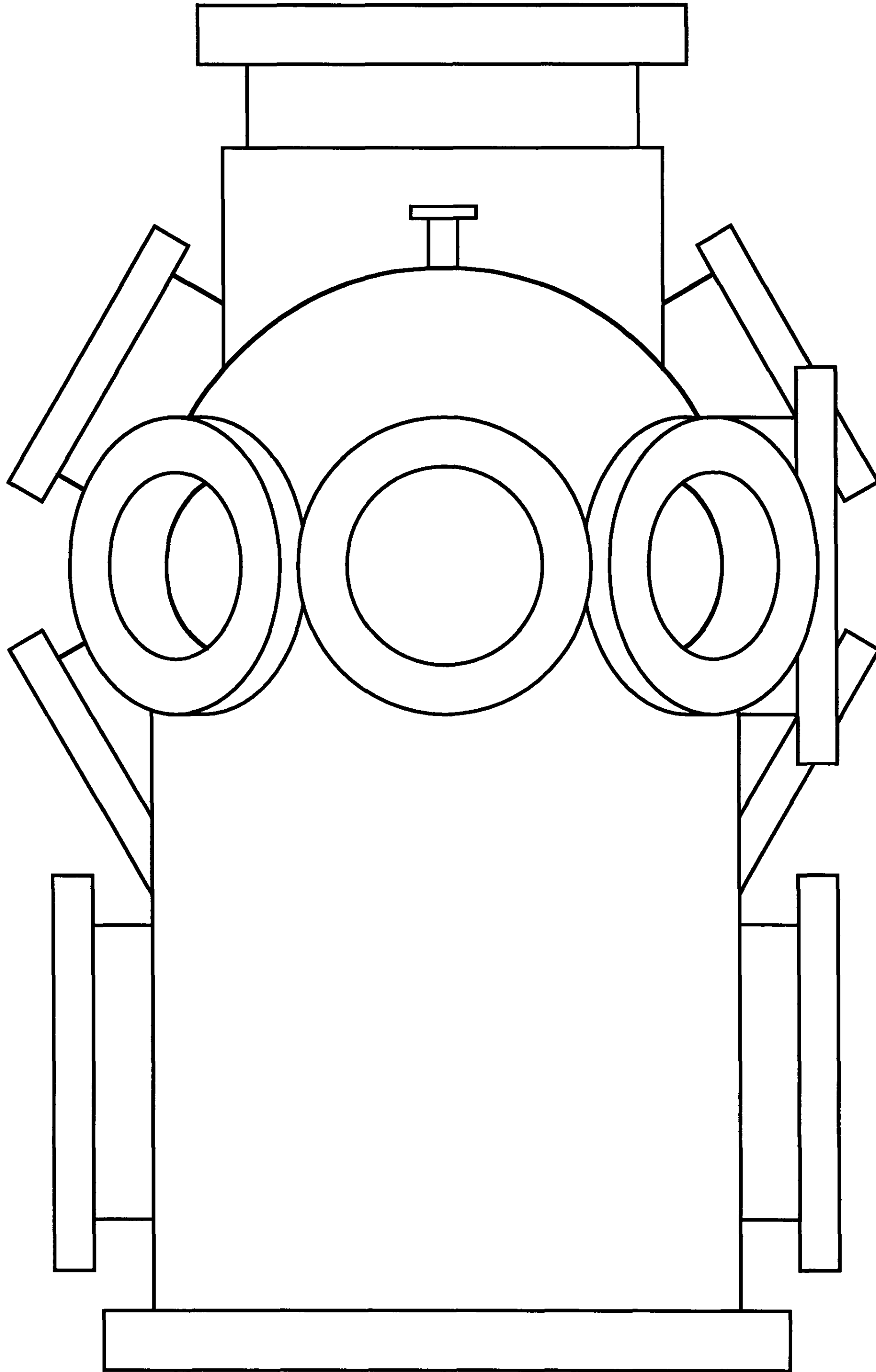

Figure A-6: Main (Etch) Chamber Rear View

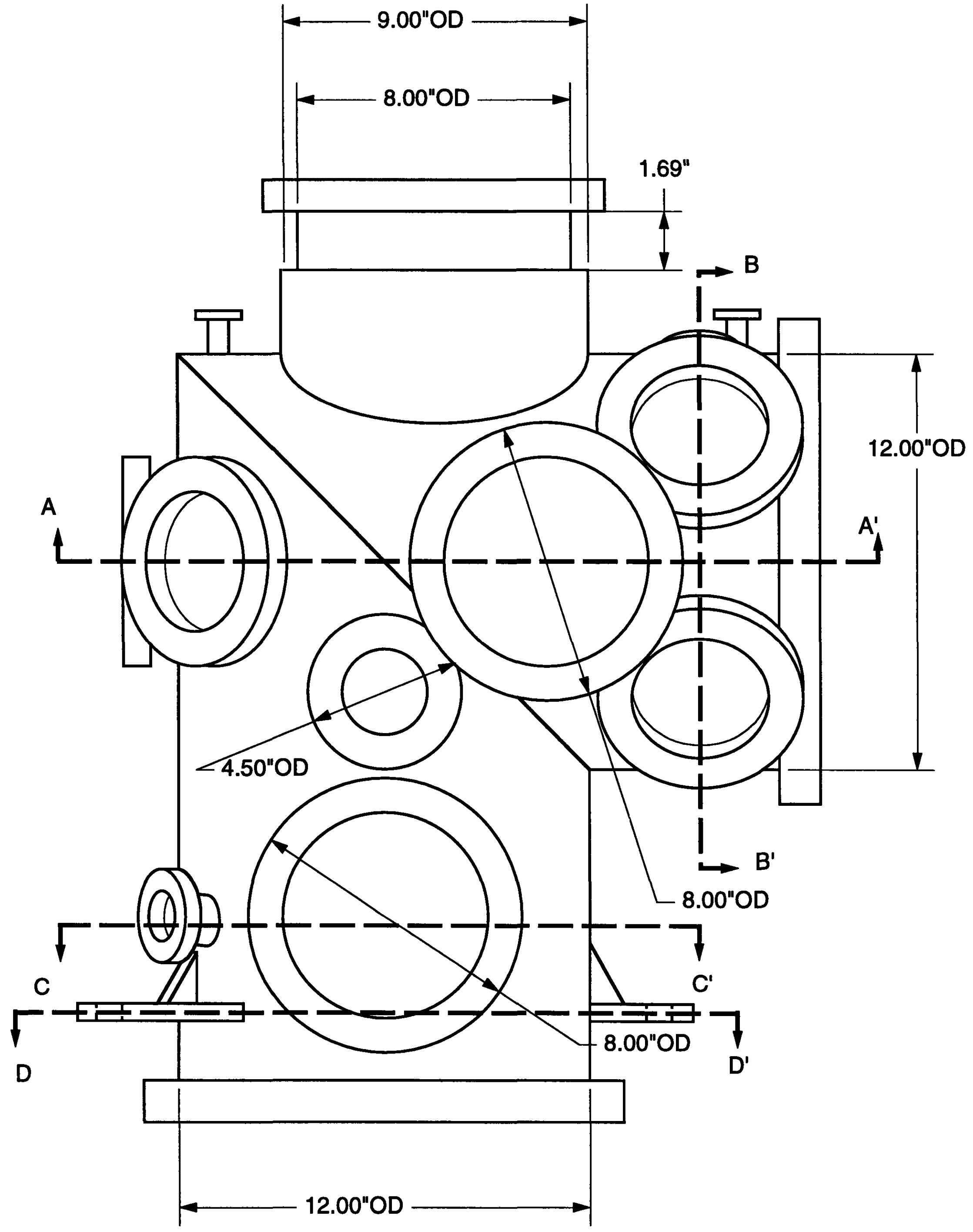

Figure A-7: Main (Etch) Chamber Side View

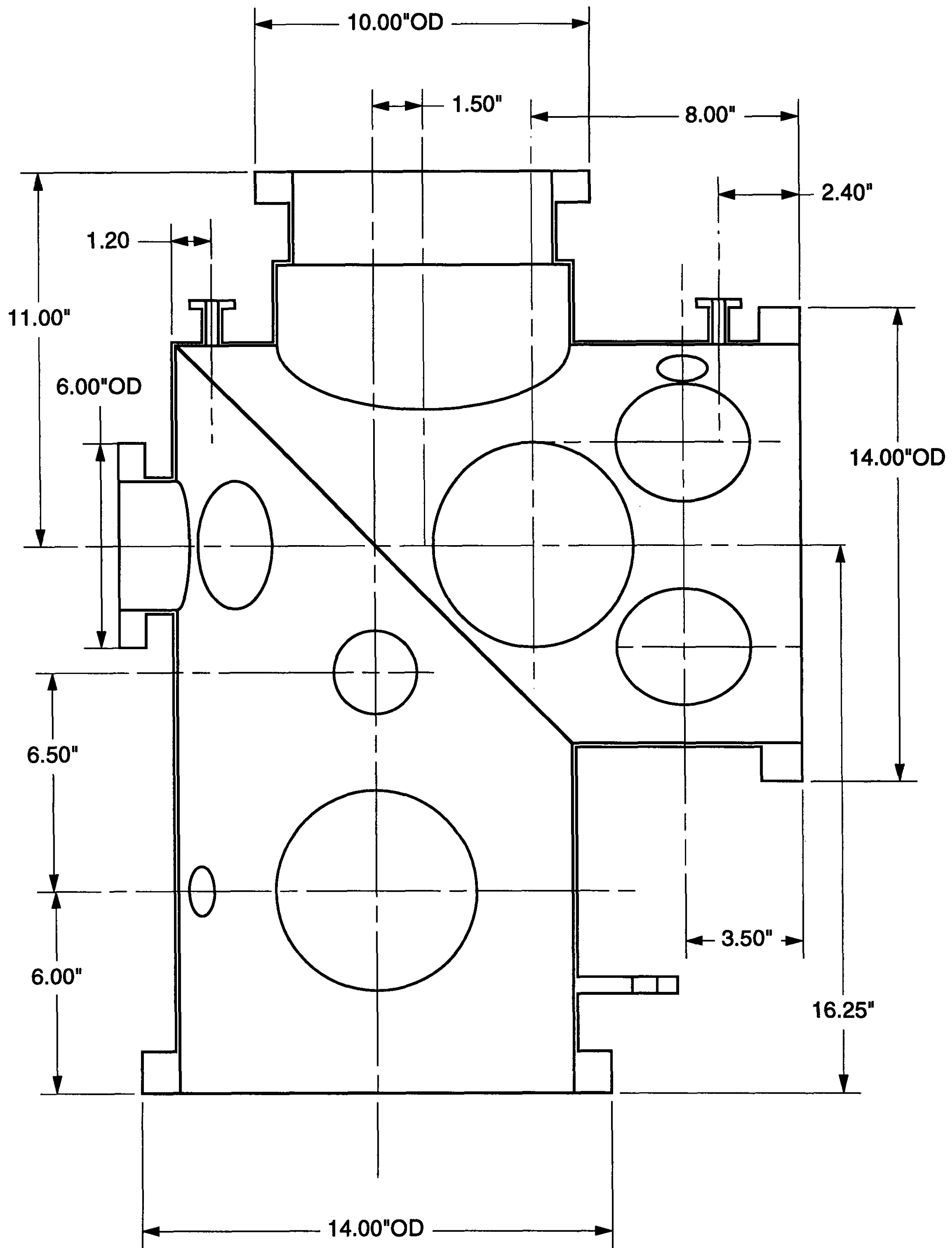

Figure A-8: Main (Etch) Chamber Vertical Cross Section

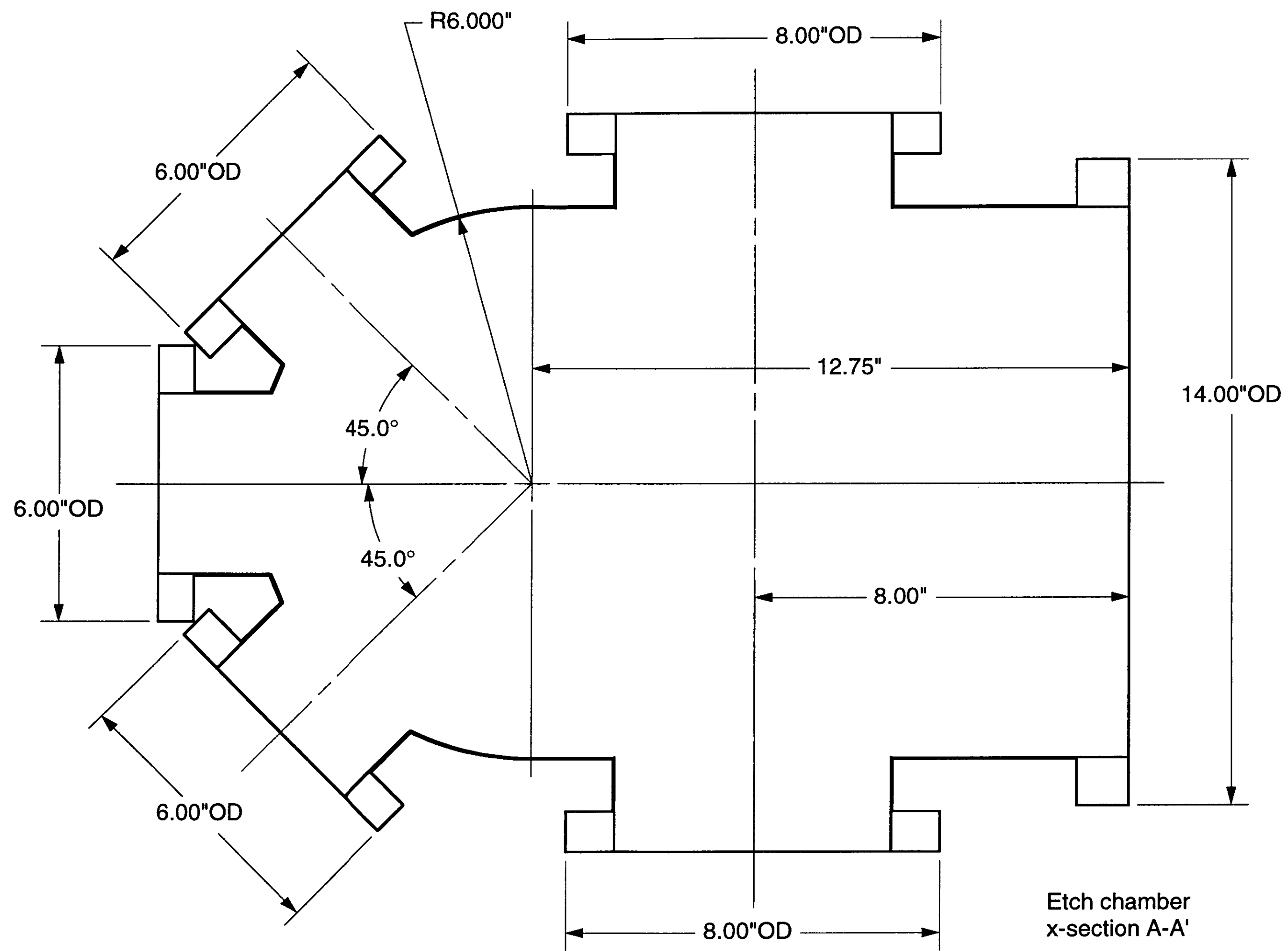

Figure A-9: Main (Etch) Chamber Cross Section A–A'

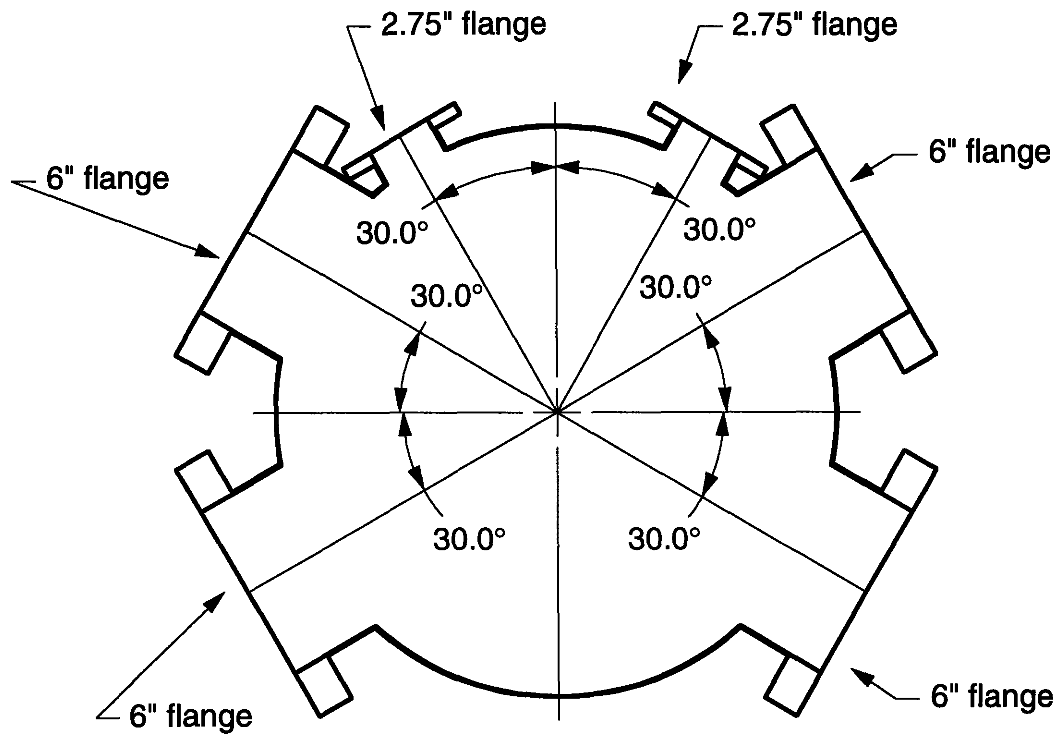

Main Chamber cross section B--B'

Figure A-10: Main (Etch) Chamber Cross Section B–B’

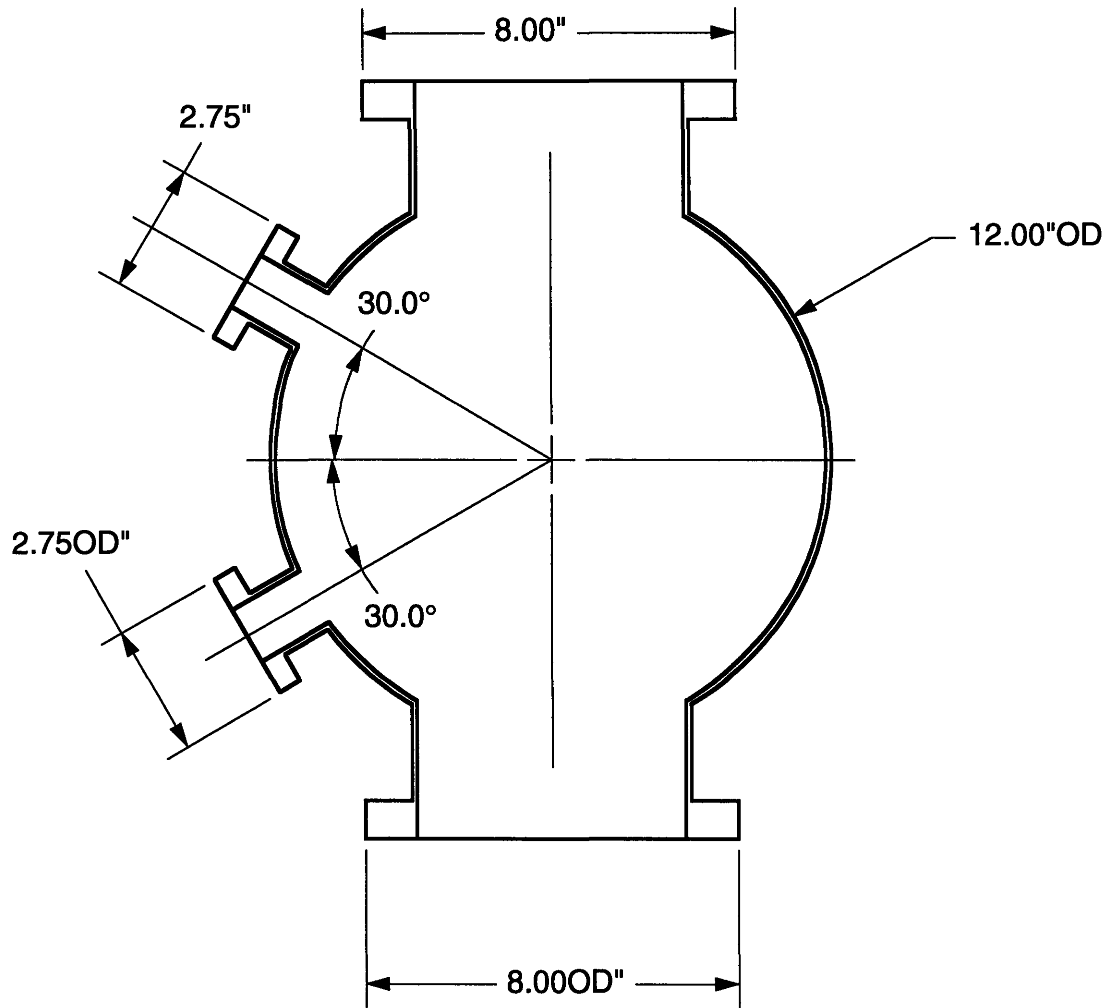

Etch Chamber Section C-C'
flange ports on trunk

Figure A-11: Main (Etch) Chamber Cross Section C–C'

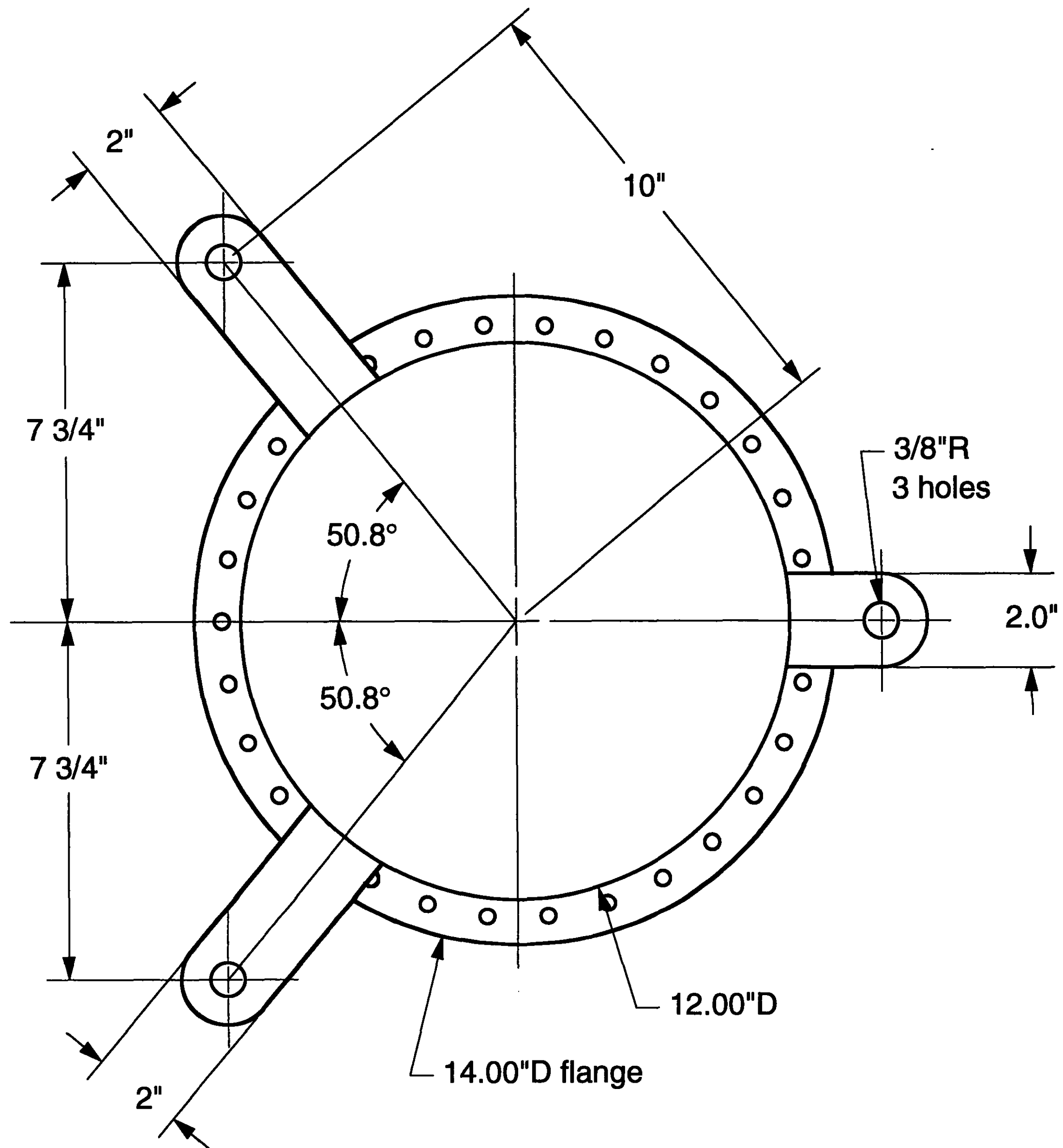

Figure A-12: Main (Etch) Chamber Cross Section D–D'

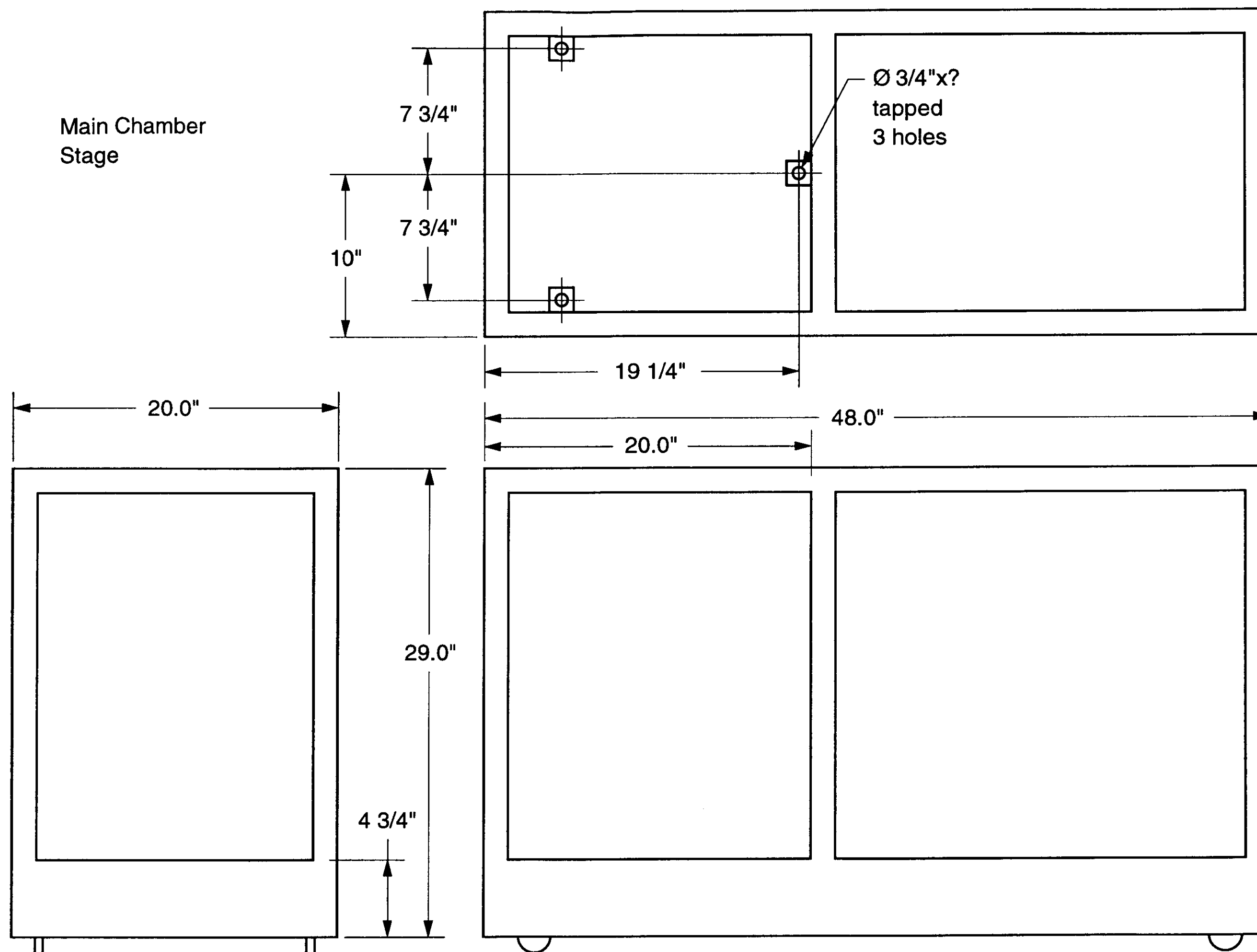

Figure A-13: Main (Etch) Chamber Support Stage

A.3 Source Chamber

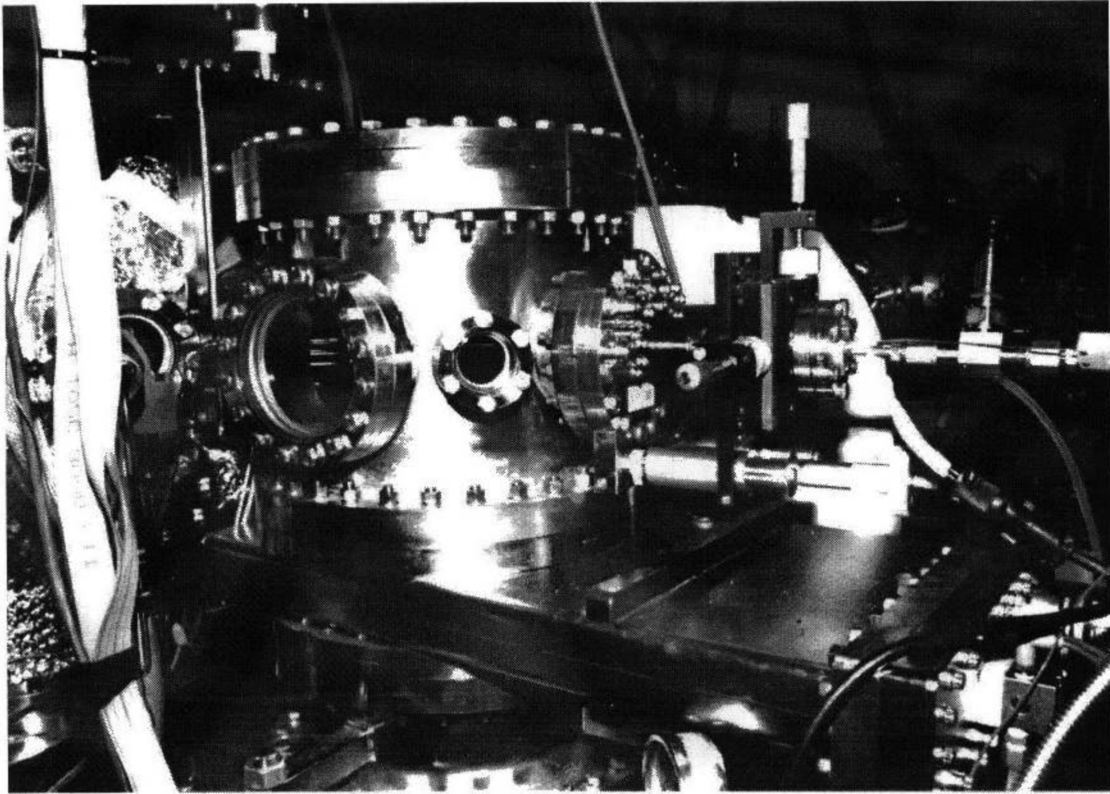

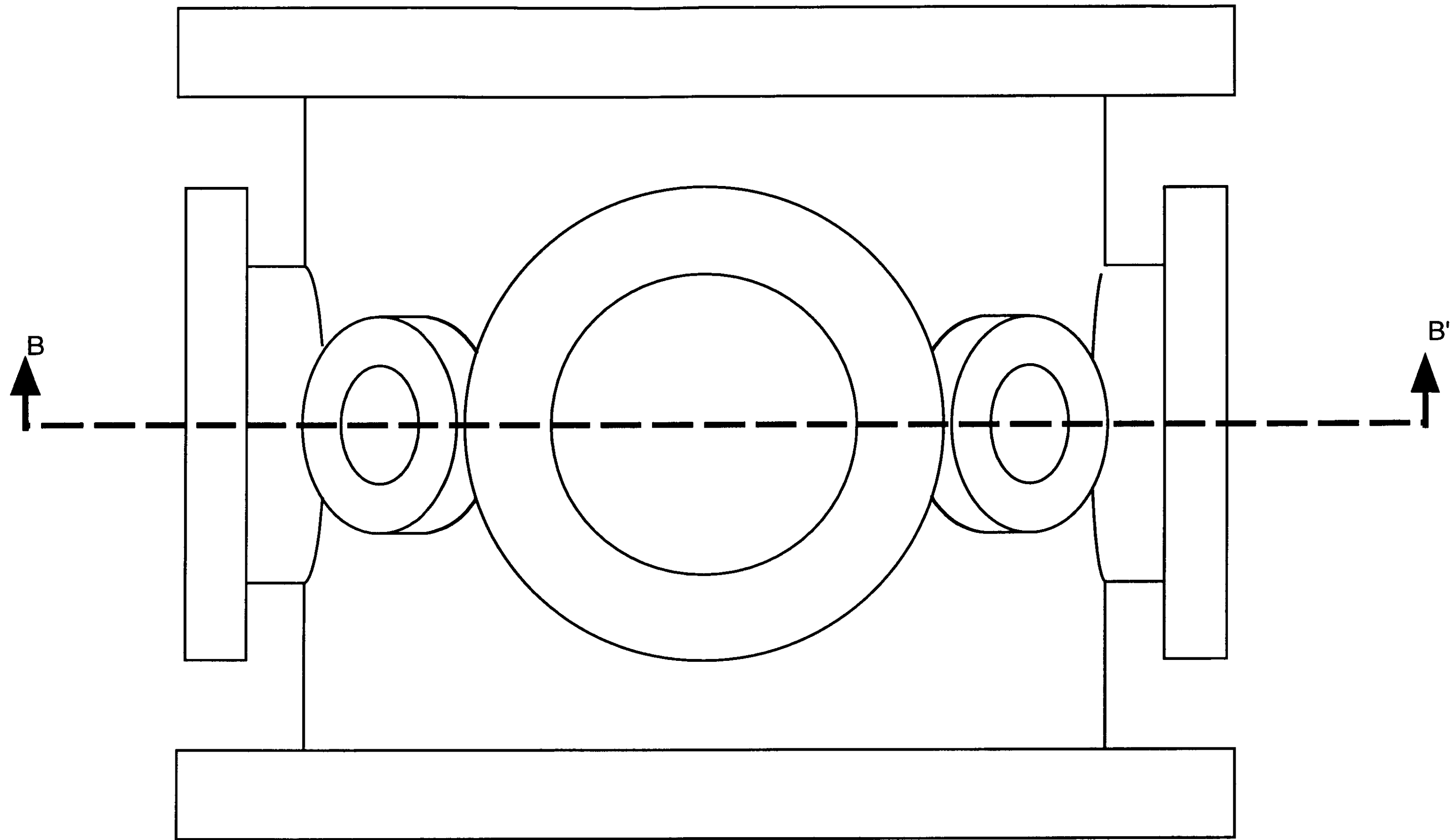

Figure A-14: Source Chamber Side View

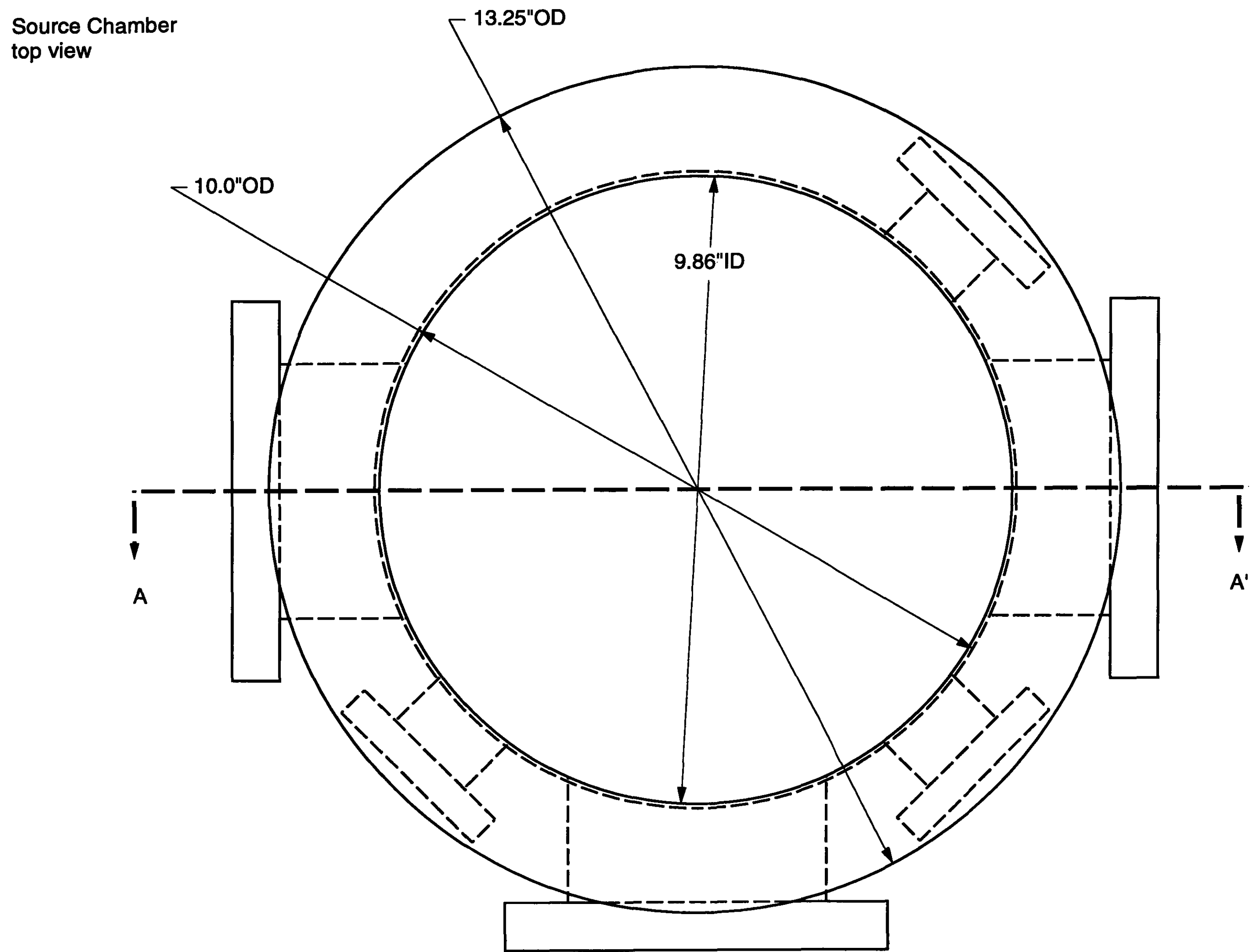

Figure A-15: Source Chamber Top View

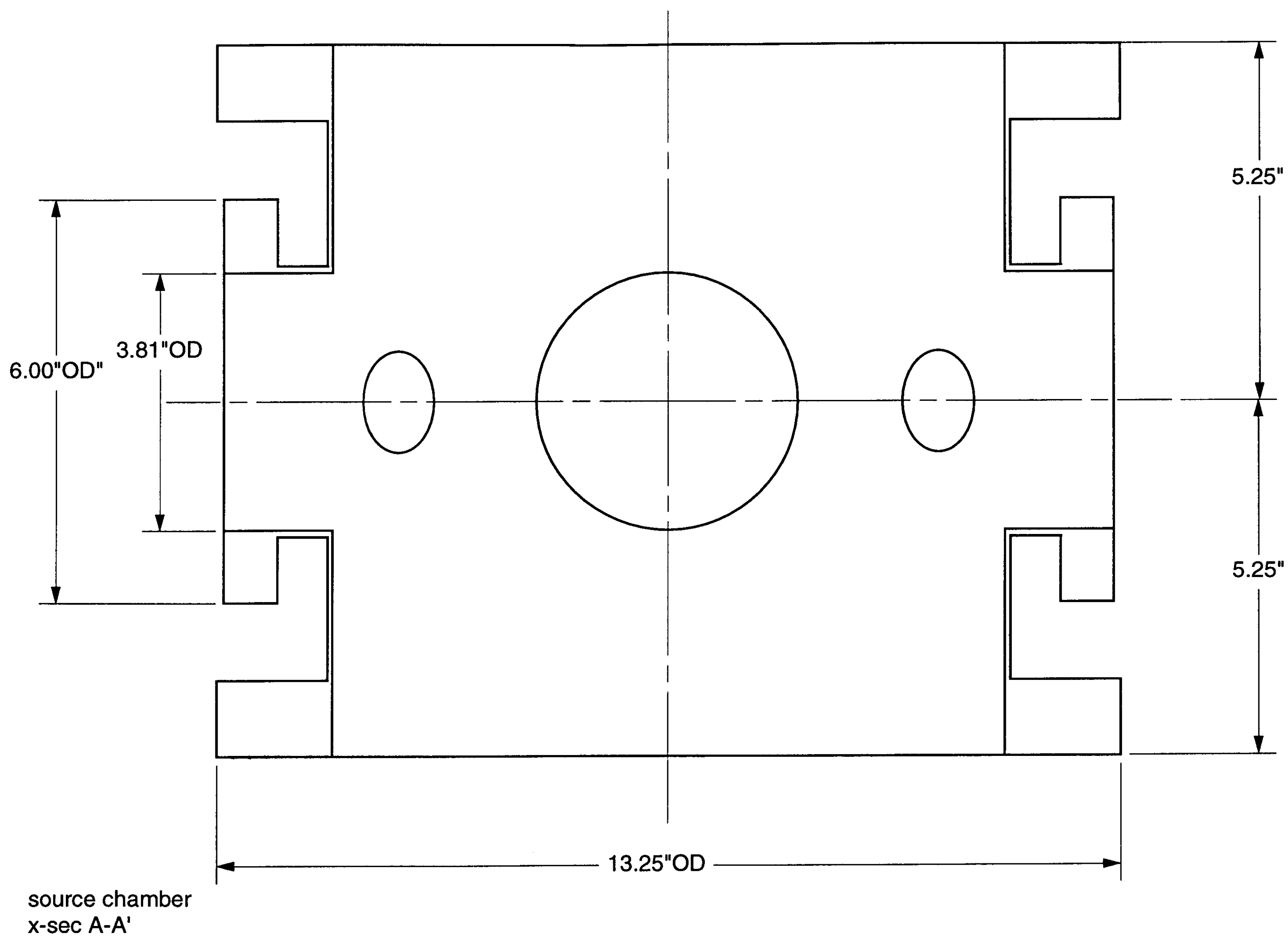

Figure A-16: Source Chamber Cross Section A–A'

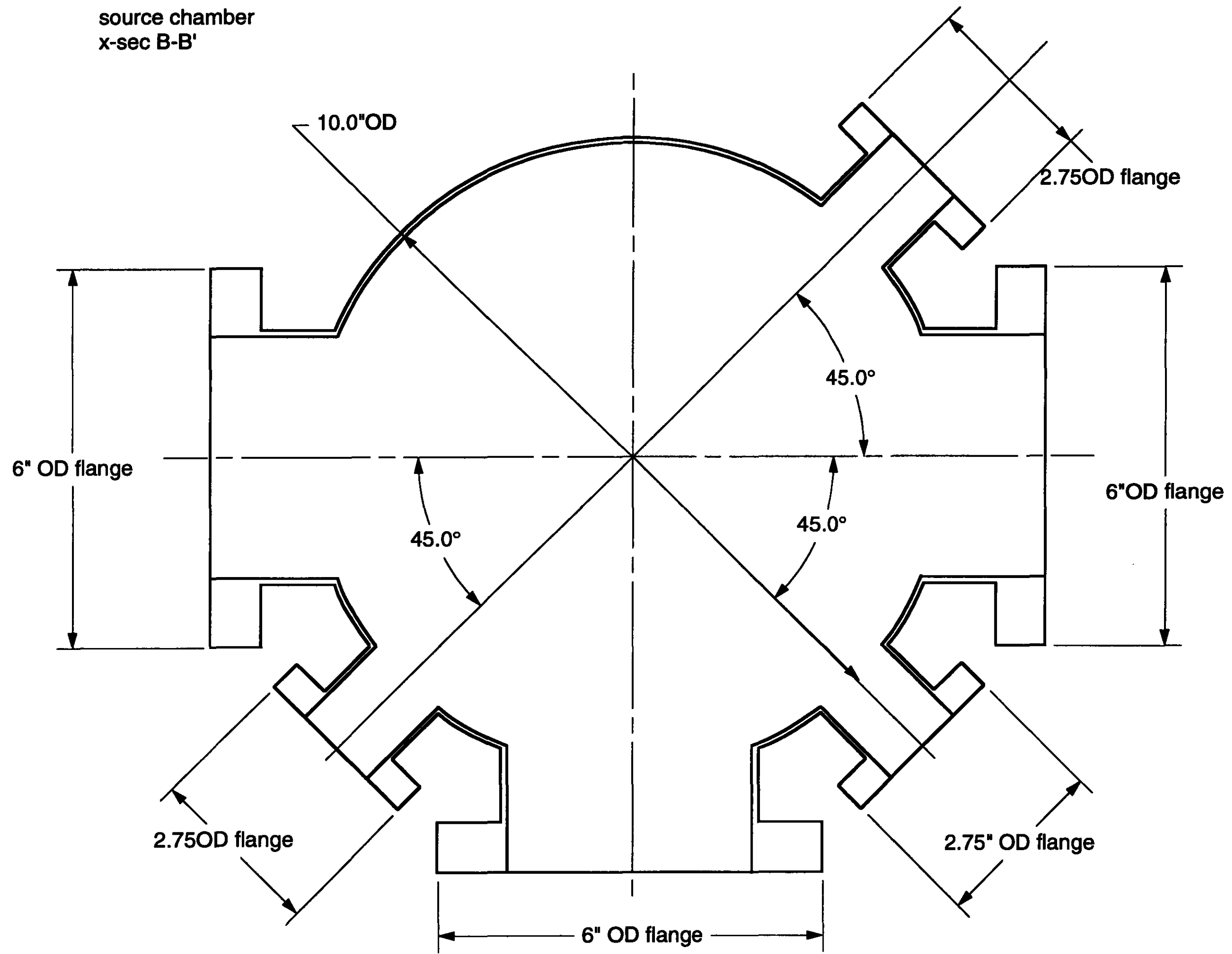

Figure A-17: Source Chamber Cross Section B–B'

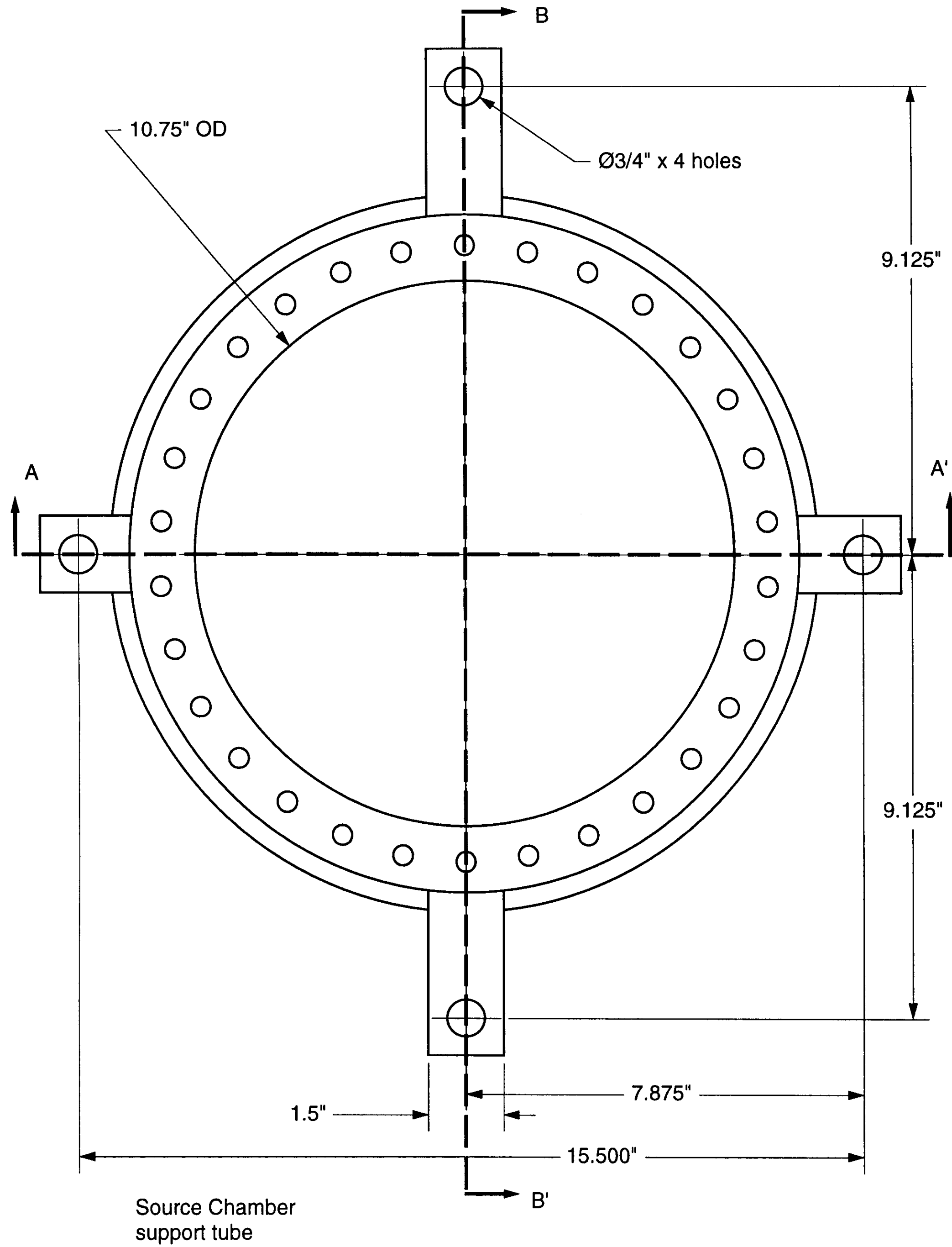

Figure A-18: Source Chamber Support Collar

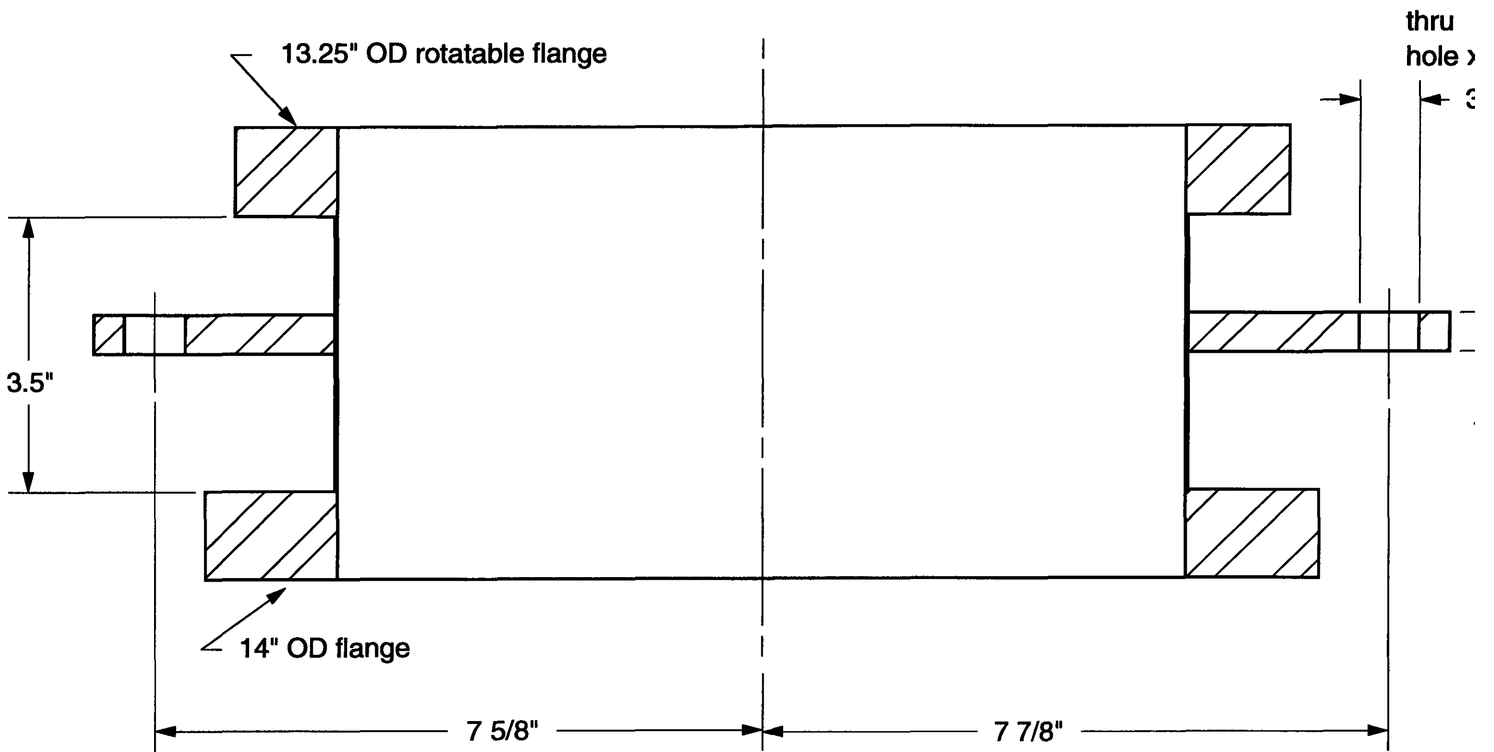

Figure A-19: Source Chamber Support Collar Cross Section A–A'

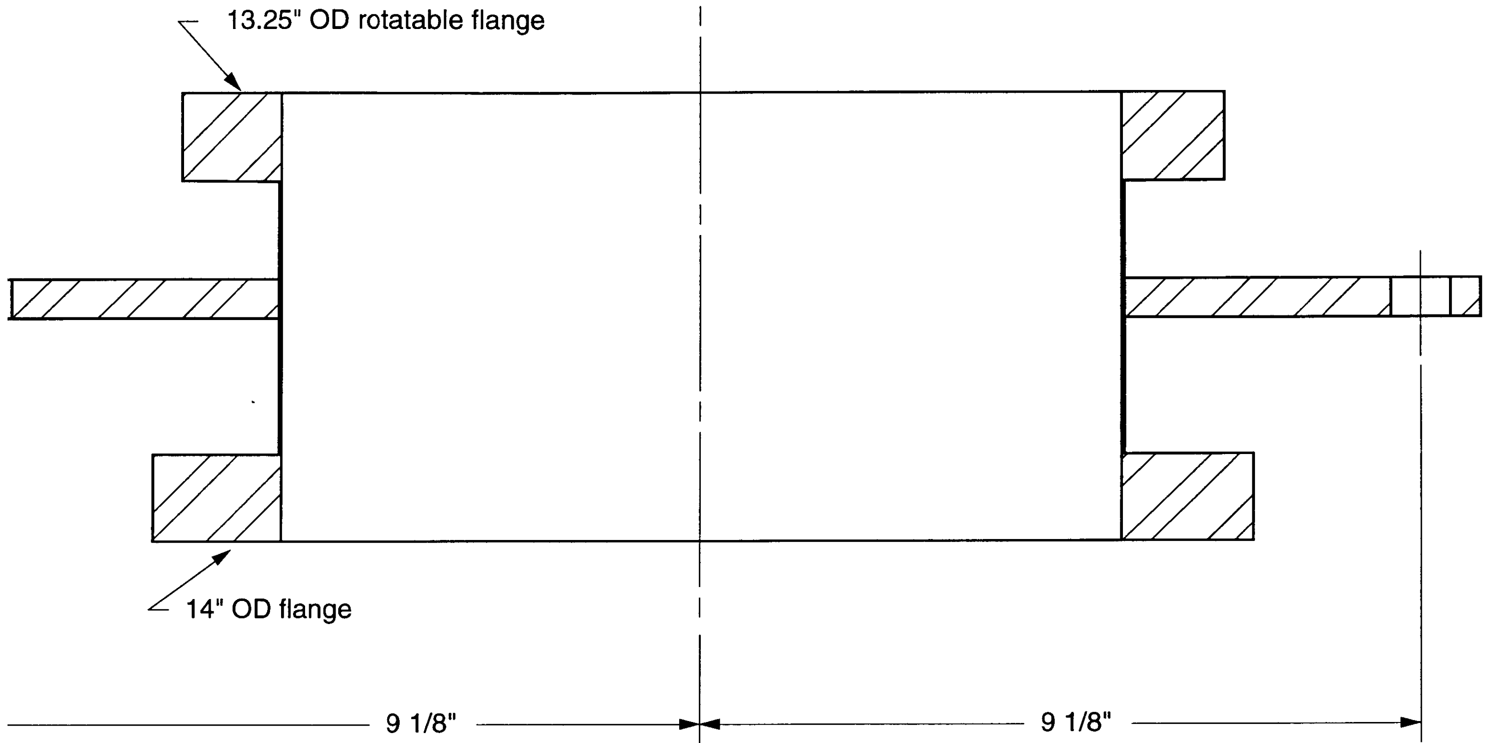

Figure A-20: Source Chamber Support Collar Cross Section B–B’

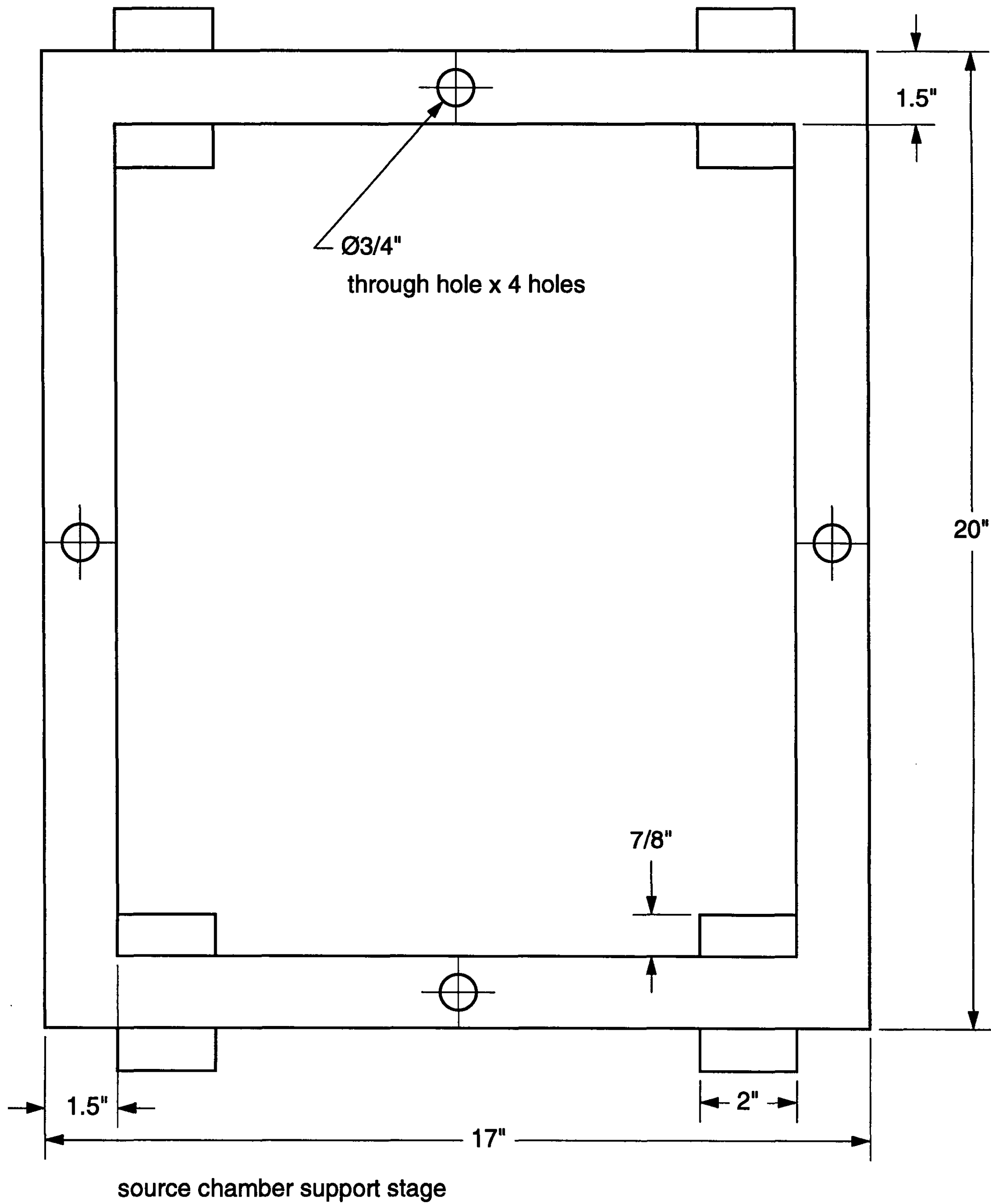

Figure A-21: Source Chamber Movable Stage Top View

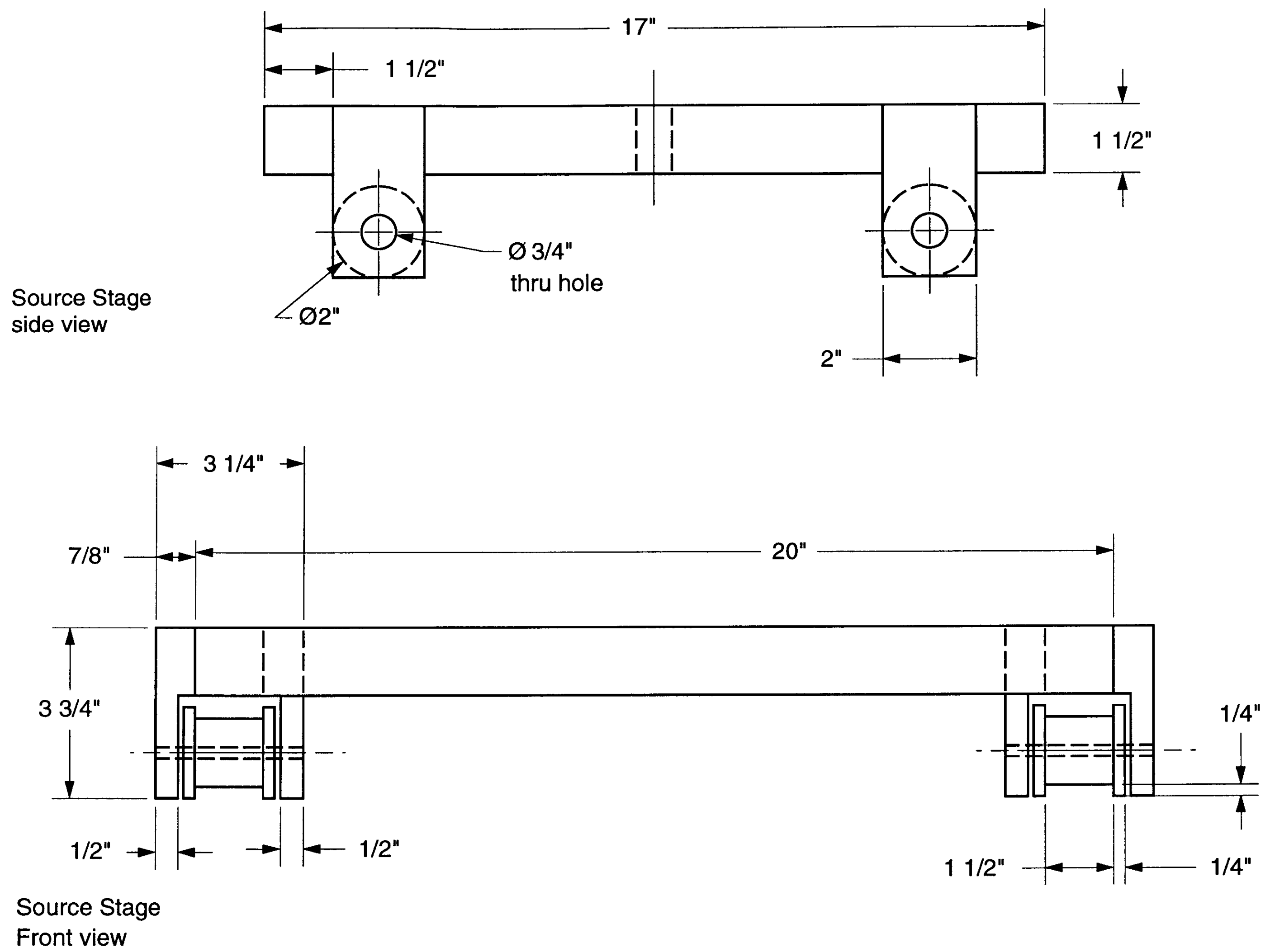

Figure A-22: Source Chamber Movable Stage Side Views

A.4 Transfer Tube

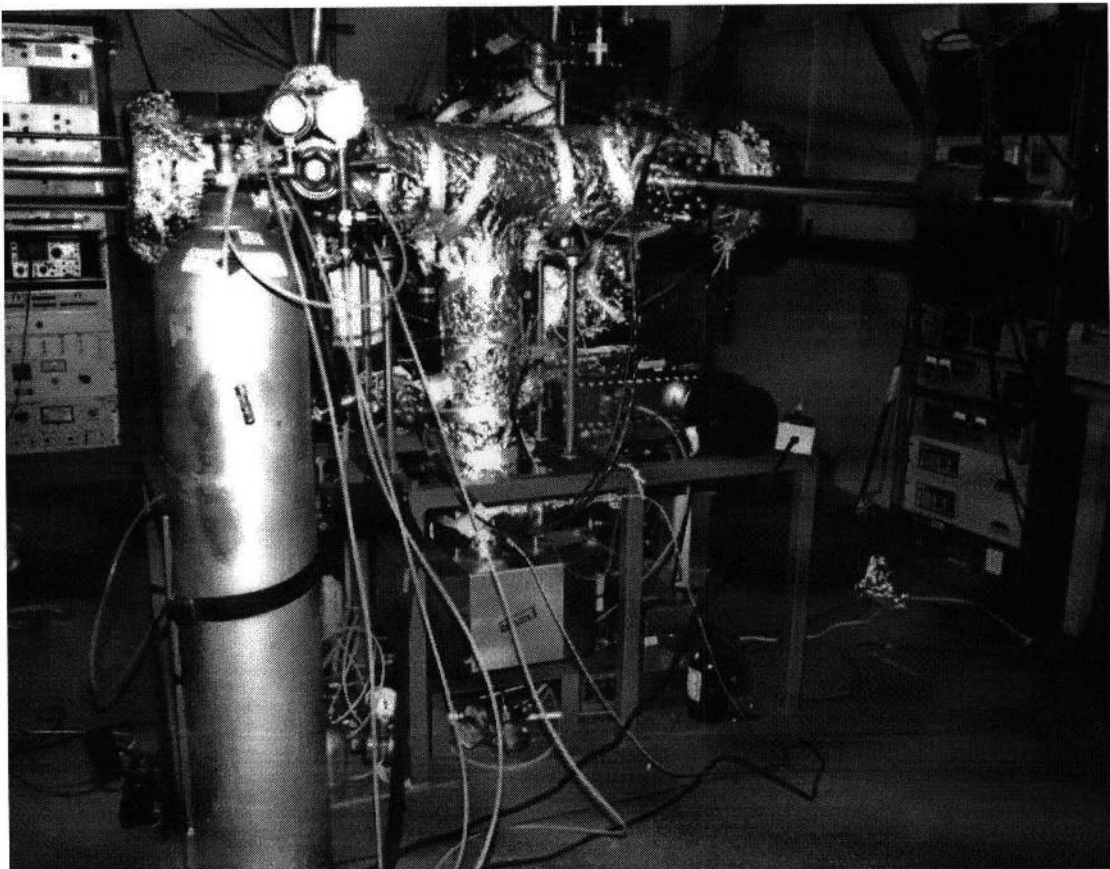

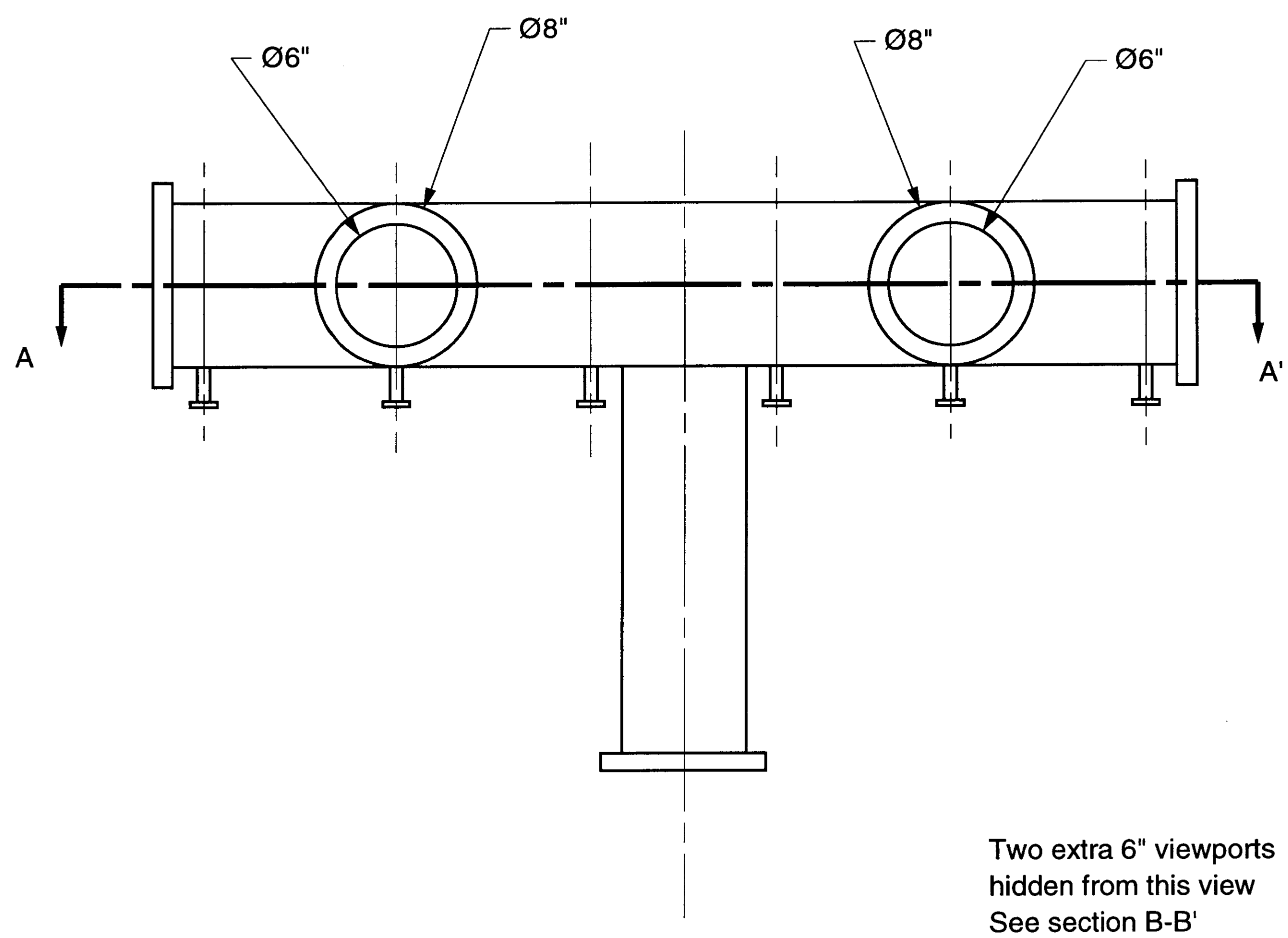

Figure A-23: Transfer Tube Chamber-side Side View

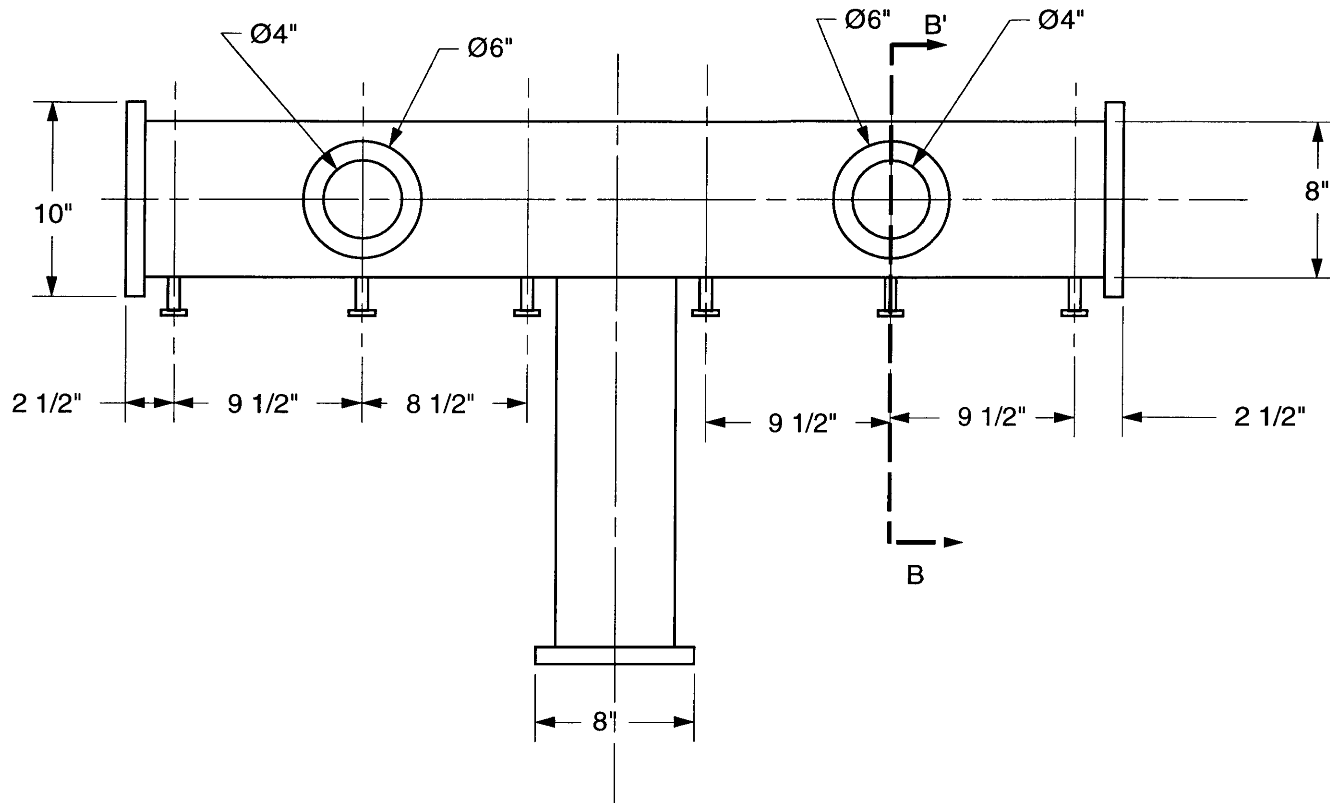

Transfer Tube
Transfer rod-Side View

Two extra 6" viewports
hidden from this view
See section B-B'

Figure A-24: Transfer Tube Transfer Rod-Side Side View

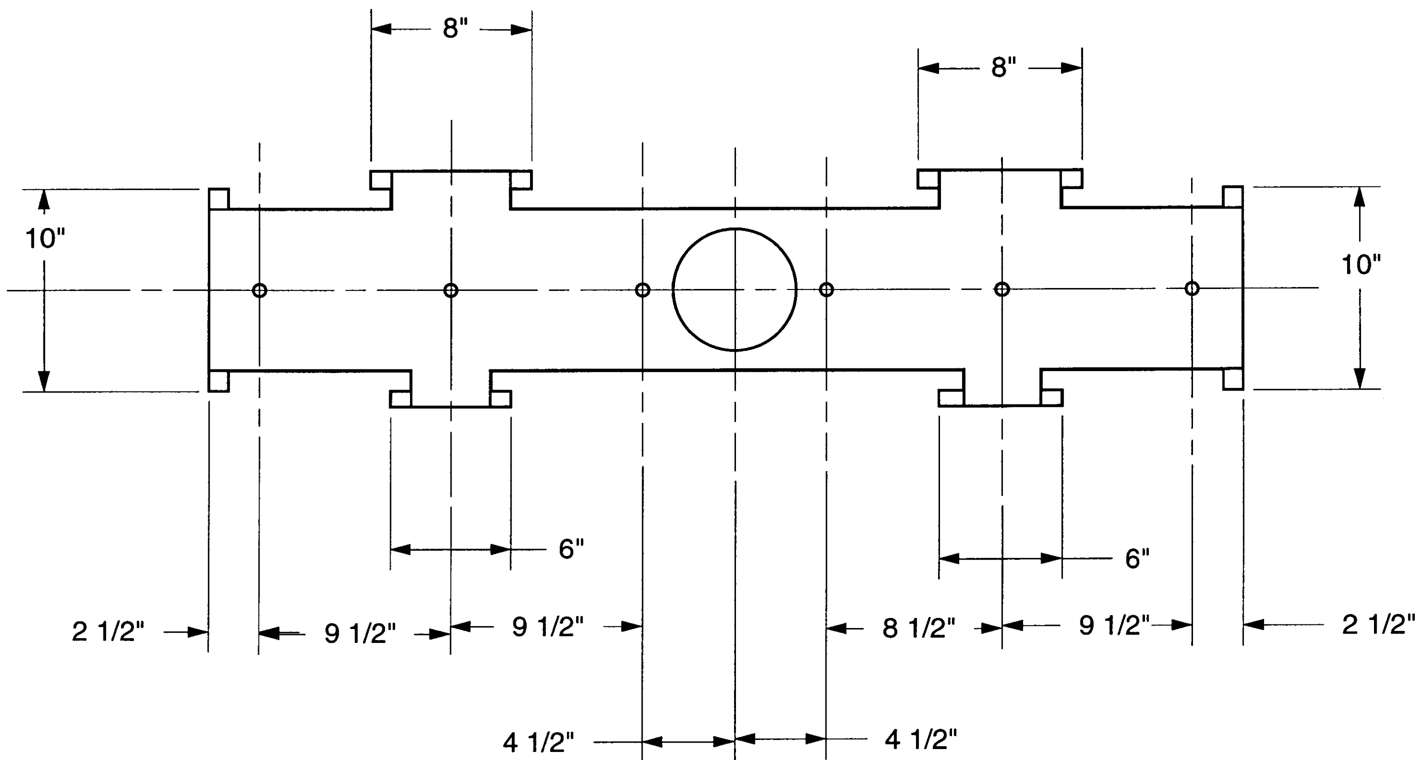

Figure A-25: Transfer Tube Cross Section A–A’

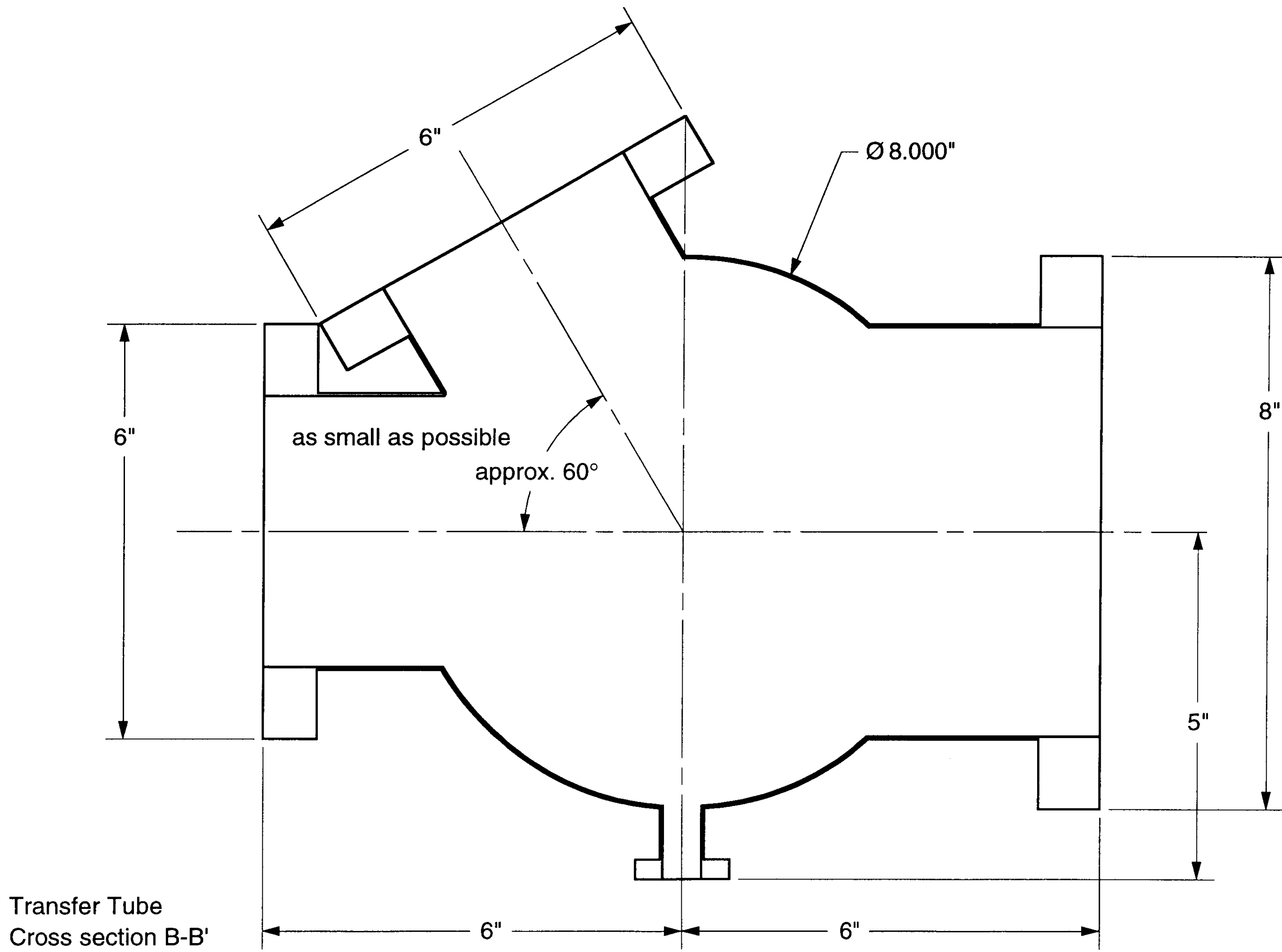

Figure A-26: Transfer Tube Cross Section B–B'

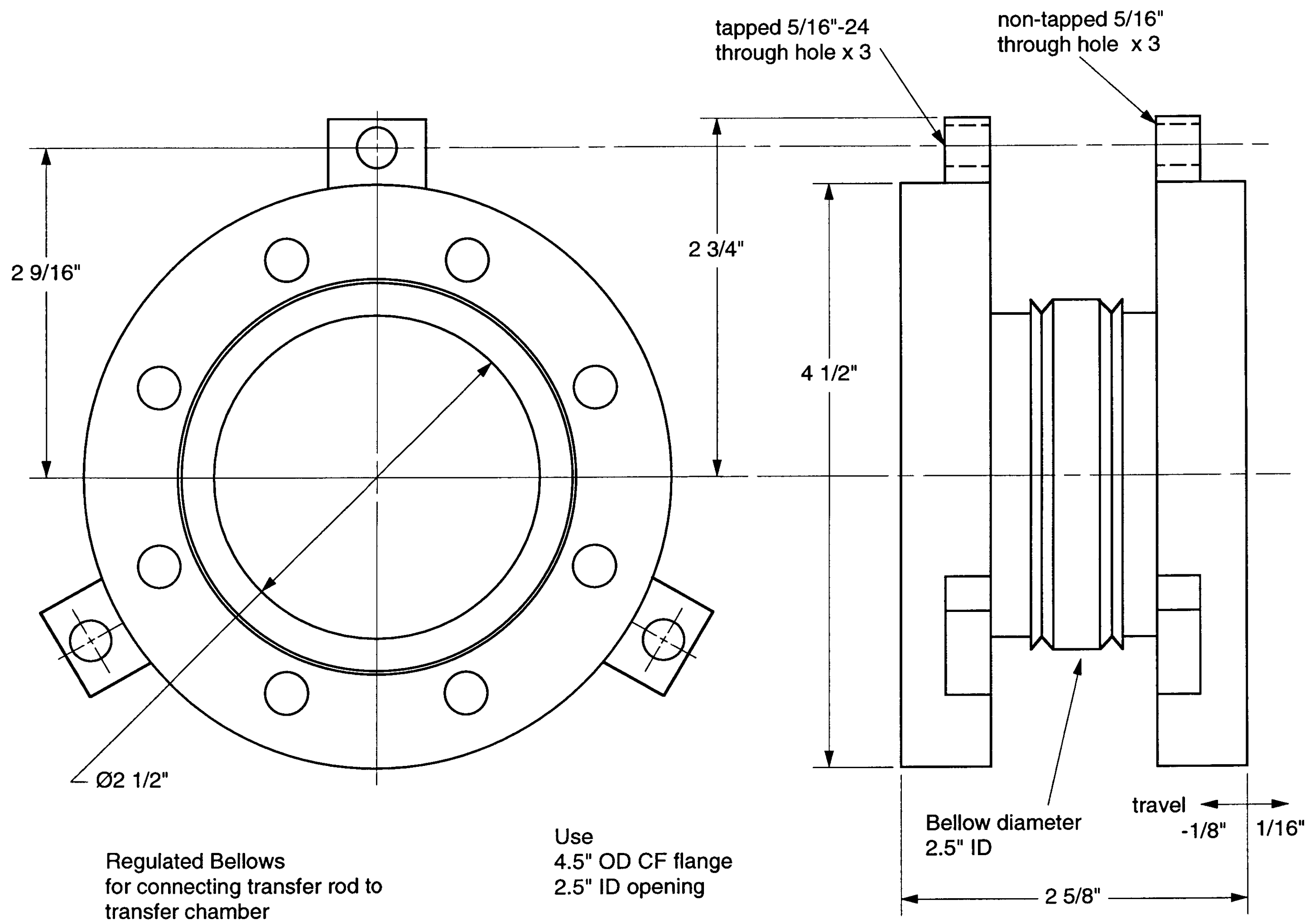

Figure A-27: Regulated bellows flange to connect the transfer rod

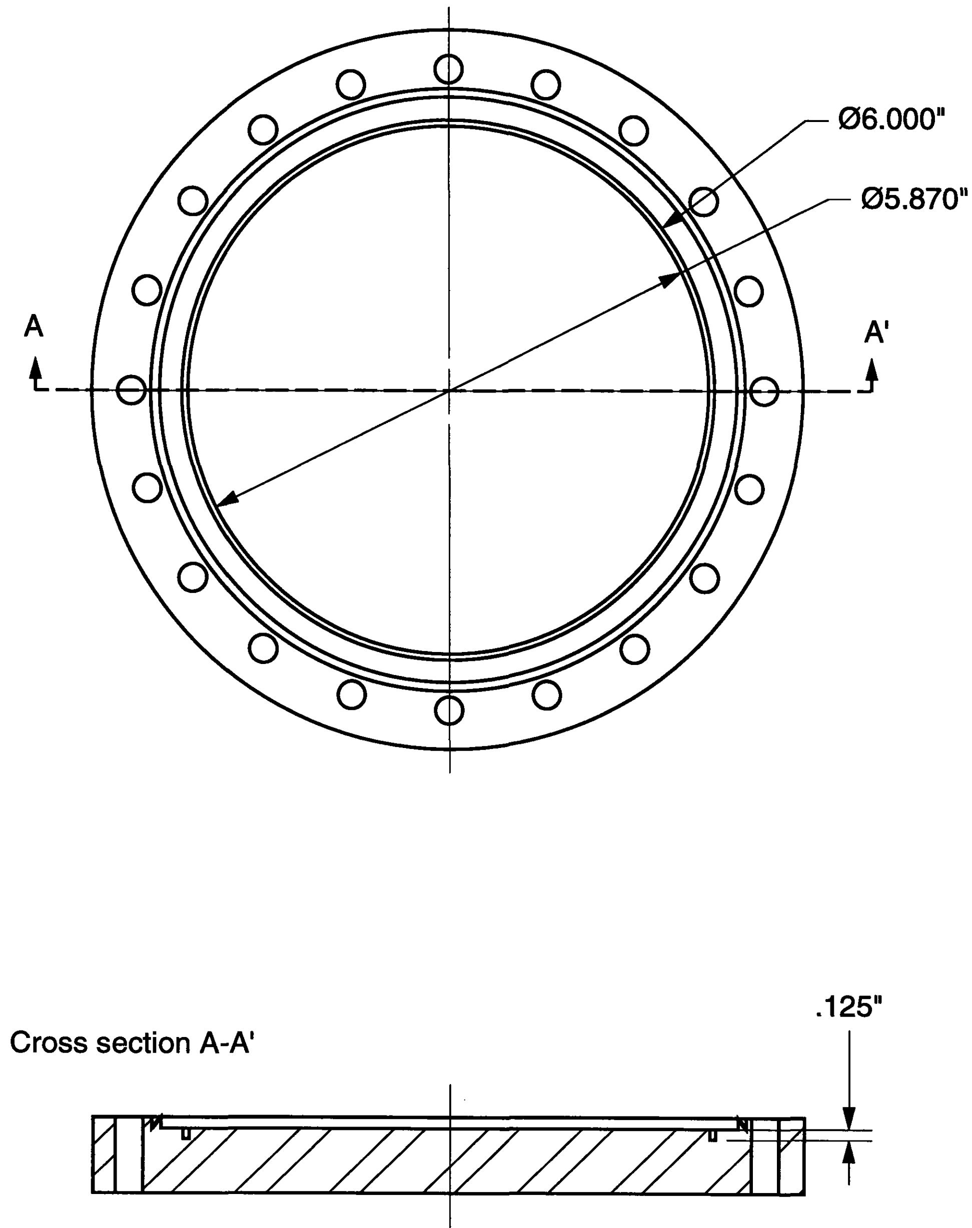

Figure A-28: Modified 8 Inch Conflat Blank Flange: used as the temporary load lock door

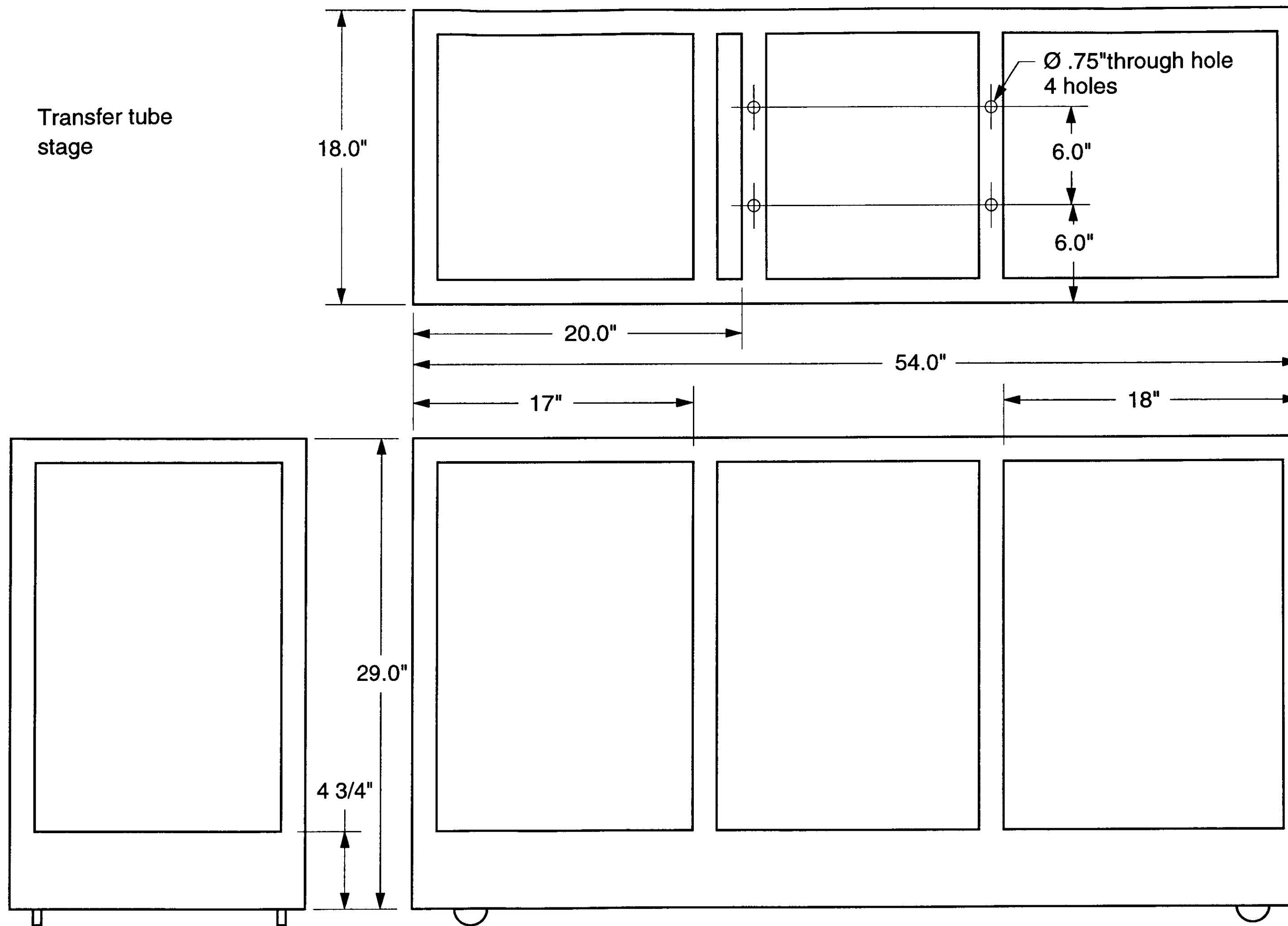

Figure A-29: Transfer Tube Stage

A.5 Nozzle

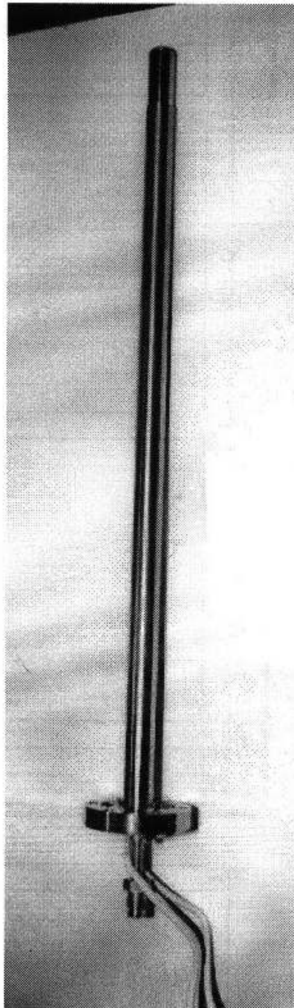

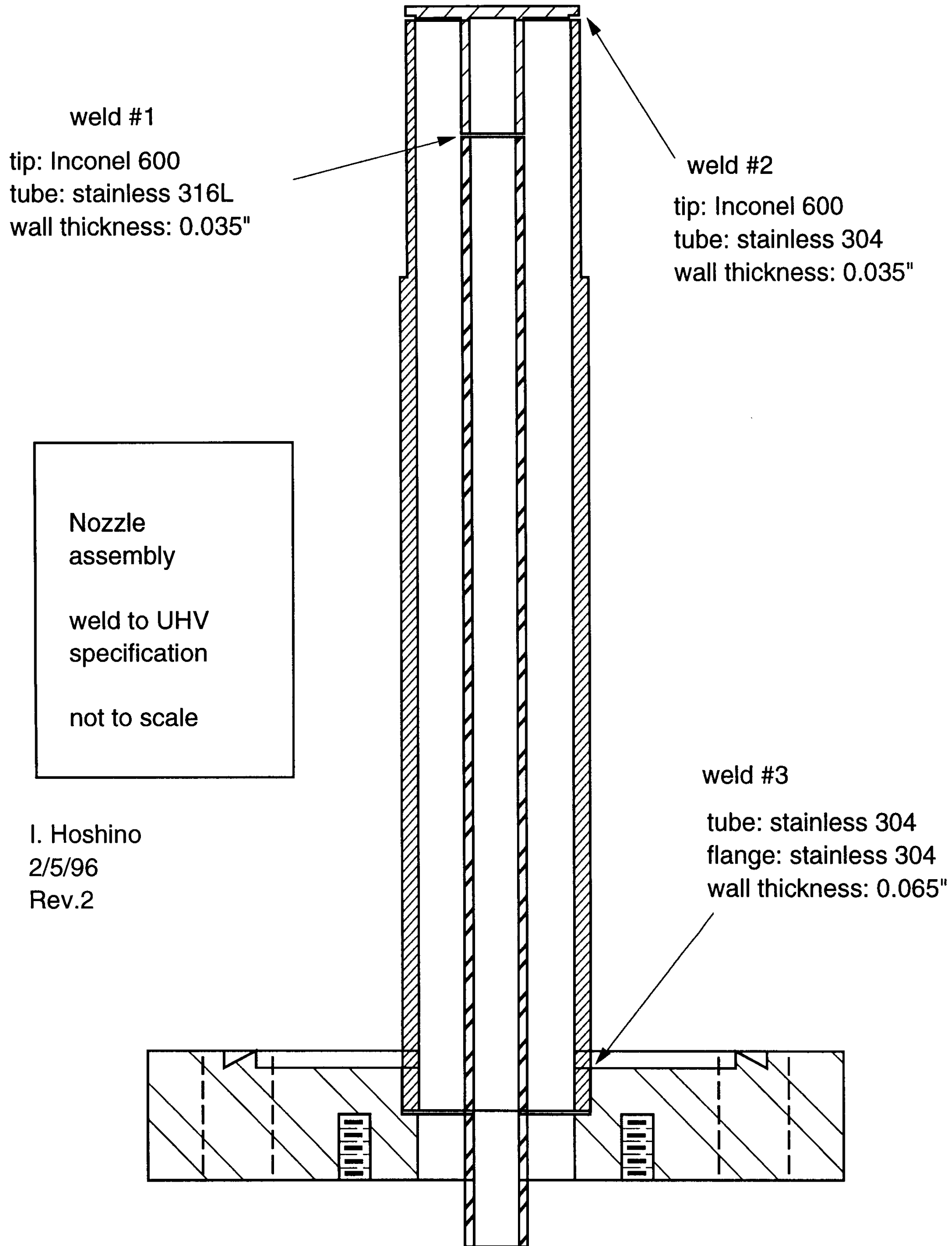

Figure A-30: Nozzle Assembly

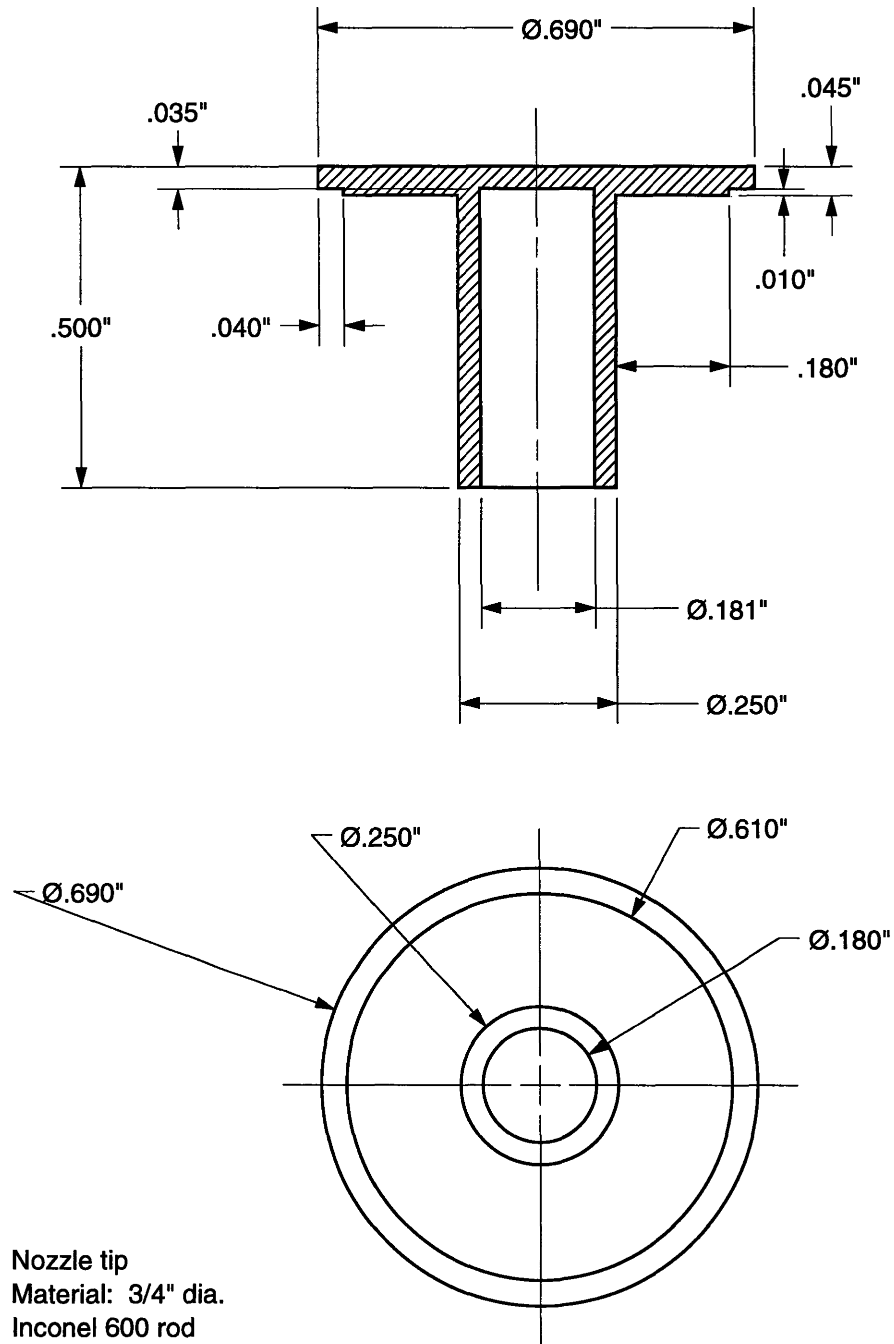

Figure A-31: Nozzle Tip

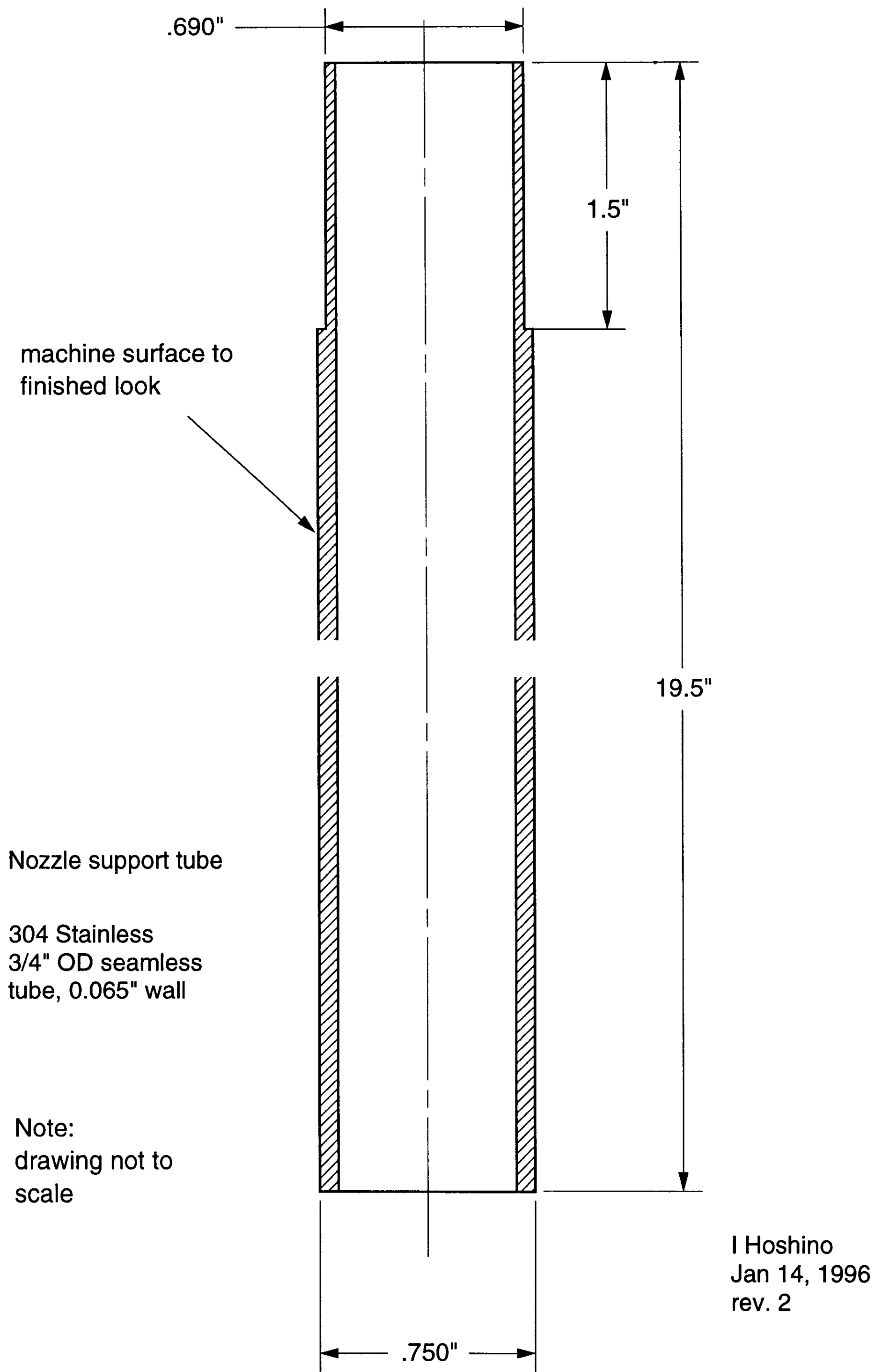

Figure A-32: Nozzle Support Tubing

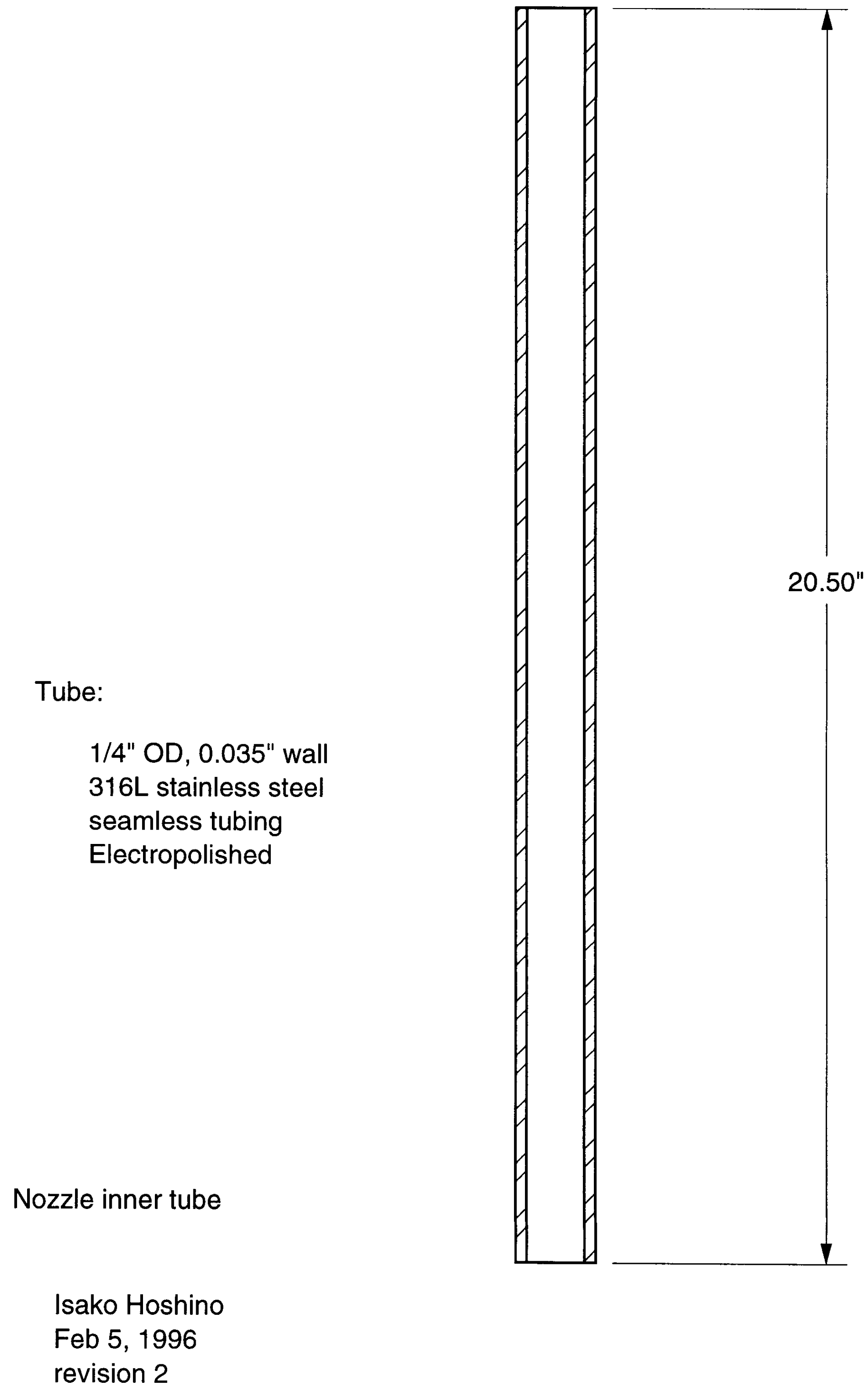

Figure A-33: Nozzle Inner Tubing

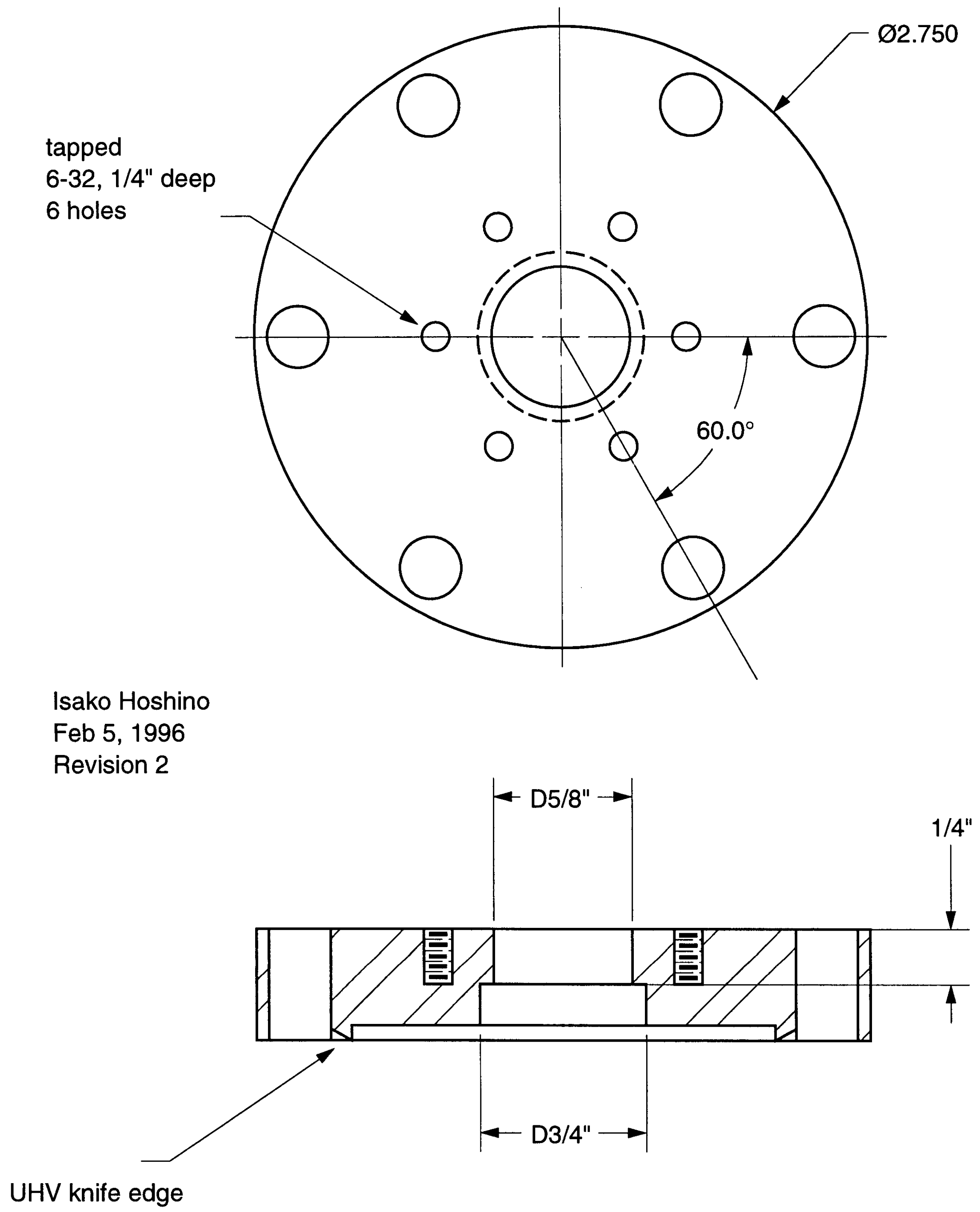

Figure A-34: Nozzle Mounting Flange

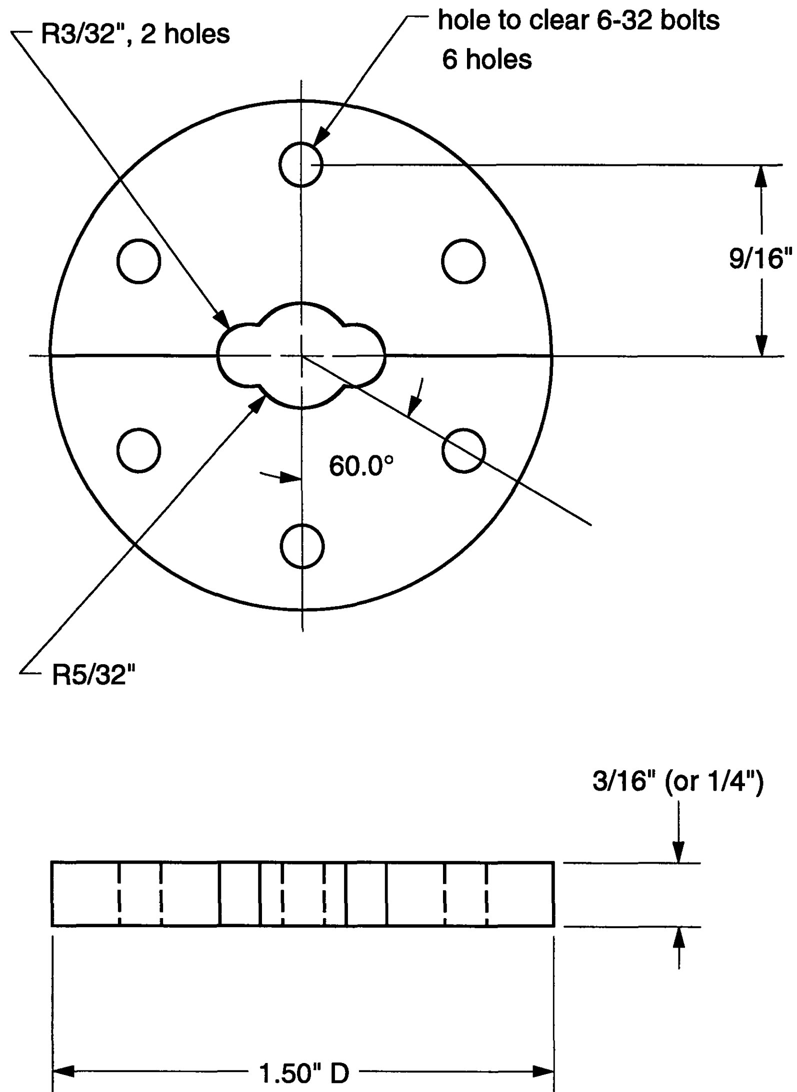

Scale 2x

Material: Aluminum

2 pieces (two semicircles. drawn together just for the sake of drawing simplicity)

Nozzle tube centering ring

Isako Hoshino
Jan. 11, 1995
revision 2

Figure A-35: Nozzle Centering Ring

A.6 Miscellaneous Schematics

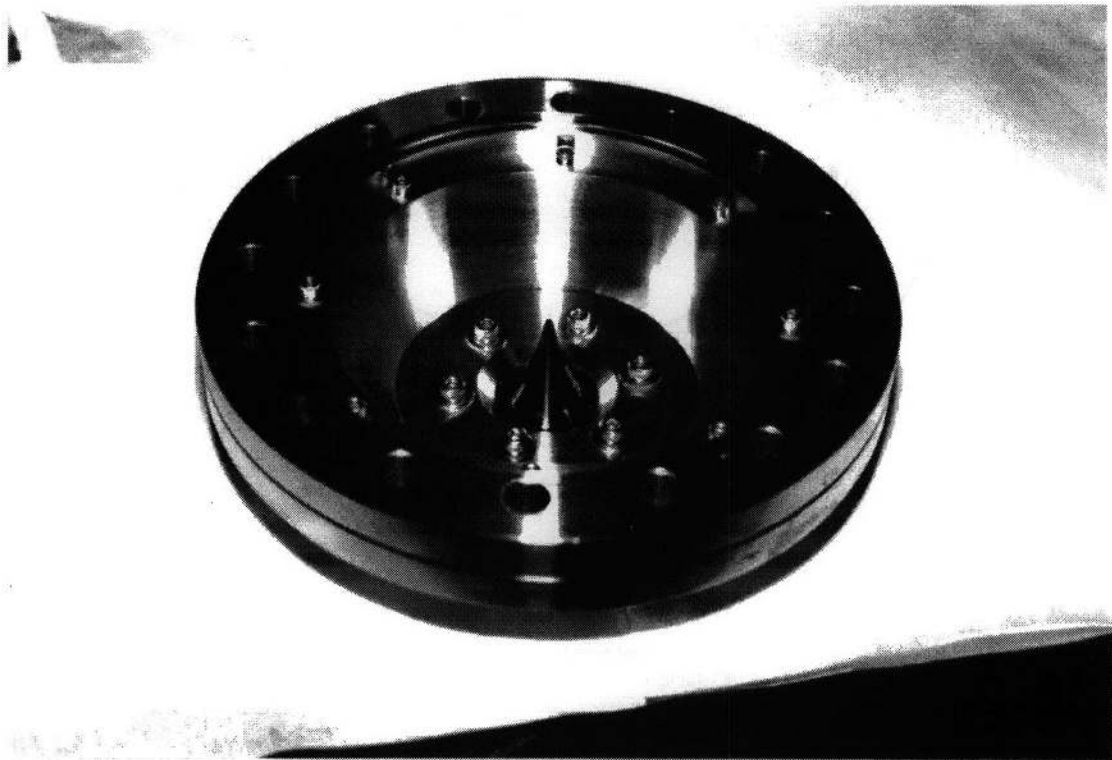

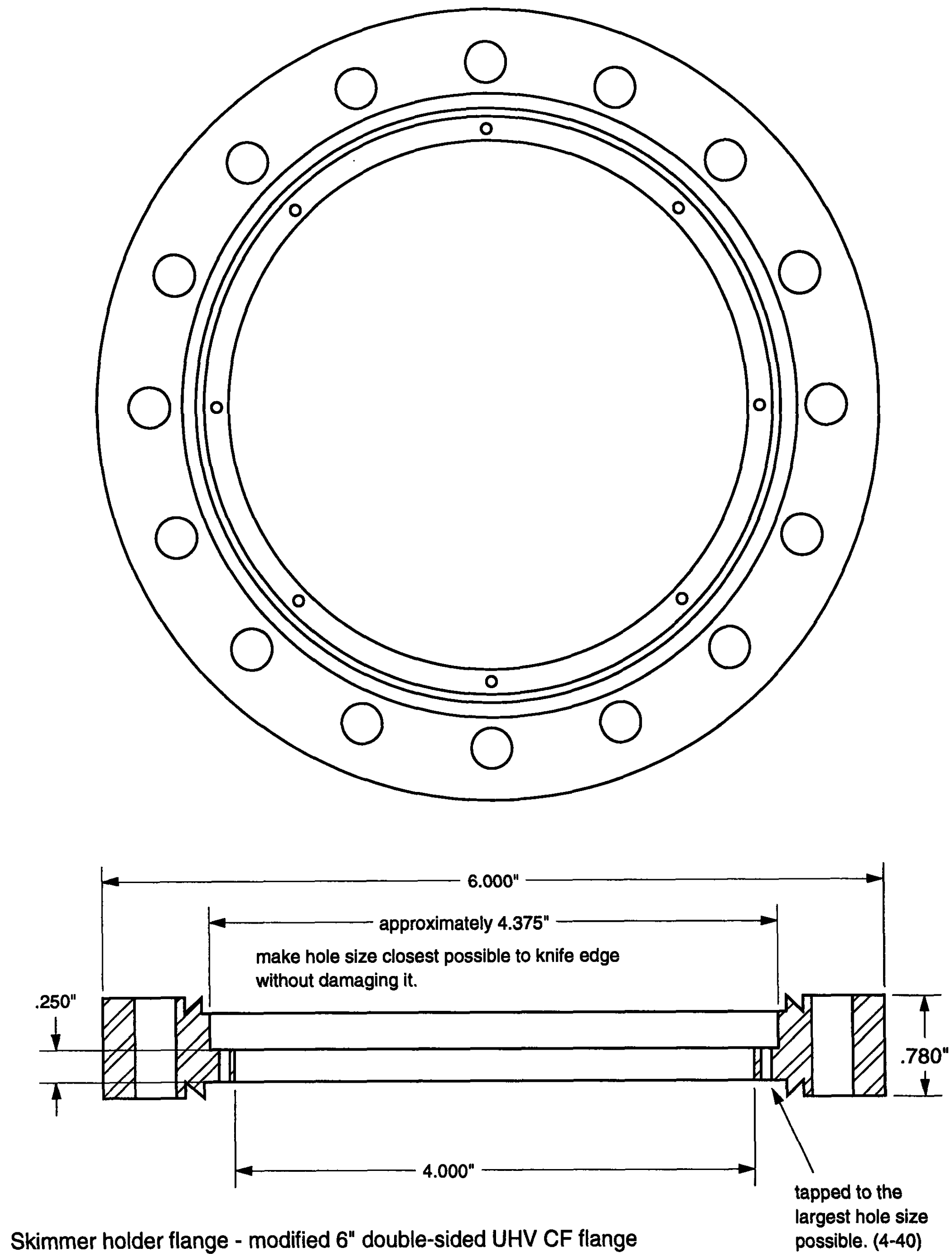

Figure A-36: Skimmer Holder Flange

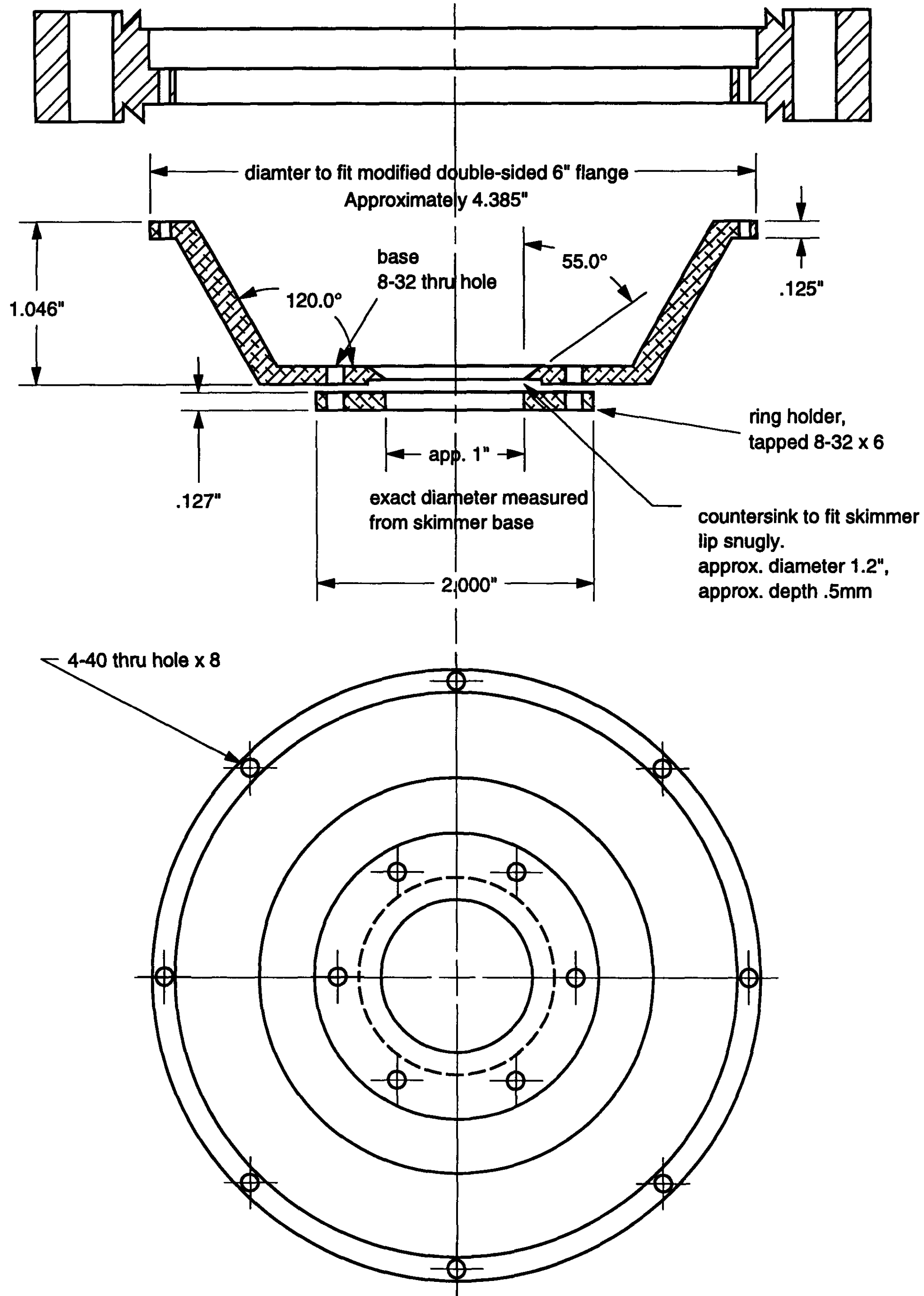

Figure A-37: Skimmer Holder

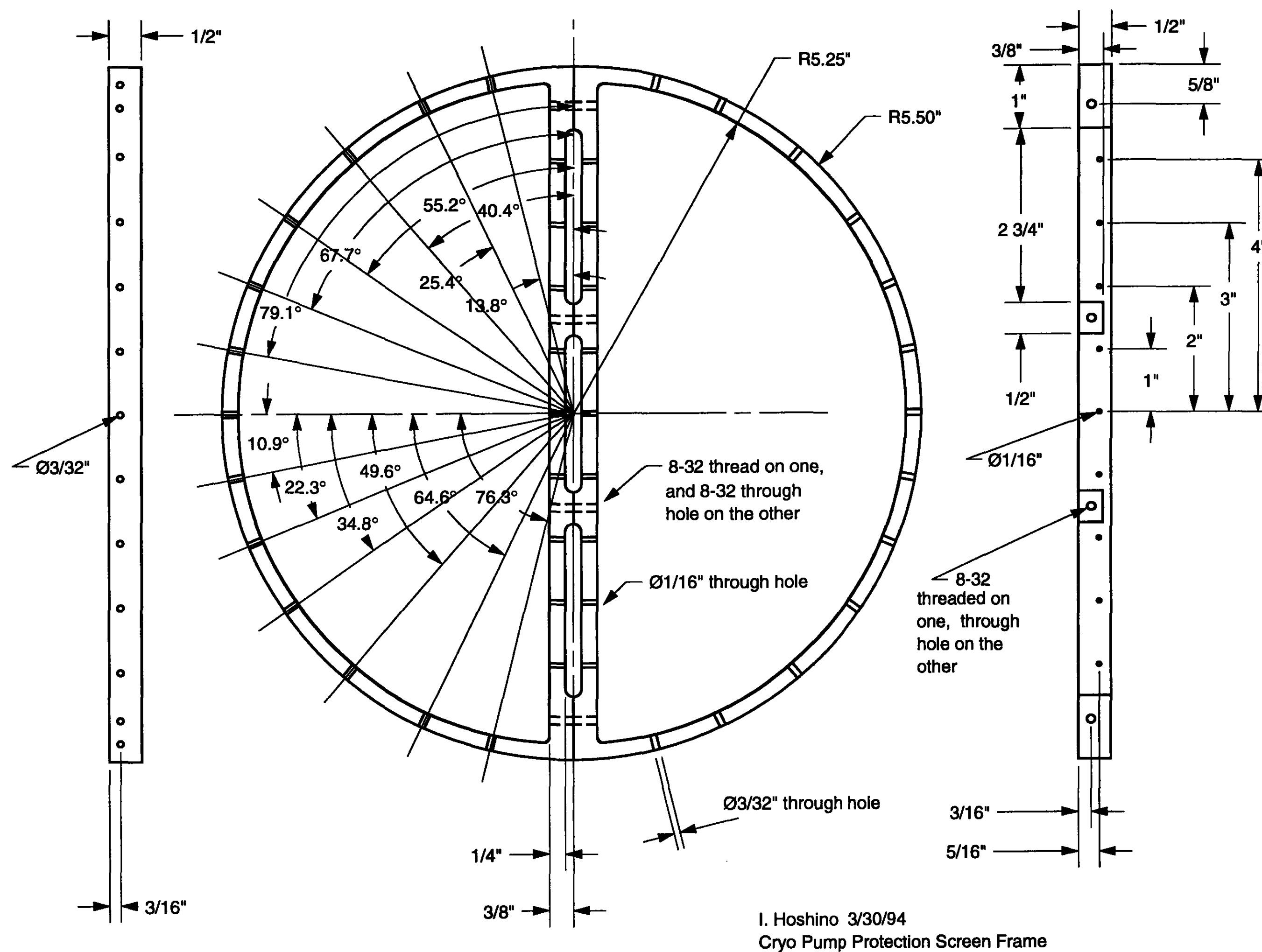

Figure A-38: Cryo Protection Screen

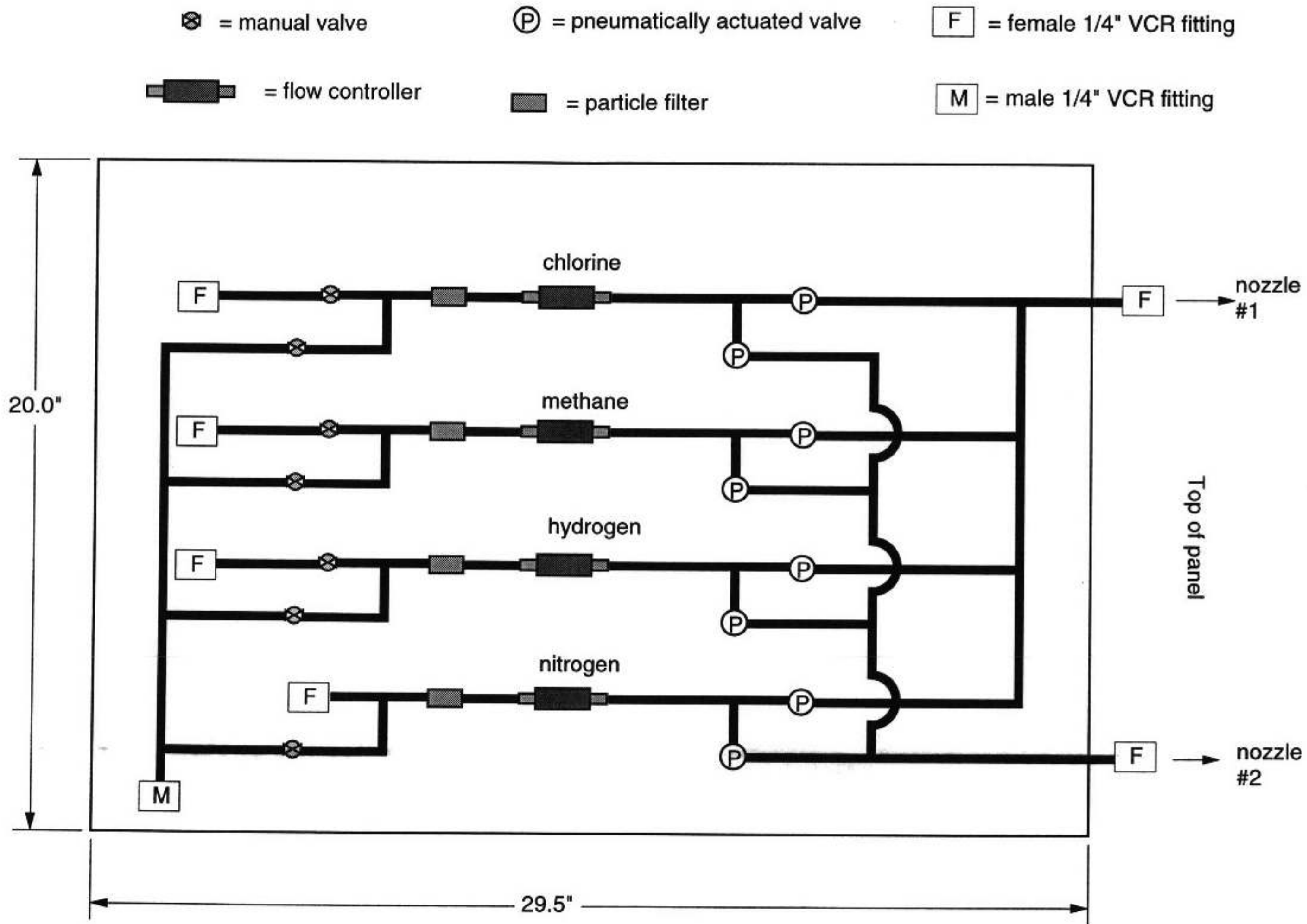

Figure A-39: Mass Flow Controller Panel

Appendix B

Vendor Source List

This section lists the model numbers, options, manufacturers and vendors of all the relevant parts purchased for the Kinetic Beam system.

B.1 General Vacuum Parts

B.1.1 Pumps

Cryo Pumps

CTI Cryogenics On–Board 10
Options: Metal-sealed cryo pump without keypad with On-Board module,
remote keypad – 19 inch rack mount,
regeneration exhaust port adaptor to 1/2 inch NPT,
14 inch OD Conflat^{TM} flange

CTI Cryogenics 8510 Compressor
220 V, 3ϕ power input
water-cooled

Rough Pump

Alcatel UM 2020 CP dual-stage rotary pump
15.9 cfm single-phase, air-cooled, corrosive chemical-resistant, stainless steel
bakable molecular sieve trap
Fomblin YL-VAX/RP 25/6 synthetic mechanical pump lubricant

Ion Pumps

Perkin–Elmer 270 l/sec Ion Pump
double 8 inch OD flange ports, no heaters

Perkin–Elmer Digitel™ 500 Ion Pump System Controller
dual pump operation capability, 110 V input power

B.1.2 Vacuum Pressure Gauges

Gauge Controllers

Granville–Phillips Model 350 Controller (source, main, flux gauge)
options: torr readout, 115 V power input, 2-channel process setpoint, RS-232 computer interface, UHV readout option

Granville–Phillips Model 307 Controller (transfer, Convectrons™)
options: dual ion gauge control, dual convectron readouts, EB degas, torr readout, side-by-side mounting

Vacuum Gauges

Granville–Phillips Model 275 Convectron™ Gauges
options: 1/4 inch NPT connector, 1.33 inch OD Conflat™ connector

Ion Gauges
Huntington Mechanical Laboratories
UHV Thoria-coated iridium Granville-Phillips compatible nude ion gauges

B.1.3 Gatevalves

MDC Vacuum

Electropneumatic gatevalves (14 inch and 13.25 inch OD)
metal-sealed bonnets, viton o-ring sealed gates,
24 VDC air actuated solenoid

Manual gatevalves (6 inch, 8 inch, 10 inch OD)
metal-sealed bonnets, viton o-ring sealed gates

B.2 Electrical Systems

B.2.1 Flow Controller Switching System

toggle switches
locking toggle switch for panel mounting, on-none-on

panel
19 inch rack mounting panel

B.2.2 Gatevalve Switch Box

box
BUD aluminum box

contactor
type ACC230UM20 (Newark #87F 2675)
110–120 V, 3-pole, 25 ampere

toggle switch
rocking toggle switch, Alcoswitch XR1 Series

B.2.3 Instrument Rack

Instrument Rack
Some model number!
Standard 19 inch instrument rack, 60 inches high, casters
vendor: Gerber Electronics

B.3 Vacuum Chambers

B.3.1 General Construction Contractors

Vacuum Chamber and Stage Manufacturing
Sharon Vacuums

UHV Welding, Machining
Sharon Vacuums (vacuum chamber),
Rentec Corp (gas panel),
Atomic Limited (nozzle welding),
Laboratories of Nuclear Science Machine Shop (nozzle machining)

Laser Drilling
Resonetics Micromachining Technology
(excimer laser drilling, 60±4 μm diameter)

B.3.2 Main Chamber

Substrate Manipulator
ISA Instruments Riber Division
Riber 2000 substrate manipulator, Model TPP

Mass Spectrometer
MKS/NGS Hiden HAL-II 201 Quadrupole Mass Spectrometer
1–300 amu, CRT-based microprocessor controller

Substrate Heater Temperature Controller
Eurotherm (Lindberg) Model 818P4
options: 0–5 VDC output, 4 programming, minute ramp rate, minute hold, 9600 baud computer interface, Type C thermocouple

Substrate Heater Power Supply
Lambda Electronics
Model LK 341 FM V Regulated Power Supply
0–20 VDC, 0–13.5 amps

B.3.3 Source Chamber

Skimmer
Beam Dynamics, Inc.
Model 2, Nickel, 1.22 mm diameter hole,

Nozzle Heater Temperature Controller
Eurotherm Model 818P4
options: 0–5 VDC output, 4 programming, minute ramp rate, minute hold, 9600 baud computer interface, Type K thermocouple

Nozzle Heater Power Supply
Lambda Electronics
Model LK 351-FM V Regulated Power Supply
0–36 VDC, 0–25 amps

B.3.4 Transfer Tube

Linear-Rotary Precision Magnetic Manipulator
Surface/Interface DBLRP
options: external polymeric bearings, 27 inch length,
end adaptor to fit Riber sample holder for 2 inch system,

4.5 inch–2.75 inch Conflat^{TM} adaptor flange in place of standard 2.75 inch double-sided Conflat^{TM} flange

Transfer Rod Regulated Mounting Bellows
4.5 inch bellows, special ordered from Huntington Mechanical Labs

Substrate Grip (on transfer rod)
Riber 2 inch molybdenum substrate grip,
M3 screws at 5 mm & 8 mm length

B.4 Nozzle

B.4.1 Nozzle Support Structures

Translation Stage
Thermionics EC–1600-1-1-2 X–Y–Z motion manipulator stage
Options: 1 inch X & Y direction motions,
2 inch Z-direction motion,
Traveling flange modification to allow clearance for screw heads

Inner Tubing
1/4 inch OD, 0.035 inch wall, seamless stainless steel 316L,
electropolished 15 RA
vendor: Stainless Pipe & Fitting

Support Tubing
3/4 inch OD, 0.065 inch wall, seamless stainless steel 304
vendor: Atlantic Stainless Co.

Nozzle Tip
Nickel 200, 3/4 inch OD rod
Inconel 600, 3/4 inch OD rod
vendor: AAA Metals Co., Inc.

Thermocouple
Omega Engineering
Type K, Inconel Sheath, ungrounded junction, 1/16 inch OD, 24 inch long

B.4.2 Nozzle Heater Materials

National Electric Wire
Ni–Cr (80%–20%) ribbon wire, 0.005 inch thick 1/8 inch wide.

approx .98 Ω/cm resistance

Zircar Alumina Refractory Sheet DM sheets
1/32 inch thick

Zircar Alumina Cement

Thermocouple Wire Ceramic Insulator
Omega Engineering
1/8 inch OD, 1/16 inchID, 6 inch long, single hole alumina tube

Electrical Wire
16 AWG copper bare wire

Wire Splice
Newark Electronics
Aluminum butt splice for 16 AWG wires

B.5 Gas Manifold

B.5.1 Gas Controller Instrumentation

4-Channel Flow Programmer
MKS Instruments, 147B
RS-232 port

Pressure Transducer
MKS Instruments, Baratron™ 127AA-10000S-SP070-90
option: 1/4 inch VCR male fitting, 10 atm pressure rating

Pressure Controller
MKS Instruments, Baratron 250C-1-D
digital display

B.5.2 Gas Panel

Mass Flow Controllers
MKS Instruments, 1461C
all-metal seal, Cajon™ 1/4 inch VCR male fittings (100 sccm, 50 sccm)

Valves

Nupro™ BNV–51(–C)
MS-SOL-2K-BN 115V Solenoid pneumatic – normally closed
vendor: Cambridge Valve & Fitting

Filters

Millipore WG2F01HR1
vendor: RenTec

Tubings

1/4 inch OD 316L Stainless Steel, electropolished to 15 RA
vendor: Rentec

Panel

RenTec

B.5.3 Miscellaneous Gas Piping

Sample Cylinder

Whitey 304 stainless steel cylinder
304L-HDF4-2250 sample cylinder, 1/4 inch NPT
vendor: Cambridge Valve & Fitting

Flexible Lines

Concoa flexible stainless steel gas piping lines.
All metal.

Hydrogen Gas Tank Regulator

Concoa Model 212-4391-CGA580
Two-stage, all stainless steel construction

Methane Gas Tank Regulator

Concoa Model 412-3911-CGA580
Two-stage, brass stock body, stainless steel diaphragm

Chlroine Gas Tank Regulator

Concoa Model 422-3391-CGA660
Single-stage, all stainless steel construction

References

[1] H. Temkin, L. R. Harriott, and M. B. Panish, "Ultrathin semiconductor layer masks for high vacuum focused Ga ion beam lithography," *App. Phys. Lett.*, vol. 53, no. 18, pp. 1478–1480, May 1988.

[2] Yukinori Ochiai, Kenji Gamo, and Susumu Namba, "Temperature dependence of maskless ion beam assisted etching of InP and Si using focused ion beam," *J. of Vac. Sci. Technol. B*, vol. 5, no. 1, pp. 423–425, Jan./Feb. 1987.

[3] K. D. Cummings, L. R. Harriott, G. C. Chi, and F. W. Ostermayer, Jr., "Using focused ion beam damage patterns to photoelectrochemically etch features in III-V materials," *Appl. Phys. Lett.*, vol. 48, no. 10, pp. 659–661, Mar. 1986.

[4] Yukinori Ochiai, Kenji Gamo, and Susumu Namba, "Maskless etching of GaAs and InP using a scanning microplasma," *J. of Vac. Sci. Technol. B*, vol. 1, no. 4, pp. 1047–1049, Oct./Dec. 1983.

[5] J. van de Ven and H. J. Nabben, "Anisotropic photoetching of III-V semiconductors," *J. Electrochem. Soc.*, vol. 137, no. 5, pp. 1603–1610, May 1990.

[6] *American Vacuum Society 40th National Symposium*, 1993.

[7] W. H. Juan and S. W. Pang, "High-aspect-ratio Si etching for microsensor fabrication," *J. of Vac. Sci. Technol. A*, vol. 13, no. 3, pp. 834–838, May/Jun. 1995.

[8] S. J. Pearton, U. K. Chakrabarti, A. Katz, C. R. Abernathy, W. S. Hobson, F. Ren, and T. R. Fullowan, "Iodine-based dry etching chemistries for InP and related compounds," in *Chemical Perspectives of Microelectronic Materials III*, vol. 282 of *Materials Research Society Symposium Proceedings*, pp. 123–130, Materials Research Society, 1992.

[9] S. J. Pearton, F. Ren, A. Katz, U. K. Chakrabarti, E. Lane, R. K. Kopf, C. R. Abernathy, C. S. Wu, D. A. Bohling, and J. C. Ivankovits, "Dry surface cleaning of plasma-etched HEMTs," in *Chemical Perspectives of Microelectronic Materials III*, vol. 282 of *Materials Research Society Symposium Proceedings*, pp. 131–138, Materials Research Society, 1992.

[10] *Plasma Etching for Microelectronic Fabrication*, 1991. Materials Research Society Technical Short Course.

[11] Konstantinos P. Giapis and Teresa A. Moore, "Hyperthermal neutral beam etching," *J. of Vac. Sci. Technol. A*, vol. 13, no. 3, pp. 959–965, May/Jun. 1995.

[12] Takashi Yunogami, Ken'etsu Yokogawa, and Tatsumi Mizutani, "Development of neutra-beam-assisted etcher," *J. of Vac. Sci. Technol. A*, vol. 13, no. 3, pp. 952–958, May/Jun. 1995.

[13] V. Swaminathan and A. T. Macrander, *Materials Aspects of GaAs and InP Based Structures.* Advanced Reference Series: Engineering, Prentice Hall, 1991.

[14] Peter P. Wegener, ed., *Molecular Beams and Low Density Gasdynamics*, vol. 4 of *Gasdynamics: A Series of Monographs.* Marcel Dekker, Inc., 1974.

[15] M. A. D. Fluendy and K. P. Lawley, *Chemical Applications of Molecular Beam Scattering.* Chapman and Hall, 1973.

[16] A. Kantrowitz and J. Grey, "A high intensity source for the molecular beam. Part I: Theoretical," *Rev. on Sci. Instrum.*, vol. 22, no. 5, pp. 328–332, May 1951.

[17] G. B. Kistiakowsky and William P. Slichter, "A high intensity source for the molecular beam. Part II:Experimental," *Rev. on Sci. Instrum.*, vol. 22, no. 5, pp. 333–337, May 1951.

[18] Giacinto Scoles, ed., *Atomic and Molecular Beam Methods*, vol. 1, ch. 2: Free Jet Sources by David R. Miller, pp. 14–53. Oxford University Press, 1988.

[19] J. B. Anderson, R. P. Andres, and J. B. Fenn, "Molecular Beams," in *Advances in Chemical Physics* (J. Ross, ed.), ch. 8: Supersonic Nozzle Beams, pp. 275–317, Interscience Publishers, 1966.

[20] Ming L. Yu and Lisa A. DeLouise, "Surface chemistry on semiconductors studied by molecular-beam reactive scattering," *Surface Science Reports*, vol. 19, no. 7/8, Jan. 1994.

[21] M. M. Audibert, C. Joffin, and J. Ducuning, "Vibrational relaxation in hydrogen–rare-gases mixtures," *Chem. Phys. Lett.*, vol. 19, no. 1, pp. 26–28, Mar. 1973.

[22] J. B. Anderson and J. B. Fenn, "Velocity distributions in molecular beams from nozzle sources," *The Physics of Fluids*, vol. 8, no. 1, pp. 780–787, May 1965.

[23] James B. Anderson, *Molecular Beams From Nozzle Sources*, pp. 1–91. Vol. 4 of Peter P. Wegener [14], 1974.

[24] Frank M. White, *Fluid Mechanics.* McGraw–Hill, 2nd ed., 1979.

[25] A. E. Zarvin and R. G. Sharafutdinov, "On the formation of supersonic molecular beam with skimmer," in *Rarefied Gas Dynamics*, vol. II, pp. 991–1000, Commissariat a l'energie atomique, 1979.

[26] C. Dankert and H. Legge, "High intensity molecular beams skimmed in continuum flow," in *Rarefied Gas Dynamics: Part II* (Sam S. Fisher, ed.), vol. 74 of *Progress in Astronautics and Aeronautics*, pp. 882–894, American Institute of Aeronautics and Astronautics, 1981.

[27] H. Ashkenas and F. S. Sherman, "The structure and utilization of supersonic free jets in low density wind tunnels," in *Rarefied Gas Dynamics* (J. H. de Leeuw, ed.), vol. II, pp. 84–105, Academic Press, 1966.

[28] Marianne McGonigal, *Reactive Chemisorption of Molecular Fluorine on Si(100).* Ph.D. dissertation, Massachusetts Institute of Technology, 1989.

[29] Robert W. Fox and Alan T. McDonald, *Introduction to Fluid Mechanics.* John Wiley & Sons, 2nd ed., 1978.

[30] T. Ishigaki, K. Shibuya, H. Sakaue, and S. H. Be, "Aluminum and stainless steel conflat flange sealing technique," in *American Vacuum Society 40th National Symposium*, 1993.

[31] Joseph R. Davis *et al.*, "Properties and Selection: Irons, Steels, and High-Performance Alloys," in *Metals Handbook*, vol. 1, pp. 930–969, ASM International, Tenth ed., 1990.

[32] Todd R. Hayes, P. A. Heimann, V. M. Donnelly, and K. E. Strege, "Maskless laser interferometric monitoring of InP/InGaAsP heterostructure reactive ion etching," *Appl. Phys. Lett.*, vol. 57, no. 25, pp. 2817–2819, 10 Dec. 1990.

[33] Naresh Chand and R. F. Karlicek, Jr., "Real-time monitoring and analysis of chemical wet etching of III-V compound semiconductors," *J. Electrochem. Soc.*, vol. 140, no. 3, pp. 703–705, Mar. 1993.

[34] P. Heimann and R. J. Schutz, "Optical etch-rate monitoring: computer simulation of reflectance," *J. Electrochem. Soc.*, vol. 131, no. 4, pp. 881–885, Apr. 1984.

[35] H. Alius and R. Schmidt, "Interference method for monitoring the refractive index and the thickness of transparent films during deposition," *Rev. Sci. Instrum.*, vol. 61, no. 4, pp. 1200–1203, Apr. 1990.

[36] C. Lavoie, S. R. Johnson, J. A. Mackenzie, T. Tiedje, and T. van Buuren, "Diffuse optical reflectivity measurements on GaAs during molecular-beam epitaxy processing," *J. of Vac. Sci. Technol. A*, vol. 10, no. 4, pp. 930–933, Jul./Aug. 1992.

[37] J. A. Sànchez-Gil, A. A. Maradudin, and E. R. Méndez, "Limits of validity of three perturbation theories of the specular scattering of light from one-dimensional, randomly rough, dielectric surfaces," *J. Opt. Soc. Am. A*, vol. 12, no. 7, pp. 1547–1558, July 1995.

[38] Jin Au Kong, *Electromagnetic Wave Theory.* John Wiley and Sons, Inc., Second ed., 1990.

[39] C. Richard Brundle, Charles A. Evans, Jr., and Shaun Wilson, "Encyclopedia of Materials Characterization," in *Materials Characterization Series: Surfaces, Interfaces, Thin Films*, pp. 698–710, Manning Publications Co., 1992.

[40] *NanoScope^R Command Reference Manual.*

[41] Ming L. Yu and Lisa A DeLouise, "Surface chemistry on semiconductors studied by molecular-beam reactive scattering," in *Surface Science Reports* [20], pp. 343–369.

[42] N. Furuhata, H. Miyamoto, A. Okamoto, and K. Ohata, "Chemical dry etching of GaAs and InP by Cl_2 using a new ultrahigh-vacuum dry-etching molecular-beam-epitaxy system," *J. Appl. Phys.*, vol. 65, no. 1, pp. 168–171, Jan. 1989.

[43] Chaochin Su, Zi-Guo Dai, Gang Ho Lee, and Matt Vernon, "A molecular beam study of the reaction of molecular chlorine with gallium arsenide," in *Chemical Perspectives of Microelectronic Materials II*, vol. 204 of *Materials Research Society Symposium Proceedings*, pp. 31–36, Materials Research Society, 1990.

[44] H. Hou, C. Su, G. Lee, Z. Dai, and M. Vernon, "Identification of the volatile reaction products of the $Cl_2(g)$ + GaAs(s) etching reaction," *J. of Vac. Sci. Technol.*, c. 1991. Paper referenced in [43], but could not be found.

[45] Takahisa Ohno, "Reactions of Cl with GaAs: A theoretical understanding of GaAs-surface etching," *Phys. Rev. B: Condensed Matter*, vol. 44, no. 15, pp. 8387–8390, 15 Oct. 1991.

[46] M. Vernon, T. R. Hayes, and V. M. Donnelly, "Intrinsic mechanism of smooth and rough morphology in etching of InP by Cl_2 determined by infrared laser interferometry," *J. of Vac. Sci. Technol. A*, vol. 10, no. 6, pp. 3499–3506, Nov./Dec. 1992.

[47] Y. L. Wang, H. Temkin, L. R. Harriott, R. A. Hamm, and J. S. Weiner, "Vacuum lithography for *in situ* fabrication of buried semiconductor microstructures," *Appl. Phys. Lett.*, vol. 57, no. 16, pp. 1672–1674, 15 Oct. 1990.

[48] Sylvia T. Ceyer, "New mechanisms for chemistry at surfaces," *Science*, vol. 249, pp. 133–139, 13 Jul. 1990.

[49] Sylvia T. Ceyer, "Collision-induced dissociative chemisorption," in *The RLE Progress Report Number 131*, The Research Laboratory of Electronics, Massachusetts Institute of Technology, 1988.

[50] David Lide, ed., *CRC Handbook of Chemistry and Physics.* CRC Press, 71st ed., 1990–1991.

[51] C. Robert, "Dampfdruckmessungen an Indiumhalogeniden," *Helvetica Physica Acta*, vol. 9, pp. 405–436, 1936.

[52] S. J. Pearton, "Dry etching techniques and chemistries for III–V semiconductors," in *Long-Wavelength Semiconductor Devices, Materials, and Processes*, vol. 216 of *Materials Research Society Symposium Proceedings*, pp. 277–290, Materials Research Society, 1990.

[53] Robert G. Wilson, *Ion Mass Spectra*, pp. 339–340. John Wiley & Sons, 1974. A Wiley–Interscience Publication.

[54] Keizo Suzuki, Susumu Hiraoka, and Shigeru Nishimatsu, "Anisotropic etching of polycrystalline silicon with a hot Cl_2 moleculat beam," *J. Appl. Phys.*, vol. 64, no. 7, pp. 3697–3705, 1 Oct. 1988.

[55] Alessandro Stano, "Chemical etching characteristics of InGaAs/InP and InAlAs/InP heterostructures," *J. Electrochem. Soc.: Solid-State Science and Technology*, vol. 134, no. 2, pp. 448–452, Feb. 1987.

[56] P. H. L. Notten, "The influence of native oxide layers of InP on the shape of etching profiles at resist edges," *J. Electrochem. Soc.*, vol. 138, no. 1, pp. 243–249, Jan. 1991.

[57] D. N. MacFadyen, "On the preferential etching of GaAs by H_2SO_4–H_2O_2–H_2O," *J. Electrochem. Soc.: Solid-State Science and Technology*, vol. 130, no. 9, pp. 1934–1941, Sept. 1983.

[58] A. W. Laubengayer and R. B. Schirmer, "The chlorides of gallium," *Amer. Chem. Soc. Journ.*, vol. 62, pp. 1578–1583, June 1940.

[59] Y. Sugimoto, K. Akita, M. Taneya, and H. Hidaka, "Submicron pattern etching of GaAs by *in-situ* electron beam lithography using a pattern generator," *Appl. Phys. Lett.*, vol. 57, no. 10, pp. 1012–1014, 3 Sep. 1990.

[60] Mototaka Taneya, Yoshimasa Sugimoto, Hiroshi Hidaka, and Kenzo Akita, "Electron-beam-induced Cl_2 etching of GaAs," *Japanese J. of Appl. Phys.*, vol. 28, no. 3, pp. 515–517, Mar. 1989.

[61] E. M. Clausen, Jr., J. P. Harbison, C. C. Chang, P. S. D. Lin, and H. G. Craighead, "Positive and negative 'resistless' lithography of GaAs by electron beam exposure and thermal Cl_2 etching," *Appl. Phys. Lett.*, vol. 57, no. 10, pp. 1043–1045, 3 Sep. 1990.

[62] A. Hase, R. Gibis, H. Künzel, and U. Griebenow, "*In-situ* native oxide removal from AlGaInAs surfaces by hydrogen radical treatment for molecular beam epitaxy regrowth," *Appl. Phys. Lett.*, vol. 65, no. 11, pp. 1406–1408, 12 Sep. 1994.

[63] C. M. Rouleau and R. M. Park, "GaAs substrate cleaning for epitaxy using a remotely generated atomic hydrogen beam," *J. Appl. Phys.*, vol. 73, no. 9, pp. 4610–4613, 1 May 1993.

[64] Masamichi Yamada, Yuichi Ide, and Kiyohide Tone, "Effect of atomic hydrogen on GaAs (001) substrate oxide studied by temperature-programmed desorption," *Jpn. J. Appl. Phys.* Pt. 2, vol. 31, no. 8B, pp. L1157–L1160, Aug. 1992.

[65] J. P. Contour, J. Massies, and A. Saletès, "*In situ* chemical etching of GaAs(001) and InP(001) substrates by gasous HCl prior to molecular-beam epitaxy growth," *J. of Vac. Sci. Technol. B*, vol. 5, no. 3, pp. 730–733, May/Jun. 1987.

[66] Krishna V. Shenoy, Clifton G. Fonstad, Jr., Anette C. Grot, and Dimitri Psaltis, "Monolithic optoelectronic circuit design and fabrication by epitaxial growth on commercial VLSI GaAs MESFETs," *Photonics Tech. Lett.*, vol. 7, no. 1, pp. 1–3, January 1995.

[67] J. F. Ahadian, S. G. Patterson, P. T. Vaidyanathan, Y. Royter, D. Mull, G. S. Petrich, W. D. Goodhue, S. Prasad, L. A. Kolodziejski, and C. G. Fonstad, Jr., "Monolitic OEICs using GaAs VLSI technology," in *SPIE Optoelectronics '97 Annual Proceedings*, (San Jose, CA), Society for Photonic Instrumentation Engineers, February 1997. to be published.

Biographical Note

Isako Hoshino was born in Tokyo, Japan in 1966 to Takao and Kaneko Hoshino. She grew up in the San Francisco Bay Area and attended Mills High School in Millbrae, CA. During her years in California, she also attended San Francisco Japanese Language School where she studied to maintain her Japanese reading, writing and speaking skills at a native level. She attended undergraduate school at the Massachusetts Institute of Technology in Cambridge, MA with scholarships from the Burlingame Rotary Club and California Scholarship Federation for 1985. She received her Bachelor of Science degree in June 1989 in the Department of Materials Science and Engineering with a double concentration in Ceramics and Electronics Materials, with a minor in Music.

Ms. Hoshino's honors include Tau Beta Pi Engineering Honor Society, Sigma Xi Research Society and a Departmental Letter of Excellence. She is also a member of Alpha Chi Sigma Professional Chemistry Fraternity which she served as a chapter advisor while the chapter was in search for a faculty advisor. As a graduate student, also at the Massachusetts Institute of Technology, she was honored as an AT&T Bell Laboratories (now Lucent Technologies) GRPW Fellow.